ON THE RATE-LIMITING STEP OF THE WGS REACTION: DESIGN OF THE MODEL CATALYST

Nuria García Moncada

Ph.D. Thesis

2017

Supervisors

Francisca Romero Sarria

José Antonio Odriozola Gordón

CONTENTS

CHAPTER 1.

GENERAL INTRODUCTION

The Water Gas Shift (WGS) reaction was discovered in 1780 by the Italian physicist Felice Fontana from the formation of an inflammable gas by quenching red-hot coal with water under a glass bell jar.[1] Shortly after, in 1783, Lavoisier formulated the reaction [$CO + H_2O \leftrightarrows CO_2 + H_2$] and gave to hydrogen its name (from Greek: *hydro = water*, and *genes = born of*).[2] However, it was not until the 20th century when the reaction achieved industrial value.

Prior to the use of WGS reaction, the H_2 production was carried out from electrolysis of water or from reactions between strong acids and iron metal. A new alternative was imperative due to the cost of these processes and the WGS reaction gains[3] its prominence with the development of ammonia synthesis process in the beginning of 20th century. In 1906 the German chemist Fritz Haber developed a process for NH_3 production at commercial scale in which 6 % of ammonia was obtained from N_2 and H_2. Haber intensified the process by adding a recycle system getting a patent for it, lately purchased by BASF.[4] Company researchers then start to test different metallic oxides, as a part of ammonia synthesis process, in order to find a catalyst able to achieve faster the WGS equilibrium state. In 1909, Haber studied the equilibrium constant (K_p) at different temperatures and observed that the constant decreases upon increasing the temperature thereby implying compromise between thermodynamics and kinetics.[5]

Thus, the progress in ammonia production from the early 20th century was the starting point for H_2 production processes development, and, particularly, for the WGS reaction understanding.

In the second half of the century, the advancements in hydrogen fuel processor technology renewed the quest for high performance WGS catalysts able to produce more H_2 reducing the CO content, which acts as contaminant for the fuel cell technology. Thus, even in present days the WGS reaction remains very important reaction for the energy production processes.

As for the WGS reactors at industrial scale, before 1960, coupled multiple beds of iron and chromium oxides with cooling interbeds were employed. This system provided CO outlet concentration of *ca.* 1 %. Later, this configuration was modified towards two separated reactors which are used nowadays: the first one at high temperature (310 – 450 ºC) with iron/chromium oxides as catalyst, and the second with Cu-based catalyst operating at low temperatures (150 – 250 ºC) to achieve CO outlet content below 0.1 %.[5] Few years later, in 1974 at the THEME Conference in Florida, hydrogen energy was proposed as viable alternative to the fossil fuel energy system and as a solution of the global environmental problems.[6] According to this objective, research activities rapidly grown to develop technologies needed for the introduction of the H_2 based energy system, including WGS reaction development specially focused on small-scale fuel processors. Thus, for instance, in April 1994 was shown the first hydrogen based mobile system: a fuel cell for a bus.[7]

Regarding the catalysts, the 21st century's large-scale WGS reaction development has allowed the install of relatively active and stable catalysts. However, these catalyst' configuration still present some disadvantages which make their applicability in mobile and

small-scale systems unfeasible.[8] For instance, the Fe- and Cr-based catalysts for high temperature WGS reaction (HT-WGS) deactivates by thermal sintering and should work in temperature range where the thermodynamic equilibrium composition presents lower CO conversion. In addition, the ratio of steam to CO is a critical parameter since operating at low ratios lead to the formation of metallic iron, methanation, carbon deposition and Fischer-Tropsch reaction.[9,10] It is also desirable to replace chromium by a non-toxic promoter and to obtain a catalyst formulation that can afford space velocities over 40000 h^{-1} for mobile and small-scale applications.[10]

On the other side, the low-temperature Cu-based catalysts (LT-WGS) provide high conversion working at low temperatures where the most favourable thermodynamic equilibrium compositions are achieved. However, their kinetics is very slow and requires very low space velocities (around 1000 – 2000 h^{-1}) and large reactor volumes. The pyrophoricity of the Cu-based catalysts is another disadvantage, the catalysts need special precaution during the start-up and shut-down processes which makes them unsuitable for fuel cell application.[11] These catalysts also present high sensitivity to sulphur and chlorine compounds and are deactivated by thermal sintering.[10,12–14]

In accordance with the previously mentioned, the development of new catalytic formulations for mobile and small-scale devices requires the use of compact catalytic bed operating at high space velocities and low-to-intermediate temperatures keeping good kinetic, stability and safety properties. In this context, precious metals like Pt,

Rh, Ru, Au and Pd supported on partially reducible oxides (CeO_2, TiO_2, ZrO_2, Fe_2O_3…) have been proposed as promising catalysts. They present usually high activity in the 250 - 400 ºC temperature range, high space velocities, some of the metals do not require a pre-reduction process and can be safely exposed to air during the start-up and shut-down without significant loss of performance.[10,15–22] The formulation based on precious metal supported on reducible oxide presents bifunctionality where the support is actively involved in water activation step (in both proposed redox or associative mechanism), which has been considered as determining-step in WGS reaction. Thus, catalyst' activity is increased when the support possess oxygen vacancies able to improve the water activation.[10,17,23–28] Gonzalez-Castaño *et al.* studied the influence of the ceria doped with Zr and Fe on the activity of supported Pt in the WGS reaction. They found better stability and activity for the bi-doped sample and attributed it to the increase of the redox cycles and Ce^{3+} - Oxygen vacancies active sites which invoke greater concentration and mobility of H species issued from water (OH and H species).[29] Moreover, in other work they have studied the influence of an added buffer layer to catalyst' capacity to dissociate water under WGS reaction conditions and they found that the addition of an reducible oxide improves the water dissociation step.[30] In the same context, other authors studied the mechanism of the WGS reaction over precious metal-based catalysts with modified supports. It is always found a high-energy barrier for water adsorption and diffusion as well as a significant influence of water pressure in the kinetics showing positive and the highest reaction orders. Grenoble *et al.*[31] studied the

influence of the supported precious metals on the WGS kinetic parameters. Germani *et al.*[26] found for structured Pt/ceria/alumina catalyst rate enhancement when the amount of the water adsorption sites increased. In the same way, Phatak *et al.*[32] studied the kinetic parameters for WGS on Pt-based catalysts and they reported in general very high-energy barriers for water dissociation but a decrease of the water apparent reaction order from 1 to 0.5 using ceria as support reflecting the improvement of the water activation step. Likewise, Grabow *et al.*[28] determined also high barriers for water adsorption and dissociation and found WGS rate limitation at low OH coverage. Kalamaras *et al.*,[33,34] studied the significant role of the oxygen vacancies in the WGS reaction mechanism and also reported reaction order 1 for the water. Moreover, they observed an increment of the catalyst' activity upon oxygen vacancies increasing.

The importance of water activation step and oxygen vacancies for the WGS reaction kinetics discussed above applies also to other than Pt precious metals.[35–37] Therefore, regardless the proposed WGS mechanism (redox or associative), the water activation step is the determining step of the reaction no matter the involved metal (Cu and/or precious metals). Consequently, the improvement of this step will lead to better catalytic activity and kinetics, thereby approaching the applicability of the WGS technology to mobile devices.

In the last years, some catalyst' formulations for H_2 production through WGS reaction have been patented. In 2005, Rogers *et al.*[38] presented a catalyst based on a precious metal (Pt or Rh) over La-doped TiO_2 support showing high activity and stability. In 2008,

Daza *et al.*[39] proposed a catalyst formulation consisting of active phase supported over a layer of rare-earth oxide promoter deposited on an oxide substrate with high superficial mobility. In 2010, Ilinich *et al.*[40] registered for the BASF company a Pt group metal dispersed on an inorganic oxide support modified with carbon-containing burn-out additive and a rare earth oxide. More recently, in 2015, Wachsman *et al.*[41] introduced a proton conducting membrane to the H_2 production device to increase the yield by H_2 removal.

The common between these formulations is the presence of mixed oxides and the introduction of rare earths. They seem to be proton conductors. Ionic conducting materials and, more specifically, the proton conductors are very attractive for a wide range of technological applications, e.g. mixed ionic-electronic conducting (MIEC) oxides for gas sensors, as catalysts, for clean energy production, as oxygen/hydrogen separation membrane,[42,43] or in solid-oxide fuel cells (SOFCs) to convert the chemical into electrical energy.[44] Generally, an ionic conductor comprises an oxide doped with aliovalent cations to create oxygen vacancies in stable structures, like perovskite, pyrochlore or fluorite-type structures.[45–47] These compounds are able to dissociate and increase the mobility of ions like O^{2-}, OH^- or H^+.[48,49]

Producing a material with both, high ionic conductivity and high stability represents still a big challenge.[50] For example, it was reported high conductivity for the $BaCeO_3$ based perovskites but a very low phase stability, contrary to the $CaZrO_3$, which presents good stability but very low conductivity.[51] In this context, doped zirconium

based oxides possess good stability and conductivity and are easy to synthesize.[52,53]

Besides the zirconia-based ionic conductors,[51,53,54] Mo-based structures also present good stability and ionic conductivity. For example, LAMOX compounds or doped molybdenum oxides and bronzes, exhibit important ion exchange capacity and, particularly, important proton mobility due to water molecules adsorbed on its surface.[55–61] Moreover, doping both groups (Zr- or Mo-based materials) with rare earths has been reported to exhibit better stabilities and good proton conductivity.[62–67]

For all above, the main objective of this research is the incorporation of proton conductors to precious metal based WGS catalyst formulation in order to promote its activity by increasing the capacity of the system to activate water due to the conductor' ability to dissociate and transport water species. Concretely, Eu-doped ZrO_2 and Mo- and Eu-doped ZrO_2 oxides with several compositions and a $Pt/CeO_2/Al_2O_3$ are used in various combinations to formulate the WGS catalyst. The present thesis is structured in 6 chapters including this introduction as first one. In the Chapter 2, it has been compiled the techniques, setups and operation conditions used during the thesis. The synthesis and characterization of the prepared materials are reported in Chapters 3 and 4. Specifically, synthesis and elemental characterization (XRD, XRF, XPS, N_2 adsorption, TPR, several spectroscopies, TEM…) of the catalyst and the mixed oxides as proton conductors have been discussed in Chapter 3. Furthermore, the ionic conductivity measurements (IS) of the prepared mixed oxides in

different controlled atmospheres (inert, oxidizing and wet conditions) has been described and discussed in Chapter 4. Besides, in this chapter has been carried out *in situ* DRIFTS measurements on the proton conductors for water adsorption leading to a proton conductivity model. Next, in Chapter 5, a screening of catalytic activity in WGS reaction on the catalyst and on physical mixtures of the catalyst with proton conductors has been carried out. The performances have been compared and related with the proton conductivity provided for each mixed oxide. Moreover, it has been tested the catalyst-proton conductor ratio, the space velocity and the structuration of the catalyst in WGS reaction. Thus, in this chapter is also reported the manufacture and characterization of the structured samples. Finally, kinetic analysis on powdered and structured samples of the best catalyst formulation, and *operando* DRIFTS were carried out to elucidate the influence and the role of the proton conductor in the reaction mechanism (Chapters 6).

In agreement with Spanish regulations, a summary in Spanish language (*Resumen*) is also added in this manuscript. The most relevant conclusions (*General Conclusions*) have been summarized at the end of the thesis.

REFERENCES

1. Burns, D. T., Piccardi, G. & Sabbatini, L. Some people and places important in the history of analytical chemistry in Italy. *Microchim. Acta* **160,** 57–87 (2008).
2. Lavoisier, A. L. *Oeuvres de Lavoisier, Vol. II*. (Imprimerie Impériale, 1862).

3. Mond, L. & Langer, C. No Title. 608 (1888).

4. Pattabathula, V. & Richardson, J. Introduction to Ammonia Production. *Chem. Eng. Prog.* **112,** (2016).

5. Rhodes, C., Hutchings, G. J. & Ward, A. M. Water-gas shift reaction: finding the mechanistic boundary. *Catal. Today* **23,** 43–58 (1995).

6. *Handbook of Hydrogen Energy*. (CRC Press Taylor & Francis Group, 2014).

7. Erickson, P. A., Tang, H.-Y. (Ray) & Vernon, D. R. in *Handbook of Hydrogen Energy* (eds. Sherif, S. A., Goswami, D. Y., Stefanakos, E. K. & Steinfeld, A.) 1020 (CRC Press Taylor & Francis Group, 2014).

8. Song, C. Fuel processing for low-temperature and high-temperature fuel cells: Challenges, and opportunities for sustainable development in the 21st century. *Catal. Today* **77,** 17–49 (2002).

9. Twigg, M. V. *Catayst Handbook*. (Wolfe Publishing Ltd., 1989).

10. Ratnasamy, C. & Wagner, J. P. Water Gas Shift Catalysis. *Catal. Rev. Sci. Eng.* **51,** 325–440 (2009).

11. Kam, R., Scott, J., Amal, R. & Selomulya, C. Pyrophoricity and stability of copper and platinum based water-gas shift catalysts during oxidative shut-down/start-up operation. *Chem. Eng. Sci.* **65,** 6461–6470 (2010).

12. Kuijpers, E. G. M., Tjepkema, R. B. & Van der Wal, W. J. J. Structure-sensitivity of the water-gas shift reaction over highly active Cu/SiO2 catalysts. *Appl. Catal.* **25,** 139–147 (1986).

13. Twigg, M. V. & Spencer, M. S. Deactivation of supported copper metal catalysts for hydrogenation reactions. *Appl. Catal. A Gen.* **212,** 161–174 (2001).

14. Spencer, M. S. The role of zinc oxide in Cu/ZnO catalysts for methanol synthesis and the water–gas shift reaction. *Top. Catal.* **8,** 259–266 (1999).

15. Farrauto, R. J. *et al.* Precious Metal Catalysts Supported on Ceramic and Metal Monolithic Structures for the Hydrogen Economy. *Catal. Rev. Sci. Eng.* **49,** 141–196 (2007).

16. Andreeva, D., Idakiev, V., Tabakova, T. & Andreev, A. Low-Temperature Water-Gas Shift Reaction over Au/α-Fe2O3. *J. Catal.* **158,** 354–355 (1996).

17. Luengnaruemitchai, A., Osuwan, S. & Gulari, E. Comparative

studies of low-temperature water-gas shift reaction over Pt/CeO2, Au/CeO2, and Au/Fe2O3 catalysts. *Catal. Commun.* **4,** 215–221 (2003).

18. Andreeva, D. *et al.* Low-temperature water-gas shift reaction over Au/CeO2 catalysts. *Catal. Today* **72,** 51–57 (2002).

19. Goerke, O., Pfeifer, P. & Schubert, K. Water gas shift reaction and selective oxidation of CO in microreactors. *Appl. Catal. A Gen.* **263,** 11–18 (2004).

20. Panagiotopoulou, P. & Kondarides, D. I. Effect of morphological characteristics of TiO2-supported noble metal catalysts on their activity for the water-gas shift reaction. *J. Catal.* **225,** 327–336 (2004).

21. Thinon, O., Diehl, F., Avenier, P. & Schuurman, Y. Screening of bifunctional water-gas shift catalysts. *Catal. Today* **137,** 29–35 (2008).

22. Ruettinger, W., Ilinich, O. & Farrauto, R. J. A new generation of water gas shift catalysts for fuel cell applications. *J. Power Sources* **118,** 61–65 (2003).

23. Panagiotopoulou, P., Papavasiliou, J., Avgouropoulos, G., Ioannides, T. & Kondarides, D. I. Water-gas shift activity of doped Pt/CeO2 catalysts. *Chem. Eng. J.* **134,** 16–22 (2007).

24. Panagiotopoulou, P. & Kondarides, D. I. Effect of the nature of the support on the catalytic performance of noble metal catalysts for the water-gas shift reaction. *Catal. Today* **112,** 49–52 (2006).

25. Sato, Y., Terada, K., Soma, Y., Miyao, T. & Naito, S. Marked addition effect of Re upon the water gas shift reaction over TiO2 supported Pt, Pd and Ir catalysts. *Catal. Commun.* **7,** 91–95 (2006).

26. Germani, G. & Schuurman, Y. Water-Gas Shift Reaction Kinetics Over ?-Structured Pt/CeO2/Al2O3 Catalysts. *Am. Inst. Chem. Eng.* **52,** 1806–1813 (2006).

27. Rodriguez, J. A., Liu, P., Hrbek, J., Evans, J. & Pérez, M. Water Gas Shift Reaction on Cu and Au Nanoparticles Supported on CeO2(111) and ZnO(0001): Intrinsic Activity and Importance of Support Interactions. *Angew. Chemie - Int. Ed.* **46,** 1329–1332 (2007).

28. Grabow, L. C., Gokhale, A. A., Evans, S. T., Dumesic, J. A. & Mavrikakis, M. Mechanism of the water gas shift reaction on Pt: First principles, experiments, and microkinetic modeling. *J. Phys. Chem. C* **112,** 4608–4617 (2008).

29. González-Castaño, M., Ivanova, S., Ioannides, T., Centeno, M. A. & Odriozola, J. A. Deep insight into Zr/Fe combination for successful Pt/CeO2/Al2O3 WGS catalyst doping. *Catal. Sci. Technol.* (2017). doi:10.1039/C6CY02551J

30. González-Castaño, M. *et al.* Structuring Pt/CeO2/Al2O3 WGS catalyst: Introduction of buffer layer. *Appl. Catal. B Environ.* **200,** 420–427 (2017).

31. Grenoble, D. C., Estadt, M. M. & Ollis, D. F. The Chemistry and Catalysis of the Water Gas Shift Reaction. *J. Catal.* **67,** 90–102 (1981).

32. Phatak, A. A. *et al.* Kinetics of the water-gas shift reaction on Pt catalysts supported on alumina and ceria. *Catal. Today* **123,** 224–234 (2007).

33. Kalamaras, C. M., Panagiotopoulou, P., Kondarides, D. I. & Efstathiou, A. M. Kinetic and mechanistic studies of the water-gas shift reaction on Pt/TiO2 catalyst. *J. Catal.* **264,** 117–129 (2009).

34. Kalamaras, C. M., Dionysiou, D. D. & Efstathiou, A. M. Mechanistic Studies of the Water–Gas Shift Reaction over Pt/CexZr1– xO2 Catalysts: The Effect of Pt Particle Size and Zr Dopant. *ACS Catal.* **2,** 2729–2742 (2012).

35. Clay, J. P., Greeley, J. P., Ribeiro, F. H., Delgass, W. N. & Schneider, W. F. DFT Comparison of Intrinsic WGS Kinetics over Pd and Pt. *J. Catal.* **320,** 106–117 (2014).

36. Vajani, G. N., Ng, S. L. & Lund, C. R. F. Rate expression for water-gas shift over a gold/ferrochrome catalyst. *Ind. Eng. Chem. Res.* **50,** 10493–10499 (2011).

37. Mullen, G. M., Gong, J., Yan, T., Pan, M. & Mullins, C. B. The Effects of Adsorbed Water on Gold Catalysis and Surface Chemistry. *Top. Catal.* **56,** 1499–1511 (2013).

38. Rogers, D. B., Walsh, T. L., Madden, M. R. & Balakos, M. W. Water gas shift catalyst on a lanthanum-doped anatase titanium dioxide support for fuel cells application. 4 (2005).

39. Daza Bertrand, L., Benito González, M. J., Isabel Gómez, R. & Padilla Palma, R. Catalizadores para conversión de monóxido de carbono en hidrógeno y su uso en el proceso catalítico de enriquecimiento en hidrógeno de una corriente de gas que puede alimentar una pila de combustible. 11 (2008).

40. Ilinich, O. M., Farrauto, R. J., Reuttinger, W. F. & Yang, X. Precious metal water-gas shift catalyst with oxide support modified

with rare earth elements. 6 (2010).

41. Wachsman, E. D., Yoon, H. S., Oh, T. & Li, J. Proton conducting membranes for hydrogen production and separation. 25 (2015).

42. Nalini, V., Haugsrud, R. & Norby, T. High-temperature proton conductivity and defect structure of TiP2O7. *Solid State Ionics* **181,** 510–516 (2010).

43. Kendall, K. R., Navas, C., Thomas, J. K. & zur Loye, H.-C. Recent Developments in Oxide Ion Conductors: Aurivillius Phases. *Chem. Mater.* **8,** 642–649 (1996).

44. Gao, Z., Mogni, L. V., Miller, E. C., Railsback, J. G. & Barnett, S. A. A perspective on low-temperature solid oxide fuel cells. *Energy Environ. Sci.* **9,** 1602–1644 (2016).

45. Stølen, S., Bakken, E. & Mohn, C. E. Oxygen-deficient perovskites: linking structure, energetics and ion transport. *Phys. Chem. Chem. Phys.* **8,** 429–447 (2006).

46. Malavasi, L., Fisher, C. A. J. & Islam, M. S. Oxide-ion and proton conducting electrolyte materials for clean energy applications: structural and mechanistic features. *Chem. Soc. Rev.* **39,** 4370–4387 (2010).

47. Huse, M., Norby, T. & Haugsrud, R. Effects of A and B site acceptor doping on hydration and proton mobility of LaNbO4. *Int. J. Hydrogen Energy* **37,** 8004–8016 (2012).

48. Sunarso, J. *et al.* Mixed ionic – electronic conducting (MIEC) ceramic-based membranes for oxygen separation. *J. Memb. Sci.* **320,** 13–41 (2008).

49. Kreuer, K. Proton Conductivity : Materials and Applications. *Chem. Mater.* **8,** 610–641 (1996).

50. Wang, S. *et al.* Novel Chemically Stable Ba3Ca1.18Nb1.82−xYxO9−δ Proton Conductor: Improved Proton Conductivity through Tailored Cation Ordering. *Chem. Mater.* **26,** 2021–2029 (2014).

51. Kreuer, K. D. Aspects of the formation and mobility of protonic charge carriers and the stability of perovskite-type oxides. *Solid State Ionics* **125,** 285–302 (1999).

52. Meredig, B. & Wolverton, C. Dissolving the Periodic Table in Cubic Zirconia: Data Mining to Discover Chemical Trends. *Chem. Mater.* **26,** 1985–1991 (2014).

53. Thangadurai, P., Sabarinathan, V., Bose, A. C. & Ramasamy, S.

Conductivity behaviour of a cubic/tetragonal phase stabilized nanocrystalline La2O3 - ZrO2. *J. Phys. Chem. Solids* **65,** 1905–1912 (2004).

54. Babilo, P., Uda, T. & Haile, S. M. Processing of yttrium-doped barium zirconate for high proton conductivity. *J. Mater. Res.* **22,** 1322–1330 (2007).

55. El Khal, H. *et al.* Effect of porosity on the electrical conductivity of LAMOX materials. *Solid State Ionics* **304,** 75–84 (2017).

56. Muñoz-García, A. B., Pavone, M., Ritzmann, A. M. & Carter, E. A. Oxide ion transport in Sr2Fe1.5Mo0.5O(6-δ), a mixed ion-electron conductor: new insights from first principles modeling. *Phys. Chem. Chem. Phys.* **15,** 6250–6259 (2013).

57. Aguadero, A., Perez-Coll, D., Alonso, J. A., Skinner, S. J. & Kilner, J. A. A new family of Mo-doped SrCoO3-delta perovskites for application in reversible solid state electrochemical cells. *Chem. Mater.* **24,** 2655–2663 (2012).

58. Vega-Castillo, J. E., Ravella, U. K., Corbel, G., Lacorre, P. & Caneiro, A. Thermodynamic stability, structural and electrical characterization of mixed ionic and electronic conductor La2Mo2O8.96. *Dalt. Trans.* **41,** 7266–7271 (2012).

59. Schöllhorn, R., Schulte-Nölle, T. & Steinhoff, G. Layered intercalation complexes of the hydrogen bronze H0.5MoO3 with organic lewis bases. *J. Less-Common Met.* **71,** 71–78 (1980).

60. Adams, S. CDW Superstructures in Hydrogen Molybdenum Bronzes HxMoO3. *J. Solid State Chem.* **149,** 75–87 (2000).

61. *Spillover of Adsorbed Species*. *Studies in Surface Science and Catalysis* **17,** (Elsevier Science Publishers B.V, 1983).

62. Magrasó, A., Kjølseth, C., Haugsrud, R. & Norby, T. Influence of Pr substitution on defects, transport, and grain boundary properties of acceptor-doped BaZrO3. *Int. J. Hydrogen Energy* **37,** 7962–7969 (2012).

63. Labrincha, J. A., Frade, J. R. & Marques, F. M. B. Protonic conduction in La2Zr2O7-based pyrochlore materials. *Solid State Ionics* **99,** 33–40 (1997).

64. Besikiotis, V., Ricote, S., Jensen, M. H., Norby, T. & Haugsrud, R. Conductivity and hydration trends in disordered fluorite and pyrochlore oxides: A study on lanthanum cerate-zirconate based compounds. *Solid State Ionics* **229,** 26–32 (2012).

65. Xia, X.-L., Liu, Z.-G., Ouyang, J.-H. & Zheng, Y. Preparation, Structural Characterization, and Enhanced Electrical Conductivity of Pyrochlore-type (Sm1-xEux)2Zr2O7 Ceramics. *Fuel Cells* **12,** 624–632 (2012).

66. Morozov, V. *et al.* Na2/7Gd4/7MoO4: a Modulated Scheelite-type Structure and Conductivity Properties. *Inorg. Chem.* **51,** 5313–5324 (2012).

67. Amsif, M. *et al.* Mo-Substituted Lanthanum Tungstate La28-yW4+yO54+d: A Competitive Mixed Electron-Proton Conductor for Gas Separation Membrane Applications. *Chem. Mater.* **24,** 3868–3877 (2012).

CHAPTER 2.

EXPERIMENTAL TECHNIQUES AND CATALYTIC TESTS

Abstract

A general definition of the experimental techniques applied during this thesis as well as a brief description of the used instrument and methods are presented in this chapter. The selected characterization techniques have the aim of correlating the catalysts' activity and their physicochemical and textural properties. In addition, a deep characterization of the proton conductors has been carried out to elucidate its role in the catalytic reaction.

Moreover, the preparation of the structured catalyst (slurry formulation) and the manufactured metallic micromonolithic support are also shown.

In this chapter, it has been introduced the performed catalytic tests of WGS reaction, the *operando* studies like DRIFTS and EXAFS in WGS reaction conditions and the kinetic tests. The applied conditions and the scheme of the used rigs are also exhibited.

2.1. CHARACTERIZATION TECHNIQUES

2.1.1. Thermogravimetric Analysis (TGA) and Differential Thermal Analysis (DTA).

TGA is used to measure the amount of weight change of a material, either as a function of increasing temperature, or isothermally as a function of time, in different atmospheres. For its part, DTA measures any temperature difference between the sample and an inert reference which both are made to undergo identical thermal cycles. Thus, very similar to DSC technique, the amount of energy absorbed or released by a sample when it is heated or cooled is detected provides quantitative and qualitative data on endothermic (heat absorption) and exothermic (heat evolution) processes. The area under a DTA peak is the enthalpy change and is not affected by the heat capacity of the sample.

The measurements were carried out in a TA Instruments Q600 Simultaneous TG/DTA/DSC instrument, which allow to get the information at the same time, on the same instrument and same sample. Thus, the analysis differentiates endothermic and exothermic events, which have no associated weight change (e.g. melting and crystallization) from those which involve a weight change (e.g. degradation). The measurements were performed in air atmosphere from room temperature to 900 ºC with a heating rate of 10 $^{o}C \cdot min^{-1}$.

2.1.2. X-Ray Diffraction (XRD).

X-ray diffraction (XRD)[1] is a basic no destructive analytical technique used for phase identification of a crystalline material. XRD is based on constructive interference of monochromatic X-rays

diffracted by the planes in a crystalline sample. A diffraction peak is observed when the Bragg's Law is satisfied (Eq. 2.1); this is, the incident rays interact with a crystalline plane producing a diffracted ray (constructive interference):

$$n\lambda = 2d \sin\theta \qquad [2.1]$$

This law relates the wavelength of electromagnetic radiation (λ) to the diffraction angle (θ) and the lattice spacing (d) in the crystalline sample. By scanning the sample through a range of 2θ angles, all possible diffraction directions of the lattice of the powdered material should be observed. From these measurements information on the unit cell type, dimensions (by calculation of lattice parameters from lattice spacing and observed planes associated to the diffraction peaks) and crystallite size by Scherrer equation are also obtained:

$$\tau = \frac{K\lambda}{\beta \cos\theta} \qquad [2.2]$$

where τ is the crystallite size, K is a constant that usually depends on the shape factor of the material and normally is between 0.87 and 1.0 (0.93 in this Thesis), λ is the incident wavelength (1.54 Å) and β is the full width at half maximum (FWHM) of the 2θ reflection. This value is normally calculated by using a standard as follows:

$$\beta = \beta_{sample} - \beta_{standard} \qquad [2.3]$$

In this study, the selected standard was Si with a $\beta_{standard}$ = 0.1 measured on the 2θ=28.37 reflection. β_{sample} value was obtained from the data analysis using X'pert HighScore Plus 3.0.4. software.

The XRD structural analysis of the solids was performed on an X'Pert Pro PANalytical instrument. Diffraction patterns were obtained using Cu Kα radiation (40 mA, 45 kV) over a 2θ-range of 10-90 º and using a step size of 0.05 º and a step time of 80.

2.1.3. Textural Properties by N_2 Adsorption: specific surface area, pore volume and pore size.

The textural properties were determined by N_2 adsorption and desorption varying the pressure at liquid nitrogen temperature. This measurement generates the adsorption-desorption isotherms whose analysis provides the amount of adsorbed N_2 on the tested sample, thereby allowing to determine the accessible surface area of the material to an adsorbate per mass unit, the pore volume and the pore size distribution.[2]

The experiments were performed in a Micromeritics ASAP 2020 instrument where the samples were previously degassed for 4 h at 250º C in vacuum. The specific surface area is determined by the BET method[3] and corresponds to the sum of the inner surface of the pores plus the outer surface of the grains. The Barrett-Joyner-Halenda (BJH) method by the desorption isotherm was used for determining the pore size distributions. Pore volume represents the inner and outer granular volume and the average pore size (Å) is calculated as the ratio of the pore volume and the specific surface area and normalized using a coefficient that depends on the pores shape.

2.1.4. X-Ray Fluorescence (XRF).

XRF is an analytical technique that can be used to determine the chemical composition of a wide variety of sample. It can analyse elements from beryllium (Be) to uranium (U) in concentration ranges from 100 wt% to sub-ppm levels. XRF is a robust technique which provides both qualitative and quantitative types of information on a sample.

XRF[4,5] is the emission of characteristic "secondary" (or fluorescent) X-rays from a material that has been excited by bombarding with high-energy X-rays or gamma rays. It measures the wavelength and intensity of 'light' (X-rays in this case) emitted by energized atoms in the sample. In XRF, irradiation by a primary X-ray beam from an X-ray tube causes emission of fluorescent X-rays with discrete energies characteristic of the elements present in the sample. The wavelength of this fluorescent radiation can be calculated from Planck's Law:

$$\lambda = \frac{\hbar\, c}{E} \qquad [2.4]$$

In this thesis, the chemical composition of the prepared solids was obtained by X-ray fluorescence spectrometry (XRF) using an AXIOS PANalytical spectrometer with Rh source of radiation working at 40 kV. For the experiments, the samples were previously dispersed in boric acid pellets and covered by thin wax film.

2.1.5. X-Ray Photoelectron Spectroscopy (XPS).

X-ray photoelectron spectroscopy (XPS)[6] is a surface-sensitive quantitative spectroscopic technique that measures the elemental composition at the parts per thousand range, empirical formula and chemical and electronic state of the elements that exist within the material. XPS is one of the most powerful tools to characterize the surface of catalysts since the binding energy of the measured photoelectrons depend on the chemical environment of the atom. Therefore, this technique is used to determine the oxidation state, the coordination and the quantity of the different components of the catalyst surface.

XPS spectra are obtained by irradiating the sample with a X-ray beam while simultaneously measuring the kinetic energy and number of electrons that escape from the upper top 0 to 10 nm of the material surface. For the measure, it is required high vacuum ($P \sim 10^{-8}$ Torr) or ultra-high vacuum (UHV; $P < 10^{-9}$ Torr).

XPS were recorded on a Leybold-Hereus LHS-10/20 spectrometer equipped with an ultra-high vacuum (UHV) system operating at $5 \cdot 10^{-9}$ Torr and a dual X-ray source, of which the Al Kα (1485 eV) was selected. Binding energy correction was performed by fixing C 1s level at 284.6 eV. Spectra were analysed with CasaXPS software and Gaussian-Lorentzian (70:30) curves were used for the fittings. Narrow scans were acquired at binding energy intervals associated with the Zr 3d, Eu 3d, Mo 3d, O 1s and C 1s levels. In order to quantify the band areas and obtain superficial atomic percentages, Zr

$3d_{5/2}$, Eu $3d_{5/2}$ and Mo $3d_{5/2}$ peaks areas corrected with their respective Scofield factors for Al Kα source were used.

2.1.6. Transmission Electron Microscopy (TEM) and Scanning Electron Microscopy (SEM).

The electron microscopy is a technique that employs as lighting source an electronic beam possessing a very short long wave which interacts to the sample.[7]

In the TEM microscopy, the electron beam passes through an ultra-thin sample. The image is formed from the interaction of the transmitted electrons through the system; the image is magnified and focused onto an imaging device, such fluorescent screen, a photographic film or to be detected by a sensor such as CCD camera. This technique allows the evaluation of the micromorphology of the catalysts as well as the presence of different crystalline phases. This technique permits the analysis of nanomaterials from some nanometres (low resolution TEM) up to angstroms (high resolution TEM).

In the SEM microscopy, instead to pass through the sample, the electron beam scans the surface of the sample generating secondary electrons from the sample allowing the image generation. This technique also provides morphological information of the surface but its resolution limit is lower (in the best case, above 1 nm) than that offered by the TEM microscopy.

Additionally, both techniques allow the study of the chemical composition through Energy dispersive X-Ray spectroscopy (EDX)

from the radiation emitted by the sample when it is excited with electromagnetic radiation.

In this work, SEM analysis was performed on a Hitachi S4800 SEM-FEG microscope equipped with a cold cathode field emission gun with voltage from 0.5 to 30 kV and resolution of 1nm at 15 kV. The microscope has coupled a Bruker-X Flash-4010 EDX detector with a resolution of 133 eV (at the MnKα line) and a detector with sample holder to work in transmission mode (STEM-in- SEM). The TEM micrographs were recorded on a Philips CM-200 instrument. The spatial resolution in the High-Resolution Transmission Electron Microscopy (HRTEM) mode was 0.25 nm. The electron diffraction diagrams were acquired with a diffraction camera length of 440 mm. Powdered samples were supported on a holey carbon-coated copper grid without using any liquid.

2.1.7. Raman Spectroscopy.

Raman spectroscopy is a technique used to observe vibrational, rotational and other low-frequency modes in a system. It is commonly used in chemistry to provide structural information of the studied sample because of the relation between the observed bands in the respective spectra and their molecular symmetry.

Raman spectra are originated from the polarization caused after the sample irradiation with energies in the ultraviolet, visible or near-infrared range. The laser light interacts with molecular vibrations, photons or other excitations in the system, resulting in the energy of the laser photons being shifted up or down. The shift in energy gives

information about the vibrational modes in the system. The Raman effect occurs when electromagnetic radiation interacts with a solid, liquid, or gaseous molecule's polarizable electron density and bonds. The spontaneous effect is a form of inelastic light scattering, where a photon excites the molecule in either the ground (lowest energy) or excited rotational and vibrational energy level within an electronic state.[8] This excitation puts the molecule into a virtual energy state for a short time before the photon scatters inelastically. The intensity of the Raman scattering is proportional to this polarizability change. Therefore, the Raman spectrum, scattering intensity as a function of the frequency shifts, depends on the rotational and vibrational energy level within an electronic states of the molecule.

In this thesis, europium luminescence is also observed when the Eu-containing samples are excited with Raman laser. However, this phenomenon should be separately analysed considering that this emission implies f-f transitions and they do not correspond to vibrational or rotational energy associated to the Raman spectroscopy.

The Raman spectroscopy analysis was carried out in a dispersive Horiba Jobin Yvon LabRam HR800 microscope. Raman spectra were obtained by using a 532.14 nm (green) laser excitation source with a ×50 microscope objective. The power of the laser on the sample is 20 mW with a 600 $g \cdot mm^{-1}$ grating. Two types of filters were used: D1 filter which reduces the laser to 2 mW to avoid a saturated signal in the 1000 – 4000 cm^{-1} range, and D0.6 filter to have a laser of 5 mW for the 200 – 1000 cm^{-1} range. A confocal pinhole of 1000 µm was

employed for all the measurements reported. Prior to the analysis, the Raman spectrometer was calibrated using a silicon wafer reference. Moreover, in order to observe the molybdenum oxide structure in some samples, a 785 nm (red) laser excitation source with a ×100 microscope objective was also used.

In situ Raman experiments were performed in a Linkam CCR1000 cell coupled to the Raman spectrometer equipment. This cell is capable of operating under flow conditions up to 1000 ºC. The sample was initially dehydrated in situ at 450 ºC for 1 h with a heating rate of 10 ºC·min^{-1} in a flow of 50 mL·min^{-1} of nitrogen. Afterwards, the sample was cooled down to 200 ºC and a flow of 50 mL·min^{-1} of nitrogen saturated with water at room temperature was introduced. The temperature was increased up to 450 ºC recording a spectrum every 50 ºC after 15 min stabilization using the same experimental conditions mentioned above using the green laser.

2.1.8. UV-Vis Spectroscopy.

UV-Visible spectroscopy (UV-Vis) refers to absorption or reflectance spectroscopy in the ultraviolet-visible spectral region corresponding to electronic transitions in the measured samples. This means, that it uses light in the visible and adjacent regions, near-UV and near-infrared (NIR).

The absorption or reflectance in the visible range directly affects the perceived colour of the samples. This technique is complementary to the fluorescence spectroscopy. Meanwhile fluorescence deals with transitions from the excited to the ground state, the absorption

measures transitions from the ground to the excited state.[9] There are three main transitions that can be considered:

- d-d transitions: they are typical of transition metals ions. These electronic transitions principally give rise to absorption in the visible region and are therefore responsible for the colour of transition metal complexes.
- Charge-transfer transitions: they involve an electronic transfer from occupied orbitals towards empty ones.
- π - n* and n - π* transitions: they normally occur on organic molecules due to the electronic transitions between n and π orbitals.

The UV–vis spectra were recorded on an Avantes spectrometer model AvaLight-DH-S-BAL. All the spectra were collected in absorbance mode using $BaSO_4$ as reference.

2.1.9. Impedance Spectroscopy (IS).

IS[10] is a powerful method of characterizing many of the electrical properties of materials and their interfaces with electronically conducting electrodes. It may be used to investigate the dynamics of bound or mobile charge in the bulk or interfacial regions of any kind of solid or liquid material: ionic, semiconducting, mixed electronic–ionic conductors, and even insulators (dielectrics). This method allows the study of conducting and dielectric materials whose electrical properties involve a dipolar rotation and where the conduction could be electrical and/or ionic. Moreover, this technique presents the particularity of distinguish between the different

contributions of each region or interface of the material like grain, grain boundary or sample-electrode interface since their response time and characteristic frequencies are different, and they can be analysed by reference to an equivalent circuit which contains a series array of parallel ideal RC elements. Fundamentals of IS virtually always assumed that the properties of the electrode–material system are time-invariant, being thereby one of the basic purposes to determine these properties, their interrelations and their dependences on such controllable variables as temperature, oxygen partial pressure, applied hydrostatic pressure, and applied static voltage or current bias.

Electrical measurements are usually made with cells having two identical electrodes applied to the faces of a sample in the form of a circular cylinder or rectangular parallelepiped. Although IS deals directly with complex quantities, analogously to the resistance, the impedance is a measure of the ability of a circuit to resist the flow of electrical current. Electrochemical impedance is usually measured by applying an AC potential from a few hertzs (μHz for adequate resolution of interfacial processes) up to MHz of magnitude (in the range of bulk' stimulations) to an electrochemical cell analysing the current passing through it.

According to the Ohm's Law (R=V/I) and assuming that a sinusoidal potential excitation is applied, the response to this potential is an AC current signal which can be analysed as a sum of sinusoidal functions (a Fourier series), where the potential energy (V) and the current intensity (I) are expressed as follows:

$$V(t) = V_0 \sin(\omega t) \quad [2.5]$$

$$I(t) = I_0 \sin(\omega t + \theta) \quad [2.6]$$

where *t* is the time, V_0 and I_0 are the amplitude terms of potential and intensity, respectively, θ is the phase and the frequency is $\omega = 2\pi f$.

Using Fourier transformation and applying Ohm's Law, the complex impedance is expressed as:

$$Z(j\omega) = {V(j\omega)}/{I(j\omega)} \quad [2.7]$$

$$Z(\omega) = Z' + jZ'' \quad [2.8]$$

where $Re(Z) \equiv Z' = |Z|\cos(\theta)$ and $Im(Z) \equiv Z'' = |Z|\sin(\theta)$.

For conductivity analysis, the samples were previously sintered into pellets by Spark Plasma Sintering (SPS) technique in a Dr. Sinter Inc. Instrument (Kanagawa, Japan) model 515S equipped with a 10 mm diameter cylindrical graphite die/punch setup in a vacuum chamber (Scheme 2.1). The sintering temperature was 900 ºC for 5 minutes with a heating rate of 100 ºC·min^{-1} and applied uniaxial pressure of 50 MPa. Pellets were then cooled to room temperature and polished in order to eliminate the carbon deposited on the surface.

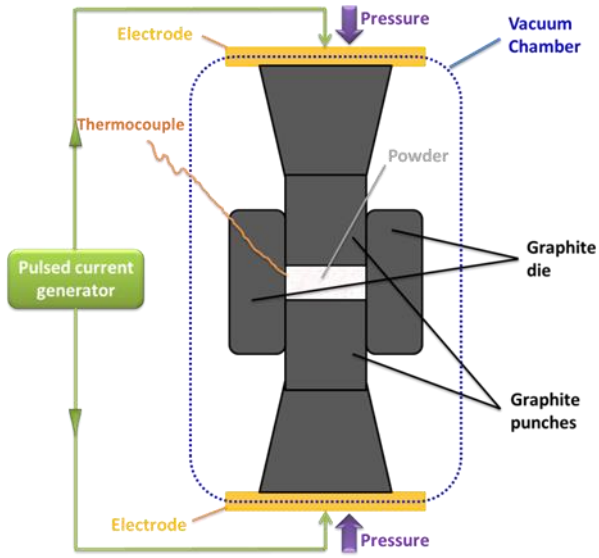

Scheme 2. 1 Vacuum hot pressing sintering furnace for SPS

The conductivity measurements were performed in an impedance spectrometer Agilent (HP) model 4294A over a frequency range of 100 Hz to 4 MHz with an AC voltage of 0.1 V. Pellets were previously coated with silver by painting both surfaces of the pellets with a colloidal solution and then removing the solvent at 600 ºC in Ar for 3 h. The silver coating is the contact film between sample and platinum electrodes. The impedance measurements were carried out from room temperature to 700 ºC in a flow of Ar, O_2/Ar (from 10 to 100 % of oxygen) and H_2O/Ar (from 20 vol.% to 50 vol.% of water), thereby studying the influence of oxygen and water on the conductivity. Before the impedance measurements, the samples were dehydrated *in situ* in dry air at 600 ºC for 3 h.

2.1.10. Infrared Spectroscopy (IR).

Infrared (IR)[11] spectroscopy is one of the most common and widely used spectroscopic techniques due to its usefulness in determining structures of compounds. IR spectroscopy is very sensitive to determination of functional groups since different functional group absorbs different particular frequency of IR radiation. It can also be used for both qualitative and quantitative analysis of complex mixtures.

In the IR region of the electromagnetic spectrum, molecular vibrational frequencies can be measured. A polychromatic light is passed through a sample and the intensity of the transmitted light is measured at each frequency. When molecules absorb IR radiation, transitions occur from a ground vibrational state to an excited vibrational state.

Absorption of IR radiation is typical of molecular species that have a small energy difference between the rotational and vibrational states. For a molecule to be IR active there must be a change in dipole moment as a result of the vibration that occurs when IR radiation is absorbed. Dipole moment is a vector quantity and depends on the orientation of the molecule and the photon electric vector. The dipole moment changes as the bond expands and contracts. When all molecules are aligned as in a crystal and the photon vector points along a molecular axis such as z. Absorption occurs for the vibrations that displace the dipole along z. Vibrations that are totally x or y polarized would be absent.

The IR spectroscopy was performed in transmission mode being the IR radiation passed through the sample. The samples were pelletized without any diluent presenting a diameter of 15 mm. FTIR spectra were recorded using THERMO NICOLET Avatar 380 FT-IR Spectrophotometer, equipped with a DTGS/KBr detector, and accumulating 128 scans at a spectral resolution of 4 cm^{-1}. The experiments were performed *in situ* using a purpose-made IR cell from room temperature to 400 ºC connected to a conventional vacuum adsorption apparatus with a residual pressure lower than 10^{-5} mbar.

2.1.11. Temperature Programmed Reduction (TPR).

TPR[12] analysis provides useful information about the surface properties of solid material, not only of a purely analytical nature but also, and more importantly, about the condition of species present in and on solids. From TPR analysis valuable information like the reducibility of the species present in the solid or the interaction between supported phases and the supports also related to the particle size can be studied.

The essence of the technique is the reduction of a solid by a gas at the same that the temperature of the system is changed in a predetermined way. Chemical information is derived from the record of the analysis of the gaseous products. The most common reductive gas used in such experiments is hydrogen.

The TPR experiments were performed using 5 % H_2 in Ar and the temperature was increased at 10 ºC/min. The feed stream is divided in

two lines; one of them is passed through the sample contrary to the other one which is employed as reference. The difference between the H_2 inlet and the outlet was measured as a function of the temperature by using a thermal conductivity detector (TCD). A molecular sieve 13X was used to retain the H_2O produced during the reduction. For the quantitative analysis the TCD signal was calibrated with a CuO pattern (Strem Chemicals 99.999%).

2.1.12. Diffusive Reflectance Infrared Fourier Transformed Spectroscopy (DRIFTS).

When infrared radiation is directed onto the surface of a solid sample two types of reflected radiations may occur. One is the specular reflectance and the other is the diffuse reflectance. The specular component is the radiation that directly reflects off the sample surface (it is the radiation that is not absorbed by the sample).

Diffuse reflectance is the radiation that penetrates into the sample and then emerges. In the ideal case, the angular distribution of this radiation will follow Lambert´s law. The interpretation of the diffusive radiation is based on the theory developed by Kubelka-Munk (equation 2.9) by which the measured diffuse reflectance is transformed to a magnitude proportional to the extinction coefficient:

$$F(R_\infty) = \frac{(1-R_\infty)^2}{2R_\infty} \propto \frac{\kappa}{\sigma} \qquad [2.9]$$

In practice, R_∞ is the reflectance of a layer so thick that further increase of the thickness does not change the reflectance[13], κ is the absorbance in cm^{-1} and σ is the dispersion factor that it is assumed to

be independent of the wavelength for particles with grain size higher than the light wavelength.

The DRIFTS spectra characterize the sample qualitatively and quantitatively by similar principles as any normal absorption spectroscopy. Quantitative DRIFTS analysis shows good linearity between the intensity of the bands and the concentration of very dilute samples.[14] DRIFTS become an important method in heterogeneous catalysis due to its ability to provide accurate data with almost no sample preparation and to its applicability on the so called *operando* studies providing information about the species formed during the reaction.

The experiments were carried out in a THERMO/Nicolet model iS50 spectrometer equipped with a MCT detector and a Praying Mantis High Temperature Reaction chamber with ZnSe windows (Harrick). Spectra were obtained by averaging 32 scans with a resolution of 4 cm^{-1}. Approximately 200 mg of sample was placed in the Harrick reaction chamber. The spectrometer bench was continuously purged with pure nitrogen to eliminate CO_2 and water vapour contributions to the spectra. The background spectrum was collected without sample using an aluminium mirror. For the experiments in wet conditions the adequate amount of water was fed continuously by using a HPLC pump and vaporising the liquid in a homemade evaporator.

2.1.13. X-Ray Absorption Spectroscopy (XAS): X-Ray Absorption Near Edge Structure (XANES) and Extended X-Ray Absorption Fine Structure (EXAFS).

X-ray Absorption Spectroscopy (XAS) includes both EXAFS and XANES. XAS is a site-specific probe of the distribution of valence electrons, local structure, and chemistry around a selected absorber atom. Moreover, it does not require crystalline order and is therefore an ideal technique to investigate matter in all its forms: crystals, liquids, glasses, and gases. XAS is the measurement of the X-ray absorption coefficient (μ) of a material as a function of energy. X-rays of a narrow energy resolution are shone on the sample and the incident and transmitted X-ray intensity are recorded on increasing the energy of the incident X-ray.[15] The number of X-ray photons that are transmitted through a sample (I_t) is equal to the number of X-ray photons shone on the sample (I_0) multiplied by a decreasing exponential that depends on the type of atoms in the sample, the absorption coefficient (μ) , and the thickness of the sample (x):

$$I_t = I_0 e^{-\mu x} \qquad [2.10]$$

The absorption coefficient is obtained by taking the *ln* ratio of the incident X-ray intensity to the transmitted one. When the incident X-ray energy matches the binding energy of an electron of an atom within the sample, the number of X-rays absorbed by the sample increases dramatically, causing a drop in the transmitted X-ray intensity. This results in an absorption edge. Each element on the periodic table has a set of unique absorption edges, corresponding to

the different binding energies of its electrons. This gives XAS element selectivity.

XANES represents the normalized absorption spectrum and can be used to determine the average oxidation state of the element in the sample. The XANES spectra are also sensitive to the coordination environment of the absorbing atom. For its part, EXAFS spectra are displayed as graphs of the absorption coefficient (μ) of a given material versus energy, typically in a 500 – 1000 eV range beginning before an absorption edge of an element in the sample. The X-ray absorption coefficient is usually normalized to unit step height. This is done by regressing a line to the region before and after the absorption edge, subtracting the pre-edge line from the entire data set and dividing by the absorption step height, which is determined by the difference between the pre-edge and post-edge lines at the value of E_0 (on the absorption edge). The dominant physical process in EXAFS is the one where the absorbed photon ejects a core photoelectron from the absorbing atom, leaving behind a core hole. The atom with the core hole becomes excited. The ejected photoelectron's energy will be equal to that of the absorbed photon minus the binding energy of the initial core state. The ejected photoelectron interacts with electrons in the surrounding non-excited atoms. If the ejected photoelectron is taken to have a wave-like nature and the surrounding atoms are described as point scatters, it is possible to imagine the backscattered electron waves interfering with the forward-propagating waves. The resulting interference pattern shows up as a modulation of the measured absorption coefficient, thereby causing the oscillation in the EXAFS spectra. A simplified

plane-wave single-scattering and multiple-scattering theory is used for interpretation of EXAFS spectra.

In this work, Pt L_3-edge and Ce L_3-edge EXAFS/XANES spectra were collected at beamline CLAESS of Alba Synchrotron in Spain, where synchrotron X-rays are highly penetrating and its brilliance allow concentrations of the absorbing element can be as low as a few ppm. The spectra were taken in the "fluorescence-yield mode" for Pt and in "transmission-yield mode" for Ce. The powdered samples were diluted with X-ray-transparent BN (to avoid the signal saturation but have the maximal signal) and pressed into pellets.

2.2. CATALYTIC ACTIVITY (WGS REACTION)

The WGS reaction has been carried out at atmospheric pressure in a home-made setup coupled to an on-line ABB gas analyser (AO2020) equipped with an IR detector in a tubular fixed bed reactor of 9 mm in diameter for powder catalysts and of 18 mm in diameter for structured catalysts.

Figure 2.1 Home-made WGS reaction setup.

The catalytic tests were studied in the 180-350ºC temperature range using two different feeds named *model conditions* (4.5% CO, 30% of H_2O and N_2 as balance) and *real conditions* (9% CO, 30% of H_2O, 11% CO_2 and 50% H_2). Previously, the catalysts were reduced in 10 % H_2 balanced with N_2 for 30 min at 350 ºC.

The Pt-based catalyst loading was always 0,1 g (with or without the added ionic conductor) and all the experiments were carried out at 80000 $mL \cdot h^{-1} \cdot g_{cat}^{-1}$ space velocity. Moreover, in the case of powdered samples, particles sizes sieved between 600 and 800 µm were selected and the catalytic bed volume was always of 0.4 cm^3 (adding inert quartz in the same particle size range when needed). This way an also constant volumetric space velocity of 20000 h^{-1} is attained. For the structured samples cases, the catalytic constant volume was 6.8 cm^3 getting the volumetric space velocity of 1176 h^{-1}.

Concerning to the structured catalysts, metallic FeCrAlloy – Iron/Chromium foil (Fe72.8/Cr22/Al5/Y0.1/Zr0.1, GoodFellow) with 0.05 mm in thickness was used for the manufacture of the micromonoliths. Flat and corrugated foils were co-rolled in pairs resulting in cylindrical metallic micromonoliths with 17 mm in diameter and 30 mm in height (Figure 2.2). The metallic foils were firstly washed with acetone and, afterwards, the manufactured micromonoliths were again washed in an ultrasonic bath with acetone for 30 minutes. The cleaned micromonoliths were calcined in air for 22 h at 900 ºC in order to create an Al_2O_3 layer on the metallic surface by segregation from the material which will improve the porosity of the contact surface and, consequently, the subsequent adhesion of the catalyst.

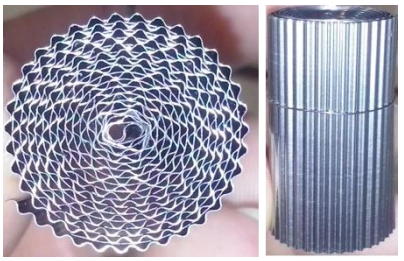

Figure 2.2 Manufactured metallic micromonolith.

The catalyst was deposited on the metallic micromonoliths by washcoating. A stable suspension with adequate viscosity was formulated by mixing 80 wt.% of deionized water, 6 wt.% of commercial aqueous solution of Al_2O_3 (20 wt.% of alumina, Nyacol) and 14 wt.% of catalyst sieved below 50 µm. The slurry was aged for *ca.* 24 h under continuous stirring. The bare monolith, was then immersed at a constant rate of 3 $cm \cdot h^{-1}$ into the formulated slurry,

kept for one min into the colloidal dispersion and then withdrawn at 3 $cm \cdot h^{-1}$. The colloid excess was removed by blowing air inside the channels to avoid their obstruction. Finally, the impregnated micromonolith is dried at 100 ºC for 30 minutes. This process is repeated until the desired amount of catalyst is loaded. Then the structured catalyst is calcined at the same conditions than the original catalytic powder but with a temperature rate of 2 $ºC \cdot min^{-1}$, in order to slowly remove the leftovers without creating porosity or fissures.

2.3. KINETICS (WGS REACTION)

These experiments were carried out in the Laboratory of Catalysis and Catalytic Processes (LCCP) in Politecnico di Milano (Italy). The powdered and structured samples were the same prepared in Sevilla for the characterization and WGS experiments. The kinetic studies of WGS reaction were performed from 175 ºC to 400 ºC changing the inlet flow composition keeping the total flow rate and again the space velocity at 80000 $mL \cdot h^{-1} \cdot g_{cat}^{-1}$ with 0.1 g of the catalyst in all cases. Because of instrument/installation limitations the tested powdered catalysts were sieved between 800 and 1000 μm and the CO_2 component in the reactant mixture could not be introduced.

The kinetic study of WGS reaction on powdered catalysts was carried out at atmospheric pressure in a home-made rig coupled to an on-line μGC analyser (SRA Instruments R3000) equipped with two columns with Ar and He as carrier gas, respectively, and a Thermal Conductivity Detector (TCD). In this rig, the water introduction was achieved making the N_2 pass through a temperature-controlled saturator (Vertex Thermometer). The catalytic bed (0.4 cm^3) was

placed in a quartz reactor of 7 mm in diameter fixed by quartz wool on both ends. The reaction temperature was controlled by placing a K thermocouple of 0.5 mm in the middle of the catalytic bed. The reactor was heated inside a tubular furnace (Carbolite 2408) from 175 ºC to 400 ºC.

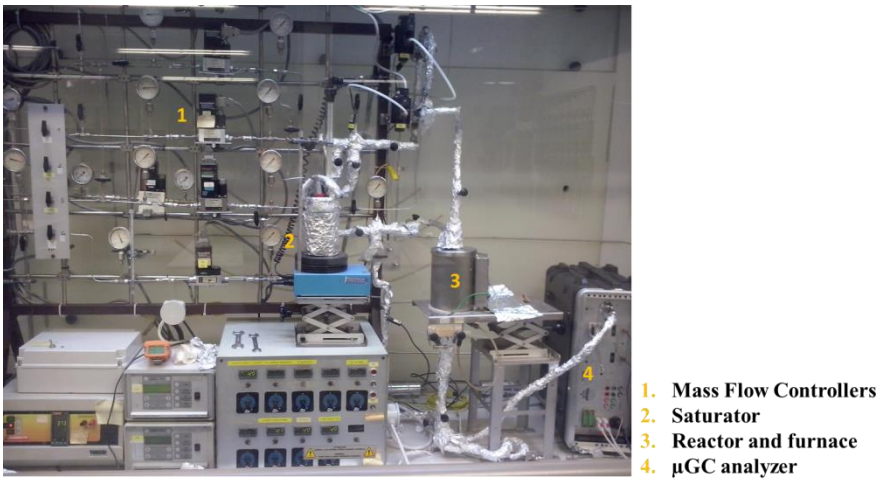

Figure 2.3 Rig for kinetic study of WGS reaction on powdered catalysts.

The experiments in structured catalyst were also performed in a home-made rig at atmospheric pressure coupled to an on-line µGC analyser (Agilent 3000 A µGC) equipped with two columns with Ar and He as carrier gas, respectively, and a Thermal Conductivity Detector (TCD). Here, the water introduction was carried out by a digital pump (Gilson 302) swept along with N_2. After a home-made evaporator line, a λ module (Lambda Meter ETAS) and a humidity sensor (Humidity&Temperature transmitter HMT334, Vaisala) monitored with LabView software were used to measure the exact inlet water concentration. After the reactor, a condenser ABB Advance SCC-C at 3 ºC was added to remove the high amount of

water before going in µGC analyser. The monolithic catalyst was fixed by two inert foams and placed in the previously measured isothermal part of the tubular stainless reactor inside a tubular furnace (Carbolite Furnaces Tersid s.r.l.Milano). Two thermocouples were used: one that controls the furnace temperature, on the external diameter of the reactor, and a second one in the central channel of the micromonolith which is longitudinally mobile along the height of the structured catalyst as it is shown in scheme 2.1. With this thermocouple, the exact temperature along the sample is measured in each tested temperature step during the reaction, providing thereby a temperature profile along the micromonolith in real-time.

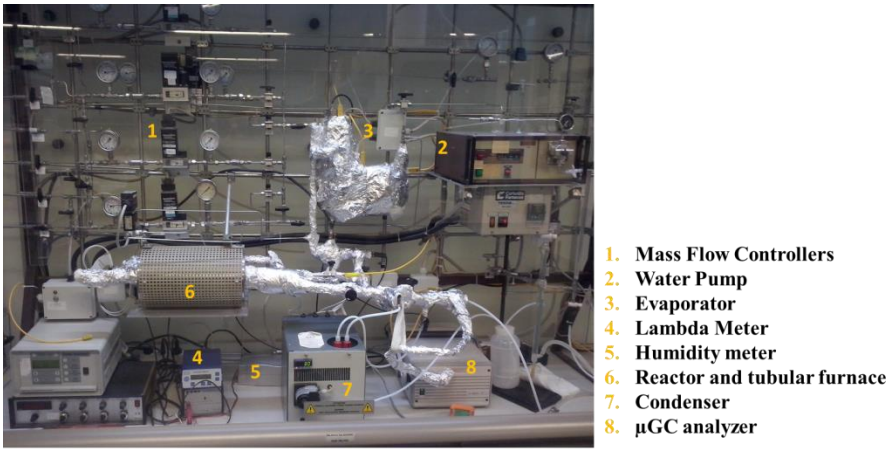

Figure 2.4 Rig for kinetic study of WGS reaction on structured catalysts.

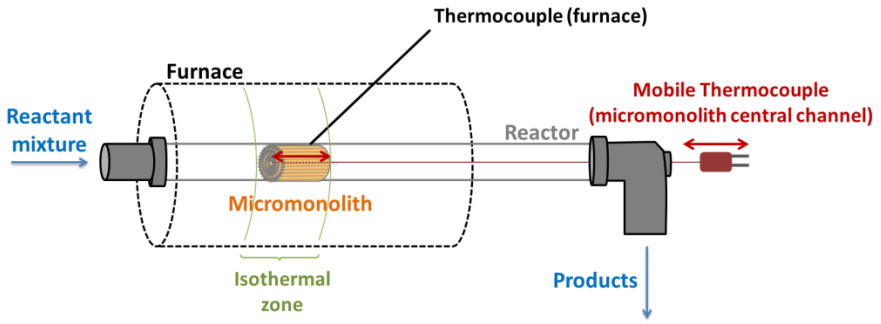

Scheme 2.2 Structured catalyst and thermocouples positions.

REFERENCES

1. Cullity, B. D. *Elements of X-Ray Diffraction*. (Addison-Wesley Publishing Company INC., 1978).
2. Micromeritics Instrument Corporation. *Gas Adsorption Theory*. http://www.micromeritics.com/Repository/Files/Gas_Adsorption_Theory_poster.
3. Brunauer, S.; Emmett, P.H. and Teller, E. "Adsorption of Gases in Multimolecular Layers" *J. Am. Chem. Soc.* **60,** 309–319 (1938).
4. Jenkins, R. *X-Ray Fluorescence Spectrometry, 2nd Edition*. (John Wiley & Sons, Inc., 1999).
5. Gupta, A.K. "Total Reflection X-Ray Fluorescence Spectroscopy - Working Principles" *Int. J. Core Eng.* **1,** 36–55 (2014).
6. Hüfner, S. *Photoelectron Spectroscopy. Principles and Applications*. (Springer-Verlag Berlin Heidelberg, 2003).
7. Hall, C.E. *Introduction to Electron Microscopy*. (McGraw-Hill, 1953).
8. Bumbrah, G.S. and Sharma, R.M. "Raman spectroscopy – Basic principle, instrumentation and selected applications for the characterization of drugs of abuse" *Egypt. J. Forensic Sci.* **6,** 209–215 (2016).
9. "Basic UV-Vis Theory , Concepts and Applications" *ThermoSpectronic* 1–28 (2013).
10. *Impedance Spectroscopy Theory, Experiment, and Applications*. (John Wiley & Sons, Inc., 2005).

11. Osibanjo, R.; Curtis, R. and Lai, Z. *Infrared Spectroscopy*. (Chemistry LibreTexts MindTouch - NSF - UCDavis University of California, 2017).

12. Jones, A. and McNicol, B. *Temperature-Programmed Reduction for Solid Materials Characterization*. (Marcel Denker, Inc., 1986).

13. Völz, H.G. "Practical pigment testing with the aid of the Kubelka-Munk theory" *Prog. Org. Coatings* **13,** 153–169 (1985).

14. Craciun, R.; Miller, D.J.; Dulamita, N. and Jackson, J.E. "Diffuse Reflectance Infrared Fourier Transform Spectroscopy (DRIFTS) Applied in Heterogeneous Catalysis Studies" *Prog. Catal.* **5,** 55–76 (1996).

15. Bianconi, A. *X-Ray Absorption Principles, Applications, Techniques, of EXAFS, SEXAFS and XANES*. (WILEY, 1988).

CHAPTER 3.

SYNTHESIS AND CHARACTERIZATION

Abstract

A conventional $Pt/CeO_2/Al_2O_3$ catalyst has been synthesized and characterized. In this chapter, the textural and physicochemical properties of the catalyst are presented and discussed in order to explain its catalytic activity as well as to determine some operation conditions like activation step, which it has been stablished according to TPR analysis.

In addition, Eu-doped ZrO_2 and Mo- and Eu-doped ZrO_2 materials have been prepared with different amount of dopants as proton conductors. Their phases and structures and textural properties have been analysed according to their composition. The objective is to compare these features with the conductivity and their promotional role in WGS reaction discussed in next chapters.

3.1. INTRODUCTION

Pt-based catalysts have been successfully tested in many different processes becoming the standard catalyst for many oxidation and reduction reactions. Platinum is commonly used in heterogeneous catalysis for hydrogenation-dehydrogenation reactions, reforming of oxygenates, aromatization reactions, oxygen reduction reaction and electrocatalysis in general including fuel cells devices, and other important specific reactions like CO oxidation and methanation.[1–6]

In a WGS reaction context, besides Fe/Cr and Cu based catalysts for the high and low temperature WGS reaction, respectively, precious metals are being studied in recent years as promising WGS catalysts, like Pt, Au or Pd,[7,8] due to the necessity of compact catalyst beds for mobile devices applications.[9] These precious metal-based catalysts provide good CO conversions for low-medium temperature reducing the WGS reaction to only one reactor. Moreover, by using precious metals safety problems like the pyrophoricity of Cu based catalysts are avoided.[10] The good behaviour of the Pt active phase resides in its dual capacity for activating CO and H_2O by itself.[7] Further, a large number of catalyst formulations were proposed that incorporates the active phase (Pt) on a reducible oxide support, such as CeO_2, TiO_2 or Fe_2O_3.[11–15] These formulations are bifunctional, both Pt and support have a role in the reaction mechanism, and have shown better performances in WGS reaction. In the same way, the previous proposed supports are commonly supported on alumina as a textural promoter since provides high specific surface and stabilizes the crystallites against agglomeration during the reaction.[7]

Therefore, a typical Pt-based catalyst for WGS reaction is considered for this work. Concretely, Pt active phase loaded over a commercial CeO_2-supported alumina as support is going to be synthesized and characterized in this chapter.

Besides the catalyst, in this chapter it will be shown and discussed the synthesis and characterization of mixed oxides ionic conductors. As it was pointed out in the Introduction chapter, ionic conductors and, more specifically, proton conductors are very attractive for a wide range of technological applications.[16–18]

Generally, high temperature ion conductors consist in oxide materials doped with aliovalent cations. For instance, this is the case of acceptor-doped perovskites (ABO_3) where the substitution of A-site or B-site cations for others metals with different oxidation state creates oxygen vacancies.[19,20] The high stability of these structures and the presence of oxygen vacancies allow the conductivity of ions like O^{2-}, OH^- or H^+. However, synthesis of materials with both high ionic conductivity and high stability has been challenging during the last years.[21] It has been extensively studied compounds based on cubic doped zirconia, since these materials, like $CaZrO_3$, exhibits ionic conductivity and good stability.[22] Moreover, these compounds present the advantage of easy synthetization to obtain these cubic structures.[23,24] Thus, doping zirconia with aliovalent cations creates good ionic conductors with high stability. Besides perovskite-type materials, the conductivity and stability of pyrochlore/fluorite type oxides has also been studied.[25,26] In general, doping with rare earth metals (La, Sm, Eu, Gd…) results in enhanced chemical stability and

good ionic conductivity at temperatures lower than undoped oxides.[23,27–29]

Moreover, the Mo addition can improve the conductivity of a mixed oxide since Mo compounds normally exhibit mixed ionic and electronic conductivity (MIEC).[30,31] Thus, studying different Mo loadings is interesting since a change from proton to electron conductivity is shown as a function of the Mo content; for low Mo concentration proton conductivity is dominant, but on increasing the Mo content, the crystal symmetry decreases and the electronic conductivity becomes more important. Moreover, the adopted structure on increasing the Mo loading is the result of oxygen vacancies ordering, this reduces the ionic conductivity and increases its activation energy, also according to other ionic conductors.[32–34]

Besides the conducting properties of Mo-based MIEC, Eu-doped Mo oxides have been reported to form bronzes showing a semiconductor behaviour, these materials are capable of holding H_2 or water molecules between the α-MoO_3 layers.[35,36] In the same way, MoO_3 compounds forms bronzes or are reduced on adding H_2.[36–40] The H_2 is dissociated and bonded as –OH or –OH_2 groups, depending on the H_2 concentration. The H_2 inclusion in MoO_3 phase does not control the electronic properties but has influence in the crystal structure, affecting thereby the hydrogen mobility.[41–43] According to Ressler and co-workers,[40] above ~200 ºC the hydrogen is introduced in the Mo oxide structure forming bronzes. On increasing the temperature, from ~370 ºC, reduced nuclei MoO_2 phases start to appear. Because of these properties, Mo bronzes have been

considered to numerous applications, among which H_2 membrane separation by proton conductivity, sensors or H_2 storage devices are found.[31,42,44] These bronze structures also exhibit ion-exchange properties due to their ionic structure[41,45–47] make them very attractive for the aim of this work.

Therefore, this chapter presents the synthesis of Eu- and Eu-and Mo-doped zirconium oxides together with a thorough characterization of them in order to relate their physicochemical properties with their ionic conductivity (Chapter 4) and hence their influence in WGS reaction (Chapter 5).

3.2. $Pt/CeO_2/Al_2O_3$ CATALYST

3.2.1. Synthesis of 2 wt.% of Pt over CeO_2/Al_2O_3 commercial support by wet impregnation method.

In a typical preparation of the $Pt/CeO_2/Al_2O_3$ catalyst (labelled PtCeAl), 2 wt.% of Pt was loaded over a CeO_2/Al_2O_3 commercial support (mass ratio of 20:80 of ceria/alumina, Puralox) by the wet impregnation method. An appropriate amount of the Pt precursor (tetrammine platinum (II) nitrate solution, Johnson Matthey) was previously mixed with an acetic acid solution 1M in a Pt:Acid molar ratio of 1:1,1. Then, the Pt solution was added over the commercial support and vigorously stirred at room temperature. Next, the solvent was evaporated at reduced pressure in a rotary evaporator and the obtained solid was dried at 100 ºC for 12 h. Finally, the dried solid was calcined at 350 ºC for 8 h using a heating rate of 5 ºC/min.

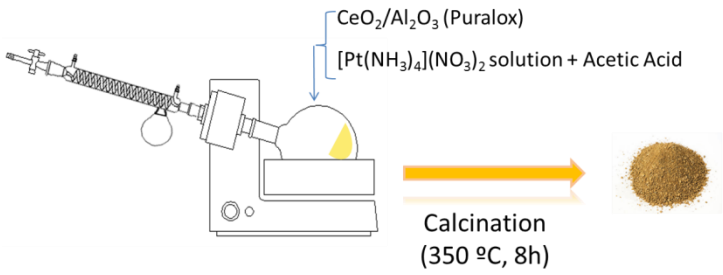

Scheme 3.1 Synthesis of PtCeAl catalyst by wet impregnation method, dried in a rotary evaporator and calcination conditions.

3.2.2. Elemental characterization of $Pt/CeO_2/Al_2O_3$ catalyst.

3.2.2.1 Textural properties, XRD, XRF and TEM.

The chemical composition and textural properties of the PtCeAl catalyst are summarized in Table 3.1. Thus, by XRF the 20:80 ceria/alumina ratio of the support was verified as well as the Pt loading quite close to the targeted value of 2 wt. %. The addition of the active phase implies a reduction of the BET surface area of the support (160 m^2/g) according to its technical data (Puralox SCFa-160 Ce20)[48], although the average pore size and pore volume of the catalyst are quite similar to that of the support alone, meaning no occlusion of the porosity by the impregnation method.

Table 3.1 Composition and textural properties of the PtCeAl catalyst.

S_{BET} (m^2/g)	D_p (nm)	V_p (cm^3/g)	XRF* (wt. %)
110	8.84	0.264	1.8 Pt (2.0) 18.8 CeO_2 (19.6) 79.4 Al_2O_3 (78.4)

** Nominal value of the chemical composition among parenthesis.*

The adsorption-desorption N_2 isotherm of the prepared PtCeAl catalyst (Figure 3.1) can be described as type IV according to BDDT[49] classification with a small hysteresis, or a pseudo-type II,[50] which could indicate a slit-shaped type pores or a low degree of pore curvature (hysteresis curve type H_3 according to IUPAC classification).[51] Although only the initial monolayer–multilayer section of the isotherm is reversible, the whole adsorption branch of the H_3 loop appears to exhibit the same shape as a type II isotherm. This pseudo-type II character is associated with the metastability of the adsorbed multilayer (and delayed capillary condensation).

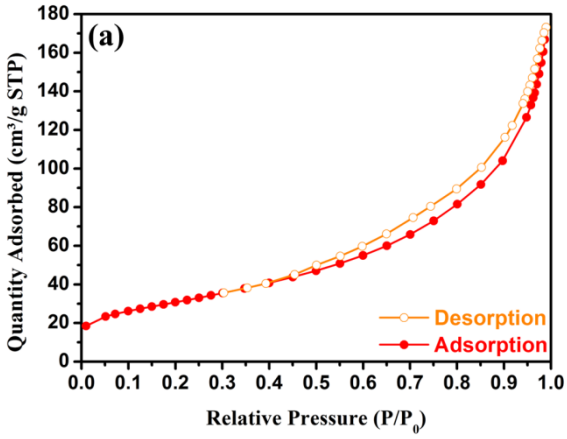

Figure 3.1 N_2 Adsorption-Desorption Isotherm of the PtCeAl catalyst.

On the other side, the X-ray diffractogram of the PtCeAl catalyst (Figure 3.2) exhibits diffraction lines corresponding to the CeO_2 [JCPDS: 00-034-0394] and ɣ-Al_2O_3 [JCPDS: 01-077-0396] phases of the commercial Puralox support, but there is no evidence of the Pt phase, which could mean a quite small Pt nanoparticle sizes, although further characterization is mandatory for this issue.

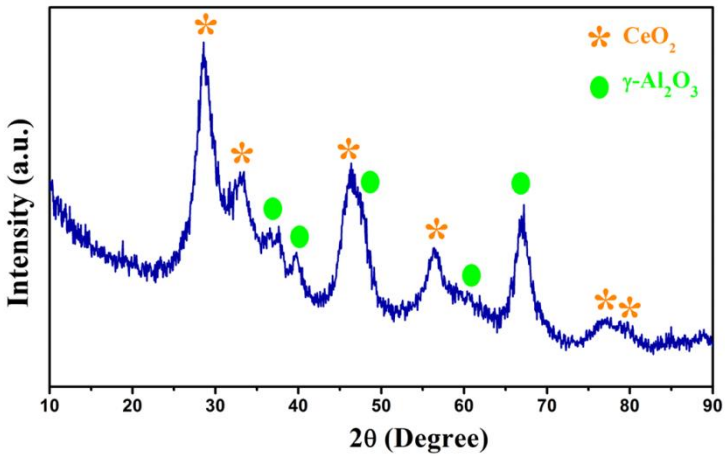

Figure 3.2 XRD of the PtCeAl catalyst.

The inspection of the TEM images of the PtCeAl catalyst does not evidence Pt particles, which could indicate a high dispersion of the Pt. As it can be noticed in Figure 3.3, two selected areas (dotted yellow boxes) allow to measure the interplanar spacing of 3.1 Å, which could be associated to the (111) planes of the cubic $Fm\bar{3}m$ phase of the CeO_2. In the electron diffraction pattern shown as an inset in Figure 3.3, the cubic phase is also recognized as well as polycrystalline character.

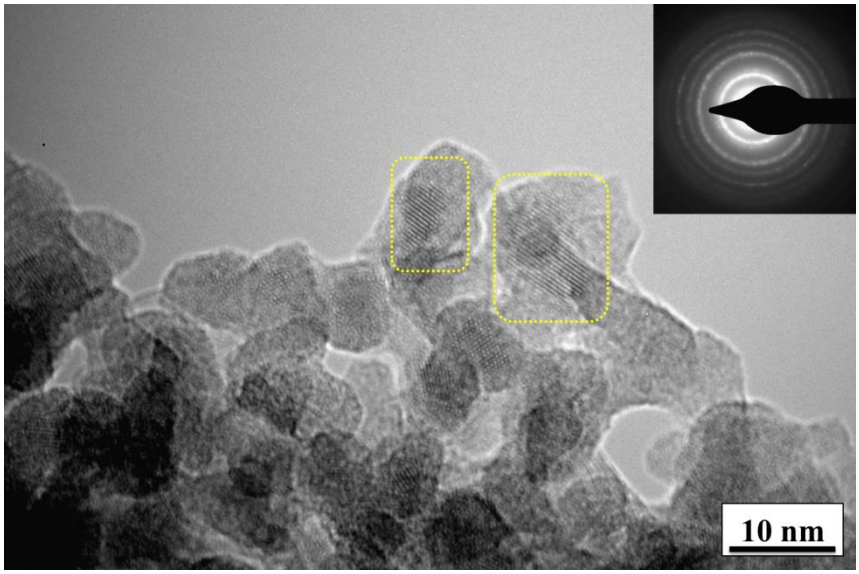

Figure 3.3 TEM image of PtCeAl catalyst. SAED shown as an insert in the micrograph.

Although the Pt particle size remains unsolved, Pt dispersion as well as TPR and EXAFS analysis are discussed in the next point providing more information about this issue. Moreover, no matter the size is, PtCeAl catalyst is always the same synthesized powder, keeping thereby its properties whatever they are. The variable object of study is basically the ionic conductor in order to understand and improve the water activation step in WGS reaction.

3.2.2.2 TPR, Pt dispersion by *in situ* IR spectroscopy and XANES-EXAFS analysis.

Temperature programed reduction (TPR) has been carried out in order to stablish the Pt activation conditions for the WGS reaction. As it can be noticed in Figure 3.4, two general reduction processes at ~220 and ~361 ºC are described. In general, the platinum reduction

process strongly depends on the metal loading, the metal dispersion, the nature of the support, the synthesis method and the temperature treatment.[52–54] The H_2-TPR profile of the PtCeAl catalyst has been then compared in Figure 3.4 with the CeAl support in order to analyse the reduction associated to ceria, as well as with a 2 wt.%Pt supported on an undoped commercial alumina support also prepared by wet impregnation. As Al_2O_3 is a non-reducible oxide, the H_2 consumption in this Pt/Al_2O_3 sample must be entirely assigned to the reduction of the platinum species, whose process will appear at different temperatures depending on the Pt particle size and its interaction metal – support. Thus, Merlen *et al.*[55] observed three different reduction peaks around 100, 180 and 300 ºC associated to PtO_x species with different particle sizes and metal – support interactions: the smaller the particles, the stronger the interaction and hence the higher the temperature of reduction.[56,57] In this context, taking into account that the reduction processes appear at relatively high temperatures (220 and 361 ºC) in the PtCeAl profile and considering that platinum phases were not detected by XRD, the TPR data seem to indicate small Pt particle sizes in the prepared sample.

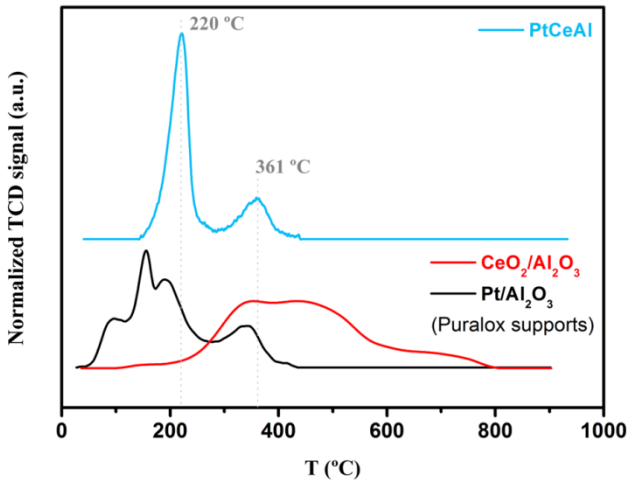

Figure 3.4 H_2-TPR profiles of the PtCeAl catalyst compared to the commercial ceria-alumina Puralox support and the 2 wt. % of Pt over commercial alumina Sasol.

A quantitative analysis of the reducibility of the sample has been carried out after calibrating the TCD signal using a standard CuO pattern (Strem Chemicals 99.999%). Thus, the reducibility has been defined as:

$$\%\ Reducibility = \frac{Experimental\ H_2\ consumption}{Theoretical\ H_2\ consumption} \cdot 100 \qquad [3.1]$$

Accordingly, the total H_2 consumption (up to ~ 450 ºC) respect to the theoretical one, assuming Pt^{4+} species ($PtO_2 + 2H_2 \rightarrow Pt + 2H_2O$), indicates a 365.53 % of reducibility. This over-consumption could be due, besides the Pt reduction process, to other processes like Ce^{4+} reduction or carbon deposits hydrogenation reactions. Considering only the first observed reduction process around 220 ºC, the calculated reducibility still shows over-consumption (270.30 %). Consequently, from ~300 ºC the Pt is assumed to be completely

reduced. Moreover, by comparison of the TPR profiles of Pt/Al_2O_3 and CeO_2/Al_2O_3 samples, the last peak at around 361 ºC should be associated to the reduction of ceria or to the hydrogenation of carbonaceous species. According to the TPR data, and taking into account the calcination temperature of the PtCeAl sample, a reduction at 350 ºC in a 10 % of H_2/N_2 flow for 30 min was selected as the catalyst activation step to completely reduce the Pt particles and to avoid high calcination temperatures that favour the particle sintering.

Since Pt particles have not been identified or measured by the techniques previously used, an estimate of metal dispersion and particle size by *in situ* IR spectroscopy of CO adsorption was performed. The sample was pelletized (21 mg of PtCeAl pressed into a disk of 15 mm in diameter) and activated *in situ* under H_2 (130 mbar) at 400 ºC for 1h. Subsequent degasification in vacuum with a residual pressure lower than 10^{-5} mbar was carried out to "*clean*" the surface from impurities. Then, at RT and in vacuum conditions, two spectra of the sample and the gas phase were recorded as references. Next, small doses of CO (~2 mbar in a 2.11 ml volume, each time) were introduced and both sample and the gas phase were analysed *in situ* by FTIR spectroscopy in agreement with Perrichon and co-workers' method.[58] The analysis of the υ_{CO} (Figure 3.5a) show an intense band at 2069 cm^{-1} associated to CO linearly adsorbed on Pt active sites. The intensity of this band increases on increasing the amount of CO, where each spectrum corresponds to a new dose of ~2 mbar of CO up to metal saturation is achieved. The exhibited broad tail to lower wavenumbers indicates different Pt coordination and/or sizes.[58,59] On the other side, the band at 1830 cm^{-1} is assigned to

doubly bridged Pt_2CO species. The amount of bridged CO is so low and only becomes a little significant near to saturation. The integration of the intensity of the band at 2069 cm^{-1} is then considered to provide an estimate of the amount of Pt active sites considering a 1:1 adsorption stoichiometry for CO:Pt. Thus, the integrated intensity of the band at 2069 cm^{-1} increases linearly with the introduction of CO up to ~1.7 µmol (Figure 3.5b), where a change of the slope indicates the Pt saturation, *i.e.*, the adsorbed CO monolayer on Pt.

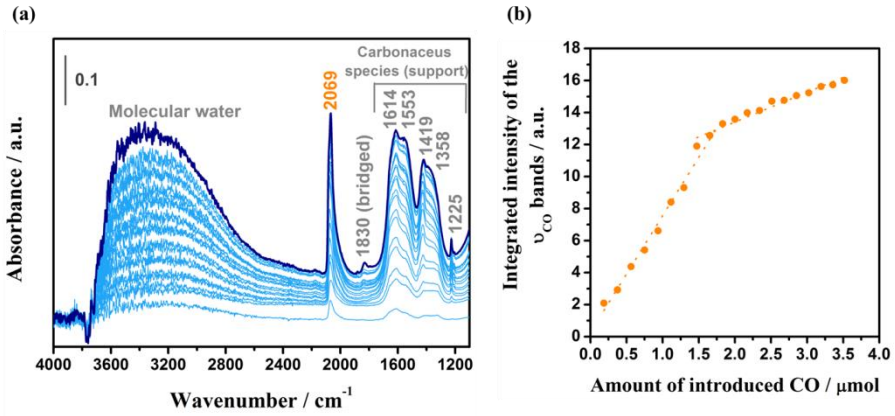

Figure 3.5 (a) Difference spectra on increasing the amount of CO by small doses on PtCeAl catalyst at RT. (b)Integrated intensity of the bands at 2069 cm^{-1} associated to linear adsorbed CO on Pt as a function of the amount of introduced CO.

Considering the amount of Pt in the tested PtCeAl sample and the amount of accessible Pt sites according to the adsorbed linear CO determined by *in situ* FTIR spectroscopy, the dispersion is estimated as:

$$D_{Pt}(\%) = \frac{Accesible\ amount\ of\ Pt\ by\ CO\ adsorption}{Total\ amount\ of\ Pt\ in\ the\ sample} \cdot 100 \qquad [3.2]$$

Accordingly, the estimated Pt dispersion in PtCeAl catalyst is ~79%. This value is slightly over-estimated since the introduction of CO also shows adsorbed molecular water formation as well as carbonaceous species (carbonates, bicarbonates…) absorbed on the ceria/alumina support (bands from 1620 to 1200 cm^{-1}),[60] which may indicate the appearance of reactions like WGS that consume CO modifying the dispersion measurement. However, the estimated value can be acceptable if it is compared to those shown in Gonzalez's work,[61] where Pt dispersions of 59 % and 70 % were found for 4 wt.% of Pt over CeO_2/Al_2O_3 and for 2 wt.% of Pt over $Ce_{0.8}Fe_{0.2}O_2/Al_2O_3$, respectively, measured at -77 ºC in order to avoid the ceria contribution through CO oxidation.

Assuming Pt dispersion of 79 %, Pt particles sizes of 1.5 – 2 nm are expected according to several relations between dispersion and metal surface area average diameter for Pt particles defined elsewhere.[62–64] These small Pt particle sizes are perfectly possible in good agreement with the absence of Pt diffraction peak in XRD analysis and also unobservable Pt particles in TEM images.

Finally, PtCeAl catalyst was analysed by X-ray Absorption spectroscopy (XAS) in beamline BL-22 CLAESS in Alba Synchrotron. The XANES-EXAFS spectra of Pt and Ce L_3-edges were collected (see Chapter 2). The analysis of the Ce L_3-edge spectra at RT of the synthesized PtCeAl sample has provided an accurate description of the initial structure of the catalyst.

The Ce L_3-edge XANES absorption line (5727 eV, Figure 3.6) shows two different peaks (commonly labelled B_1 and C) according

to the presence of a majority of Ce^{4+} oxidation state.[65,66] The lower energy absorption peak (B_1) is commonly attributed to the absorption from 2p level into the 5d with the 4f orbital remaining unoccupied, resulting in $Ce[2p^5 4f^0 5d^1]O[2p^6]$ state configuration. Additionally, the second absorption peak at higher energies of the Ce^{4+} oxidation state is attributed to the transit from the oxygen valence band to the ceria 4f shell leaving a hole in the oxygen valence band, leading a final configuration as $Ce[2p^5 4f^1 5d^1]O[2p^5]$.

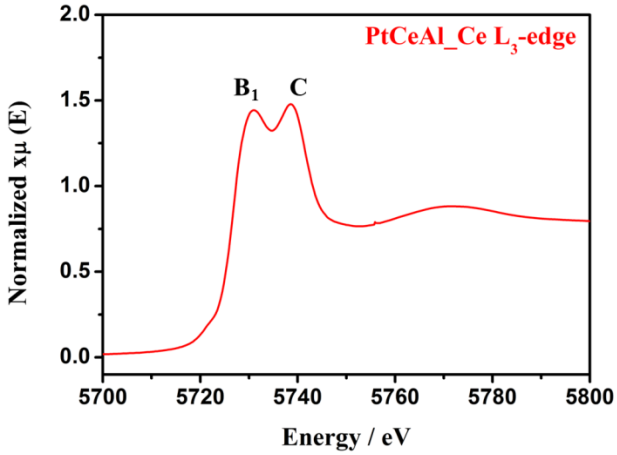

Figure 3.6 XANES spectrum at RT for Ce L_3-edge of prepared PtCeAl catalyst.

On the other side, the EXAFS analysis for the Ce L_3-edge of the PtCeAl catalyst has been fitted to a proposed structure model. From the proposed structure, the associated parameters of the different coordination shells (j) respect to the ionized atom (Ce in this case) can be fitted by the EXAFS function:[67]

$$\chi(k) = \sum_j \frac{N_j f_j(k) e^{-2k^2\sigma_j^2} e^{-2R_j/\lambda(k)}}{kR_j^2} \sin\left[2kR_j + \varphi_j(k)\right] \qquad [3.3]$$

where k [$k = (2m(E - E_0)/\hbar^2)^{1/2}$] is the wave number of the photo-electron, m is the electron mass, E_0 is the adsorption edge energy (5727 eV for the Ce sample), $\hbar$ is Planck constant, N_j is the number of neighbouring atoms of each coordination sphere, R is the distance to neighbouring atom, λ is the mean-free-path of the photo-electron, σ_j^2 is the Debye-Waller factor associated to the disorder in the neighbour distance, and $f_j(k)$ and $\varphi_j(k)$ are amplitude and phase functions, respectively, related to scattering properties of the atoms neighbouring the excited atom and characteristic of each element, since depend on the Z atomic number.

A structure based on a cubic γ-Al_2O_3 (bulk) exhibiting the (111) face over which CeO_2 phase in the same orientation is loaded, is proposed. The good fit (dotted line, Figure 3.8) has indicated that an only one Ce monolayer adopting $Fm\bar{3}m$ structure is loaded over the alumina, also exposing the (111) face. This $Fm\bar{3}m$ structure for the ceria is in good agreement with that observed by TEM:

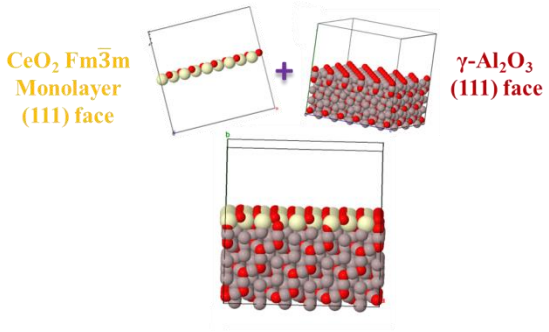

Figure 3.7 Model of cubic CeO_2/Al_2O_3 support of PtCeAl catalyst.

Moreover, in concordance with XRD and TEM, no Pt contribution from the Ce L_3-edge excitation has been observed. Therefore, small

Pt particles highly dispersed are expected, thereby supporting the estimated Pt dispersion and particle size analysed above.

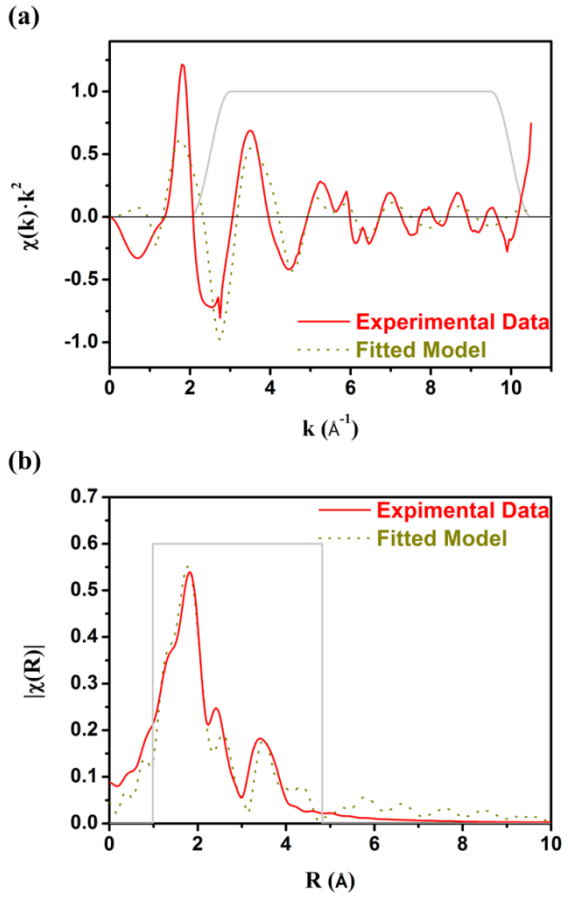

Figure 3.8 EXAFS in k space (a) and in R space (b) of the PtCeAl catalyst corresponding to Ce L_3-edge measurement. Experimental (red line) and fitted (dotted line) spectra. Data range used for the fit delimited with grey box.

From the EXFAS function [χ(k), Figure 3.8a], by Fourier Transform, is possible to describe separately the contribution of each coordination shell (j), whose modulus (|χ(R)|) of all contributions is represented in Figure 3.8b. The fit on the model previously presented

provides a first shell of 7±1 oxygen atoms between Ce and Al atoms layers for region below ceria monolayer. In addition, other oxygen coordination shell at slightly different distance due to the adsorbed water on the surface in these conditions provides an average coordination number of 3,2. A second coordination shell of Al atoms, whose coordination number oscillates between 2-3, is also observed. Next, the coordination sphere corresponding to the Ce atoms present in the same ceria monolayer exhibits an approximate coordination number of 3.5, slightly lower than theoretical 4 atoms. Finally, the furthest coordination shell considered in the model is again oxygen (12 atoms).

The reduced numbers of coordination atoms in the fitted model are consistent with an uncomplete loaded ceria monolayer. Considering the 20:80 mass ratio of the support (CeO_2/Al_2O_3 Puralox), the specific surface of the un-doped Al_2O_3 support (160 m^2) and the (111) face of CeO_2 with a surface of 25.35 $Å^2$ according to the $Fm\bar{3}m$ ceria lattice parameter (a = 5.41 Å) with 1.25 Ce atoms per unit cell, the calculated occupancy of ceria monolayer is 88.73 %. Therefore, only the ~89 % of the ceria monolayer is really loaded, which supports the approximate coordination numbers.

3.2.3. Partial conclusions.

The Pt particles loaded in PtCeAl catalyst could not be identified or measured by XRD or TEM. However, the Pt dispersion analysis by CO adsorption analysed by *in situ* FTIR has indicated a high dispersion of ~79 % corresponding to a particle sizes in 1.5-2 nm range. These calculations are also supported by EXAFS analysis on

Ce L_3-edge, which has not shown contribution from Pt scattering, indicating the low probability of the photo-electron from Ce atoms to find Pt atoms.

In addition, the EXAFS analysis provide a structure model of the PtCeAl catalyst were the Pt nanoparticles are highly dispersed on an uncomplete ceria $Fm\bar{3}m$ monolayer (88.73 % of the monolayer) over the γ-Al_2O_3 bulk, both phases growing on (111) face.

On the other side, the XANES analysis has shown that the Pt and Ce are in oxidized state before activation in WGS. Then, the H_2-TPR experiments have revealed different reduction steps involving the Pt and Ce reduction up to 361 ºC. According to the quantitative analysis, in the first reduction peak the reducibility of the Pt exceeds the 100 %. Therefore, the Pt is considered completely reduced under 350 ºC, also supported by reported data and by the TPR profiles of Pt/Al_2O_3 and CeO_2/Al_2O_3 samples for comparison. The last reduction process has been mainly related to the ceria reduction. Consequently, and having the calcination temperature of the PtCeAl catalyst (350 ºC) in mind, the activation step of the catalyst has been stablished at 350 ºC for 30 min. in a 10 % of H_2 flow.

3.3. Zr-BASED PROTON CONDUCTORS

3.3.1. Synthesis of Eu-doped ZrO_2 and Mo- and Eu-doped ZrO_2 compounds series.

Two series of compound have been synthesized: Eu-doped ZrO_2 samples with 2, 5, 7, 9, 10, 12 and 15 mol.% of Eu_2O_3 (labelled ZrEu_x, where x indicates the nominal mol.% of Eu_2O_3), and Mo-

and Eu-doped ZrO_2 materials where a 95:5 ZrO_2:Eu_2O_3 molar ratio has been fixed and the MoO_3 content was set equal to 5, 7 or 12 mol.% (named ZrEuMo_x, where x stands for the nominal mol.% of MoO_3). The ZrEu_5 sample has been chosen as the bare proton conductor for adding Mo since, as it will be seen later, it shows the highest proton conductivity (Chapter 4) and the best promotion effect on the PtCeAl catalyst in WGS reaction (Chapter 5).

The co-precipitation method at room temperature was used for the synthesis of these compounds. Thus, the appropriate amount of 0.1 M aqueous solution of europium (III) nitrate pentahydrate (Sigma-Aldrich) was slowly added to a 0.1M aqueous solution of zirconium (IV) oxynitrate hydrate (Sigma-Aldrich) under continuous stirring. The initial pH value of the solution was in the 1-2 range, then the pH was increased until 8 by adding an ammonia solution (30 vol.%, Panreac). Afterwards, the solution was aged for 1.5 hours at room temperature under stirring. The obtained white precipitate was filtered, washed with distilled water and then submitted to dryness at 100 ºC overnight. Finally, the solid was calcined in air at 500 ºC for 5h to remove the nitrate leftovers according to the TG-DTA analysis (Figure 3.9). In the case of the Mo-series, after the convenient amount of the Eu solution over Zr solution, the suitable amount of 0.1M aqueous solution of ammonium molybdate tetrahydrate ($(NH_4)_6Mo_7O_{24}$, Alfa Aesar) was also slowly added under continuous stirring. The procedure of increasing the pH up to 8 for the precipitation and the drying and calcination processes were the same. The products obtained in this series are pale yellow.

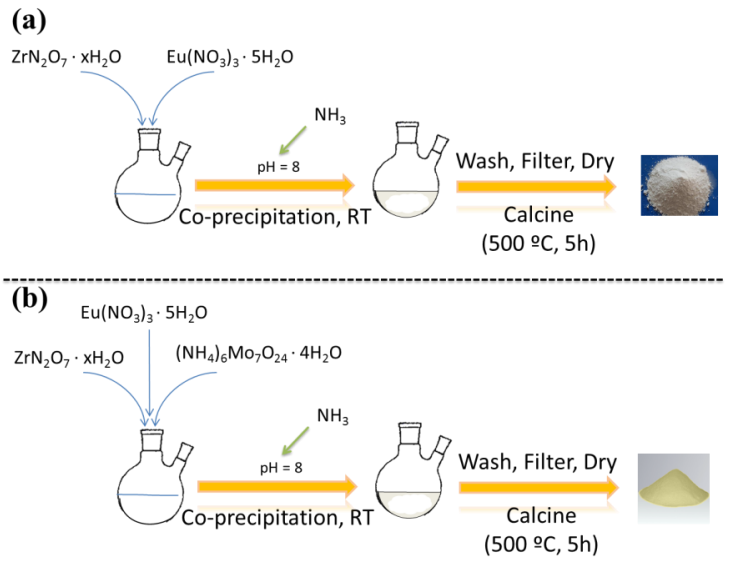

Scheme 3.2 (a) Synthesis process of Eu-doped ZrO_2 compounds series and (b) synthesis process of Mo- and Eu-doped ZrO_2 compounds series.

As is mentioned above, prior to the final calcination step, the precipitated ZrEu_x solids were analysed by TG-DTA in order to stablish the softest possible calcination conditions to remove the nitrate precursors but avoiding sintering of the powders. TG-DTA data of the dried ZrEu_5 (experimental conditions are described in Chapter 2) are presented in Figure 3.9. This profile is representative of the behaviour of all synthesized samples.

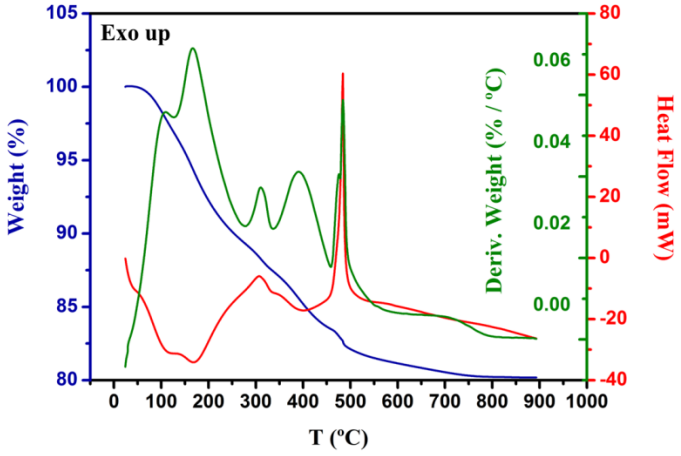

Figure 3.9 TG-DTA analysis of the synthesized ZrEu_5 sample. TG data (blue), DTG (green) and DTA (red).

A 20 % total weight loss is observed in the TG-DTA profile. A complex decomposition pattern showing multiple overlapping decompositions steps are observed in the low-medium temperature range. At low temperatures (100 - 200 ºC), endothermic processes corresponding to water elimination are described. Nitrate decomposition occurs at temperatures between 300 ºC and 500 ºC in a complex process characterizes by an initial endothermic step and a sharp final exothermic process. This is a common pattern for nitrate decomposition that usually occurs very exothermically with more intense mass loss after melting (endothermal) and sometimes phase changes (also endothermal). The absence of nitrate leftovers has been further checked together with the structural and electronic properties of the synthesized materials. This will be analysed in the next section.

3.3.2. Elemental characterization (XRD, N_2 adsorption, TEM, XRF and XPS).

The ionic radius of the Eu^{3+} dopant, 0.95 Å, is slightly higher than that of the Zr^{4+} cation, 0.84 Å, of the hosting lattice. However, despite the good matching of the Eu^{3+} and Zr^{4+} ionic radii, ZrO_2 and Eu_2O_3 are not completely miscible as it should be expected by their different crystal structures and valences. Therefore, cubic solid solutions appear just in a limited compositional range. These solid solutions may contain a relative large number of environments for Eu^{3+} cations, from isolated ions to large clusters of associated Eu^{3+} ions and oxygen vacancies.[68] For Eu:Zr molar concentrations 1:1 oxygen vacancies order and cubic pyrochlore structures develop.[69] The lattice constant of low Eu content defective fluorite solid solutions follows Vegard's law, which implies an enlargement of the lattice constant as well as an increase in the number of oxygen vacancies,[69] deviations from this model may be due to the existence of short-range pyrochlore-like structures over the extended defect fluorite structure of the solid solution.[70] To elucidate the structural properties of the Eu-doped ZrO_2 prepared materials XRD measurements were carried out. The diffractograms of the prepared materials, once calcined, are presented in Figure 3.10. For Eu_2O_3 loadings below 9 mol.%, the solids maintain a cubic fluorite type structure ($Fm\bar{3}m$) of the $Eu_xZr_{1-x}O_{2-0.5x}$ solid solution [JCPDS: 01-078-1303] characteristic of Eu-doped ZrO_2 compounds.[69–71] All the diffraction peaks slightly shift toward lower angles on adding europium to the ZrO_2 phase. At higher europium loadings, either a segregated Eu oxide phase or short-range defect ordering appears. A close inspection of the diffraction line

corresponding to the (111) crystallographic plane, Figure 3.10b, allows noticing the enlargement of the FWHM on increasing the Eu content as well as the presence of a shoulder that may be compatible with both the presence of a segregated Eu oxide phase or with short-range defect ordering producing pyrocholore-like structures within the cubic material. At the highest Eu_2O_3 contents analysed diffraction lines tend to overlap, which difficult further analysis. Therefore, 10 mol.% Eu_2O_3 corresponds to the maximal europium content allowed in the host zirconium oxide lattice. In consequence with this experimental observation, we can establish that the solubility limit of Eu_2O_3 in ZrO_2 resulting in homogeneous defect fluorite solid solutions is around 10 mol.% of Eu_2O_3. This is in agreement with literature data, substitution-type non-stoichiometric solid solutions are known to be formed on the ZrO_2-Eu_2O_3 system. The ones based on cubic modifications of ZrO_2 form the so called "defect fluorite" structure.[72] This substitution increases the concentration of oxygen vacancies and may be represented by the Kröger-Vink formulation.[73]

$$xEu_2O_3(ZrO_2) \longrightarrow 2xEu'_{Zr} + xV_O^{\cdot\cdot} \qquad [3.4]$$

This formula is assumed to be correct for whatever the polymorphs of the ZrO_2 phase, monoclinic (M), tetragonal (T) and cubic (fluorite-type, F). However, the Ln_2O_3 solubility depends on the crystalline structure: 2 mol.% in the monoclinic phase, less than 5 mol.% in the tetragonal phase and up to 80 mol.% in the fluorite-type solid solutions.[73] For europium, the solubility limit has been fixed in ~55 mol.%.[74]

Despite the high solubility described in most works, it has be taken into account that most studies have been carried out at temperatures well above 1000ºC. The ZrO_2-Eu_2O_3 phase diagram reported by Kiparisov *et al.* from 1100 to 2700 ºC is reproduced by Andrievskaya.[73] It is stated the formation of a T phase solid solution for Eu_2O_3 contents below 2 mol.%, a mixture of T and F solid solutions for Eu_2O_3 contents in the range 2-12 mol.%, pure F phase above these values and an ordered pyrochlore structure for Eu_2O_3 contents around 50 mol.%.

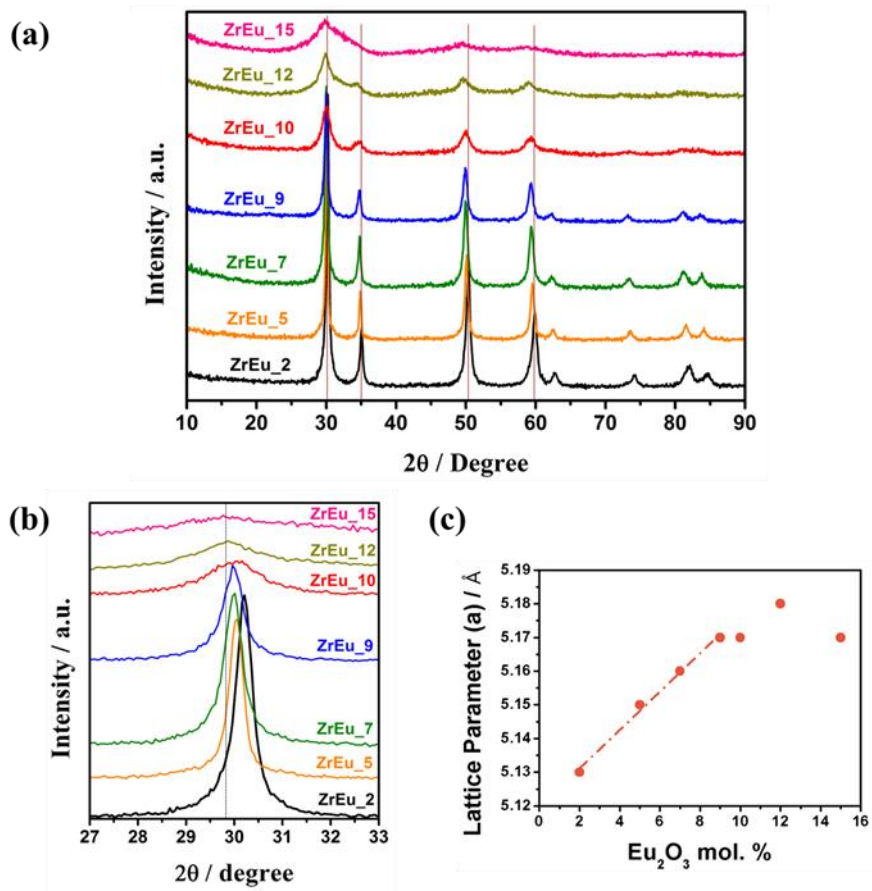

Figure 3.10 XRD data for the Eu-doped ZrO_2 materials (ZrEu_x, where x indicates the nominal mol.%of Eu_2O_3). (a) XRD pattern, (b) expanded view of the XRD pattern showing the diffraction line corresponding to the (111) crystallographic plane and (c) lattice parameter of ZrEu_x samples on increasing the Eu content.

Figure 3.10c presents the relationship between the europium content of the samples and the lattice parameters calculated for a cubic structure using the experimental d-spacing (equation 3.2) of the main diffraction lines.

$$\frac{1}{d^2} = \frac{h^2+k^2+l^2}{a^2} \qquad [3.5]$$

The addition of molybdenum to the ZrEu_5 sample does not modify its XRD pattern, Figure 3.11. Neither diffraction angles nor line diffraction intensities are modified on adding Mo within the studied range of compositions. This would indicate that the isomorphic substitution of either Eu or Zr in the cubic lattice may be discarded. By considering the ionic radii of the involved cations, 0.84 and 0,95 Å for Zr^{4+} and Eu^{3+} cations, respectively, the formation of a solid solution is thermodynamically possible, as discussed above; however, these radii are meaningful higher than that of Mo(VI). The significantly smaller radius of the Mo^{6+} cation (0.41-0.73 Å depending on its coordination) may result in either the filling of intersticials tetrahedral holes in the zirconia lattice or in a surface segregation pinning the growth of the zirconia nanoparticles. As the lattice parameter of the zirconia phase remains unaltered as well as the absence of new diffraction lines on Mo doping allows discarding the inclusion of the Mo cation in the zirconia host lattice. If the hypothesis of a superficial Mo oxide phase is assumed, the absence of diffraction lines for MoO_x species may be expected since its loading is well below the monolayer capacity in good agreement with Chary *et al.*' work.[75] It was early shown that adding oxoanions to zirconia stabilizes its surface,[76] among them, oxoanions of transition metals in their highest oxidation state (*e.g.* Cr, W and Mo).[77,78] These additions after drying the precipitated zirconia may hinder the agglomeration and growth of ZrO_2 nanoparticles, preventing the formation of Zr–O–Zr bonds from Zr–OH moieties, as observed earlier.[79] This cannot be observed after adding Mo to dried ZrO_2 samples. However, by adding molydates to wet gels, the surface tension is modified and the porous

structure of the gel is preserved. Therefore, it is concluded that on adding Mo to ZrO_2 even in the precipitation stage formation of surface molybdates occurs hindering zirconia crystallization and favoring high surface areas.[80] However, no evidences are obtained from the XRD data and, therefore, other characterization techniques are mandatory to identify the molybdenum dopant presence and structure.

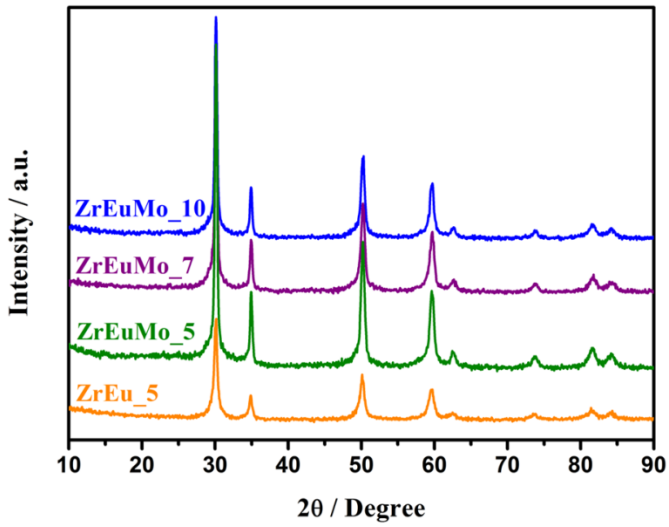

Figure 3.11 XRD of ZrEuMo_x samples compared with the bare (Mo-undoped) ZrEu_5 sample of the previous synthesized series.

The crystallite size of the ZrEu_x and ZrEuMo_x samples have been estimated by Scherrer's equation (Chapter 2) on the (111) crystallographic plane of the solid solution. Overall, it should be noted a decrease of the crystallite size when increasing the europium content (Table 3.2). This behaviour is similar to that previously observed for the solid solutions formed between CeO_2 and aliovalent trivalent cations including europium.[81,82] The crystallite size trend is usually associated with surface energetics and is related to the

number of surface oxygen vacancies induced by doping with aliovalent cations in ZrO_2 or CeO_2 matrices.[83] Regarding the diffractograms shown above, the intensity of the peaks on increasing the Eu content decreases and, above a certain limit, may overlap the diffraction lines of segregated Eu oxide and Eu-doped cubic ZrO_2 phases. Therefore, crystallite size estimation may be highly doubtful for the highest Eu concentration analysed since diffraction lines of more than one phase overlap. Mo addition to the ZrEu_5 sample does not modify average crystalline domain as estimated using the Scherrer's equation to the FWHM of the diffraction line corresponding to the (111) crystallographic plane. This again suggests that aliovalent substitution of Zr-Eu solid solution cations by Mo should not be considered.

Table 3.2 Textural properties determined by N_2-adsorption at 77 K and crystallite sizes estimated through the FWHM of the (111) diffraction line using the Scherrer's equation for ZrEu_x and ZrEuMo_x samples.

Sample	Crystallite size (nm)	S_{BET} ($m^2 \cdot g^{-1}$)	Pore volume ($cm^3 \cdot g^{-1}$)	Pore size (nm)
ZrEu_2	24	68	0.072	3.8
ZrEu_5	33	42	0.020	3.4
ZrEu_7	21	19	0.015	2.2
ZrEu_9	19	25	0.021	2.4
ZrEu_10	6	10	0.008	2.3
ZrEu_12	-	9	0.007	2.5
ZrEuMo_5	32	74	0.058	2.4
ZrEuMo_7	36	88	0.067	2.4
ZrEuMo_10	32	85	0.063	2.4

The textural properties of the mixed oxides once calcined are also summarized in Table 3.2. The specific BET surface area, pore volume and average pore radius decreases on increasing the europium content. However, Mo-containing sample present higher surface area, smaller pore volume and radius, showing these textural properties no dependence on the Mo content. These observations are better than that found by Chary *et al.*[75] They studied MoO_3/ZrO_2 catalysts prepared by wet impregnation of monoclinic ZrO_2 supports at pH=8, and they observed the formation of surface MoO_3 phases for Mo loadings above 9% and the modification of the monoclinic phase in a mixture of monoclinic, tetragonal and cubic phases, in which the surface area upon Mo loading slightly increases. A similar system studied by Matsuoka *et al.*[84] prepared by wet impregnation at pH=10 with ammonium heptamolybdate resulted in a drastic surface area reduction upon 10% Mo loading. The textural properties of the samples prepared by co-precipitation (Table 3.2) at pH=8 results in higher surface areas and a monophasic support presenting a cubic structure for the Eu-modified ZrO_2 samples.

The N_2 adsorption-desorption isotherms of all the ZrEu_x samples are similar, as an example the one for the ZrEu_5 sample is shown in Figure 3.12a. The addition of Mo does not modify the shape of the N_2 adsorption-desorption isotherms as can be seen in Figure 3.12b for the ZrEuMo_5 sample. These isotherms can be classified as type IV characteristic of mesoporous solids (2-50 nm).[49,51] However, the high convexity of the curve for relative pressures (P/P_0) below 0,5 may suggest the existence of pores with radii close to that of micropores. The steeply increase of the adsorbed volume on increasing P/P_0 is

even more pronounced for the Mo-modified samples. For instance, the pore size distribution for MCM-41 materials using DFT methods was calculated considering the attraction potential of the pore walls on the N_2 molecule.[85] The method allows estimate the adsorption energy distribution as a function of pore sizes. On applying this method to different MCM-41 materials with different pores sizes it appears evident the isotherm convexity and the average pore radius in the range 2,8-4,0 nm.[86] These authors show that the amount adsorbed in the low-pressure region increases with a decrease in the pore size of the samples probably because of the enhancement of the gas - surface interactions caused by an increase in the curvature of pore walls. In these cases, the capillary condensation is indistinguishable from the monolayer formation process.[51] The estimate pore size distribution for the ZrEu_5 mixed oxide sample, selected as representative of the general behavior, shows a monomodal distribution (Figure 3.12c) centered at 3,4 nm. As expected for more steeply isotherms on adding Mo to the solid solution the average pore size decreases upon molybdenum addition, Table 3.2.

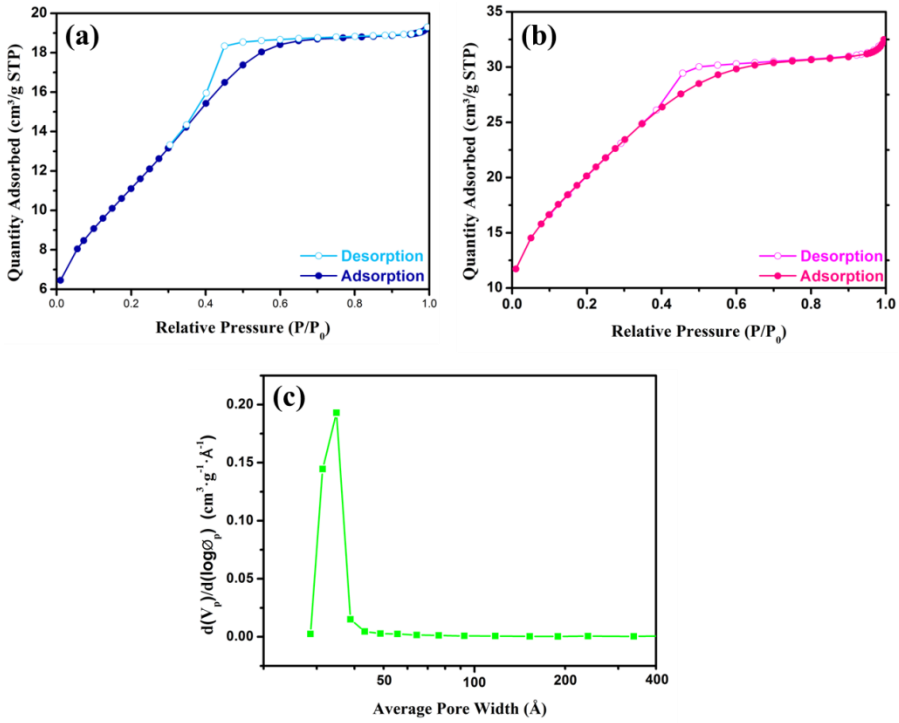

Figure 3.12 N_2 Adsorption-Desorption Isotherm at 77K of (a) ZrEu_5 and (b) ZrEuMo_5. (c) Pore size distribution of the ZrEu_5 sample calculated by the BJH desorption method.

On the basis of the textural properties and XRD data of the synthesised samples , further characterization like TEM, XRF, XPS, UV-Vis and Raman spectroscopies and TPR are going to be study only on ZrEu_2, ZrEu_5, ZrEu_7, ZrEu_12 and ZrEuMo_x series, since ZrEu_2 and ZrEu_5 are the samples with the highest BET surface area, ZrEu_12 sample consists in a solid solution containing Eu up to the solubility limit together with segregated Eu oxide phase, ZrEu_7 represent an intermediate concentration and ZrEuMo_x series still needs characterization to identified the Mo phase and the effect of the Mo concentration.

The pore size distribution of the synthesized ionic conductors determined using the BJH method is confirmed by TEM, where a high porosity of the samples with a homogeneous presence of 2-3 nm diameter pores are clearly seen. Figure 3.13 presents TEM micrographs and pore size distribution analysis, as an insert, for the ZrEu_2, ZrEu_5, ZrEu_7 and ZrEu_12 samples. The average pore diameters for all samples measured using the TEM images (between 2 and 3 nm) are consistent with the values obtained by N_2 adsorption. On the other hand, it is also noticeable that the pore concentration decreases on increasing the europium content. This suggests the formation of a segregated Eu oxide phase as suggested above from the XRD analysis.

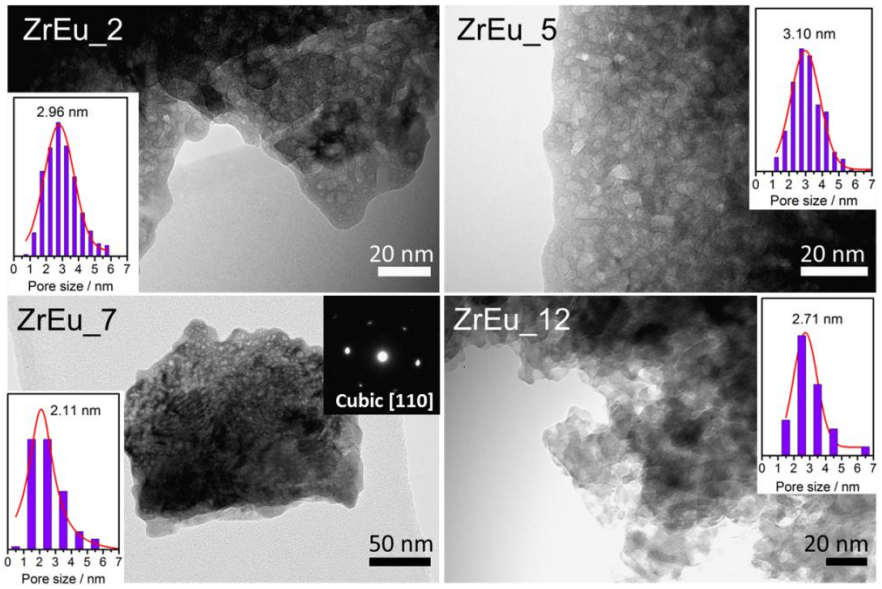

Figure 3.13 TEM micrographs and pore size distribution of the samples ZrEu_x (x = 2, 5, 7, 12).

All the synthesized Eu-doped zirconia solids exhibit a polycrystalline nature. For example, the inspection of the images of the ZrEu samples shown in Figure 3.13 confirms the presence of particles constituted by very small oxide crystals. However, in some cases the analysis, by selected area electron diffraction (SAED), of this type of particles clearly demonstrates their monocrystalline character. The electron diffraction pattern shown as an inset in Figure 3.13 corresponds to the ZrEu_7 particle of the figure. A typical electron diffraction pattern taken along [111] zone axis of the cubic phase is clearly recognized. In Figure 3.14, a different electron diffraction pattern taken from a larger area on sample ZrEu_2 is shown. The presence of typical diffraction rings demonstrates the polycrystalline nature of the sample. The observed rings are mainly due to the presence of the fluorite structure of the mixed oxide as revealed by their match with the first five theoretical reflections, inset in the image. Apart of these characteristic rings, some other reflections, in the form of light weak spots between the second and third rings, are observed on the experimental diffraction pattern. The measurements of the d-spacing that originates these extra spots are in agreement with the $(21\bar{1})$ planes of a zirconium oxide monoclinic phase. Focusing on the analysis of High Resolution Images, it is also possible to distinguish different nanocrystals showing both cubic and monoclinic structure. In this sense, zone A of image in Figure 3.14 shows periodic contrasts at 2.9 Å which can be assigned to (111) planes of the cubic structure. The digital diffraction pattern (DDP) obtained from this image corresponds to the [110] zone axis of the fluorite structure of the mixed oxide. On the contrary, the monoclinic

phase is detected in the zone B of the image. The interplanar spacing of 3.7 Å could be associated to the (001) or (110) planes of the monoclinic phase. Other areas have been analysed and interplanar spacings of 5.0 Å, according to the (100) planes of the monoclinic phase, have been measured. These observations are in agreement with the presence of the monoclinic phase in the ZrEu_2 sample, indicating that in some parts of the solid exist segregated monoclinic ZrO_2 due to the poor europium content in this sample. For samples containing above 5 mol.% of Eu_2O_3, the cubic structure is identified as the unique phase according to the formation of the solid solution analysed by XRD.

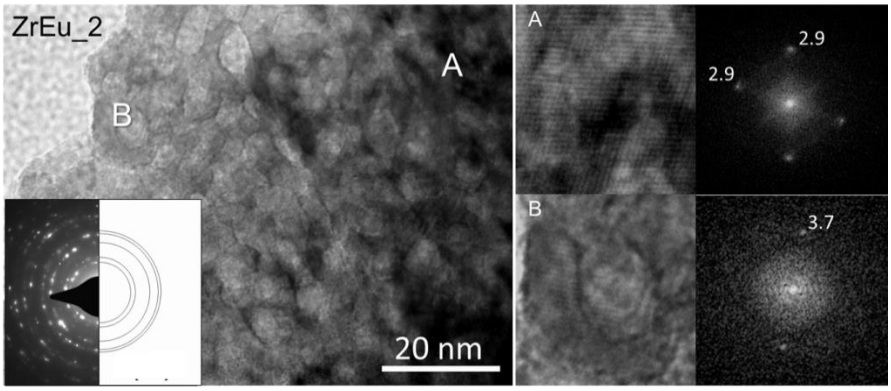

Figure 3.14 TEM micrograph and electron diffraction diagrams of the selected areas of the sample ZrEu_2.

In the same way, ZrEuMo_x samples show monocrystalline and polycrystalline zones as well as cubic structure. The porosity measured form the TEM images (Figure 3.15) is also in agreement with the data reported in Table 3.2 and discussed above from N_2 adsorption analysis.

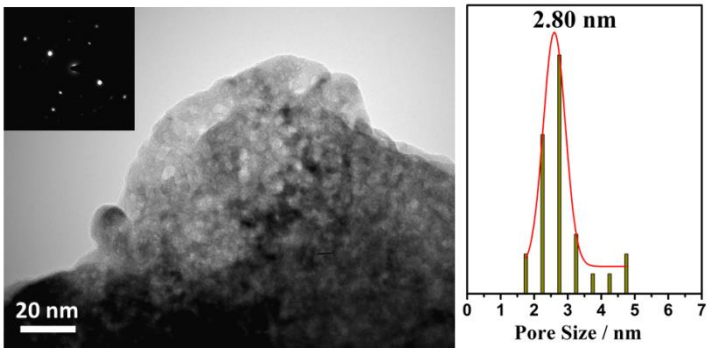

Figure 3.15 TEM micrograph, electron diffraction and pore size distribution of the ZrEuMo_5 sample.

In addition, to complete the elemental characterization, the chemical composition of the bulk and surface of the solids were determined by XRF and XPS in the operational conditions reported in Chapter 2. The chemical composition measured by XRF is in fairly good agreement with the targeted values (Table 3.3), indicating an appropriate bulk composition with that proposed by the co-precipitation synthesis method.

Table 3.3 Chemical composition of the prepared ionic conductors.

Sample / at. %	ZrEu_2	ZrEu_5	ZrEu_7	ZrEu_12	ZrEuMo_5	ZrEuMo_7	ZrEuMo_10
Zr	68.84 (69.94)	62.70 (64.35)	58.27 (60.93)	52.95 (53.28)	58.4 (60.9)	56.2 (59.6)	55.1 (57.5)
Eu	5.51 (4.77)	12.80 (11.29)	17.95 (15.28)	24.21 (24.21)	11.9 (10.7)	11.9 (10.4)	12.2 (10.1)
Mo	-	-	-	-	4.5 (3.6)	6.5 (5.0)	7.2 (7.1)
O	25.65 (25.29)	24.50 (24.36)	23.78 (23.79)	22.84 (22.51)	25.2 (24.8)	25.4 (25.0)	25.5 (25.3)

Nominal values in parenthesis.

The high resolution XPS analysis of Zr(3d), Eu(3d) and O(1s) levels allows estimate the surface composition of the prepared solids. The measured surface concentration of Eu and Zr is plotted in Figure 3.16 against the bulk composition measured by XRF. It is clear that all solid solutions are quite homogeneous being the surface and bulk compositions almost identical since all the measured surface concentrations deviates less than 10% from the measured XRF values. However, within the mentioned 10% error the solid that shows the higher deviations is the ZrEu_12 that, as was observed by XRD, forms a segregated Eu oxide phase. Therefore, an excess of Eu oxide may remain on the surface resulting in the biggest error observed within this series.

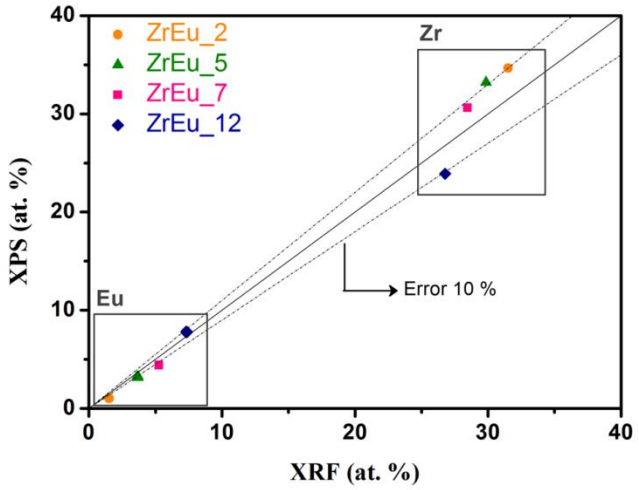

Figure 3.16 Comparison of the atomic percent of Eu and Zr determined by XPS in the surface and XRF in the bulk for the samples ZrEu_x (x = 2, 5, 7 and 12). Representation of the deviation of 10 % (dot line) from the ideal homogeneous solid solution (solid line).

On the other hand, important differences are revealed on analysing the bulk-to-surface atomic composition of the ZrEuMo_x, mainly respect to the Mo concentration. Figure 3.17 plots the Mo/Zr, Mo/Eu and Eu/Zr atomic ratios for each ionic conductor (ZrEuMo_x, x = 5, 7 and 10) calculated by XRF, stating thereby the bulk composition, and by XPS showing the composition in the surface. It must be considered that the synthesis procedure fixes a constant 95:5 molar ratio of the Zr:Eu oxides and that this composition results in a homogenous solid solution; therefore, the Eu/Zr atomic ratio must be constant for the three Mo-doped samples. However, it is noticeable the much lower surface than bulk Eu/Zr ratio (Figure 3.17a), indicating that Eu atoms have been preferentially covered, then reducing its apparent concentration in the surface and, consequently, the observed Eu/Zr surface ratio. Moreover, contrary to the Mo/Zr surface ratio (Figure 3.17c), which is equal to the Mo/Zr bulk ratio, that increases on increasing the amount of Mo added, the Mo/Eu surface ratio (Figure 3.17b) shows an increment of the Mo content at the expense of Eu surface concentration increasing this difference on increasing the Mo content. Therefore, the molybdenum atoms are preferentially placed over europium atoms. These observations evidence the idea of a surface segregation of the molybdenum phase over the Zr-Eu solid solution proposed by XRD analysis. This Mo phase sits preferentially on Eu sites.

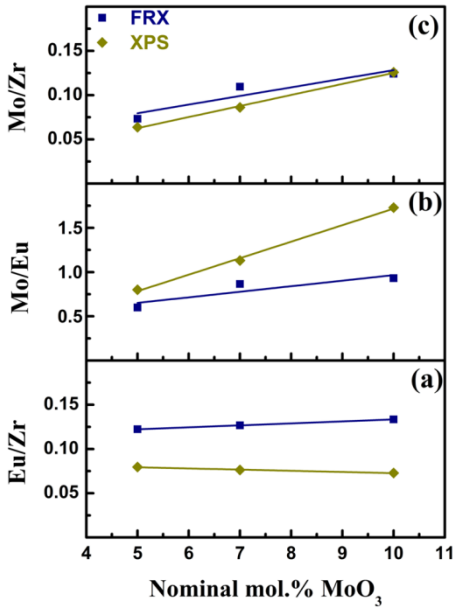

Figure 3.17 Atomic ratios in the bulk analysed by XRF and in the surface analysed by XPS for all ZrEuMo_x samples (where x shows the nominal amount of MoO_3, x= 5, 7 and 10 mol.%). (a) Eu/Zr ratio, (b) Mo/Eu ratio and (c) Mo/Zr ratio.

In light of the exposed results, it can be concluded that the used synthesis method results in a homogeneous mesoporous Eu-doped ZrO_2 solid solutions, in which a homogeneous oxygen vacancies distribution is expected. On adding Mo, the specific surface area increases and a surface segregated molybdenum phase appears on top of the Zr-Eu solid solution whose crystalline structure is not altered. This Mo oxide phase is situated on the surface covering preferentially the Eu atoms, although further characterization is mandatory to identify the Mo structure.

3.3.3. UV-Vis spectroscopy, Raman spectroscopy and TPR.

UV-Vis and Raman spectroscopy are of interest to uncover the structures exhibited by the amorphous and/or not detected phases, specially the proposed superficial Mo oxide phase that cannot be detected by XRD and, therefore, remains unknown.

Figure 3.18 plots together the UV-Vis absorption spectra of the ZrEu solid solutions (ZrEu_x, $5 \leq x \leq 12$) and a monoclinic ZrO_2 samples taken as reference for comparison. It is clear, that the presence of Eu^{3+} ions in the host zirconia structure provokes the appearance of a strong charge transfer transition band below 350 nm that exhibits a red-shift on increasing the europium content. This phenomenon can be explained by a narrowing of the band gap, by the appearance of intragap energy levels caused by the dopants or by the absorption caused by the created oxygen vacancies as reported by Serpone.[87] Besides this strong absorption feature in the UV region, much weaker characteristic absorptions ascribed to Eu^{3+} were also identified, these can be assigned to transitions from the $^7F_0$ ground state to $^5D_1$, $^5D_2$ and $^5L_6$ states of Eu^{3+}, respectively.[88–90]

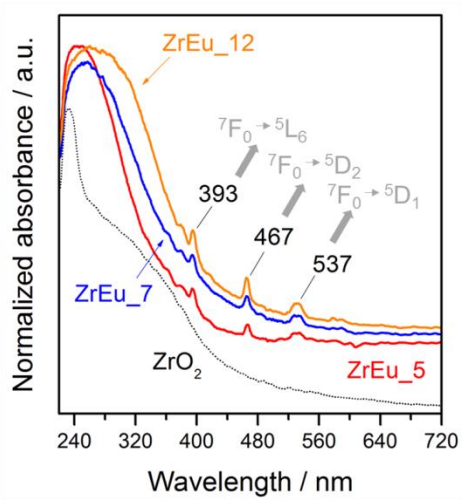

Figure 3.18 UV-Vis spectroscopy at room temperature of selected ZrEu_x samples and ZrO_2 spectrum as a reference for comparison.

These ZrEu_x samples were also analysed by Laser Raman spectroscopy using a 530 nm excitation laser (Figure 3.19). Europium dispersed in the host zirconia matrix caused luminiscence due to f→f transitions that dominates the Raman spectrum. In fact, the zirconia Raman spectrum is hidden by the europium luminescence. Table 3.4 compiles all the transitions according to the Raman shift position and the total absorption energy.[91] The luminescence profiles (wavelengths, relative intensities and widths) of these samples are in general similar to those observed for Eu^{3+} ions in other materials.[92–94] In general, transitions towards the $^5D_1$ excited state are observed at wavenumbers below 560 nm (Raman shift less than ~1000 cm^{-1}). At 579 nm the $^7F_0 \rightarrow {}^5D_0$ transition occurs, this transition only appears for Eu^{3+} ions with low symmetries, which indicates that Eu ions are associated to oxygen vacancies. The $^7F_1 \rightarrow {}^5D_0$ transition is identified at ~591 nm. This transition splits in three components between 588

and 594 nm (1791, 1860 and 1954 cm^{-1} Raman shifts). This splitting necessarily indicates that the symmetry is orthorhombic or less which again points to the association between Eu and oxygen vacancies.[91] Therefore, as stated by Goff *et al.*,[95] the oxygen vacancies defect clusters depend on the concentration of the aliovalent cations justifying the modification observed in the $^7F_1 \rightarrow {}^5D_0$ transition upon the increase of the europium concentration. The transition $^7F_2 \rightarrow {}^5D_0$ (around 607 nm), at higher Raman shifts, is strongly influenced by the local symmetry of Eu^{3+} ion and the nature of the ligands. According to several authors,[92–94,96] the relative intensity of the $^7F_2 \rightarrow {}^5D_0$ transition is higher than that of the $^7F_1 \rightarrow {}^5D_0$. The intensity ratio $(^7F_2 \rightarrow {}^5D_0)/(^7F_1 \rightarrow {}^5D_0)$ relates to the symmetry of the Eu coordination environment; thus, the lower the ratio, the higher the site symmetry. In these samples, the $(^7F_2 \rightarrow {}^5D_0)/(^7F_1 \rightarrow {}^5D_0)$ ratio increases with the Eu content, this is, there is a loss of symmetry of the europium site on increasing the Eu content, indicating again the association of the Eu atoms and the oxygen vacancies. Moreover, the $^7F_2 \rightarrow {}^5D_0$ transition is also affected by the contribution of emissions from higher excited states ($^5D_1$, $^5D_2$, $^5D_3$) in this energy range,[91] as it can be noticed in the 634 nm signal that shifts to higher energies on increasing the europium loading and, at the same time, an increase in its intensity is also observed.

Table 3.4 f → f transitions for synthesized Eu doped zirconia compounds.

Raman Shift (cm^{-1})	Wavelength (nm)	Transition	Raman Shift (cm^{-1})	Wavelength (nm)	Transition
260	540	$^7F_2 \rightarrow {}^5D_1$ $^7F_1 \rightarrow {}^5D_1$	1954	594	$^7F_1 \rightarrow {}^5D_0$
327	542	$^7F_2 \rightarrow {}^5D_1$ $^7F_1 \rightarrow {}^5D_1$	2324	607	$^7F_2 \rightarrow {}^5D_0$
560	548	$^7F_2 \rightarrow {}^5D_1$ $^7F_1 \rightarrow {}^5D_1$	2443	612	$^7F_2 \rightarrow {}^5D_0$
628	550	$^7F_2 \rightarrow {}^5D_1$ $^7F_1 \rightarrow {}^5D_1$	2985	633	$^7F_2 \rightarrow {}^5D_0$
720	553	$^7F_2 \rightarrow {}^5D_1$ $^7F_1 \rightarrow {}^5D_1$	3024	634	$^7F_2 \rightarrow {}^5D_0$
1530	579	$^7F_0 \rightarrow {}^0D_0$	3180	641	$^7F_3 \rightarrow {}^5D_0$
1791	588	$^7F_1 \rightarrow {}^0D_0$	3460 3472	652 653	$^7F_3 \rightarrow {}^5D_0$
1860	591	$^7F_1 \rightarrow {}^5D_0$	3645	660	$^7F_3 \rightarrow {}^5D_0$

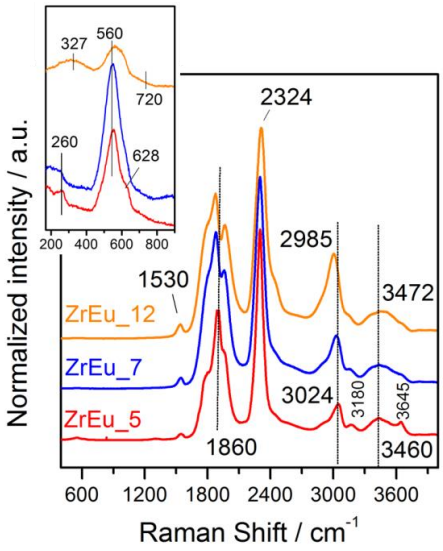

Figure 3.19 Raman spectroscopy of the selected ZrEu_x samples at room temperature.

Once ZrEu_x samples have been studied by UV-Vis and Raman spectroscopies, the same analysis on ZrEuMo_x series can also provide information about the formed Mo oxide structure. The molybdenum phase on Eu-doped zirconia mixed oxide can generate different Mo oxides phases or results in a MoO_x layer for high loadings;[36,97–99] however, its crystallinity in these compounds has not been enough to be identified by XRD technique.

Several authors have studied similar systems. Chippindale and Cheetham[36] reported paramolybdate species ($Mo_7O_{24}^{6-}$) as the most convenient precursor for the preparation of α–MoO_3 layers. In the same way, a MoO_3 phase is formed above 300 ºC upon decomposition of heptamolybdate[100]. Moreover, Hu *et al.*[101] studied by Raman spectroscopy and EXAFS analysis the different phases formed upon impregnation of ammonium heptamolybdate solution

over different supports like ZrO_2 as a function of Mo loading. They observed that the support nature, its isoelectric point and the solution pH affect the nature of the supported phase that may result in octahedral (MoO_x phases) or tetrahedral (hydrated molybdates) structures; however, they could not observe any influence of the preparation method. The Mo oxides supported on ZrO_2 in Hu's work exhibit isolated tetrahedral structures (MoO_4^{2-} in aqueous solution) for low loadings and high pH values, but octahedral ordering for high amounts of Mo. According to these authors, *ca.* 4 wt.% MoO_3 is required to form a monolayer on ZrO_2 (39 $m^2 \cdot g^{-1}$). This loading accounts for a Mo density of *ca.* 4,5 Mo atoms/nm^2. The formation of crystalline MoO_3 structures as stated by Raman at high Mo loadings. A slightly higher Mo loading (5 Mo atoms/nm^2) is determined by Xie *et al.*[102] to form a MoO_x monolayer on ZrO_2, which is in accordance with other authors[84,103–105]. Chary *et al.*[75], in a similar study with different loadings of MoO_3 on a 41 $m^2 \cdot g^{-1}$ ZrO_2 reports a 6,6 wt.% of MoO_3 as necessary to complete a monolayer. All these values are close to the 0.16 wt.% of MoO_3 per m^2 of support proposed by Van Hengstum *et al*.[103]

To estimate the Mo surface density is not an easy task. Our synthesis procedure implies the coprecipitation of Zr, Eu and Mo phases, not the impregnation of an already prepared ZrEu mixed oxide support. Two alternatives may be envisaged, the first one would consider a support of 45 $m^2 \cdot g^{-1}$ as reported in table 3.2 whereas a Mo-containing phase is on the surface of the mixed oxide. This may be consistent with a decrease in pore radius from 3,4 to 2,4 nm but cannot explain the increase in pore volume. In the second approach

the Mo-containing phase is in the surface of the mixed oxide but its relatively low concentration does not alter the surface of the solid, therefore the surface area is in the range 74-88 $m^2 \cdot g^{-1}$. This approach is consistent with a porous volume higher than in the support precipitated in the absence of molybdenum. As it is easily seen, the surface density of molybdenum is quite different depending on the approach, in the first case a MoO_3 monolayer should be attained, assuming Van Hengstum *et al.*' calculations,[103] for ca. 7,5 wt% of MoO_3 while in the second one between 12 and 14 wt% Mo is required for obtaining a statistical MoO_3 monolayer. A conservative approach may suggest that the monolayer capacity is in between these two extreme alternatives and, therefore, assume that the MoO_3 coverage in ZrEuMo_5 and ZrEuMo_7 is below the monolayer while for ZrEuMo_10 a close to unity coverage has been attained. The absence of diffraction lines associated to any Mo-containing phase may indicate either the formation of a monolayer all over the support in which tetrahedral molybdates dominates or the existence of islands of α-MoO_3 phase with sizes below the detection limit of the XRD diffractometer. XPS data (Figure 3.17) seems to better support the second hypothesis: small MoO_3 islands nucleating on Eu sites of the solid solution.

This structural hypothesis is purely speculative and in order to confirm it UV-Vis and Raman spectroscopies were carried out.

The UV-Vis spectra of ZrEuMo_x samples (Figure 3.20) show a shift of the edge energy (E_g) from ~270 nm (4.6 eV) to ~340 nm (3.6 eV) on increasing the Mo content associated to Mo-O-Mo bonds,

which, according to Tian *et al.*[97], indicates that ZrEuMo_5 sample shows predominantly isolated monomeric $[MoO_4]^{2-}$ species. On increasing the Mo concentration, $[Mo_7O_{24}]^{6-}$ clusters are formed and even a α-MoO_3 layer for the ZrEuMo_10 sample may appear. These structures are also in good agreement with the literature previously discussed and the density calculations above. Moreover, the UV-Vis spectra have been presented together with the support ZrEu_5 sample of the previous series for comparison, where the luminescence by f-f transitions of Eu has been hidden by the red shift of E_g on increasing the Mo content.

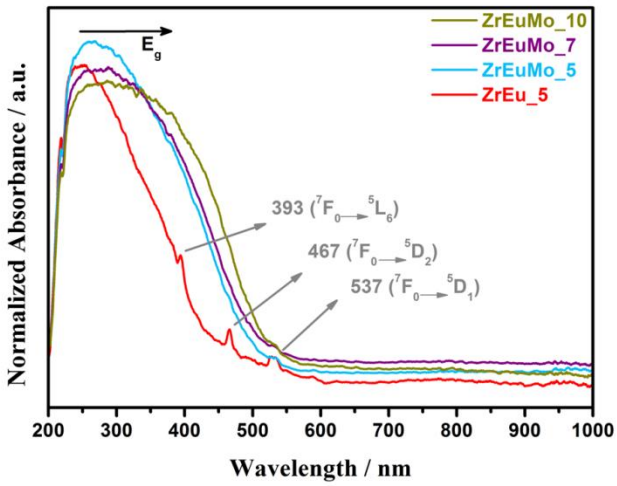

Figure 3.20 UV-Vis spectra at room temperature of ZrEuMo_x samples compared with ZrEu_5 as a reference for comparison.

Unfortunately, as it can be noticed in Figure 3.21 where the Raman spectra of ZrEuMo_x samples are also compared with ZrEu_5 sample, the intense luminescence of europium atoms hidden the Raman signals for the molybdenum species that show bands in the 200 – 400 cm^{-1} and 600 – 950 cm^{-1} ranges and therefore, to support

the proposed structures for molybdenum oxide based on the UV-Vis analysis and literature is impossible. Moreover, Raman spectra could provide information about the oxygen vacancies (MoO_x phases), the hydration of the Mo oxide or, for example, the crystalline MoO_3 phase.[43,75,99,101,106,107] Nevertheless, the Raman spectra (Figure 3.21) show the europium f-f transitions deeply discussed for ZrEu_x samples (Table 3.4 and Figure 3.19). Interestingly, in general the presence of Mo implies widening and shifting towards lower wavelengths (red shift) of the bands indicating that the f-f transitions are more favoured, especially those that include an excited state (like $^7F_1 \rightarrow {}^5D_1$, $^7F_2 \rightarrow {}^5D_1$, $^7F_2 \rightarrow {}^5D_0$ and $^7F_3 \rightarrow {}^5D_0$ transitions, Figure 3.21). Contrary, the $^7F_0 \rightarrow {}^5D_0$ transition appears at higher energy (blue shift) and the intensity is increased when the Mo is added but keept constant whatever the Mo loading within the studied range. As discussed above for ZrEu_x samples, this transition ($^7F_0 \rightarrow {}^5D_0$ at ~1530 cm^{-1} Raman shift, *i.e.* 579 nm) is exhibited when the symmetry of Eu^{3+} atoms is low. Thus, the increment of its intensity reveals the contact between Mo and Eu atoms reducing the symmetry of the latter. Moreover, as the Mo is added, the splitting shown in $^7F_1 \rightarrow {}^5D_0$ transition identified at ~591 nm (around 1880 cm^{-1} Raman shift) due to the association between the oxygen vacancies and the Eu atoms of the ZrEu_x samples becomes broader with the Mo presence due to the creation of many different Eu sites which stablishes again the influence of the Mo atoms in the Eu coordination. Analogously, it is not surprising that the $^7F_2 \rightarrow {}^5D_0$ transition (also known as hypersensitive transition) shows the most significant modified Eu luminescence by the presence of Mo atoms[91], stating again the

influence of the Mo atoms in the Eu surrounding. Furthermore, the intensity of the ($^7F_2 \rightarrow {}^5D_0$) / ($^7F_1 \rightarrow {}^5D_0$) transitions ratio, that is related to the symmetry of the Eu coordination environment (the higher the ratio, the lower the site symmetry), gets bigger on increasing the Mo content from 1.54 for ZrEu_5 sample to 2.56, 3.24 and 5.90 for ZrEuMo_5, ZrEuMo_7 and ZrEuMo_10 samples respectively, meaning a decrease of the Eu symmetry. Therefore, the changes in intensity and the shifts exhibited in Raman spectroscopy of ZrEuMo_x samples again evidences the intimate contact between the Mo and Eu atoms, supporting thereby the conclusions obtained by XPS analysis where Mo is preferentially positioned over Eu atoms.

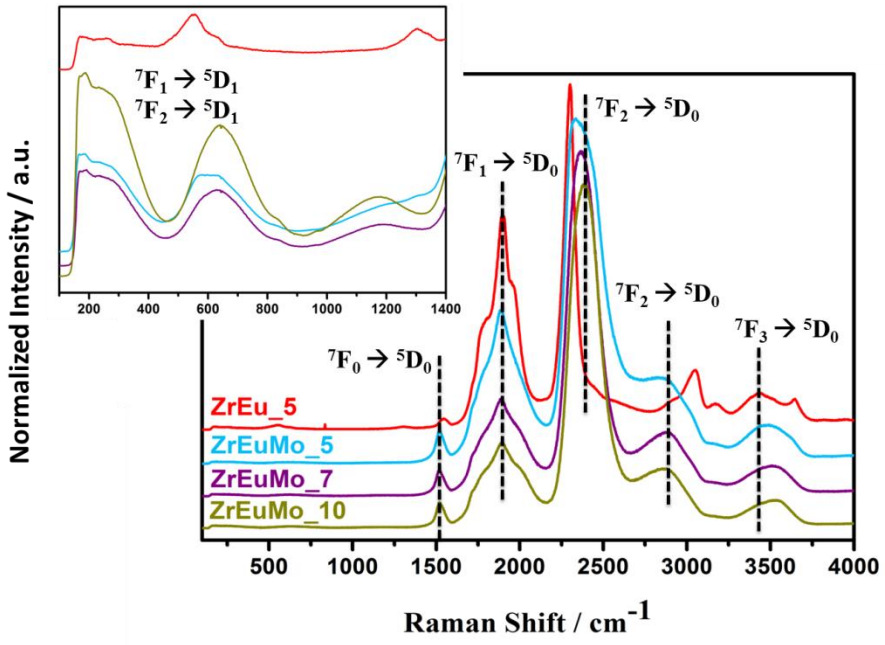

Figure 3.21 Raman spectroscopy using a green excitation laser (532.14 nm) at room temperature of ZrEuMo_x samples compared with ZrEu_5 as a reference for comparison.

To avoid luminescence as much as possible and get a further insight into the Mo-containing phase structure, Raman analysis were carried out again but with an excitation laser of 785 nm (red light) in the same ambient conditions. The use of this excitation wavelength allows to eliminate Eu luminescence in the 700-1000 cm^{-1} Raman shift range (Figure 3.22).

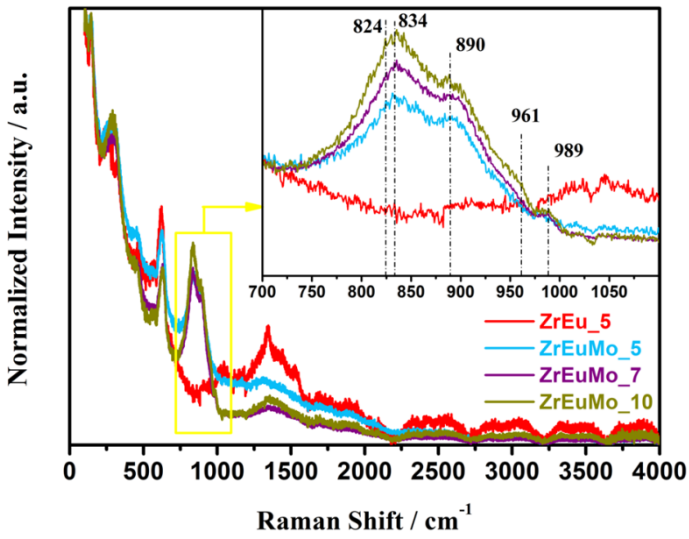

Figure 3.22 Raman spectroscopy using a red excitation laser (785 nm) at room temperature of ZrEuMo_x samples compared with ZrEu_5 as a reference for comparison.

This approach succeeds and Raman bands, distinguishable from these of the bare ZrEu_5 sample, associated to Mo-containing phases appear. A broad complex band between 700 and 1000 cm^{-1} Raman shift develops on adding Mo to the ZrEu_5 sample. This band shows clear maxima at *ca.* 830, 890, 960 and 990 cm^{-1}. The intensity of all of these bands increases on increasing coverage but the one at *ca*. 990

cm^{-1}. Collection of overlapping bands may be associated to stretching modes of both MoO_3 islands and molybdate clusters.

Terminal Mo=O bonds of isolated tetrahedral species appear at 924 cm^{-1} according to Hu *et al.*[101] These authors indicate that this band shift to 952 cm^{-1} on increasing Mo coverage on MoO_3/ZrO_2 indicating the formation of clusters containing octahedral Mo species (hydrated octahedral $[Mo_7O_{24}]^{6-}$ and $[Mo_8O_{26}]^{4-}$). On further increasing the Mo coverage a band at 820 cm^{-1} appears that is characteristic of MoO_3 species. Tian *et al.*[97] studied among others the MoO_3/ZrO_2 system as a function of Mo coverage. They ascribed bands at 919 cm^{-1} to isolated $[MoO_4]^{2-}$ anion, bands at 952 and 880 cm^{-1} that reflects the existence of $[Mo_7O_{24}]^{6-}$ clusters and a band at 820 cm^{-1} that assign to MoO_3 nanoparticles and corresponds to asymmetric stretching mode of bridging Mo-O-Mo bonds. Finally, the weak band at 989 cm^{-1} is ascribed to the symmetric stretching mode of terminal Mo=O bonds of the MoO_3 layer according to several authors.[75,97]

According to this, it must be concluded that whatever the Mo loading in these synthesized ZrEuMo_x samples, MoO_3 nanoparticles (band at 820-830 and 989 cm^{-1}) together with the presence of polymolybdate clusters, $[Mo_7O_{24}]^{6-}$ and $[Mo_8O_{26}]^{4-}$ (bands at 890 and 961 cm^{-1}) are always present. However, the line profile of the Raman spectra between 700 and 1000 cm^{-1} may not allow discarding the existence of isolated molybdate ions since their characteristic mode at 919 cm^{-1} may be hidden in the broad and complex band shown in figure 3.22.

The analysis of the UV-vis spectra together with the densities estimate allowed to propose a model for MoO_3 deposits consistent with molybdate and polymolybdate species dispersed on the ZrEu mixed oxide support at coverages below or close to the monolayer. The Raman data above clearly state the presence of Mo-containing phases of high nuclearity MoO_3 and polymolybdate clusters even for the lowest loading tested. This seems to discard the formation of a continuous monolayer and support the XPS data that points to islands of high nuclearity Mo species sitting on Eu sites.

Finally, TPR analysis of both ZrEu_x and ZrEuMo_x samples allow understand the behaviour of these materials under reducing atmospheres. The WGS reaction is usually used to increase the H_2 concentration in reformate gases while reducing the CO content. In this work, this reaction will be studied using a surrogate of natural gas reformate (described in Chapter 2) and, therefore, the feed stream will contain *ca.* 50 % of H_2. Therefore, the ionic conductor present in the catalytic system is going to be exposed to these reducing conditions, thereby being mandatory the analysis of these materials under such situations.

Not surprisingly, the H_2-TPR profiles for ZrEu_x samples do not show any reduction process. However, the introduction of reducible Mo atoms in these materials (ZrEuMo_x) exhibit two well defined reduction processes around 300 and 650 ºC (Figure 3.23). According to several authors,[75,108,109] the reduction of MoO_3 essentially happens in two steps ($MoO_3 \rightarrow MoO_2$ and $MoO_2 \rightarrow Mo$), where shoulders or weaker peaks can appear according to intermediate phases like

Mo_4O_{11}. The reduction process of bulk MoO_3 normally starts over 600 ºC. However, the required temperature to achieve the reduction of molybdenum oxide can vary depending on the amount of water in the system, the heating rate, the sample amount or the calcination temperature in the sample preparation process.[108] Moreover, if the sample is a supported MoO_3 instead of a bulk, other parameters like MoO_3–support interaction or particle size also modify the reduction temperatures. For instance, Chary *et al.*[75] reported reduction temperatures as low as 400-420 ºC for the low-temperature peak of MoO_3/ZrO_2 samples while the high-temperature peak occurred at 800-940 ºC. The first reduction peak is assigned to the reduction of octahedral species ($[Mo_7O_{24}]^{6-}$ and $[Mo_8O_{26}]^{4-}$ clusters) and the high temperature one to the reduction of tetrahedral species more strongly bound to the support. In addition, they observed that the temperature at which both reduction processes developed shifted to lower temperatures on increasing the Mo content up to reaching the monolayer coverage. The observed behaviour of ZrEuMo_x TPRs (Figure 3.23) perfectly matches with that described by Chary *et al.*,[75] where a shift to lower temperatures is shown on increasing the Mo loading up to ZrEuMo_7, from which the amount of Mo oxide probably exceed the monolayer formation at expense of octahedral species according to previously discussed data.

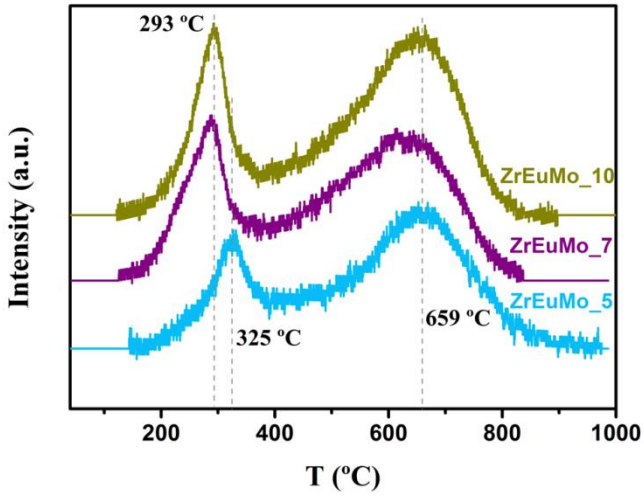

Figure 3.23 H_2-TPR profiles of prepared ZrEuMo_x samples.

Besides, these ZrEuMo_x samples show the reduction processes even at lower temperature. The observed temperatures are in good agreement with those reported by Ressler and co-workers.[40] By *in situ* studies, they found that the hydrogen is introduced in the Mo oxide structure forming bronzes over ~200 ºC forming H_xMoO_3. On increasing the temperature, from ~380 ºC, reduced nuclei MoO_2 phases start to appear. Finally, for temperatures above ~450 ºC, the reduction of MoO_3 to MoO_2 is the main process, where formation of intermediate Mo_4O_{11} phase is not discarded.

The quantitative analysis of the TPR leads to a ratio of the areas A_2/A_1 (considering A_1 the first reduction process at lower temperature and A_2 the area of the second reduction peak) of 3.3, 3.1 and 3.1 for ZrEuMo_5, ZrEuMo_7 and ZrEuMo_10, respectively. However, no elemental proposed reduction steps (Equations: 3.6 to 3.9 or 3.6 and

3.9) provide a H_2 consumption ratio of 1:3 according to the calculated areas ratio:

$$MoO_3 + H_2 \rightarrow MoO_2 + H_2O \quad [3.6]$$

$$MoO_3 + \frac{1}{4}H_2 \rightarrow \frac{1}{4}Mo_4O_{11} + \frac{1}{4}H_2O \quad [3.7]$$

$$\frac{1}{4}Mo_4O_{11} + \frac{3}{4}H_2 \rightarrow MoO_2 + \frac{3}{4}H_2O \quad [3.8]$$

$$MoO_2 + 2H_2 \rightarrow Mo + 2H_2O \quad [3.9]$$

Moreover, the calculations lead to a total reducibility (Equation 3.1) around 400 %. If only the first reduction process is considered (A_1), which is the temperature range of interest in this work, according to reduction process proposed in Eq. 3.6, the calculated reducibility are 115.6, 107.4 and 76.9 %. According to this Mo oxide over-reducibility and in agreement with Ressler's work,[40] the formation of bronzes (H_xMoO_3 type-structures) and some reduced MoO_2 phase below 350 ºC are expected and should be kept in mind for future catalytic experiments.

3.3.4. Partial conclusions.

The prepared samples (ZrEu_x, x=2, 5, 7, 9, 10, 12 and 15 mol.% of Eu_2O_3) exhibited the formation of solid solution with cubic fluorite-type structure up to 9 mol.% of Eu oxide dopant, from which a segregated cubic Eu oxide phase appears. The elemental characterization has shown a mesoporous homogeneous Zr-Eu mixed oxides, where homogeneous oxygen vacancies distribution is also expected.

The addition of amounts of Mo to ZrEu_5 sample has not modified the solid solution structure since the Mo oxide has been situated on the surface, preferentially on Eu atoms. The specific structure of Mo oxide is complex, but molybdates and polymolybdates have been formed in the surface, where the sample with the highest Mo loading is close to create a MoO_3 monolayer. These Mo-doped samples also show H_2 consumption in the temperature of interest for WGS reaction conditions, which is meanly related to bronzes formation and, likely, partial reduction to MoO_2 phase.

REFERENCES

1. Hagen, J. *Industrial Catalysis. A practical approach*. (WILEY-YCH Verlag GmbH & Co. kGaA, 2006).

2. Yu, W., Porosoff, M. D. & Chen, J. G. Review of Pt-based bimetallic catalysis: from model surfaces to supported catalysts. *Chem. Rev.* **112,** 5780–5817 (2012).

3. Davis, R. J. & Derouane, E. G. A non-porous supported-platinum catalyst for aromatization of n-hexane. *Lett. to Nat.* **349,** 313–315 (1991).

4. Wang, C., Daimon, H. & Sun, S. Dumbbell-like Pt-Fe3O4 nanoparticles and their enhanced catalysis for Oxygen Reduction Reaction. *Nano Lett.* **9,** 1493–1496 (2009).

5. Beyhan, S., Coutanceau, C., Léger, J.-M., Napporn, T. W. & Kadirgan, F. Promising anode candidates for direct ethanol fuel cell: Carbon supported PtSn-based trimetallic catalysts prepared by Bönnemann method. *Int. J. Hydrogen Energy* **38,** 6830–6841 (2013).

6. Bratlie, K. M., Lee, H., Komvopoulos, K., Yang, P. & Somorjai, G. A. Platinum Nanoparticle Shape Effects on Benzene Hydrogenation Selectivity. *Nano Lett.* **7,** 3097–3101

(2007).

7. Ratnasamy, C. & Wagner, J. P. Water Gas Shift Catalysis. *Catal. Rev. Sci. Eng.* **51,** 325–440 (2009).

8. Farrauto, R. J. *et al.* Precious Metal Catalysts Supported on Ceramic and Metal Monolithic Structures for the Hydrogen Economy. *Catal. Rev. Sci. Eng.* **49,** 141–196 (2007).

9. Ladebeck, J. R. & Wagner, J. P. in *Handbook of Fuel Cells – Fundamentals, Technology and Applications* (eds. Vielstich, W., Lamm, A. & Gasteiger, H. A.) **3,** 190–201 (John Wiley & Sons, Ltd., 2003).

10. Kam, R., Scott, J., Amal, R. & Selomulya, C. Pyrophoricity and stability of copper and platinum based water-gas shift catalysts during oxidative shut-down/start-up operation. *Chem. Eng. Sci.* **65,** 6461–6470 (2010).

11. Luengnaruemitchai, A., Osuwan, S. & Gulari, E. Comparative studies of low-temperature water-gas shift reaction over Pt/CeO2, Au/CeO2, and Au/Fe2O3 catalysts. *Catal. Commun.* **4,** 215–221 (2003).

12. Panagiotopoulou, P. & Kondarides, D. I. Effect of the nature of the support on the catalytic performance of noble metal catalysts for the water-gas shift reaction. *Catal. Today* **112,** 49–52 (2006).

13. Panagiotopoulou, P. & Kondarides, D. I. Effect of morphological characteristics of TiO2-supported noble metal catalysts on their activity for the water-gas shift reaction. *J. Catal.* **225,** 327–336 (2004).

14. Basinska, A., Maniecki, T. P. & Józwiak, W. K. Catalytic Activity in Water-Gas Shift Reaction of Platinum Group Metals Supported on Iron Oxides. *React. Kinet. Catal. Lett.* **89,** 319–324 (2006).

15. Thinon, O., Rachedi, K., Diehl, F., Avenier, P. & Schuurman, Y. Kinetics and Mechanism of the Water-Gas Shift Reaction Over Platinum Supported Catalysts. *Top. Catal.* **52,** 1940–1945 (2009).

16. Nalini, V., Haugsrud, R. & Norby, T. High-temperature proton conductivity and defect structure of TiP2O7. *Solid State Ionics* **181,** 510–516 (2010).

17. Kendall, K. R., Navas, C., Thomas, J. K. & zur Loye, H.-C. Recent Developments in Oxide Ion Conductors: Aurivillius Phases. *Chem. Mater.* **8,** 642–649 (1996).

18. Gao, Z., Mogni, L. V., Miller, E. C., Railsback, J. G. & Barnett, S. A. A perspective on low-temperature solid oxide fuel cells. *Energy Environ. Sci.* **9,** 1602–1644 (2016).

19. Huse, M., Norby, T. & Haugsrud, R. Effects of A and B site acceptor doping on hydration and proton mobility of LaNbO4. *Int. J. Hydrogen Energy* **37,** 8004–8016 (2012).

20. Stølen, S., Bakken, E. & Mohn, C. E. Oxygen-deficient perovskites: linking structure, energetics and ion transport. *Phys. Chem. Chem. Phys.* **8,** 429–447 (2006).

21. Wang, S. *et al.* Novel Chemically Stable Ba3Ca1.18Nb1.82−xYxO9−δ Proton Conductor: Improved Proton Conductivity through Tailored Cation Ordering. *Chem. Mater.* **26,** 2021–2029 (2014).

22. Kreuer, K. D. Aspects of the formation and mobility of protonic charge carriers and the stability of perovskite-type oxides. *Solid State Ionics* **125,** 285–302 (1999).

23. Thangadurai, P., Sabarinathan, V., Bose, A. C. & Ramasamy, S. Conductivity behaviour of a cubic/tetragonal phase stabilized nanocrystalline La2O3 - ZrO2. *J. Phys. Chem. Solids* **65,** 1905–1912 (2004).

24. Meredig, B. & Wolverton, C. Dissolving the Periodic Table in Cubic Zirconia: Data Mining to Discover Chemical Trends. *Chem. Mater.* **26,** 1985–1991 (2014).

25. Labrincha, J. A., Frade, J. R. & Marques, F. M. B. Protonic conduction in La2Zr2O7-based pyrochlore materials. *Solid State Ionics* **99,** 33–40 (1997).

26. Besikiotis, V., Ricote, S., Jensen, M. H., Norby, T. &

Haugsrud, R. Conductivity and hydration trends in disordered fluorite and pyrochlore oxides: A study on lanthanum cerate-zirconate based compounds. *Solid State Ionics* **229,** 26–32 (2012).

27. Xia, X.-L., Liu, Z.-G., Ouyang, J.-H. & Zheng, Y. Preparation, Structural Characterization, and Enhanced Electrical Conductivity of Pyrochlore-type (Sm1-xEux)2Zr2O7 Ceramics. *Fuel Cells* **12,** 624–632 (2012).

28. Haugsrud, R. & Norby, T. High-temperature proton conductivity in acceptor-doped LaNbO4. *Solid State Ionics* **177,** 1129–1135 (2006).

29. Díaz-Guillén, J. A. *et al.* Synthesis and electrical properties of the pyrochlore-type Gd2-yLayZr2O7 solid solution. *Bol. la Soc. Española Cerámica y Vidr.* **47,** 159–164 (2008).

30. Vega-Castillo, J. E., Ravella, U. K., Corbel, G., Lacorre, P. & Caneiro, A. Thermodynamic stability, structural and electrical characterization of mixed ionic and electronic conductor La2Mo2O8.96. *Dalt. Trans.* **41,** 7266–7271 (2012).

31. Amsif, M. *et al.* Mo-Substituted Lanthanum Tungstate La28-yW4+yO54+d: A Competitive Mixed Electron-Proton Conductor for Gas Separation Membrane Applications. *Chem. Mater.* **24,** 3868–3877 (2012).

32. Malavasi, L., Fisher, C. A. J. & Islam, M. S. Oxide-ion and proton conducting electrolyte materials for clean energy applications: structural and mechanistic features. *Chem. Soc. Rev.* **39,** 4370–4387 (2010).

33. Navrotsky, A. Thermodynamics of solid electrolytes and related oxide ceramics based on the fluorite structure. *J. Mater. Chem.* **20,** 10577–10587 (2010).

34. Chen, C.-T., Sen, S. & Kim, S. Effective Concentration of Mobile Oxygen-Vacancies in Heavily Doped Cubic Zirconia: Results from Combined Electrochemical Impedance and NMR Spectroscopies. *Chem. Mater.* **24,** 3604–3609 (2012).

35. Marcus, J., Escribe-Filippini, C., Chevalier, R. & Buder, R.

Magnetic properties and 151Eu Mössbauer spectroscopy of a new molybdenum bronze: Eu0.08MoO3. *Solid State Commun.* **62,** 221–223 (1987).

36. Chippindale, A. M. & Cheetham, A. K. in *Molybdenum: An Outline of its Chemistry and Uses* (eds. Braithwaite, E. R. & Haber, J.) 146–184 (Elsevier Science B.V, 1994).

37. Schöllhorn, R., Kuhlmann, R. & Besenhard, J. O. Topotactic redox reactions and ion exchange of layered MoO3 bronzes. *Mater. Res. Bull.* **11,** 83–90 (1976).

38. Birtill, J. J. & Dickens, P. G. Phase relationships in the system HxMoO3 (0<x<=2.0). *Mater. Res. Bull.* **13,** 311–316 (1978).

39. Adams, S. CDW Superstructures in Hydrogen Molybdenum Bronzes HxMoO3. *J. Solid State Chem.* **149,** 75–87 (2000).

40. Ressler, T., Wienold, J. & Jentoft, R. E. Formation of Bronzes during Temperature-programmed Reduction of MoO3 with Hydrogen - An In situ XRD and XAFS Study. *Solid State Ionics* **141-142,** 243–252 (2001).

41. Schöllhorn, R., Schulte-Nölle, T. & Steinhoff, G. Layered intercalation complexes of the hydrogen bronze H0.5MoO3 with organic lewis bases. *J. Less-Common Met.* **71,** 71–78 (1980).

42. Bollapragada, P. K. S. Chemical transformations using tungsten and molybdenum hydrogen bronzes. (2003).

43. Seguin, L., Figlarz, M., Cavagnat, R. & Lassègues, J.-C. Infrared and Raman spectra of MOO3 molybdenum trioxides and MoO3·xH2O molybdenum trioxide hydrates. *Spectrochim. Acta Part A* **51,** 1323–1344 (1995).

44. Aguadero, A., Perez-Coll, D., Alonso, J. A., Skinner, S. J. & Kilner, J. A. A new family of Mo-doped SrCoO3-delta perovskites for application in reversible solid state electrochemical cells. *Chem. Mater.* **24,** 2655–2663 (2012).

45. Tagaya, H., Ara, K., Kadokawa, J., Karasu, M. & Chiba, K. Intercalation of Organic Compounds in the Layered Host

Lattice MoO3. *J. Mater. Chem.* **4,** 551–555 (1994).

46. Bartha, L., Kiss, A. B. & Szalay, T. Chemistry of Tungsten Oxide Bronzes. *Int. J. Refract. Met. Hard Mater.* **13,** 77–91 (1995).

47. Szalay, T., Ludányi, A. & Kiss, B. A. Ion exchange adsorption processes on the surface of ammonium tungsten oxide bronze in aqueous media. *J. Mater. Sci.* **22,** 3543–3546 (1987).

48. Sasol Performance Chemicals. Doped aluminas. Silica-Aluminas, Mixed Metal Oxides, Hydrotalcites. *www.sasolalumina.com* 1–16 (2017).

49. Brunauer, S., Deming, L. S., Deming, W. E. & Teller, E. On a Theory of the van der Waals Adsorption of Gases. *J. Am. Chem. Soc.* **62,** 1723–1732 (1940).

50. Sing, K. S. W. & Williams, R. T. Physisorption Hysteresis Loops and the Characterization of Nanoporous Materials. *Adsorpt. Sci. Technol.* **22,** 773–782 (2004).

51. Leofanti, G., Padovan, M., Tozzola, G. & Venturelli, B. Surface area and pore texture of catalysts. *Catal. Today* **41,** 207–219 (1998).

52. Hwang, C.-P. & Yeh, C.-T. Platinum-Oxide Species Formed on Progressive Oxidation of Platinum Crystallites Supported on Silica and Silica-Alumina. *J. Catal.* **182,** 48–55 (1999).

53. Huizinga, T., Van Grondelle, J. & Prins, R. A temperature programmed reduction study of Pt on Al2O3 and TiO2. *Appl. Catal.* **10,** 199–213 (1984).

54. Yao, H. C., Sieg, M. & Plummer, H. K. J. Surface Interactions in the Pt/gamma-Al2O3 System. *J. Catal.* **59,** 365–374 (1979).

55. Merlen, E. *et al.* Characterization of Bimetallic Pt–Sn/Al2O3 Catalysts: Relationship between Particle Size and Structure. *J. Catal.* **159,** 178–188 (1996).

56. El Doukkali, M. *et al.* A comparison of sol-gel and impregnated Pt or/and Ni based γ-alumina catalysts for

bioglycerol aqueous phase reforming. *Appl. Catal. B Environ.* **125,** 516–529 (2012).

57. Mazzieri, V. A., Grau, J. M., Yori, J. C., Vera, C. R. & Pieck, C. L. Influence of additives on the Pt metal activity of naphtha reforming catalysts. *Appl. Catal. A Gen.* **354,** 161–168 (2009).

58. Perrichon, V., Retailleau, L., Bazin, P., Daturi, M. & Lavalley, J. C. Metal dispersion of CeO2-ZrO2 supported platinum catalysts measured by H2 or CO chemisorption. *Appl. Catal. A Gen.* **260,** 1–8 (2004).

59. Bazin, P., Saur, O., Lavalley, J. C., Daturi, M. & Blanchard, G. FT-IR study of CO adsorption on Pt/CeO2: characterisation and structural rearrangement of small Pt particles. *Phys. Chem. Chem. Phys.* **7,** 187–194 (2005).

60. González-Castaño, M., Ivanova, S., Ioannides, T., Centeno, M. A. & Odriozola, J. A. Deep insight into Zr/Fe combination for successful Pt/CeO2/Al2O3 WGS catalyst doping. *Catal. Sci. Technol.* **7,** 1556–1564 (2017).

61. González-Castaño, M. Design, characterization and structuring of Pt based catalysts for Water Gas Shift reaction. (2015).

62. Germani, G. & Schuurman, Y. Water-Gas Shift Reaction Kinetics Over micro-Structured Pt/CeO2/Al2O3 Catalysts. *Am. Inst. Chem. Eng.* **52,** 1806–1813 (2006).

63. Vannice, M. A. *Kinetics of Catalytic Reactions*. (Springer, 2005). doi:10.1007/b136380

64. Bergeret, G. & Gallezot, P. in *Handbook of Heterogeneous Catalysis* (eds. Ertl, G., Knözinger, H., Schuth, F. & Weitkamp, J.) 439–464 (Wiley-VCH, 1997).

65. Wang, X. *et al.* In Situ Studies of the Active Sites for the Water Gas Shift Reaction over Cu-CeO2 Catalysts: Complex Interaction between Metallic Copper and Oxygen Vacancies of Ceria. *J. Phys. Chem. B* **110,** 428–434 (2006).

66. Jacobs, G. *et al.* Water-gas shift: Comparative screening of metal promoters for metal/ceria systems and role of the metal.

Appl. Catal. A Gen. **258,** 203–214 (2004).

67. Newville, M. EXAFS analysis using FEFF and FEFFIT. *J. Synchrotron Radiat.* **8,** 96–100 (2001).

68. Voronko, Y. K., Zufarov, M. A., Zobol, A. A. & Taymbal, L. I. Site-selective spectroscopy and nearest neighbor environment of Eu3+ in monoclinic ZrO2-Ln2O3 and HfO2-Ln2O3 solid solutions. *Inorg. Mater.* **32,** 1063–1068 (1996).

69. Maram, P. S., Ushakov, S. V., Weber, R. J. K., Benmore, C. J. & Navrotsky, A. In situ Diffraction from Levitated Solids Under Extreme Conditions-Structure and Thermal Expansion in the Eu2O3-ZrO2 System. *J. Am. Ceram. Soc.* **98,** 1292–1299 (2015).

70. Nakamura, A. New defect-crystal-chemical approach to non-Vegardianity and complex defect structure of fluorite-based MO2-LnO1.5 solid solutions (M4+ = Ce, Th; Ln3+ = lanthanide) part I: Model description and lattice-parameter data analysis. *Solid State Ionics* **181,** 1543–1564 (2010).

71. Fabrichnaya, O. *et al.* Heat capacity for the Eu2Zr2O7 and phase relations in the ZrO2-Eu2O3 system: Experimental studies and calculations. *Thermochim. Acta* **558,** 74–82 (2013).

72. Tabira, Y., Withers, R. L., Barry, J. C. & Elcoro, L. The Strain-Driven Pyrochlore to 'Defect Fluorite' Phase Transition in Rare Earth Sesquioxide Stabilized Cubic Zirconias. *J. Solid State Chem.* **159,** 121–129 (2001).

73. Andrievskaya, E. R. Phase equilibria in the refractory oxide systems of zirconia, hafnia and yttria with rare-earth oxides. *J. Eur. Ceram. Soc.* **28,** 2363–2388 (2008).

74. Kim, D.-J. Lattice Parameters, Ionic Conductivities, and Solubility Limits in Fluorite-Structure MO2 Oxide (M = Hf4+, Zr4+, Ce4+, Th4+, U4+) Solid Solutions. *J. Am. Chem. Soc.* **72,** 1415–1421 (1989).

75. Chary, K. V. R., Reddy, K. R., Kishan, G., Niemantsverdriet, J. W. & Mestl, G. Structure and catalytic properties of molybdenum oxide catalysts supported on zirconia. *J. Catal.*

226, 283–291 (2004).

76. Afanasiev, P. On the metastability of ‘monolayer coverage’ in the MoO3/ZrO2 dispersions. *Mater. Chem. Phys.* **47,** 231–238 (1997).

77. Afanasiev, P., Geantet, C., Breysse, M., Coudurier, G. & Vedrine, J. C. Influence of Preparation Method on the Acidity of MoO3(WO3)/ZrO2 Catalysts. *J. Chem. Soc. Trans.* **90,** 193–202 (1994).

78. Ward, D. A. & Ko, E. I. Synthesis and Structural Transformation of Zirconia Aerogels. *Chem. Mater.* **5,** 956–969 (1993).

79. Hino, M. & Arata, K. Synthesis of Solid Superacid of Molybdenum Oxide Supported on Zirconia and Ist Catalytic Action. *Chem. Lett.* **18,** 971 – 972 (1989).

80. Afanasiev, P., Thiollier, A., Breysse, M. & Dubois, J. L. Control of the textural properties of zirconium oxide. *Top. Catal.* **8,** 147–160 (1999).

81. Bueno-López, A., Krishna, K., Makkee, M. & Moulijn, J. A. Enhanced soot oxidation by lattice oxygen via La3+-doped CeO2. *J. Catal.* **230,** 237–248 (2005).

82. Hernández, W. Y., Centeno, M. A., Romero-Sarria, F. & Odriozola, J. A. Synthesis and Characterization of Ce1−xEuxO2-x/2 Mixed Oxides and Their Catalytic Activities for CO Oxidation. *J. Phys. Chem. C* **113,** 5629–5635 (2009).

83. Ma, S.-Z. *et al.* Effect of microstructure, grain size, and rare earth doping on the electrorheological performance of nanosized particle materials. *J. Mater. Chem.* **13,** 3096–3102 (2003).

84. Matsuoka, Y., Niwa, M. & Murakami, Y. Morphology of Molybdena Supported on Various Oxides and ItsActivity for Methanol Oxidation. *J. Phys. Chem.* **94,** 1477–1482 (1990).

85. Ravikovitch, P. I., Ó Domhnaill, S. C., Neimark, A. V., Schüth, F. & Unger, K. K. Capillary Hysteresis in Nanopores:

Theoretical and Experimental Studies of Nitrogen Adsorption on MCM-41. *Langmuir* **11,** 4765–4772 (1995).

86. Kruk, M., Jaroniec, M. & Sayari, A. Adsorption Study of Surface and Structural Properties of MCM-41 Materials of Different Pore Sizes. *J. Phys. Chem. B* **101,** 583–589 (1997).

87. Serpone, N. Is the Band Gap of Pristine TiO2 Narrowed by Anion- and Cation-Doping of Titanium Dioxide in Second-Generation Photocatalysts? *J. Phys. Chem. B* **110,** 24287–24293 (2006).

88. Tang, H., Liu, Y., Luo, W., Li, R. & Chen, X. Optical Spectroscopy of Eu3+ ions in Tetragonal ZrO2 Nanocrystals. *J. Nanosci. Nanotechnol.* **11,** 9445–9450 (2011).

89. Yi, J. *et al.* Monophasic zircon-type tetragonal Eu1−xBixVO4 solid-solution: synthesis, characterization, and optical properties. *Mater. Res. Bull.* **57,** 306–310 (2014).

90. Kang, J.-G., Jung, Y., Min, B.-K. & Sohn, Y. Full characterization of Eu(OH)3 and Eu2O3 nanorods. *Appl. Surf. Sci.* **314,** 158–165 (2014).

91. Binnemans, K. Interpretation of europium(III) spectra. *Coord. Chem. Rev.* **295,** 1–45 (2015).

92. Tiseanu, C. *et al.* Order and disorder effects in nano-ZrO2 investigated by micro-Raman and spectrally and temporarily resolved photoluminescence. *Phys. Chem. Chem. Phys.* **14,** 12970–12981 (2012).

93. Ghosh, P. & Patra, A. Role of Surface Coating in ZrO2/Eu3+ Nanocrystals. *Langmuir* **22,** 6321–6327 (2006).

94. Weber, M. J., Sharp, E. J. & Miller, J. E. Optical spectra, relaxation, and energy transfer of Eu3+ and Cr3+ in a europium phosphate glass. *J. Phys. Chem. Solids* **32,** 2275–2284 (1971).

95. Goff, J. P., Hayes, W., Hull, S., Hutchings, M. T. & Clausen, K. N. Defect structure of yttria-stabilized zirconia and its influence on the ionic conductivity at elevated temperatures.

Phys. Rev. B **59,** 14202–14219 (1999).

96. Karthika, S. *et al.* Structural and optical studies of Eu3+/nanocrystallites doped titania–zirconia hybrids. *J. Alloys Compd.* **615,** 188–193 (2014).

97. Tian, H., Roberts, C. A. & Wachs, I. E. Molecular Structural Determination of Molybdena in Different Environments: Aqueous Solutions, Bulk Mixed Oxides, and Supported MoO3 Catalysts. *J. Phys. Chem. C* **114,** 14110–14120 (2010).

98. Bare, S. R. Surface Structure of Highly Dispersed MoO3 on MgO Using in Situ Mo L3-Edge XANES. *Langmuir* **14,** 1500–1504 (1998).

99. Samaranch, B., Ramírez De La Piscina, P., Clet, G., Houalla, M. & Homs, N. Study of the Structure, Acidic, and Catalytic Properties of Binary Mixed-Oxide MoO3-ZrO2 Systems. *Chem. Mater.* **18,** 1581–1586 (2006).

100. *Molybdenum: An Outline of its Chemistry and Uses*. (Elsevier Science B.V, 1994).

101. Hu, H., Wachs, I. E. & Bare, S. R. Surface Structures of Supported Molybdenum Oxide Catalysts: Characterization by Raman and Mo L3-Edge XANES. *J. Phys. Chem.* **99,** 10897–10910 (1995).

102. Xie, S., Chen, K., Bell, A. T. & Iglesia, E. Structural Characterization of Molybdenum Oxide Supported on Zirconia. *J. Phys. Chem. B* **104,** 10059–10068 (2000).

103. Van Hengstum, A. J., Van Ommen, J. G., Bosch, H. & Gellings, P. J. Preparation of supported vanadium and molybdenum oxide catalysts using metal acetylacetonate complexes. *Appl. Catal.* **5,** 207–217 (1983).

104. Bond, G. C., Flamerz, S. & Van Wijk, L. Structure and reactivity of titania-supported molybdenum and tungsten oxides. *Catal. Today* **1,** 229–243 (1987).

105. Hillerová, E., Morishige, H., Inamura, K. & Zdražil, M. Formation of monolayer of molybdena over alumina by

unconventional slurry impregnation or solvent assisted spreading method. *Appl. Catal. A Gen.* **156,** 1–17 (1997).

106. Dieterle, M., Weinberg, G. & Mestl, G. Raman spectroscopy of molybdenum oxides. Part I. Structural characterization of oxygen defects in MoO3-x by DR UV/VIS, Raman spectroscopy and X-ray diffraction. *Phys. Chem. Chem. Phys.* **4,** 812–821 (2002).

107. Mestl, G., Ruiz, P., Delmon, B. & Knözinger, H. Oxygen-Exchange Properties of MoO3: An in Situ Raman Spectroscopy Study. *J. Phys. Chem.* **98,** 11269–11275 (1994).

108. Arnoldy, P., de Jonge, J. C. M. & Moulijn, J. A. Temperature-Programmed Reduction of MoO3 and MoO2. *J. Phys. Chem.* **89,** 4517–4526 (1985).

109. Braithwaite, E. R. in *Molybdenum: An Outline of its Chemistry and Uses* (eds. Braithwaite, E. R. & Haber, J.) 1–93 (Elsevier Science B.V, 1994).

CHAPTER 4.

CONDUCTIVITY OF IONIC CONDUCTORS

Abstract

The IS of the synthesized ionic conductors has been measured in different inert, oxidizing and wet atmospheres. The ZrEu_x solid solutions show pure ionic conductivity in all cases. The ionic conductivity by vacancy-movement presents in these types of materials in inert conditions is increased in wet conditions by proton conductivity contribution according to a Grotthuss' mechanism.

The conductivity behaviour is related to the physicochemical properties of the solid solutions previously analysed (Chapter 3) showing maximal conductivity in an intermediate amount of dopant according to an organization of the created oxygen vacancies on increasing the Eu content.

The proton conductivity exhibited in wet conditions by Grotthuss' mechanism is supported by DRIFTS experiments, where adsorbed water as well as dissociated water in the oxygen vacancies can be identified.

4.1. INTRODUCTION

According to literature proton conductors are usually classified in four families of materials among them "water-containing sytems" for cation exchange membranes and "high-temperature proton conductors" like oxides are found.[1] Accordingly, good ionic conductivities have been reported by Zr-based compounds similar to the one prepared in this study, Eu-doped zirconia materials.[2–7] Moreover, Mo mixed oxide as well as hydrated Mo-based bronzes have also been reported as excellent materials for ionic conductivity and cation exchange.[8–16]

The first oxide reported showing predominantly proton conductivity was acceptor-doped thoria for temperatures above 1200 °C and low oxygen partial pressures.[17] Later, Takahashi and Iwahara started to study several materials with cubic structures which exhibited pure ionic conductivity, mixed ionic/proton conductivity and pure proton conductivity in hydrogen or water containing atmospheres.[18] Cubic cerates are among the proton conductors materials with highest conductivities.[1,19] However, zirconates present higher stability.[20] Thus, Magrasó *et al.*[21] reported ionic conductivities for $BaZrO_3$ in wet atmospheres at 700 ºC in the range of 10^{-4} $S \cdot cm^{-1}$, and Babilo *et al.*[22] found a conductivity of $7.9 \cdot 10^{-3}$ $S \cdot cm^{-1}$ for $BaZr_{0.8}Y_{0.2}O_{3-\delta}$ at 600 ºC under humidified nitrogen in an attempt to prepare $BaZrO_3$ based compounds with reproducible conductivities. Moreover, higher conductivities of ~10^{-2} $S \cdot cm^{-1}$ at 900 ºC and ~10^{-3} $S \cdot cm^{-1}$ at 600 ºC were also reported by Xia *et al.*[6] for cubic rare earth doped zirconia samples. In this way, Norby *et al.* have studied proton

conductivity in rare-earth oxides including La_2O_3 and Y_2O_3.[23,24] These are state-of-art electrolyte materials for proton conductivity showing high proton conductivity within the material grains (~10^{-2} $S \cdot cm^{-1}$) with good chemical and mechanical stability but high resistance at grain boundaries.[20]

As it is introduced in chapter 2, impedance spectroscopy (IS) technique allows to distinguish between grain and grain boundary conductivities since the electrical behaviour of a system is determined by a number of strongly coupled processes, each occurring at a different rate, this is, they are excited at different frequencies (characteristic frequency).[25] A considerable amount of materials such as electronic conductors, ionic conductors and dielectric materials, in solid ionic systems or liquid electrolytes, can be studied by this technique. The electric and/or ionic conductivity depend on the crystalline structure and defects present in the material. An extensive analysis of structures, defects (from point defects to three-dimensional defects and ordering), diffusion and conducting mechanism is reported by Tilley.[26] Ionic conductivity, in the context of solids, refers to the passage of ions across a solid under the influence of an externally applied driving force. This driving force may be an electrical potential gradient or a chemical potential gradient, *i.e.* oxygen or water partial pressures.[27] According to this, technologies based on ionic separation membranes as well as combustible cells have been developed.[28–32]

A straightforward method to create or enhance ionic conductivity is to incorporate aliovalent impurity ions into the crystal. These

impurities can, in principle, be compensated structurally by the incorporation of interstitials or vacancies, or by electronic defects, holes or electrons. Among the different materials which exhibit ionic conductivity, doped oxides with aliovalent cations are very common due to the stability of the structure, the good displayed conductivity and the ease of forming point defects like cation/anion vacancies by doping with aliovalent ions.[4,20,26,33–35] Concretely, doping zirconia with trivalent ions (Eu^{3+}) creates the fluorite phase of the zirconia (see chapter 3), where an oxygen vacancy is formed per two europium atoms to compensate the charge (Scheme 4.1), which can be formulated in Kröger-Vink notation as:

$$x\ Eu_2O_3\ (ZrO_2) \rightarrow 2x\ Eu'_{Zr} + 3x\ O_O^x + x\ V_O^{2\bullet} \qquad [4.1]$$

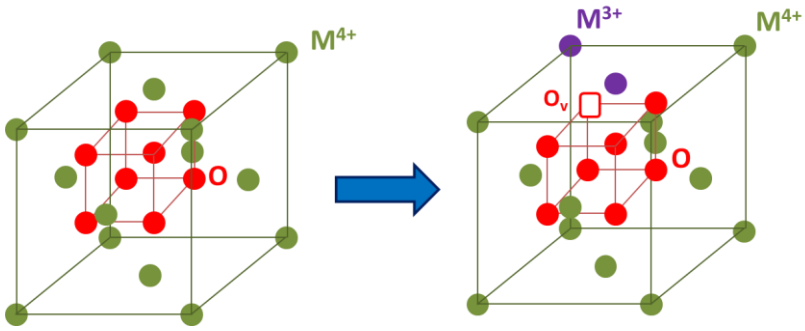

Scheme 4.1 Oxygen vacancy formation by doping ZrO_2 (M^{4+}) with a M_2O_3 oxide (M^{3+}).

These acceptor-doped ZrO_2 compounds have been reported as pure proton conductors.[36–38] The lower oxidation state of the dopant cation (Eu^{3+}) requires the formation of oxygen vacancies resulting in p-type semiconductor materials whose ionic conductivity depends on the movement of oxygen vacancies.

The ionic conduction mechanism depends on the oxide structure, the carrier species and the created defects (electronic or structural, in lattice sites or interstitial positions).[26,27] Different ionic conductivity mechanisms have been proposed for these kind of defective structures. One of the most common is the hopping mechanism, where the oxygen ions migrate jumping to a near oxygen vacancy. Thus, oxygen ions move in one direction and the vacancies move in the contrary.[26] Proton (H^+) conductivity is also possible in these p-type semiconductor materials. Under wet conditions, the water molecule is dissociated filling the oxygen vacancy where $OH^{\bullet}$ is adsorbed, and the other proton interacts with a neighbour oxygen of the lattice. Thus, under water pressure gradient or an electric field, the proton can be transferred from an $OH^{\bullet}$ to an adjacent oxygen:

$$O_O^x + V_O^{2\bullet} + H_2O \rightarrow 2\,OH_O^{\bullet} \qquad [4.2]$$

The main proton diffusion mechanism described in the literature is the Grotthuss' mechanism.[1,37]. In this process, a translational dynamics of a bigger molecule named *"vehicle"* assists the proton diffusion.[39] Concretely, in the Grotthuss' mechanism the H_2O molecules act as vehicle species for the proton mobility by H_3O^+ formation. Additional reorganization of the proton environment, which comprises reorientation of the H_2O molecules, creates an uninterrupted trajectory for proton migration.[40] Therefore, the proton transfer as well as the reorganization of its environment are the main steps of the proton conductivity, which can be the rate-limiting step in the diffusion process.[1]

As it has been described above, in acceptor-doped ZrO_2 compounds (*e.g.* in this study Eu-doped zirconia were prepared) the presence of oxygen vacancies creates p-type semiconductor materials where the oxygen and/or proton diffusion can be present. Then, the prepared Zr-based materials have been studied by IS in different conditions (atmosphere, temperature…) in order to determine the ionic/protonic conductivity as well as the activation energies. Moreover, *in situ* Raman spectroscopy and DRIFTS were also carried out in wet conditions to analyse the adsorption of the water and the possible mechanism.

4.2. IMPEDANCE SPECTROSCOPY

As it was introduced in chapter 2, IS technique allows the study of solid or liquid conducting and dielectric materials whose electrical properties involve a dipolar rotation and where the conduction can be electrical and/or ionic.[41] Moreover, this technique presents the particularity of distinguish between the different contributions of each region or interface of the material, such as grain interiors (bulk) and grain boundaries, whose resistances can be independently measured, in many cases, applying the "brick layer model" for a sintered polycrystalline sample.[25,42]

In general, the impedance spectra represented in the complex plane Z'' vs Z' (also called cole-cole plot or Nyquist plot) can describe three arcs at different frequencies (characteristic frequency, ω_0) related to the conductivity effects of grain (bulk), grain boundary and electrode-electrolyte interface regions (Scheme 4.2). These characteristic frequencies are specific for each region and each

material since they are related to the relaxation time needed after the excitation and, consequently, related to the zone of the material where the current is crossing. For example, the relaxation times for the electrons are lower than for a big non-polar molecule. Thus, the bulk usually presents lower relaxation times than grain boundaries, showing thereby the impedance arc at higher frequencies. Moreover, the capacitance values of each phenomenon indicate what region is being shown in the spectrum. Thus, the capacitance values are of the order of 10^{-12} – 10^{-11} F·cm^{-1} for the grain region, 10^{-11} – 10^{-8} F·cm^{-1} for grain boundaries and 10^{-8} – 10^{-5} F·cm^{-1} for electrode-electrolyte interface.[43]

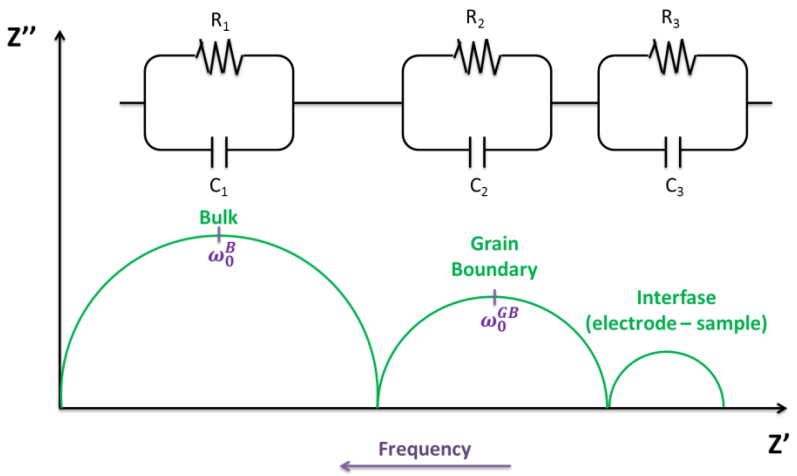

Scheme 4.2 Complex plane plot of the impedance spectroscopy and equivalent circuits.

Due to the similarity between electrical behaviour of the sample and an electric circuit for ionic conductors in complex impedance spectroscopy, it is possible to fit the impedance arcs with mathematical expressions for R-C (Resistance - Capacitance) or R-

CPE (Resistance - Constant Phase Element) circuits. An ideal ionic conductor acquires a completely capacitive response and another completely resistive similar to a parallel R-C electric circuit. However, for a real ionic conductor is preferable to compare it with a parallel R-CPE electric circuit considering that it does not show a total capacity, but a mixed capacitive-resistive behaviour defined by three components: one resistive, other capacitive and a varying coefficient between 0 and 1 and whose value indicates its capacitive degree (0 means completely resistive and 1 completely capacitive).[25] Consequently, the spectra of all the samples are fitted to an equivalent circuit (Scheme 4.2) using Zview program. From the fits, the resistance (R) of each region of the material and the total resistance are obtained. Therefore, the capacitances are also calculated in the same fitting, indicating what region of the material is representing each arc in the impedance spectrum as it has been reported before. The capacitance can be calculated according to impedance function:[25]

$$C = \frac{Z''}{2\pi f\left(Z'^2 + Z''^2\right)} \qquad [4.3]$$

where Z'' is the imaginary part of the impedance, Z' the real part of the impedance and f is the frequency.

Moreover, from resistance, the specific values for the material (the resistivity -ρ- and the conductivity -σ) have been calculated for the grain, the grain boundary as well as the total conductivity:[42]

$$\rho_i = R_i \frac{A}{l} \qquad [4.4]$$

$$\sigma_B = \frac{1}{\rho_1} \quad [4.5]$$

$$\sigma_{GB} = \frac{1}{\rho_2} \cdot \frac{C_1}{C_2} \quad [4.6]$$

$$\sigma_T = \frac{1}{\rho_T} = \frac{1}{(R_1+R_2)\cdot\frac{A}{l}} \quad [4.7]$$

where A is the area of cross section of the pelletized sample, l is the thickness of that pellet, R_i and C_i are the resistance and the capacitance from the fit for each arc, ρ is the resistivity and σ is the conductivity. B indicates the bulk, GB the grain boundary and T the total measurement.

The impedance arcs of the Eu-doped zirconia samples selected in the previous characterization (Chapter 3), ZrEu_2, ZrEu_5, ZrEu_7 and ZrEu_12, were measured as a function of the gaseous environment. Three different atmospheres were analysed, argon, oxygen - argon and wet argon. The different conditions were analysed by sweeping oxygen and water partial pressures in a wide range. For every specific atmosphere, the impedance experiments were performed from room temperature to 700 ºC in order to estimate the activation energy (E_a) for the conduction process by Arrhenius equation (Equation 4.8). Previously to these experiments, a dehydration step was carried out *in situ* in dried air at 600 ºC for 3 h.

$$\sigma \cdot T = \sigma_0 \cdot e^{-\frac{E_a}{k_B \cdot T}} \quad [4.8]$$

In the next table are summarized the experimental conditions:

Table 4.1 Summary of experimental conditions in IS experiment.

Atmosphere	**Ar**	**O_2/Ar**	**H_2O/Ar**
Temperature range (ºC)	RT - 700	RT - 700	200 - 700
Partial Pressure of O_2 or H_2O (vol.%)	-	0 - 100	0 - 50

4.2.1. Basic Characterization of the sintered samples.

The Eu-doped ZrO_2 samples were sintered by SPS technique (Chapter 2) in order to obtain compact face-parallel pellets for the impedance measurements. Then, XRD was carried out in the same conditions that for powdered samples to verify the preservation of the phase.

After the sintering process, the diffraction peaks (Figure 4.1) keep the relative intensities and the same exact position showing also the same shift on increasing the Eu content according to the formation of solid solution already analysed (Chapter 3). The phase continues being cubic $Fm\bar{3}m$ corresponding to the solid solution. Therefore, the X-ray diffraction shows no significant changes in general, but the ZrEu_2 sample. The powdered sample that already shows monoclinic ZrO_2 in zones with poor dopant content (Chapter 3) and the low Eu loading transforms into the tetragonal $P4_2/nmc$ ZrO_2 phase [JCPDS: 00-042-1164] upon the sintering process. This transformation from

monoclinic to tetragonal phase of the zirconia under SPS conditions is expected according to other studies about zirconia phases.[44,45]

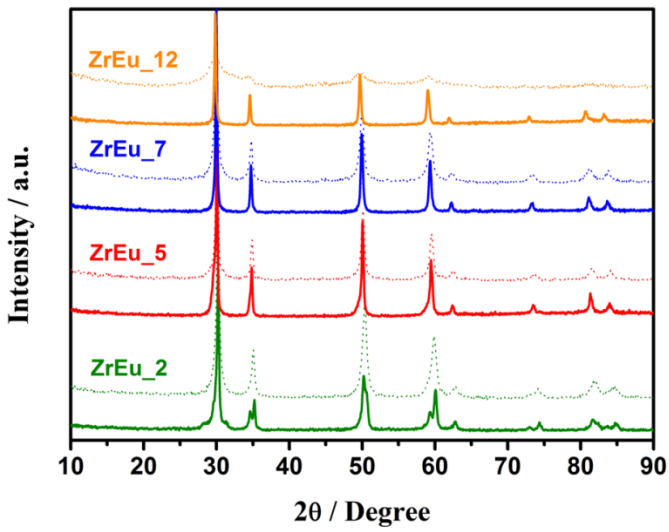

Figure 4.1 XRD of the sintered samples (solid lines) compared with the original powdered samples (dotted lines).

Moreover, as in the powder samples, lattice parameters calculated according to a cubic phase as well as crystallite sizes determined by Scherrer's equation on (111) crystallographic plane were estimated (Table 4.2). The observed crystallite size increase is expected according to a sintering process, but the preservation of the lattice parameters indicates the conservation of the cubic phase of these stable solid solutions. Therefore, regarding the diffractograms and the lattice parameters, the sintered samples, required for the impedance measurements, are quite representative of the powdered samples, since the conductivity depends on the structure of the sample among other parameters.[26]

Table 4.2 Lattice parameter and crystallite size of powdered samples and sintered samples (marked with a previous "p").

Sample	Lattice Parameter, a (Å)	Crystallite size (nm)	Sample	Lattice Parameter, a (Å)	Crystallite size (nm)
ZrEu_2	5.13	24	**pZrEu_2**	5.12	59
ZrEu_2	5.15	33	**pZrEu_5**	5.15	44
ZrEu_2	5.16	21	**pZrEu_7**	5.16	79
ZrEu_2	5.18	-	**pZrEu_12**	5.18	67

The same procedure was performed for ZrEuMo_x samples. Unfortunately, the SPS sintering followed by the painting process for the impedance measurement (Chapter 2) transform the cubic phase of the solid solution into ZrO_2 tetragonal and segregated Mo oxide, thereby obtaining non-representative samples for the ionic conductivity measurement.

4.2.2. IS in inert atmosphere (Ar).

The IS measurements in inert conditions (Ar atmosphere) show distinguishable impedance arcs over 200 ºC in all samples. As a representation for all the temperature range, complex impedance plots measured at 350 ºC in Ar for all solids are plotted in Figure 4.2. Two arcs accounting for bulk and grain boundary contribution are clearly shown for ZrEu_2, ZrEu_5 and ZrEu_7 samples. The total impedance of these materials is significantly lower (~10^5 Ω·m) than that of the

ZrEu_12 sample (~10^6 Ω·m). Moreover, the difference between the characteristic frequencies of both conduction processes (bulk and grain boundary) decreases on increasing the total impedance resulting in just one arc for the sample containing 12 mol.% of dopant. Unlike the capacitance or the resistance, which depend on the geometry, the characteristic frequency only depends on the material nature.[42] This allows to distinguish and, consequently, to measure the bulk, grain boundary and total impedances independently as well as their conductivities. However, as the impedance data for the ZrEu_12 solid show only one arc, these data are not enough by themselves to reveal the magnitudes of either bulk or grain boundary conductivities.[42]

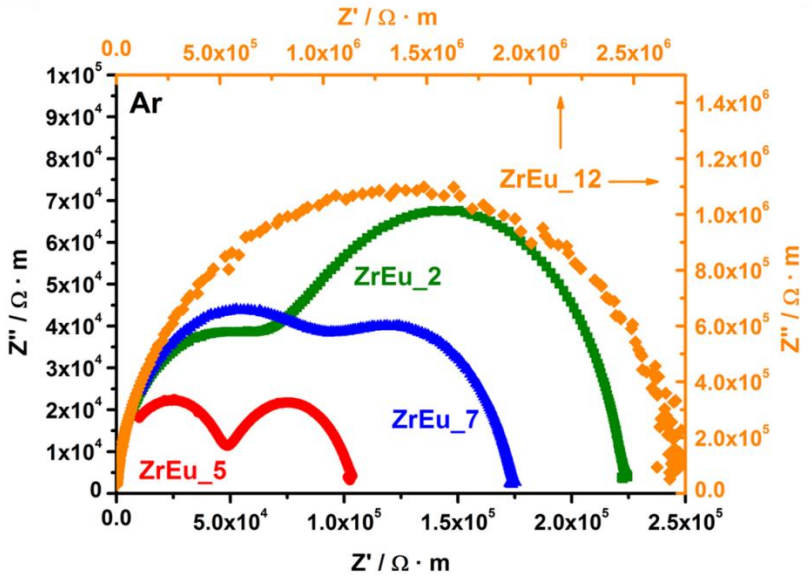

Figure 4.2 Complex plane plot of the normalized impedance spectroscopy of the sintered samples at 350 ºC in dry inert conditions (in Ar atmosphere). The ZrEu_2, ZrEu_5 and ZrEu_7 samples are associated to left and down axis (black), meanwhile ZrEu_12 sample are plotted respect to right and up axis (orange).

Whatever the temperature, the shapes of the impedance arcs are similar to those observed at 350ºC (Figure 4.2) for the four analysed samples, but with a proportional reduction of the impedances on increasing the temperature that agrees with a typical semiconductor behaviour, for which conductivity increases with the temperature.

The highest total conductivity (lowest impedance), in the studied temperature range, is exhibited by the ZrEu_5 sample as observed in Figure 4.2 and also in Figure 4.3, where the calculated total conductivities by equation 4.7 are represented in the studied temperature range. Therefore, the conductivity reaches a maximum for 5 mol.% of Eu_2O_3, indicating thereby an optimal amount of dopant. For this sample (ZrEu_5) the total conductivity at 600 ºC is $2 \cdot 10^{-3}$ $S \cdot cm^{-1}$, in agreement with the state-of-art electrolyte materials and also with other Zr-based proton conductors already discussed in the *Introduction* section.[6,21,22]

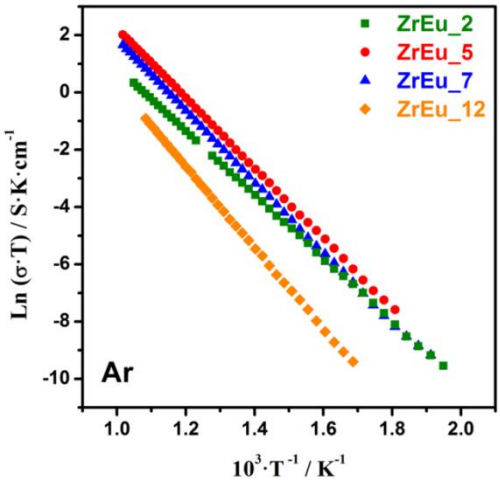

Figure 4.3 Total conductivities of the samples for the measured temperature range in dry conditions (in Ar atmosphere).

Analogous to the total impedances/conductivities, the conductivities of the bulk and grain boundaries contributions were calculated (Figure 4.4). The conductivities of the grain boundaries are several orders of magnitude lower than that of the bulk for all samples, again in agreement with other similar materials found in the literature.[6,20–22] As it was observed in the complex plane plot of the impedances (Figure 4.2) where the arcs were progressively approximating until only one arc was distinguished for ZrEu_12 sample, the conductivities also reflect an approach of the bulk and grain boundary conductivities, but more significant for the grain boundary contribution on increasing the Eu content. This could be explained by an increment of the Eu concentration in the grain boundaries on increasing the loading meaning a higher oxygen vacancies concentration.

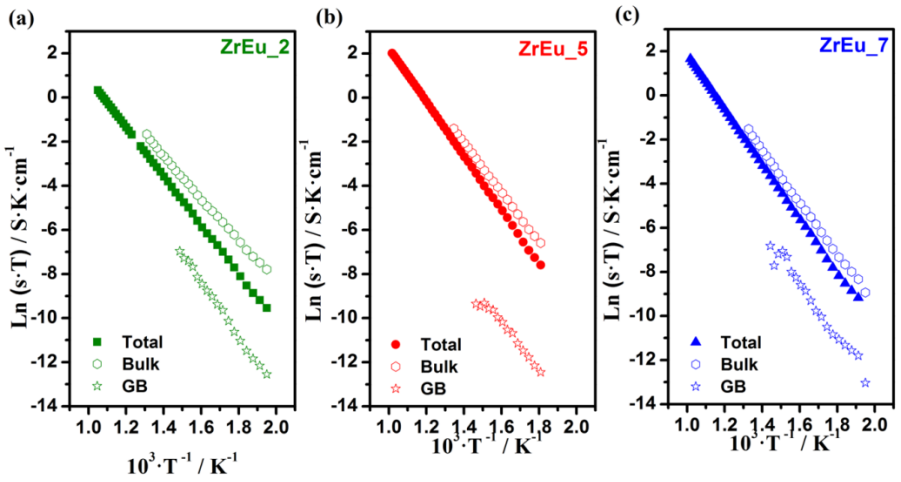

Figure 4.4 Total, bulk and grain boundaries conductivities of the samples for all measured temperature range in dry conditions (in Ar atmosphere).

From these calculated conductivities, the activation energies for the conduction processes were estimated. The calculated activation energies vary from 0.953 to 1.220 eV on increasing the Eu content of the studied solids (Table 4.3). These values, according to the literature,[46] are characteristic of pure ionic conductors (~1 eV), as expected since acceptor-doped ZrO_2 compounds have been reported as pure ionic conductors.[36] The lower oxidation state of the aliovalent cation in these materials requires the formation of oxygen vacancies, this results in p-type semiconductor materials whose conductivity in inert flow depends on the movement of the vacancies.

Table 4.3 Total activation energies of the ionic conductors in inert atmosphere (Ar).

Sample	**ZrEu_2**	**ZrEu_5**	**ZrEu_7**	**ZrEu_12**
E_a(eV)	0.953	1.055	1.062	1.220

In principle, the conductivity should depend on the concentration of oxygen vacancies, being higher on increasing the number of oxygen vacancies; however, the ZrEu_5 solid shows the highest conductivity. This is explained by some authors as a consequence of the association of oxygen vacancies and dopant ions, thereby blocking the movement of the holes, which results in a decrease of the conductivity.[37,47,48] For example, studies and simulations for yttria-doped zirconia have shown the preferential formation of clusters between the two dopant ions and the associated oxygen vacancy, which is located as second nearest neighbours and is

displaced along <111> fluorite direction.[26,49] This oxygen vacancy-dopant ion association results in a maximum in the conductivity at 5 mol.% europia dopant. Moreover, the activation energy calculation shows insignificant but changing values as a function of the Eu content, such the E_a increases proportionally to the europium content thus supporting the idea of an association of the oxygen vacancies.

4.2.3. IS in O_2/Ar atmospheres.

The impedance behaviour (types of arcs, variation of bulk and grain boundary conductivities as a function of Eu content as well as the increase of the conductivities at higher temperatures) is similar to that previously discussed for inert flow, as it can be observed in Figure 4.5. The total conductivity for the ZrEu_5 sample is again the highest among the studied materials whatever the oxygen partial pressure is. Therefore, all the considerations discussed and concluded before for the conductivity of the samples in inert conditions is the same in oxygen atmosphere. The activation energies calculated from the data plotted in Figure 4.5b also exhibit similar values in O_2 atmosphere than in inert conditions (Table 4.4):

Table 4.4 Total activation energies of the ionic conductors in pure O_2 atmosphere.

Sample	**ZrEu_2**	**ZrEu_5**	**ZrEu_7**	**ZrEu_12**
E_a(eV)	0.943	1.065	1.090	1.229

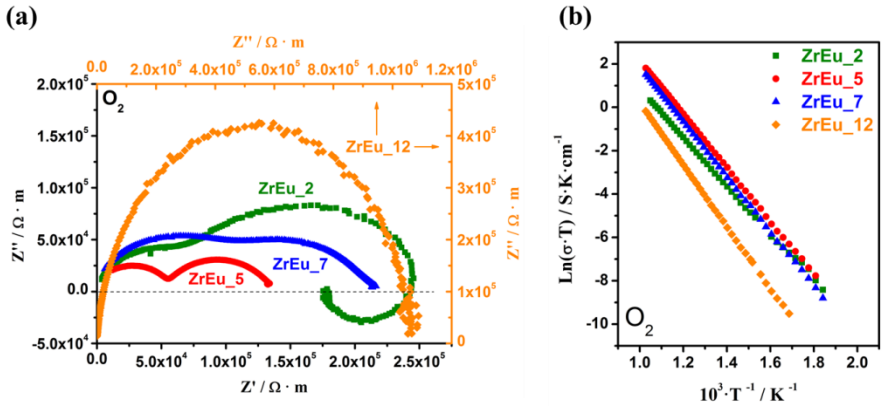

Figure 4.5 (a) Complex plane plot of the normalized impedance spectroscopy of the sintered samples at 350 ºC in pure O_2 atmosphere. The ZrEu_2, ZrEu_5 and ZrEu_7 samples are associated to left and down axis (black), meanwhile ZrEu_12 sample are plotted respect to right and up axis (orange).(b) Total conductivities of the samples for the measured temperature range in pure O_2 atmosphere.

Paying attention to the ZrEu_2, it is noticeable an inductive effect at low frequencies. This phenomenon usually appears when some imperfections in the surface of the sample or in the sample-electrode interface are present, like in studies of corrosion in materials.[25,50] Then, this effect appears probably because of the porosity of the sintered sample is higher than in the other samples showing a more irregular surface in contact with the electrode.

Comparing now the effect of the oxygen partial pressure, the samples were tested in several O_2/Ar flows in the same conditions as in 100 % of Ar (section 4.2.1) and in 100 % O_2 (Figure 4.5) atmospheres. As it is observed in Figure 4.6 the conductivity is not affected by the oxygen partial pressure. In this figure, the impedance of the ZrEu_5 sample at 350 ºC in different oxygen partial pressures is plotted as representative of the behaviour of all samples in the

studied temperature range. From 10 to 100 vol.% of oxygen, the impedance responses and the calculated magnitudes are exactly the same for every sample. Thus, the oxygen pressure has not influence on the conduction phenomena. However, a slight increment of the impedance between 0 (in Ar) and 10% of oxygen partial pressures is observed; this, probably due to oxygen adsorbed on the conductor surface according to a Langmuir adsorption behaviour.[51] Surface vacancy filling by gaseous phase oxygen should result in a vacancy annihilation and therefore in a slight conductivity decrease. Once the solid is saturated in oxygen (lower than 10 vol.% of O_2), the conductivity is not affected by the oxygen partial pressure. Moreover, it is remarkable the fact that the oxygen presence mainly modifies the impedance of the grain boundary, which implies that the detrimental oxygen adsorption is taking place in the surface of the grains but not inside, in the bulk. In order to verify this possible oxygen adsorption, other characterization techniques will be necessary.

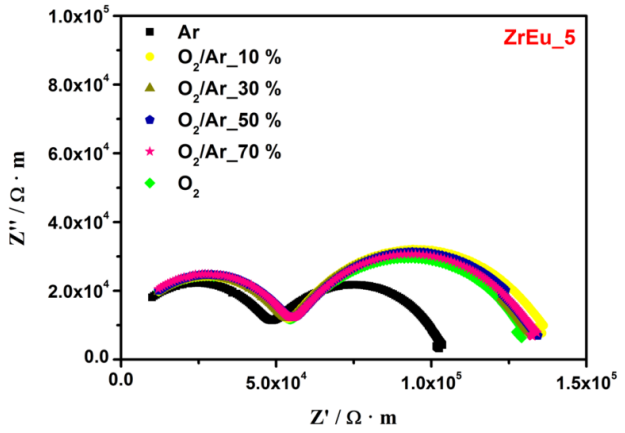

Figure 4.6 Complex plane plot of the normalized impedance spectroscopy of the sintered ZrEu_5 sample at 350 ºC in different O_2 partial pressures atmospheres.

Likewise the previous conditions, activation energies of the samples in the different oxygen partial pressures were also calculated, evidently getting the same values independently of the oxygen pressure from 10 to 100 % of O_2.

4.2.4. IS in H_2O/Ar atmospheres.

Finally, the samples were tested in several water partial pressures following the same procedure as before, but starting at 200 ºC to avoid condensed water in the system. Unlike the oxygen atmosphere, the experiments with different water pressures (represented at 350 ºC for 20 % of H_2O in Figure 4.7) show that the impedance arcs are modified by the water presence. Consequently, besides the conductivity present in inert and oxygen conditions, other contribution is appearing that is not affected by oxygen but by water. This may indicate that the Grotthuss' mechanism operates in these solids. As it was mentioned before, this proton conductivity is expected in these types of solids and the necessity of the oxygen vacancies to dissociate the water molecules to have the ions which allow the Grotthuss' mechanism is in agreement with the existence of an optimal amount of dopant, since the oxygen vacancies continue determining the conduction mechanism by the water dissociation step.

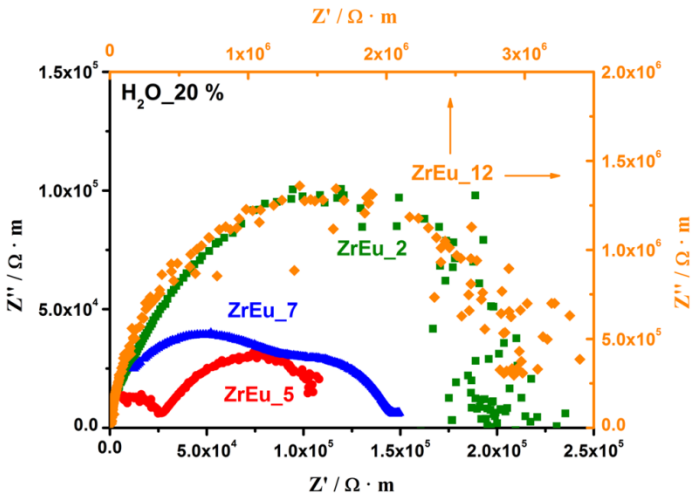

Figure 4.7 Complex plane plot of the normalized impedance spectroscopy of the sintered samples at 350 ºC in wet conditions (20 vol.% of H_2O). The ZrEu_2, ZrEu_5 and ZrEu_7 samples are associated to left and down axis (black), meanwhile ZrEu_12 sample are plotted respect to right and up axis (orange).

There are some significant changes when the water is introduced. Only one arc is exhibited now by the ZrEu_2 sample, implying thereby no distinction between the bulk and the grain boundary contributions. Since the total impedance has been slightly reduced, the overlap of both arcs is probably caused by an increase of the conductivity of the grain boundary by the water presence more than by the decrease of the bulk conductivity. Also the ZrEu_5 and ZrEu_7 samples show a small increment of the total conductivity (decrease of the total impedance). When the water is introduced, it is very noticeable the increase of the bulk conductivity of the ZrEu_5 sample, whose impedance decrease from $5 \cdot 10^4$ Ω·m in inert conditions (Figure 4.2) to $2.6 \cdot 10^4$ Ω·m in wet conditions (Figure 4.7).

Then, the ZrEu_5 sample is shown for a deeper discussion of the results in wet conditions, since this sample exhibit the highest ionic conductivity in all tested atmospheres and temperatures. In Figure 4.8 it has been plotted the impedance arcs in dry Ar (Fig. 4.8a) and wet (Fig. 4.8b) conditions of the ZrEu_5 sample on progressive increasing the temperature in the range of interest. It is important to notice that on increasing temperature the impedance indeed decreases, although for the highest temperatures the impedance in either Ar or H_2O/Ar is hardly different. From low temperature to ~330 ºC the reduction of the total impedance by the water presence is meaningful. Then, the impedances become equal. Therefore, the influence of the water probably providing proton conductivity only appears at low temperatures. For temperatures higher than ~330 ºC the effect of the water disappears and the total impedances maintain the same behaviour than in inert conditions.

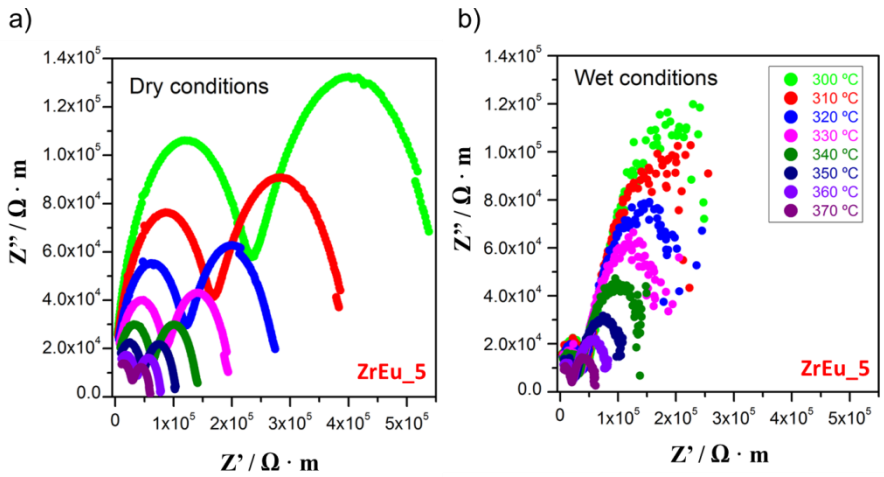

Figure 4.8 Complex plane plots of the normalized impedance spectroscopy of the sintered ZrEu_5 sample in (a) wet conditions (20 vol.% of H_2O in Ar) and (b) dry conditions (Ar atmosphere) at different temperatures.

Besides the comparison of the impedance arcs, other way to see the effect of the water is to contrast the conductivities in the different atmospheres (Figure 4.9). The increment of the total conductivity is again observed for low temperatures and stops over 300 - 330 ºC.

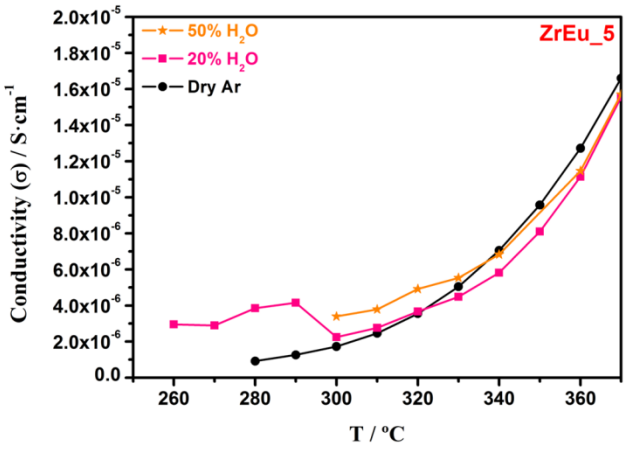

Figure 4.9 Conductivities of ZrEu_5 sample in dry and wet atmospheres on increasing the temperature.

Therefore differences in the impedance/conductivity at low temperatures must be related to the presence of adsorbed water on the ionic conductor surface that is significant at low temperatures and almost negligible at higher temperatures. However, to assess the influence of water in the conductivity, a further characterisation of the adsorbed species in H_2O/Ar atmospheres was performed by *in situ* Raman spectroscopy and DRIFTS measurements on ZrEu_5 and ZrEu_12 samples, since they show the best and the worst ionic conductivity in the tested conditions.

4.3. *IN SITU* RAMAN SPECTROSCOPY AND DRIFTS

In order to understand the role of water, *in situ* spectroscopic studies were carried out for the highest conductivity sample, ZrEu_5, and, for the sake of comparison, for the sample with the smallest conductivity within the ones tested, ZrEu_12. *In situ* Raman studies were performed in the same conditions as previous *ex situ* Raman experiments with the red laser (chapter 3) but in H_2O/N_2 flow from 200 ºC to 450 ºC with a previous activation in N_2 flow at 450 ºC for 1 h to dehydrate the sample for comparison with IS measurement conditions. The spectra for both samples in wet conditions as a function of temperature are shown in Figure 4.10 together with the spectra of the activated samples. The number, positions and relative intensities of all the bands are similar for both N_2 and H_2O/N_2 atmospheres whatever the temperature tested. It is evident that both samples exhibit the same profile than *ex situ* Raman spectra performed at ambient conditions at room temperature (see Chapter 3, Figure 3.16). In order to compare the activation step and the experiments with H_2O/N_2 flow, it has been displayed the last spectrum at 450 ºC in N_2 with the spectra in H_2O/N_2 in temperature for each sample. Comparing the profiles at 450 ºC in dry and wet conditions, it can be noticed that the intensity and the Raman shift positions hardly changes. The intensity ratio $(^7F_2 \rightarrow {}^5D_0)/(^7F_1 \rightarrow {}^5D_0)$ increases less than 5 % upon heating 450 ºC, this must be related to the homogeneous distribution of the europium within solid solution which results just in the modification of the europium sites at the surface upon dehydration.

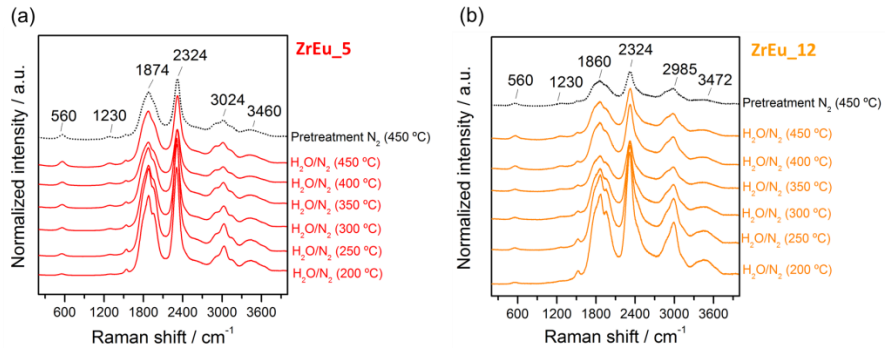

Figure 4.10 In situ Raman spectroscopy of the samples (a) ZrEu_5 and (b) ZrEu_12 in wet conditions from 200 ºC to 450 ºC and in dry conditions at 450 ºC for comparison.

In situ DRIFTS measurements were used to describe the effect of physisorbed and/or dissociated water in the ionic conductivity. Firstly, the samples were pretreated at 600 ºC for 1 h under flow of H_2/Ar to dehydrate the sample and eliminate the water adsorbed on the surface. The initial spectra and the final spectra after the pretreatment are shown in Figure 4.11a and 4.11b, respectively. As can be observed in Figure 4.11a, both ZrEu_5 and ZrEu_12 samples before activation are highly hydrated and the spectra are dominated by a very broad absorption band centered at 3300 cm^{-1} that can be assigned to the OH stretching modes of both undissociated water molecules and hydroxyl species interacting by hydrogen-bonding.[52] On the counterpart, the bending mode associated to the δ_{HOH} mode appears as a shoulder at 1647 cm^{-1} that can be attributed to non-dissociated/physisorbed water and also contains contributions from lone-pair Lewis-coordinated water.[52,53] The intensities of these bands in both samples suggest a lower ability to absorb water of the ZrEu_12 sample. On the other hand, the set of features that appear in

the 1100-1600 cm^{-1} range in both samples can be assigned to residual carbonates/carboxylates like compounds.[53] The presence of these species is unavoidable since the atmospheric CO_2 adsorption on zirconia and Eu-doped zirconia leads to the formation of carbonate species during the calcination process remaining occluded in the structure of pores of these materials. As revealed by high resolution electron microscopy (see chapter 3), the samples present a significant amount of micropores with size ranging from 2 to 3 nm and carbonate species can be anchored in these cavities. This observation is in good agreement with the results reported by Daturi *et al*.[54]

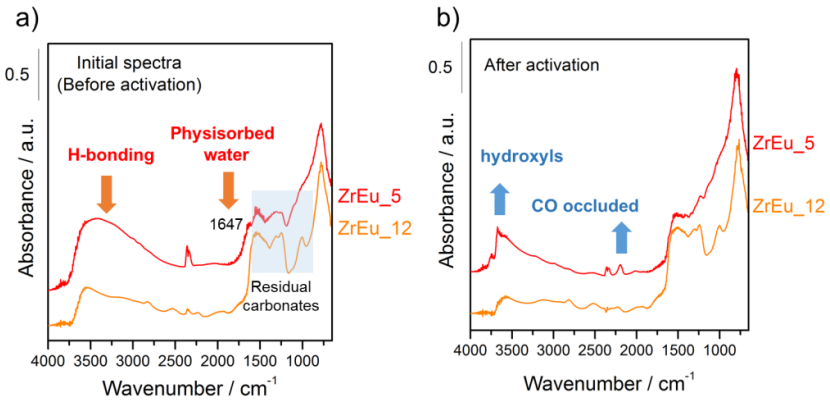

Figure 4.11 In situ DRIFTS measurement (a) at room temperature before activation and (b) at 200 ºC after activation for the samples ZrEu_5 and ZrEu_12.

The spectral dehydration pattern of both ZrEu_5 and ZrEu_12 samples are presented in Figure 4.11b. After treatment at 600 ºC in flow of H_2/Ar, it is noticeable the disappearance of the broad band associated to non-dissociated water in the ZrEu_5 sample and the appearance of a new hydroxyl species. The interaction via hydrogen-bonds between the water molecules and the hydroxyl species is

responsible for the non-appearance of this hydroxyl bands before activation. Additionally, it can be observed a new band around 2100 cm^{-1} that has been attributed to CO occluded in the pores or cavities as it will be discussed later. In contrast, the sample ZrEu_12 presents the broad band around 3300 cm^{-1} observed before activation (decreased in intensity) and any new band attributable to OH species is detected.

Now, the effect of water adsorption in the 200-450 ºC temperature range on the surface of ZrEu_5 and ZrEu_12 samples after activation is investigated. These results are presented in two different wavenumber regions: 3800–3200 cm^{-1} for hydroxyl groups and 3000–2000 cm^{-1} for the $^7F_0 \rightarrow {}^7F_J$ electronic transitions of Eu and possible CO occluded in the pores. As it can be noted in the wavenumber region for OH-stretching modes, the activated sample ZrEu_5 (Figure 4.12a) clearly shows two new bands at 3765 and 3675 cm^{-1}, respectively, ascribable to the ν_{OH} stretching modes of terminal and tribridged hydroxyl groups,[52] that are formed during the activation by water desorption. Under a flow of H_2O/Ar, the appearance of a broad band centered at around 3720 cm^{-1} suggests the formation of a "new" type of hydroxyls.

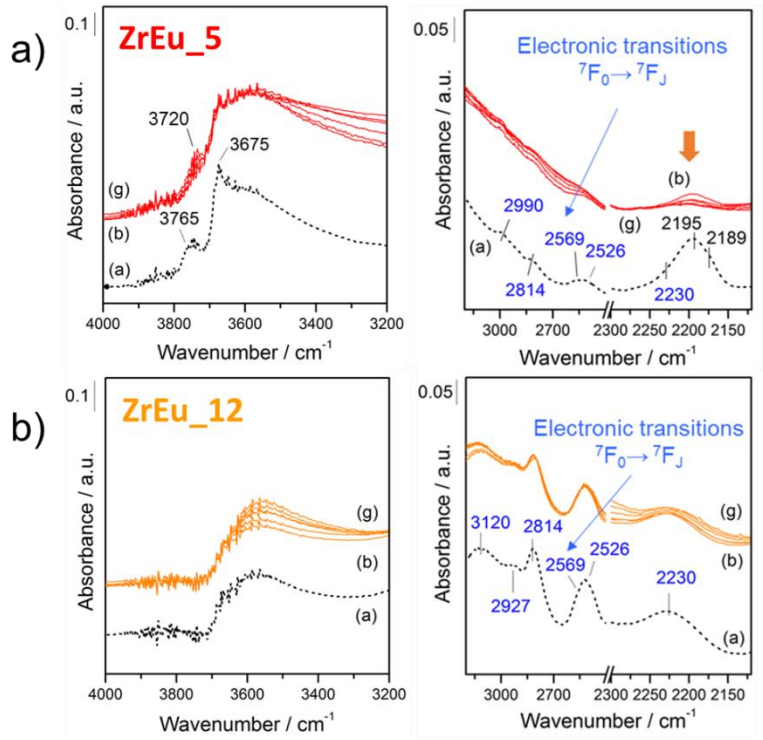

Figure 4.12 DRIFTS difference spectra in wet conditions respect to the dried spectrum after activation step (spectra a), from 200 ºC (spectra b) to 450 ºC (spectra g).

A more detailed analysis of difference spectra (taking as reference the spectrum of the activated surface) clearly evidences the decrease of the bands at 3765 and 3675 cm^{-1} and that the broad feature observed at 3720 cm^{-1} is composed by two bands 3700 and 3724 cm^{-1} (Figure 4.13). According to Cerrato *et al.*,[52] hydroxyls type (I) of monoclinic ZrO_2 interacts weakly with water molecules, which provokes a shift to lower wavenumbers (from 3775 cm^{-1} to 3695 cm^{-1}). These data permit to attribute the band at 3700 cm^{-1} to type (I) hydroxyls weakly interacting with water molecules. However, the interaction of hydroxyls at 3675 cm^{-1} (tribridged, more acidic ones)

with water is stronger and generates a broad band at lower wavenumbers (3300 cm^{-1}). The "new" band appearing in presence of water at 3724 cm^{-1}, may be tentatively attributed to hydroxyls type (II).[52] Most authors stand up for the absence of these hydroxyls in monoclinic ZrO_2 due to the short Zr-Zr distance (~2 Å) in this structure that impedes the stabilization of OH bonded to two metallic cations. In the case of stabilized cubic zirconia doped with trivalent cations, the metal-metal distance become larger[55] and the presence of OH(II) may be possible. Therefore, we propose that this band is associated to the presence of oxygen vacancies created by doping with Eu^{3+}. As the temperature increases (from 200 ºC to 400 ºC) the band at 5248 cm^{-1} corresponding to ($\nu+\delta_{HOH}$) combination bands of water molecules[56] progressively decreases, being completely absent when the temperature reaches 300ºC. In these conditions, the band at 3724 cm^{-1} is still observed at the same position, which suggests that these hydroxyls groups do not interact with the water molecules. We believe that the –OH generation takes place on the vacancies on every structural defect close to the Eu centers. This explanation is in good agreement with Kock *et al*.[57] They found that the doping of zirconia with Y_2O_3 creates defects near the Y^{3+} centers in which new hydroxyls groups can be formed. From these observations, we may propose a surface on which free OH groups and water molecules coexist, providing an adequate situation to favours the Grotthuss' mechanism at least at temperatures lower than 300 ºC.[58]

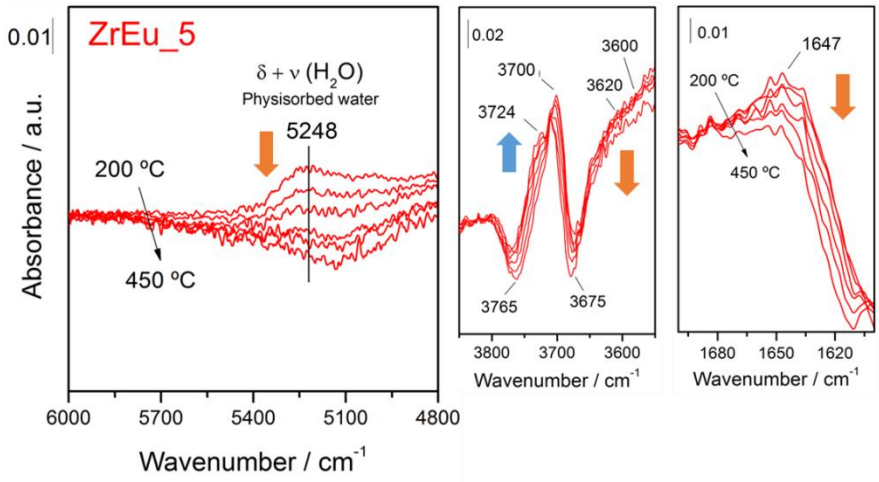

Figure 4.13 DRIFTS difference spectra of ZrEu_5 sample in wet conditions respect to the dried spectrum after activation step from 200 ºC to 450 ºC magnifying water adsorption regions.

In the 3000–2000 cm^{-1} region (Figure 4.12), it is evident the presence of different bands that corresponding to low energy transitions from the ^7F ground term to the ^7F_J levels. This type of transitions are characteristic of Eu^{3+}-doped inorganic matrices and can be observed by infrared spectroscopy due to its low energy.[59] Additionally, after activation a feature composed by two bands at 2195 and 2189 cm^{-1} that are characteristic of CO confined in the cavities of the material pores is observed.[54] The occluded carbonates in the pores of the material are reduced in presence of hydrogen generating CO that remains anchored inside the cavities. The treatment with water upon increasing temperature leads to the complete disappearance of both ν(CO) bands forming likely again carbonate species that are reversibly restored with the treatment. According to the model proposed by Daturi *et al.*,[54] the treatment under hydrogen at 600 ºC produces a confined reduction of the

surface mobilizing oxygens from the bulk and changing partially the coordination inside the cavities. The reoxidation with water produces a reconstitution of the previous carbonate species inside the cavities or additionally generate new hydroxyl species by dissociation of water at the oxygen vacancies.

The effect of water adsorption, after activation of the ZrEu_12 sample, as a function of temperature is shown in Figure 4.12b. It must be noticed that this sample and the ZrEu_5 one behave completely different and the presence of free hydroxyls in the the ZrEu_12 sample after activation is much lower. In consequence, the amount of adsorbed water could be negligible since the number of centers available for interaction via H-bond is restricted. As it is well-known, ionic conductivity of pure zirconia is improved by the introduction of acceptor dopants like Eu that besides stabilizing the cubic structure at low temperatures, increase the concentration of oxygen vacancies.[37] However, a large amount of dopant element can result prejudicial and the improvement of ionic conductivity is no longer observed as it has been analysed above. Moreover, the possible formation of segregated europia phases in the ZrEu_12 sample as well as the lower specific surface, may result in a decrease in the concentration of surface hydroxyls and thereby the interaction with the water molecules. In the 3000-2000 cm^{-1} wavenumber region, the intensity of the bands associated to the f-f electronic transitions are notably increased due to the higher concentration of europium. However, the bands associated to the CO occluded do not appear. This fact can be explained considering that the concentration of pores in this sample is significantly lower as can be observed by TEM (see Chapter 3, Figure

3.10). Raz *et al*.[60] investigated the adsorption of water layers on yttrium stabilized zirconia and suggested the first water layer to be chemisorbed on the Zr sites whereas the second layer is physisorbed on top of the chemisorbed water layer. Here, it is proposed an analogous model in which the dissociation of water takes place on the vacancies. Thus, the dissociation of water molecules takes place on specific sites generating hydroxyl species whereas the coordination of undissociated water occurs through interactions with surface hydroxyls.

As it is mentioned above, the enhancement of the conductivity caused by the inclusion of the water is distinguishable at low temperature but is negligible at high temperature (over ~330 ºC) as it is shown by its impedance response in Fig. 4.8 or by its conductivity data in Figure 4.9. This behaviour can be explained by desorption of the water because of the temperature increase, hence it is obtained the same value of conductivity as in argon atmosphere for high temperature. Moreover, the band at 5248 cm^{-1} ascribed above to the physisorbed water, also disappears for high temperature (Figure 4.13). The intensity of the physisorbed water band decreases with temperature and above 330 ºC the signal is almost zero as plotted in Figure 4.14. Though the band associated to hydroxyl groups generated on the surface vacancies (3724 cm^{-1}) is increasing as we can see in Figure 4.14, we can conclude that the proton conduction phenomena are influenced and improved by the presence of physisorbed water available for the Grotthuss' mechanism according to the impedance and DRIFTS analysis.

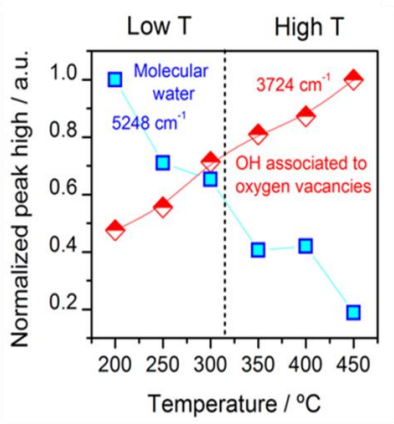

Figure 4.14 Variation of the normalized intensity with the temperature of the bands associated to physisorbed water (5248 cm^{-1}) and dissociated water (3724 cm^{-1}) of sample ZrEu_5 analysed by DRIFTS in wet conditions.

Therefore, the conductivity of these europium doped zirconia samples is the same in both inert and wet conditions at high temperature (from ~300 ºC) due to the absence of physisorbed water from this temperature. At lower temperatures, on the other side, the dissociated water in the oxygen vacancies (band at 3730 cm^{-1}) and the adsorbed water create layers of water molecules whose interaction allows proton conductivity by Grotthuss' mechanism which increases the total conductivity in this temperature range. This layer model represented in Figure 4.15 is in agreement with the model suggested by Kock *et al*.[57]

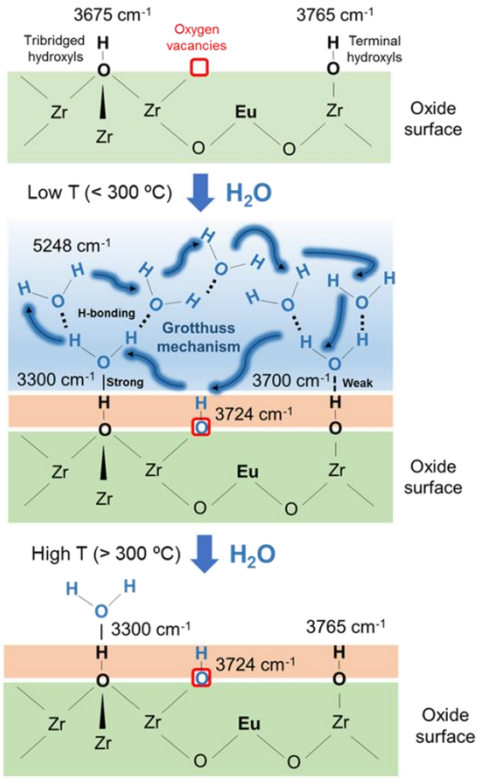

Figure 4.15 Water layer model proposed for Eu doped ZrO_2 samples and the effect of the water and the temperature.

4.4 Partial Conclusions

The prepared mixed oxides exhibit ionic conductivity typical of a p-type semiconductor created by the presence of oxygen vacancies. They show activation energies around 1 eV according to a pure ionic conductor material. Moreover, the maximal conductivity is found for ZrEu_5 sample, indicating an optimal amount of dopant (5 mol.% of Eu_2O_3) from which the association between oxygen vacancies and dopant atoms hinders the conductivity and increases the activation energy.

It has been demonstrated additional proton conductivity by Grotthuss' mechanism under wet conditions for low temperatures, where superficial water is still present. It is required dissociated water in the oxygen vacancies and superficial water to generate the proton conductivity. Thus, only for temperatures below ~300 ºC both conditions exist and an increment of the total conductivity is observed.

According to DRIFTS and impedance analysis, it is possible to conclude a layer model where, under wet conditions, the dissociated water in the oxygen vacancies interacts with superficial water improving the conductivity by Grotthuss' mechanism. When the temperature exceeds 300 ºC, the superficial water disappears because of the high temperature, exhibiting thereby the same conductivity than in inert conditions.

These experiments reveal that the synthetized europium doped zirconia compounds are pure proton conductors whose conductivity is improved at low temperatures in wet conditions. Therefore, the addition of these proton conductors in a catalytic system where the diffusion of the water is a rate-limiting step, like WGSR, can play an important role in its performances.

REFERENCES

1. Kreuer, K.-D. Proton Conductivity: Materials and Applications. *Chem. Mater.* **8,** 610–641 (1996).

2. Imanaka, N. & Adachi, G. Rare earth contribution in solid state electrolytes, especially in the chemical sensor field. *J. Alloys Compd.* **250,** 492–500 (1997).

3. Thangadurai, P., Sabarinathan, V., Bose, A. C. & Ramasamy, S. Conductivity behaviour of a cubic/tetragonal phase stabilized nanocrystalline La2O3 - ZrO2. *J. Phys. Chem. Solids* **65,** 1905–1912 (2004).

4. Labrincha, J. A., Frade, J. R. & Marques, F. M. B. Protonic conduction in La2Zr2O7-based pyrochlore materials. *Solid State Ionics* **99,** 33–40 (1997).

5. Besikiotis, V., Ricote, S., Jensen, M. H., Norby, T. & Haugsrud, R. Conductivity and hydration trends in disordered fluorite and pyrochlore oxides: A study on lanthanum cerate-zirconate based compounds. *Solid State Ionics* **229,** 26–32 (2012).

6. Xia, X.-L., Liu, Z.-G., Ouyang, J.-H. & Zheng, Y. Preparation, Structural Characterization, and Enhanced Electrical Conductivity of Pyrochlore-type (Sm1-xEux)2Zr2O7 Ceramics. *Fuel Cells* **12,** 624–632 (2012).

7. Haugsrud, R. & Norby, T. High-temperature proton conductivity in acceptor-doped LaNbO4. *Solid State Ionics* **177,** 1129–1135 (2006).

8. Schöllhorn, R., Kuhlmann, R. & Besenhard, J. O. Topotactic redox reactions and ion exchange of layered MoO3 bronzes. *Mater. Res. Bull.* **11,** 83–90 (1976).

9. Schöllhorn, R., Schulte-Nölle, T. & Steinhoff, G. Layered intercalation complexes of the hydrogen bronze H0.5MoO3 with organic lewis bases. *J. Less-Common Met.* **71,** 71–78 (1980).

10. Adams, S. CDW Superstructures in Hydrogen Molybdenum Bronzes HxMoO3. *J. Solid State Chem.* **149,** 75–87 (2000).

11. Amsif, M. *et al.* Mo-Substituted Lanthanum Tungstate La28-yW4+yO54+d: A Competitive Mixed Electron-Proton Conductor for Gas Separation Membrane Applications. *Chem. Mater.* **24,** 3868–3877 (2012).

12. Tagaya, H., Ara, K., Kadokawa, J., Karasu, M. & Chiba, K. Intercalation of Organic Compounds in the Layered Host

Lattice MoO3. *J. Mater. Chem.* **4,** 551–555 (1994).

13. Vega-Castillo, J. E., Ravella, U. K., Corbel, G., Lacorre, P. & Caneiro, A. Thermodynamic stability, structural and electrical characterization of mixed ionic and electronic conductor La2Mo2O8.96. *Dalt. Trans.* **41,** 7266–7271 (2012).

14. Lo, J.-C. *et al.* La2Mo2O9-based electrolyte: Ion conductivity and anode-supported cell under single chamber conditions. *J. Am. Ceram. Soc.* **94,** 806–811 (2011).

15. Morozov, V. *et al.* Na2/7Gd4/7MoO4: a Modulated Scheelite-type Structure and Conductivity Properties. *Inorg. Chem.* **51,** 5313–5324 (2012).

16. El Khal, H. *et al.* Effect of porosity on the electrical conductivity of LAMOX materials. *Solid State Ionics* **304,** 75–84 (2017).

17. Shores, D. A. & Rapp, R. A. Hydrogen Ion (Proton) Conduction in Thoria-Base Solid Electrolytes. *J. Electrochem. Soc.* **119,** 300–305 (1972).

18. Takahashi, T. & Iwahara, H. Solid-state ionics: protonic conduction in perovskite type oxide solid solutions. *Rev. Chim. Min.* **17,** 243–253 (1980).

19. Iwahara, H., Esaka, T., Uchida, H. & Maeda, N. Proton conduction in sintered oxides and its application to steam electrolysis for hydrogen production. *Solid State Ionics* **3-4,** 359–363 (1981).

20. Kochetova, N., Animitsa, I., Medvedev, D., Demin, A. & Tsiakaras, P. Recent activity in the development of proton-conducting oxides for high-temperature applications. *RSC Adv.* **6,** 73222–73268 (2016).

21. Magrasó, A., Kjølseth, C., Haugsrud, R. & Norby, T. Influence of Pr substitution on defects, transport, and grain boundary properties of acceptor-doped BaZrO3. *Int. J. Hydrogen Energy* **37,** 7962–7969 (2012).

22. Babilo, P., Uda, T. & Haile, S. M. Processing of yttrium-doped

barium zirconate for high proton conductivity. *J. Mater. Res.* **22,** 1322–1330 (2007).

23. Norby, T., Dyrlie, O. & Kofstad, P. Protonic Conduction in Acceptor-Doped Cubic Rare-Earth Sesquioxides. *J. Am. Ceram. Soc.* **75,** 1176–1181 (1992).

24. Norby, T., Dyrlie, O. & Kofstad, P. Protons in Ca-doped La2O3, Nd2O3 and LaNdO3. *Solid State Ionics* **53-56,** 446–452 (1992).

25. *Impedance Spectroscopy Theory, Experiment, and Applications*. (John Wiley & Sons, Inc., 2005).

26. Tilley, R. J. D. *Defects in solids*. (John Wiley & Sons, Inc., 2008).

27. Sunarso, J. *et al.* Mixed ionic-electronic conducting (MIEC) ceramic-based membranes for oxygen separation. *J. Memb. Sci.* **320,** 13–41 (2008).

28. Balachandran, U. *et al.* Development of mixed-conducting oxides for gas separation. *Solid State Ionics* **108,** 363–370 (1998).

29. Petric, A., Huang, P. & Tietz, F. Evaluation of La-Sr-Co-Fe-O perovskites for solid oxide fuel cells and gas separation membranes. *Solid State Ionics* **135,** 719–725 (2000).

30. Zuo, C., Zha, S., Liu, M., Hatano, M. & Uchiyama, M. Ba(Zr0.1Ce0.7Y0.2)O3-d as an Electrolyte for Low-Temperature Solid-Oxide Fuel Cells. *Adv. Mater.* **18,** 3318–3320 (2006).

31. Li, Y., Rui, Z., Xia, C., Anderson, M. & Lin, Y. S. Performance of ionic-conducting ceramic/carbonate composite material as solid oxide fuel cell electrolyte and CO2 permeation membrane. *Catal. Today* **148,** 303–309 (2009).

32. Zhang, C., Sunarso, J. & Liu, S. Designing CO2-resistant oxygen-selective mixed ionic–electronic conducting membranes: guidelines, recent advances, and forward directions. *Chem. Soc. Rev.* **46,** 2941–3005 (2017).

33. Kreuer, K. D. Proton-Conducting Oxides. *Annu. Rev. Mater. Res.* **33,** 333–359 (2003).

34. Kreuer, K. D. Aspects of the formation and mobility of protonic charge carriers and the stability of perovskite-type oxides. *Solid State Ionics* **125,** 285–302 (1999).

35. Yashima, M. Invited Review: Some recent developments in the atomic-scale characterization of structural and transport properties of ceria-based catalysts and ionic conductors. *Catal. Today* **253,** 3–19 (2015).

36. Furøy, K. A., Haugsrud, R., Hänsel, M., Magrasó, A. & Norby, T. Role of protons in the electrical conductivity of acceptor-doped BaPrO3, BaTbO3, and BaThO3. *Solid State Ionics* **178,** 461–467 (2007).

37. Malavasi, L., Fisher, C. A. J. & Islam, M. S. Oxide-ion and proton conducting electrolyte materials for clean energy applications: structural and mechanistic features. *Chem. Soc. Rev.* **39,** 4370–4387 (2010).

38. Shimura, T., Fujimoto, S. & Iwahara, H. Proton conduction in non-perovskite-type oxides at elevated temperatures. *Solid State Ionics* **143,** 117–123 (2001).

39. Kreuer, K.-D., Rabenau, A. & Weppner, W. Vehicle Mechanism, A New Model for the Interpretation of the Conductivity of Fast Proton Conductors. *Angew. Chemie Int. Ed. English* **21,** 208–209 (1982).

40. van Grotthuss, C. J. T. Sur la décomposition de l'eau et des corps qu'elle tient en dissolution à l'aide de l'électricité galvanique. *Ann. Chim.* **58,** 54–73 (1806).

41. Macdonald, J. R. Impedance Spectroscopy. *Ann. Biomed. Eng.* **20,** 289–305 (1992).

42. Haile, S. M., West, D. L. & Campbell, J. The role of microstructure and processing on the proton conducting properties of gadolinium-doped barium cerate. *J. Mater. Res.* **13,** 1576–1595 (1998).

43. Hodge, I. M., Ingram, M. D. & West, A. R. Impedance and modulus spectroscopy of polycrystalline solid electrolytes. *J. Electroanal. Chem.* **74,** 125–143 (1976).

44. Fabris, S., Paxton, A. T. & Finnis, M. W. A stabilization mechanism of zirconia based on oxygen vacancies only. *Acta Mater.* **50,** 5171–5178 (2002).

45. Howard, C. J., Hill, R. J. & Reichert, B. E. Structures of ZrO2 polymorphs at room temperature by High-Resolution Neutron Powder Diffraction. *Acta Crystallogr.* **B44,** 116–120 (1988).

46. Fonseca, F. C., Muccillo, R., De Florio, D. Z., Ladeira, L. O. & Ferlauto, A. S. Mixed ionic-electronic conductivity in yttria-stabilized zirconia/carbon nanotube composites. *Appl. Phys. Lett.* **91,** 243107–1 – 243107–3 (2007).

47. Chen, C.-T., Sen, S. & Kim, S. Effective Concentration of Mobile Oxygen-Vacancies in Heavily Doped Cubic Zirconia: Results from Combined Electrochemical Impedance and NMR Spectroscopies. *Chem. Mater.* **24,** 3604–3609 (2012).

48. Navrotsky, A. Thermodynamics of solid electrolytes and related oxide ceramics based on the fluorite structure. *J. Mater. Chem.* **20,** 10577–10587 (2010).

49. Goff, J. P., Hayes, W., Hull, S., Hutchings, M. T. & Clausen, K. N. Defect structure of yttria-stabilized zirconia and its influence on the ionic conductivity at elevated temperatures. *Phys. Rev. B* **59,** 14202–14219 (1999).

50. Grundmeier, G., Jüttner, K.-M. & Stratmann, M. in *Materials Science and Technology: A Comprehensive Treatment: Corrosion and Environmental Degradation, Volumes I+II* 285–381 (WILEY-YCH Verlag GmbH & Co. kGaA, 2006).

51. Xia, X., Oldman, R. J. & Catlow, C. R. A. Oxygen adsorption and dissociation on yttria stabilized zirconia surfaces. *J. Mater. Chem.* **22,** 8594–8612 (2012).

52. Cerrato, G., Bordiga, S., Barbera, S. & Morterra, C. Surface characterization of monoclinic ZrO2. I Morphology, FTIR spectral features, and computer modelling. *Appl. Surf. Sci.* **115,**

53–65 (1997).

53. Merle-Méjean, T., Barberis, P., Othmane, S. Ben, Nardou, F. & Quintard, P. E. Chemical Forms of Hydroxyls on/in Zirconia: An FT-IR Study. *J. Eur. Ceram. Soc.* **18,** 1579–1586 (1998).

54. Daturi, M., Binet, C., Bernal, S., Pérez Omil, J. A. & Lavalley, J. C. FTIR study of defects produced in ZrO2 samples by thermal treatment. Residual species into cavities and surface defects. *J. Chem. Soc. Faraday Trans.* **94,** 1143–1147 (1998).

55. Li, P., Chen, I.-W. & Penner-Hahn, J. E. Effect of Dopants on Zirconia Stabilization—An X-ray Absorption Study: I, Trivalent Dopants. *J. Am. Ceram. Soc.* **77,** 118–128 (1994).

56. Vimont, A. *et al.* Investigation of Acid Sites in a Zeotypic Giant Pores Chromium (III) Carboxylate. *J. Am. Chem. Soc.* **128,** 3218–3227 (2006).

57. Köck, E.-M., Kogler, M., Klötzer, B., Noisternig, M. F. & Penner, S. Structural and Electrochemical Properties of Physisorbed and Chemisorbed Water Layers on the Ceramic Oxides Y2O3, YSZ, and ZrO2. *ACS Appl. Mater. Interfaces* **8,** 16428–16443 (2016).

58. Motta, A., Gaigeot, M.-P. & Costa, D. Ab Initio Molecular Dynamics Study of the AlOOH Boehmite/Water Interface: Role of Steps in Interfacial Grotthus Proton Transfers. *J. Phys. Chem. C* **116,** 12514–12524 (2012).

59. Binnemans, K. Interpretation of europium(III) spectra. *Coord. Chem. Rev.* **295,** 1–45 (2015).

60. Raz, S., Sasaki, K., Maier, J. & Riess, I. Characterization of absorbed water layers on Y2O3 - doped ZrO2. *Solid State Ionics* **143,** 181–204 (2001).

CHAPTER 5.

WATER GAS SHIFT (WGS) REACTION

Abstract

The catalytic tests in WGS reaction have been carried out on powdered and structured samples keeping the same space velocity (WHSV) in all cases. Bare PtCeAl catalyst as well as the physical mixtures comprised of the catalyst and a proton conductor in a mass ratio of 1:5 have been studied in two different feeding conditions. The presence of the proton conductor leads to a higher catalyst' activity in terms of CO conversion in all tested conditions and mixtures. These results are also in concordance to the trend observed in the proton conductivity behaviour. The analysis of the proton influence indicates that the promoter effect is indeed related to the water activation step. Some parameters like catalyst / proton conductor ratio or space velocity have been also studied.

The structured m-PtCeAl+ZrEuMo_5 sample exhibits the best activity in the tested conditions when high amount of H_2 is present. The analysed stability of this sample is believed to be due to the deactivation of the proper PtCeAl catalyst by deposition of carbonaceous species.

5.1. INTRODUCTION

As presented in the *Introduction* (Chapter 1), the Water Gas Shift (WGS) reaction ($CO + H_2O \leftrightarrows H_2 + CO_2$) is usually carried out at industrial scale in two series of adiabatic reactors. In the first, the high-temperature water gas shift reaction (HT-WGS) takes place between 350 – 450 ºC on promoted Fe/Cr oxide catalysts and reduces the CO content from 10 – 50 wt. % at the outlet of the reforming step to about 3 – 5 wt. % CO. In the second step, Cu based catalysts are used in the 190 – 250 ºC temperature range (Low-Temperature Water Gas Shift reaction – LT-WGS) to further decrease the CO till levels under 0.5 wt. %.[1,2] Considering the slightly exothermic character of the WGS reaction ($\Delta H_R^0 = -41.1\ kJ/mol$), the overall process is favoured at low temperatures where the kinetics is slow and where low space velocities and large reactor volumes are required for higher reaction yields. Therefore, both WGS reaction steps (HT and LT) require large reactors with low space velocities (about 3000 - 4000 h^{-1} for the former and 1000 - 2000 h^{-1} for the later LT reactor). Consequently, within an hypothetical mobile device, the WGS reaction unit will occupy around 75% of the total volume for the complete H_2 production process (which involves steam reforming step, WGS unit and PROX reactor) and the PEM fuel cell.[1]

Precious metal-based catalysts for WGS reaction have been developed in last decades in response to the necessity of more compact catalyst beds for mobile devices applications.[3] The advantages of using precious metals like Pt, as active phase, are mainly its high activity at low-to-medium temperatures (250 – 400

ºC) and the zero order for CO in the reaction rate expression allowing to achieve equilibrium reaction with minimal volume, in opposite to the Cu-based catalyst where the CO order is close to 1.[4,5] Moreover, despite the high activity at low temperatures of the Cu-based catalysts, its low cost and its good stability, the Cu-based catalysts present important problems like its pyrophoricity, the needed special precaution during the start-up and shut-down processes and the necessary pre-activation step,[6] which are also avoided with Pt-based catalyst.

Another important advantage of using Pt instead of Cu, is that Pt exhibits a dual capacity for activating CO and H_2O.[2] The reported Pt catalyst' formulations usually include reducible oxide support, such as CeO_2, TiO_2 or Fe_2O_3 ,[7–13] aiming bifunctionality, i.e., both Pt and support have a role in the reaction mechanism. These formulations have shown better performances in WGS reaction mainly due to the increment of their oxygen storage capacity (OSC) involved in the water activation step.[14–18] At this point, it is important to take into consideration that several mechanisms have been proposed for WGS reaction. They are generally divided in two groups: redox and associative mechanisms. However, some questions are still under debate, which mechanism is prevailing or the nature of formed intermediates (formates or carboxyl species) and the role of the observed adsorbed species, are they spectators or really play a role in the reaction mechanism? Besides the nature of the catalyst and support, the reaction conditions also change and determine the reaction mechanism.[2,15,19,20] For instance, and considering the redox mechanism, the presence of reducible oxide support in H_2 and CO

rich operation conditions creates a reducing atmosphere, where the redox process may be inhibited.[2] Furthermore, no matter the mechanism, associative or redox, the activation of the water continues being problematic since the activation energies for the dissociation step, the binding energies of the protons and hydroxyl ions on the active phase and the thermodynamic barrier for the water adsorption and dissociation on the catalyst present high positive values.[4,21–23] In the same context, some authors suggested water activation as the rate-limiting step whatever the mechanism and catalysts, either precious metal-based catalysts like Pt and Au, or transition metals like Ag, Ni, Cu, Rh.[24–28]

Therefore, as it was established in the aim of this work (Chapter 1), it is important to assist the catalyst in the water activation step to achieve better performances. Then, proton conductors, capable to activate the water in the WGS operation temperature range (Chapter 4), have been added to the catalyst, physically mixed, and tested in WGS reaction. These samples are then compared to the bare catalyst in the same conditions in order to observe the proton conductor influence.

Additionally to the introduction of a proton conductor in the catalytic system' formulation, the preparation of structured catalyst appears as another efficient way to reduce the reactor volume. It has been reported that the use of micromonolithic structured catalysts reduces the reactor volume to one half for the same WGS efficiency.[29] Pt-based structured catalysts over micromonolithic supports have been reported showing promising results regarding

catalyst activity and stability.[1,18,30] More specifically, the longitudinal parallel channel micromonoliths allow higher space velocities avoiding significant pressure drops. Moreover, better use of reactor volume and catalyst coverage can be achieved with these structures, since the exposed area is larger and the system allows the use of thin catalytic layers.[31] As a consequence, better control of the layer thickness improves and can avoid diffusional problems.

Micromonoliths are often manufactured using metallic or ceramic substrates. Metallic support presents important advantages against ceramic ones, like much higher thermal conductivity and mechanical shock resistance. Thus, the highest heat diffusion provides virtually isothermal conditions along the micromonolith and avoids the formation of hot-spots. Moreover, the use of metallic sheets thinner than their ceramic homologues, allows the manufacture of denser unit cell per surface (cpsi) systems with higher exposed surface and thinner catalytic layers.[32]

For all above and along this chapter, the catalytic performance of the powdered and structured proton conductors mixed samples will be compared with the bare PtCeAl catalyst in the reaction conditions detailed in Chapter 2.

5.2. WGS Reaction on Powdered Catalysts

The WGS reaction has been carried out in the 180-350ºC temperature range for the feeding conditions previously described in the Experimental section (*Model* and *Industrial* conditions). The PtCeAl catalyst (0.1 g in all cases) was tested separately or physically

mixed with a series of ionic conductors (ZrEu_x or ZrEuMo_x series). All experiments were performed using catalyst particle size between 600 and 800 μm at high space velocities of 80000 $mL \cdot h^{-1} \cdot g_{cat}^{-1}$ (WHSV) and 20000 h^{-1} (GHSV), adding quartz with the same particle size if necessary to keep the catalytic bed volume.

In the first screening, the mixed samples were prepared using 1:5 catalyst-to-ionic conductor mass ratio to guarantee the complete contact between both fractions. The WGS activity of the bare PtCeAl sample in both *model* and *industrial* feed conditions is presented in Figure 5.1 (a) and (c). Catalysts with similar formulation but tested at much lower space velocities (2000 – 4000 h^{-1}) were able to achieve thermodynamic equilibrium from ~250 ºC in similar *Model* conditions.[33,34] However, at higher space velocities (as in this work), the reaction on PtCeAl attains the equilibrium at 350 ºC in *Model* conditions and does not achieve it in *Industrial* conditions. The harder conditions (5-fold higher space velocity) were chosen in order to avoid the maximum permitted conversion, which widens the reaction temperature window, and therefore, allowing a proper study of the ionic conductor effect. Thus, this effect should be noticeable. Moreover, pointing to future applicability in mobile devices, the favourable effect of proton conductor addition is interesting indeed at high space velocity.

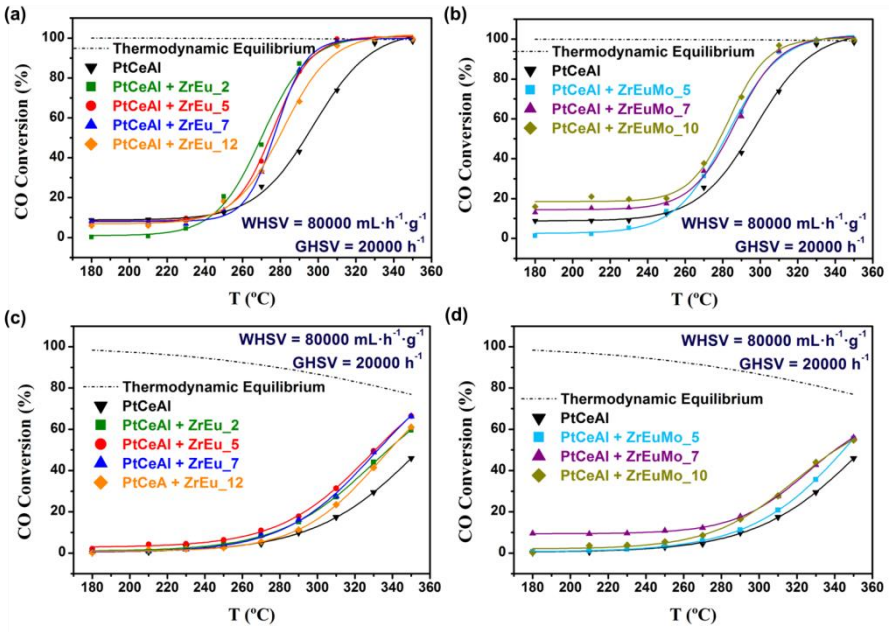

Figure 5.1 Catalytic activity of PtCeAl catalyst and ionic conductor systems (mass ratio 1:5) in WGS reaction in Model conditions (4.5 % CO, 30 % H_2O in N_2) –a and b – and in Industrial conditions (9 % CO, 30 % H_2O, 11 % CO_2 and 50 % H_2) –c and d. GHSV = 20000 h^{-1}. WHSV = 80000 $mL \cdot h^{-1} \cdot g_{cat}^{-1}$. The amount of PtCeAl catalyst in all tests was 0.1 g.

Mixing the PtCeAl catalyst with proton conductor results in higher CO conversions for all prepared series (ZrEu and ZrEuMo). It must be underlined that the CO conversion improvement starts at temperatures above 270 – 290 ºC. If in a rough approach we consider that kinetic control occurs at low temperature and diffusion control at higher temperatures it should be argued that the proton conductor just help in favouring the reactant diffusion step of the WGS reaction. It may be hypothesized that the presence of proton conductor more probably favours the water supply to the PtCeAl catalyst either dissociated or in molecular form. As the water availability increases higher CO conversions are attained. It must be pointed out that the

acceleration of the water activation step, whatever the WGS reaction mechanism, results in higher reaction rates. As the proton conductors by themselves show no activity in the WGS reaction (data not shown), the higher WGS activity exhibited by the catalytic systems which include proton conductors, may indicate that the ionic conductor only acts as a water-enhancer at the service of the catalyst. This ionic conductor concept was recently proven on studying the effect of several ionic conductors on different catalytic systems operating under different mechanisms. This work was patented by our research group[35] and revealed an evident promoter effect in the temperature range in which the activity of the catalyst starts to be appreciable. Therefore, whatever the catalyst or ionic conductor nature, the latter helps the water activation according to the proper catalyst mechanism. Regarding the tests in *Industrial* feed, the conductor' promoter effect is also observable (Figure 5.1 c) and d), thereby supporting the conclusion that the promoter effect is related to the water activation step in the reaction mechanism and not to the reaction conditions, again being noticeable when the catalytic activity start to be appreciable.

As demonstrated in Chapter 4, in the RT-300ºC temperature range the conductivity of the mixed oxide proton conductors is significantly enhanced in the presence of water. The surface presence of Zr-O-Eu sites determines that type II hydroxyl were possible in cubic ZrO_2 based solid solution phases. Moreover, molecular water remains adsorbed on the proton conductor surface favouring a Grotthuss-like mechanism which increases the total conductivity in this temperature range. According to this, the ionic conductors increase the CO

conversion activity of the catalyst by increasing water concentration close to Pt sites. The proton conductor helps the water activation whatever the catalyst, the feed or the ionic conductor nature. In this way all differences in terms of activity within the series (Figure 5.1) only depend on the characteristics of the proton conductors. This is confirmed by the lower promoter effect observed for the ZrEu_12 sample on the WGS activity (Figure 5.1a). This sample results in small water activation effect indeed as proton conductor; this is in good agreement with its conductivity analysis by impedance spectroscopy (Chapter 4). The meaningfully lower conductivity and higher activation energy of ZrEu_12 sample is reflected in significantly lower activity of the PtCeAl + ZrEu_12 system than for the rest of samples (ZrEu_2, ZrEu_5 and ZrEu_7 samples). On the other side, ZrEu_2, ZrEu_5 and ZrEu_7 samples show similar conductivities, especially in the WGS reaction operation temperature range. This result is also mirrored in the catalytic tests, where higher CO conversions in *Model* and *Industrial* conditions are observed for these PtCeAl proton conductor coupled systems. No clear differences between these three samples are observed indicating again that the WGS activity promotion is related to the conducting properties of the added proton conductors.

Moreover, no clear effect on molybdenum addition is observed. Similar tendencies are obtained on increasing the Mo content and from this point only the ZrEuMo_5 sample will be further studied. In addition, ionic conductors and diluent quartz were tested in WGS reaction in the same conditions without catalyst in contemplation of verifying their catalytic inactivity. These results support again the

role of the proton conductors as water-enhancer species but not as active catalysts by themselves.

Furthermore, different parameters like catalyst/ionic conductor ratio and the space velocity have been studied. For this analysis, the samples ZrEu_5 and ZrEuMo_5 have been chosen, being the former with the highest conductivity between its series and also the bare formulation of the Mo-series. The variation of the catalyst/ionic conductor ratio for these two samples (ZrEu_5 and ZrEuMo_5) and its influence on the catalytic activity, starting with 1:5 as the reference and decreasing the conductors' quantity is presented in Figure 5.2. In terms of CO conversion, the ratio 1:1 seems to be the optimal for the PtCeAl + ZrEu_5 sample. On the contrary, the mixture of the PtCeAl catalyst with ZrEuMo_5 conductor requires a mass ratio of 1:2 to achieve a maximal activity in both *Model* and *Industrial* feeding. These observations indicate that the proton conductor in the reference mixtures (ratio 1:5) is in excess. Then, less amount of proton conductor would be necessary and, consequently, smaller reactor volume and/or higher space velocity are possible.

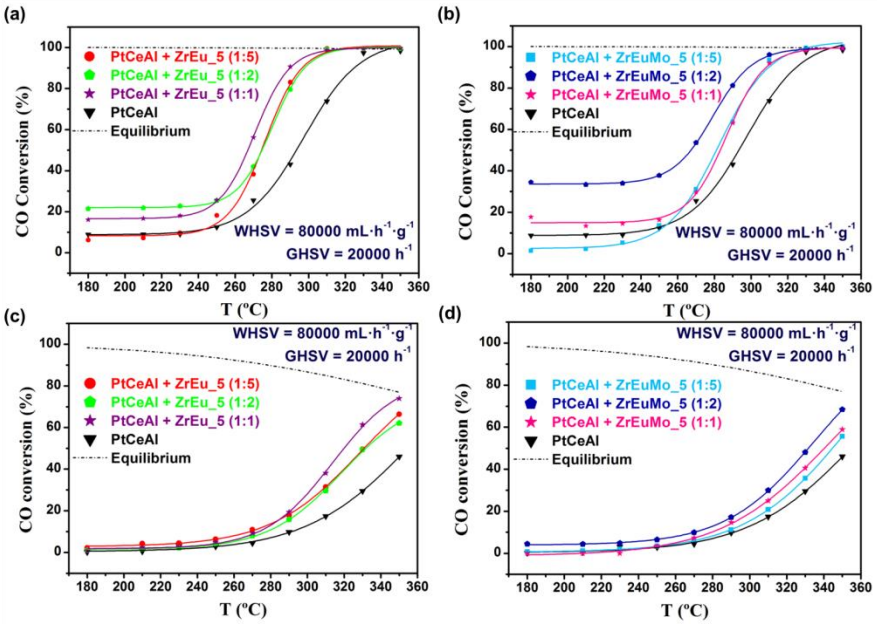

Figure 5.2 Catalyst/Conductor mass ratio influence on the catalytic activity for PtCeAl + ZrEu_5 and PtCeAl + ZrEuMo_5 samples in WGS; Model conditions (4.5 % CO, 30 % H_2O in N_2) –figures a and b – and Industrial conditions (9 % CO, 30 % H_2O, 11 % CO_2 and 50 % H_2) – figures c and d. GHSV = 20000 h^{-1}. WHSV = 80000 $mL \cdot h^{-1} \cdot g_{cat}^{-1}$. The amount of PtCeAl catalyst in all tests was 0.1 g.

Some catalytic systems (figures 5.2a and 5.2b) show unexpectedly high CO conversion at low temperatures (below 250 ºC) in *Model* conditions. The apparent consumption of CO is believed to be due to gas adsorption on the samples, since the formation of CO_2 was not observed indicating the absence of WGS reaction.

Finally, both samples were also tested at different space velocities maintaining the reference mass ratio of 1:5 (Figure 5.3). As for the other tests, the behaviour of the systems in WGS depends firstly on the feeding conditions and then on space velocity (in terms of WHSV). In *Model* conditions, where only CO and water are

introduced, the Mo-contained sample shows minor decrease of activity on increasing the WHSV. This can be explained by the promotional effect of Mo oxide presence and the available higher water concentration for ZrEuMo_5 sample respect to the ZrEu_5 provided by superficial Mo oxide as it was discussed in previous chapters. Thus, besides the contained/supplied water by ZrEu_5 material, the superficial Mo oxide also can adsorb more water in its structure. In *Industrial* conditions, the behaviour is similar for both samples. However, at higher space velocity the decrease of activity shown by Mo-contained sample is more significant. This fact can be explained by the fast adsorption of H_2 on Mo oxide thus reducing its water-enhancement effect. This observation is in good agreement with the H_2-TPR analysis for those samples.

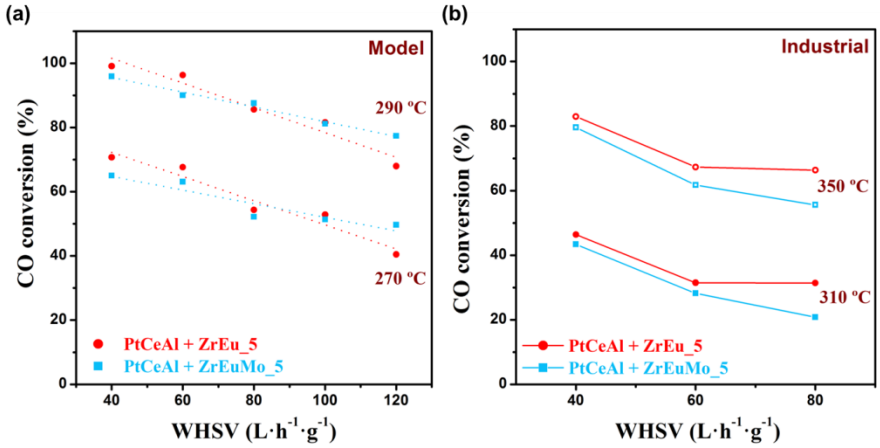

Figure 5.3 WHSV influence on the activity of the PtCeAl + ZrEu_5 and PtCeAl + ZrEuMo_5. Mass ratio of 1:5 at different temperatures in both feeding conditions: (a) Model conditions (4.5 % CO, 30 % H_2O in N_2) and (b) Industrial conditions (9 % CO, 30 % H_2O, 11 % CO_2 and 50 % H_2). The amount of PtCeAl catalyst in all tests was 0.1 g.

5.3. WGS Reaction on Structured Catalysts

Structured catalysts were also tested in WGS reaction in the same conditions as powdered samples with the same catalyst charge (0.1 g of PtCeAl in all cases). The use of structured catalyst will also clarify if the activity improvement observed in the presence of proton conductor is due to thermal and/or dilution effect or, indeed, is caused by the conducting effect on the reaction mechanism. Moreover, as mentioned before, the use of metallic micromonoliths provides good thermal conductivity and higher exposed surface for the same amount of catalyst due to the thin catalyst layer where mass transfer problems should be neglected.

Specifically, two structured catalysts, bare PtCeAl and physically mixed with ZrEuMo_5 in 1:5 mass ratio, were prepared. The metallic micromonolith manufacturing, the slurry optimization, the catalyst impregnation and the elemental characterization of the structured catalyst are shown below.

5.3.1. Metallic micromonoliths manufacture and preparation of the slurry.

Metallic Fecralloy foils 0.05 mm in thickness were used for the micromonoliths manufacturing (see Chapter 2). This material is normally used because of the facility to produce a superficial alumina layer after some thermal pre-treatment, which improves the adhesion of the catalyst.[36] As described in Chapter 2, the clean metallic sheets (flat and corrugated) were co-rolled together to result in cylindrical metallic micromonoliths of 17 mm in diameter and 30 mm in height with calculated cell density of 1588 cpsi and an exposed surface of

540 cm^2. The cleaned micromonoliths were calcined in air for 22 h at 900 ºC to create the α-Al_2O_3 layer on the metallic surface formed by segregation from the bulk material. This layer improves the porosity and the contact surface of the micromonolith and, consequently, helps the catalyst adhesion.[37,38] This manufacture procedure (Figure 5.4) has been studied and optimized by Martinez *et al.*[18,38–40]

The impregnation of the catalyst was carried out by washcoating or dip coating processes.[31,36,41] Once the slurry with the catalyst was prepared, the micromonolith was completely immersed at constant velocity of 3 $cm \cdot min^{-1}$ and submerged for a minute and then emerged at the same velocity of 3 $cm \cdot min^{-1}$. The slurry excess was removed by air blowing to liberate the channels and to avoid clogging. The impregnated micromonolith was dried at 100 ºC for 30 minutes and the impregnation process was repeated until the desired amount of catalyst was loaded. Then final structured catalyst was calcined at the same conditions as the original catalyst powder with lower rate of 2 $ºC \cdot min^{-1}$ in order to recondition the catalyst without creating porosity or fissures in the catalytic layer.[39]

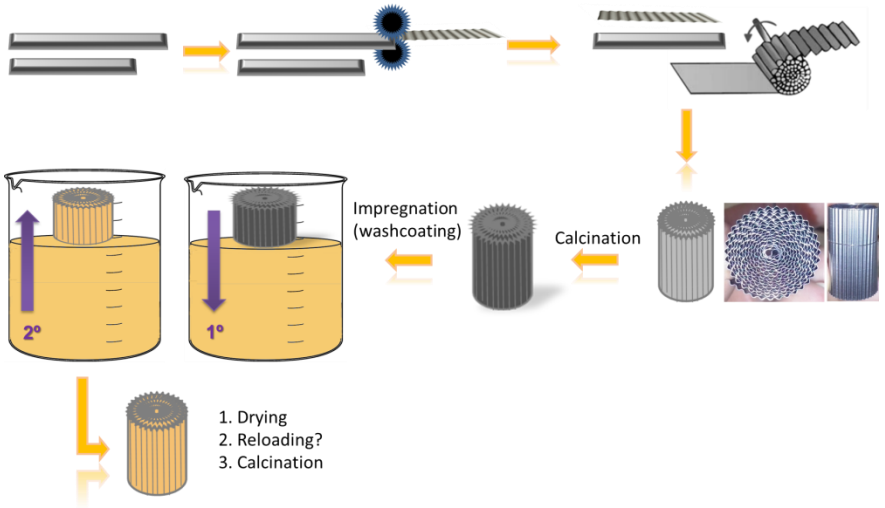

Figure 5.4 Scheme of the micromonolith manufacture and catalyst impregnation process.

Before impregnation, the slurry preparation was optimized regarding the viscosity and the Z potential of the suspension. The optimization of the slurry has the aim to avoid particles agglomeration and to help the obtaining of well-controlled homogeneous thin layer over the micromonolith walls which prevents diffusional problems, catalyst loss, fractures or peeling. The main variables to control are solids' particle size, and viscosity and pH of the slurry.[41,42] The solid samples were grinded with ZrO_2 balls at 500 rpm 15 min and at 200 rpm 10 min for PtCeAl and ZrEuMo_5 sample, respectively (Retsch PM100 instrument). The desired sizes according to the literature should be around 10 µm or less.[41,42] The resulting particle sizes were measured by laser diffraction (LD) of the colloidal system dispersed in deionized water with a MALVERN MasterSizer instrument. The particle size distributions were fitted to a

Gaussian curve and the D[0,5] and D[4,3] are summarized in Table 5.1. As presented in the table the milling condition resulted in particle sizes rounding the limiting value of 10 μm.

Table 5. 1 Milling conditions and meaured particle size.

Sample	Milling conditions	Particle size (μm)
PtCeAl	500 rpm – 15 min	D[0,5] = 3.72 D[4,3] = 14.12
ZrEuMo_5	200 rpm – 10 min	D[0,5] = 6.54 D[4,3] = 11.09

The Z potential curves for the samples (Figure 5.5a) have been fitted to a Boltzmann equation. The solids present Z potential within the 6 – 8 pH range indicating that for a stable slurry the pH of the suspension must be far from this range. In addition, the viscosity of the slurry was analysed at different stirring velocities. The same variation of the viscosity was observed for both slurries, being the value obtained at 250 rpm around 2.5 cp lower to the optimally suggested according to literature of 5 cp.[42] These data correspond to the final slurry formulation using only colloidal alumina (Nyacol ®) as additive, whose role is to help the adhesion of the catalyst. The summary of the measured pH and viscosities of each slurry is reported in Figure 5.5 and Table 5.2.

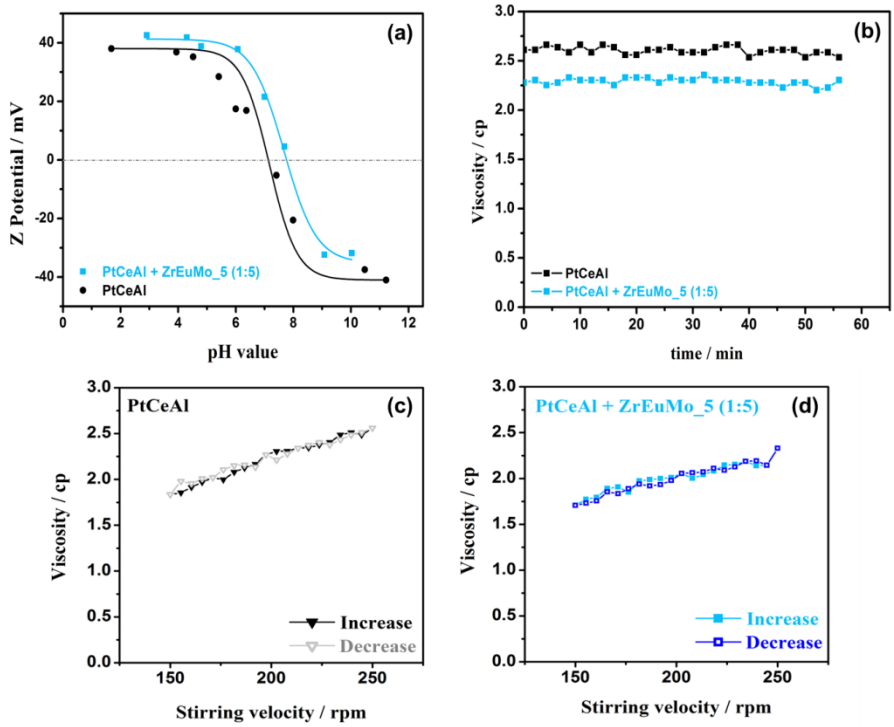

Figure 5.5 Properties of the prepared slurries: Z potential curves (a), viscosity at 250 rpm. (b), and viscosity on increasing the stirring velocity for PtCeAl sample (d) and for PtCeAl + ZrEuMo_5 (1:5) sample.

Table 5.2 Properties of the prepared slurries.

Colloidal sample (slurry)	pH* (Z pot. = 0)	pH slurry	Viscosity slurry (cp)
PtCeAl	7.12	5.35	2.6
PtCeAl + ZrEuMo_5 (1:5)	7.77	3.87	2.2

**pH at zero Z potential of the colloidal suspension (Figure 5.5).*

The used final slurry formulation was 80 wt.% of deionized water, 6 wt.% of commercial aqueous solution of Al_2O_3 (20 wt.% of

alumina, Nyacol) and 14 wt.% of sieved catalyst below 50 µm. Prior use, the slurry was aged effectively in a closed vessel for 24 h under continuous stirring.

5.3.2. Characterization of structured catalysts.

According to the optimal slurry formulation and the impregnation method detailed above, two structured catalysts were prepared (PtCeAl catalyst, labelled m_PtCeAl and 1:5 physical mixture of PtCeAl + ZrEuMo_5, labelled m_PtCeAl+ZrEuMo_5, both corresponding to 0,1 g PtCeAl catalyst load). These samples were posteriori characterized and compared to the original powders.

After the washcoating process, the remaining slurries were dried and calcined in the same conditions as loaded micromonoliths. The calcined slurries were analysed by XRD to compare them with the original powders and to observe if any modification during the coating process occur. The intensities and positions of the diffraction peaks for both samples (PtCeAl and the PtCeAl + ZrEuMo_5 mixture) are not modified by the slurry preparation and all present phases are preserved for the structured catalysts as expected (Figure 5.6).

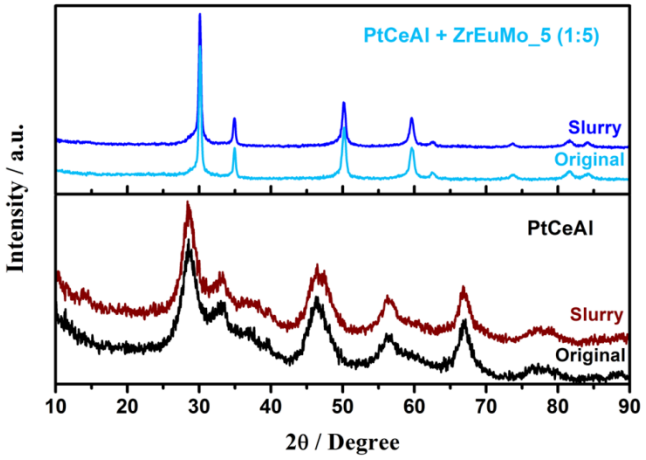

Figure 5.6 XRD of dried and calcined slurry after impregnation process. Comparison with the original powdered samples.

The structured catalysts were analysed by N_2 adsorption (Table 5.3). A slight increase of the specific surface of the monolithic m_PtCeAl catalyst in respect to the original powder (see chapter 3) was observed, due to the addition of colloidal alumina for the slurry stabilization. The specific surface of the structured m_PtCeAl+ZrEuMo_5 sample was compared to the calculated value for the original powders (PtCeAl and ZrEuMo_5, chapter 3) and considering a mass proportion of 1:5. The calculated values are 80 m^2/g of S_{BET}, 0.09 cm^3/g of porous volume and 3.473 nm of porous diameter. Therefore, m_PtCeAl+ZrEuMo_5 sample (Table 5.3) almost preserved its S_{BET} after the impregnation process being detected insignificant increase of the average pore size. Regarding the pore size distribution of the structured sample (Figure 5.7), two pore size contributions are clearly distinguished, one at ~3 nm and another at ~8 nm. Both fractions correspond to the initial pore sizes found for

the original ZrEuMo_5 and PtCeAl powders, respectively (Chapter 3).

Table 5.3 Textural properties of the structured catalysts.

Structured sample	S_{BET} (m^2/g)	V_p (cm^3/g)	$Ø_p$ (nm)
m_PtCeAl	134	0.24	7.0
m_PtCeAl+ZrEuMo_5 (1:5)	85	0.15	5.3

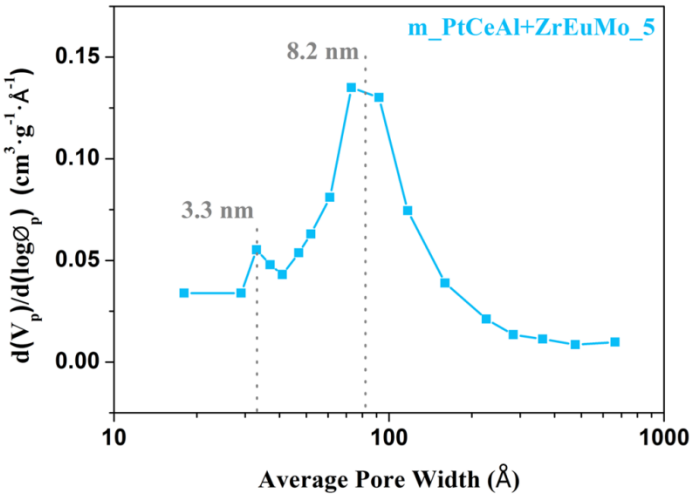

Figure 5.7 Pore size distribution of structured m_PtCeAl+ZrEuMo_5 sample calculated by BJH desorption method.

Finally, scanning electron microscopy (SEM) technique was used to observe the homogeneity and thickness of the catalytic layer on micromonolith. In Figure 5.8a SEM image of the manufactured

micromonolith after thermal treatment and before the catalytic layer impregnation is shown, where the characteristic needle-like shape alumina layer is identified.[36,37] In Figure 5.8b, the transversal cross section of the m_PtCeAl+ZrEuMo_5 sample is presented where the measurement of the layer reveals *c.a.* 3 µm in thickness, in good concordance with the calculated theoretical layer (Table 5.4) and comparable to other reported similar structured catalysts.[18] Thickness theoretical calculations are based on the compact structure density, the textural properties (porosity and BET surface of the sample), the exposed surface of the micromonolith (540 cm^2) and the used catalyst loading. The m_PtCeAl+ZrEuMo_5 sample presents the highest loading and consequently its layer is thicker. Thus, both structured catalysts present active layers below 3 µm, which allows us to neglect possible diffusional problems, in agreement with other studies, where such problems become important within the 10 - 20 µm range thickness.[43,44] Farrauto *et al.* also reported similar structured catalysts for WGS reaction with no diffusional limitations.[1]

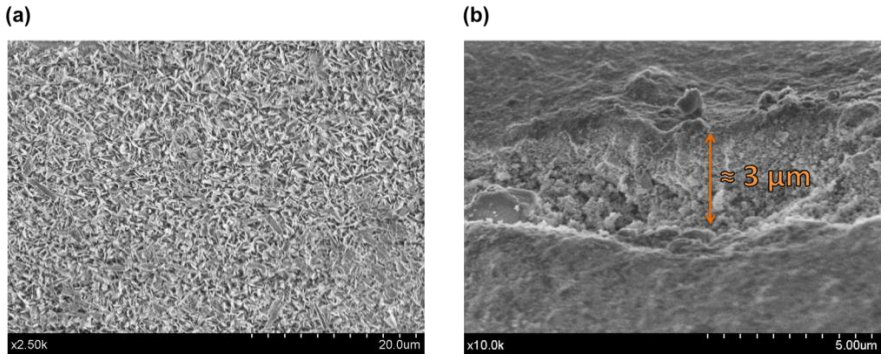

Figure 5.8 SEM images of (a) the created α-Al_2O_3 layer of the pre-treated micromonolith and (b) catalytic layer thickness observed by the transversal section of the m_PtCeAl+ZrEuMo_5 sample loaded on the micromonolith.

Table 5.4 Properties of structured samples.

Structured Sample	Catalyst loading (g)	Theoretical thickness of the catalytic layer (µm)	Adherence (%)*
m_PtCeAl	0.1281	0.881	94.46
m_PtCeAl+ZrEuMo_5 (1:5)	0.5482	2.778	94.44

** Adherence (weight percentage) calculated by the difference between the catalyst loading before and after the adherence test on the structured catalysts.*

Finally, the structured catalysts were subjected to an adherence test based on the one proposed by Yasaky *et al.*[45] Concretely, the monolithic catalysts were immersed in acetone bath under ultrasonic frequency for 30 min. The adherence based on the difference in weight of the loading on the micromonolith measured before and after the adherence test is summarized in Table 5.4. The weight losses (around 5%) are acceptable and comparable to those studied by Frias *et al.*[36] for loadings around 0.1 g of catalyst over AISI 304 and Fecralloy supports.

5.3.3. Catalytic tests in WGS reaction.

The WGS experiments over both structured samples were carried out in the conditions of the powdered catalysts, i.e. space velocity (WHSV) of 80000 $ml \cdot h^{-1} \cdot g_{cat}^{-1}$ using 0.1 g of PtCeAl catalyst, from 180 to 350 ºC in *Model* and the *Industrial* conditions previously described.

Similarly to powdered samples, the structured m_PtCeAl+ZrEuMo_5 catalyst shows higher activity in terms of CO conversion compared to m_PtCeAl sample (Figure 5.9). Considering that the better thermal conductivity of the metallic support evite the formation of the hot-spots, and also that the obtained thin catalytic layer evite the diffusional problems, the positive effect on activity is indeed due only to proton conductivity. Actually, the m_PtCeAl+ZrEuMo_5 catalyst shows the highest activity of all studied samples, powders and micromonoliths, in *Industrial* conditions. This significant influence can be explained by the better contact between the reactant flow and structured catalyst where the entire catalytic layer is available for the reaction, thereby increasing the effect of the proton conductor.

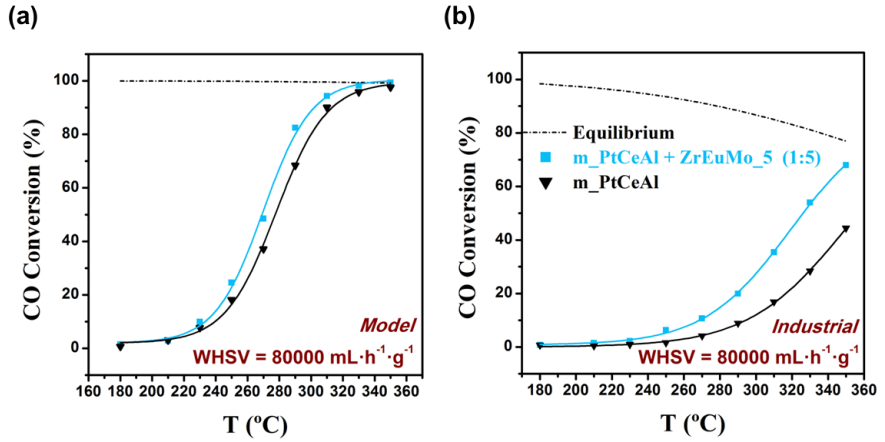

Figure 5.9 WGS activity of structured catalysts in (a) Model Conditions (4.5 % CO, 30 % H_2O in N_2) and (b) in Industrial Conditions (9 % CO, 30 % H_2O, 11 % CO_2 and 50 % H_2). WHSV = 80000 mL·h^{-1}·g$_{cat}^{-1}$.

As described in Chapter 4, the bare ZrEu_5 sample (without Mo) displays proton conductivity below ~320 ºC and is not reduced under

H_2 flow. On the other hand, the ZrEuMo_5 sample can provide higher amount of adsorbed water and, also, can create bronzes and hydrated bronzes at higher temperatures under H_2 flow according to the literature and to the features presented in Chapter 3.[46–50] In fact, the H_2-TPR experiments (see Chapter 3, Figure 3.20) show H_2 consumption from ~200 ºC, which more likely influences catalyst' performance. Since the main difference between *Model* and *Industrial* conditions is the presence of 50 % of H_2 in the inlet flow, a notable effect on Mo containing sample is expected and actually observed. A significant increment of CO conversion in *Industrial* conditions on m_PtCeAl+ZrEuMo_5 catalyst is detected. Moreover, the beneficial effect of the proton conductivity over 300 ºC for Mo-doped sample cannot be excluded although its measurement has been impossible in our experimental set-up.

5.4. Stability of the Catalysts

As the m_PtCeAl+ZrEuMo_5 sample shows the best activity and will be used for kinetic analysis, its stability under WGS *Industrial* conditions have to be studied. The stability test temperature was fixed to 330 ºC, where the CO conversion is around 50 % ensuring the complete use of active sites and distinguishable changes in catalyst' activity. For comparison, powdered PtCeAl sample in the same conditions (Figure 5.10) was carried out.

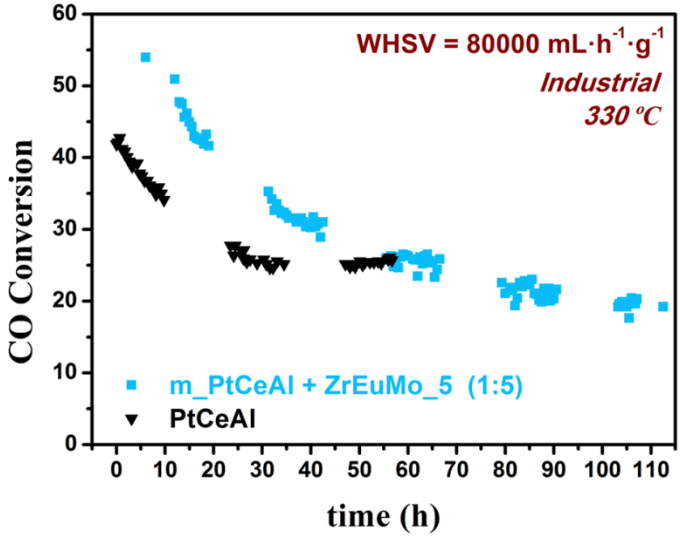

Figure 5.10 Stability of the catalysts measured at 330 ºC in Industrial conditions (9 % CO, 30 % H_2O, 11 % CO_2 and 50 % H_2) and space velocity (WHSV) of 80000 mL·h^{-1}·g_{cat}^{-1}.

Fast deactivation of the sample is observed, 50% loss of the initial CO conversion occurs. It is believed that this process is associated to the deactivation of the PtCeAl catalyst by itself as the same trend is observed for both samples. Comparing the structured and powdered unpromoted catalyst, the deactivation plots show the same profile with the same deactivation velocity, suggesting that the catalyst loses activity no matter the presence of promoter. The later suggests that the deactivation process occurs over the catalyst and it is not influenced by WGS mechanism alteration. And effectively the major drawback of the precious metal-based catalysts for WGS reaction is their deactivation.[2] Several authors pointed out CeO_2 support sintering and Pt particles occlusion and metal active surface decrease as deactivation factors[51,52] meanwhile other reflect on active sites hindering by formed carbonaceous species during the reaction.[53,54]

However, the alumina helps in keeping ceria an Pt particles small and dispersed.[2,55] Thus, the most significant deactivation factor for these catalysts should be the formation of carbonate species which remain adsorbed on the surface altering the water activation sites. The latter is confirmed by the different inductive time for deactivation present by the PtCeAl catalyst and the m-PtCeAl+ZrEuMo_5 catalyst. A difference of 6 to 7 hours is observed which could indicate that the proton conductor supplies more effectively activated water species in comparison to the bare catalyst. Then, the proton conductor by itself is not as efficient as ceria surface and the blocking of the later with carbonaceous species continues to deactivate the catalyst in the same manner as bare PtCeAl sample. Nevertheless the PtCeAl+ZrEuMo_5 catalyst still provides higher activity until achieving the stable state. When the catalyst deactivates, hardly differences occur no matter the involved sample. Two different situations can be summarized: the proton conductor is also deactivated as the ceria support is, thereby getting m_PtCeAl+ZrEuMo_5 sample the same activity as PtCeAl, or the effect of the proton conductor is unappreciable because of the low activity of the proper catalyst (~20 % of CO conversion).

Several authors report good stability of the cubic-type ionic conductors under WGS experimental conditions. Zhang *et al.*[56] studied the stability of fluorite-type $La_2Ce_2O_7$ under wet conditions and found that a pressure of 1 GPa is necessary to modify the structure. Moreover, the introduction of Zr was reported to enhance the stability of the ionic conductors.[57,58] Joulia *et al.*[59] observed good stabilities of $Re_2Zr_2O_7$ conductor under both, reducing and oxidant atmospheres at high temperatures. In addition, previously to these

catalytic tests, some repetitions of IS measurements were carried out with sintered ZrEu_5 sample exhibiting the same behaviour. Furthermore, the powdered ZrEu_5 sample was also analysed by XRD before and after wet atmosphere simulating the IS experiments conditions getting the same diffractograms (data not shown).

Therefore, and considering that the proton conductors no matter its nature do not changes during the reaction, the deactivation of the m-PtCeAl+ZrEuMo_5 sample can be mainly attributed to the carbonate species formation. Their possible formation will be analysed by *operando* studies by DRIFTS in WGS reaction conditions and the results commented in the next chapter.

5.5 Partial Conclusions

The catalytic experiments in WGS reaction show that the presence of ionic conductor always increases the activity of the reference PtCeAl catalyst in terms of CO conversion, being the benefit in good agreement with sample' proton conductivity observed by IS. Thus, higher the conductivity higher the observed CO conversion. Moreover, the beneficial effect only appears when the catalyst starts to work, thereby acting as a promoter of the catalyst' proper mechanism in the WGS reaction. The role of proton conductors is then the promotion of the water activation step.

The change of the catalyst / ionic conductor ratio show that the activity promotion could occur at lower proton conductor charge. On the other side, the variation of the space velocity reveals different behaviours for Mo-doped and undoped materials in *Model* and

Industrial conditions, due to the important interaction of the present inlet H_2 with Mo oxide.

Finally, structured m-PtCeAl+ZrEuMo_5 sample provides the highest activity in *Industrial* conditions. This sample has been then chosen for kinetic analysis as well as for *operando* studies. Before them the stability of the sample has been tested and shows fast deactivation probably due to the carbonate species formation.

REFERENCES

1. Farrauto, R. J. *et al.* Precious Metal Catalysts Supported on Ceramic and Metal Monolithic Structures for the Hydrogen Economy. *Catal. Rev. Sci. Eng.* **49,** 141–196 (2007).

2. Ratnasamy, C. & Wagner, J. P. Water Gas Shift Catalysis. *Catal. Rev. Sci. Eng.* **51,** 325–440 (2009).

3. Ladebeck, J. R. & Wagner, J. P. in *Handbook of Fuel Cells – Fundamentals, Technology and Applications* (eds. Vielstich, W., Lamm, A. & Gasteiger, H. A.) **3,** 190–201 (John Wiley & Sons, Ltd., 2003).

4. Phatak, A. A. *et al.* Kinetics of the water-gas shift reaction on Pt catalysts supported on alumina and ceria. *Catal. Today* **123,** 224–234 (2007).

5. Koryabkina, N. A., Phatak, A. A., Ruettinger, W. F., Farrauto, R. J. & Ribeiro, F. H. Determination of kinetic parameters for the water-gas shift reaction on copper catalysts under realistic conditions for fuel cell applications. *J. Catal.* **217,** 233–239 (2003).

6. Kam, R., Scott, J., Amal, R. & Selomulya, C. Pyrophoricity and stability of copper and platinum based water-gas shift catalysts during oxidative shut-down/start-up operation. *Chem. Eng. Sci.* **65,** 6461–6470 (2010).

7. Luengnaruemitchai, A., Osuwan, S. & Gulari, E. Comparative

studies of low-temperature water-gas shift reaction over Pt/CeO2, Au/CeO2, and Au/Fe2O3 catalysts. *Catal. Commun.* **4,** 215–221 (2003).

8. Panagiotopoulou, P. & Kondarides, D. I. Effect of the nature of the support on the catalytic performance of noble metal catalysts for the water-gas shift reaction. *Catal. Today* **112,** 49–52 (2006).

9. Panagiotopoulou, P. & Kondarides, D. I. Effect of morphological characteristics of TiO2-supported noble metal catalysts on their activity for the water-gas shift reaction. *J. Catal.* **225,** 327–336 (2004).

10. Basinska, A., Maniecki, T. P. & Józwiak, W. K. Catalytic Activity in Water-Gas Shift Reaction of Platinum Group Metals Supported on Iron Oxides. *React. Kinet. Catal. Lett.* **89,** 319–324 (2006).

11. Vignatti, C., Avila, M. S., Apesteguía, C. R. & Garetto, T. F. Catalytic and DRIFTS study of the WGS reaction on Pt-based catalysts. *Int. J. Hydrogen Energy* **35,** 7302–7312 (2010).

12. Yang, M. *et al.* A Common Single-Site Pt(II)-O(OH)x- Species Stabilized by Sodium on 'active' and 'inert' Supports Catalyzes the Water-Gas Shift Reaction. *J. Am. Chem. Soc.* **137,** 3470–3473 (2015).

13. Kalamaras, C. M., Dionysiou, D. D. & Efstathiou, A. M. Mechanistic Studies of the Water–Gas Shift Reaction over Pt/CexZr1– xO2 Catalysts: The Effect of Pt Particle Size and Zr Dopant. *ACS Catal.* **2,** 2729–2742 (2012).

14. Grenoble, D. C., Estadt, M. M. & Ollis, D. F. The Chemistry and Catalysis of the Water Gas Shift Reaction. *J. Catal.* **67,** 90–102 (1981).

15. Germani, G. & Schuurman, Y. Water-Gas Shift Reaction Kinetics Over micro-Structured Pt/CeO2/Al2O3 Catalysts. *AIChE* **52,** 1806–1813 (2006).

16. Andreeva, D. *et al.* Gold based catalysts on ceria and ceria-alumina for WGS reaction (WGS Gold catalysts). *Top. Catal.*

44, 173–182 (2007).

17. Rodriguez, J. A., Liu, P., Hrbek, J., Evans, J. & Pérez, M. Water Gas Shift Reaction on Cu and Au Nanoparticles Supported on CeO2(111) and ZnO(0001): Intrinsic Activity and Importance of Support Interactions. *Angew. Chemie - Int. Ed.* **46,** 1329–1332 (2007).

18. González-Castaño, M. *et al.* Structuring Pt/CeO2/Al2O3 WGS catalyst: Introduction of buffer layer. *Appl. Catal. B Environ.* **200,** 420–427 (2017).

19. Olympiou, G. G., Kalamaras, C. M., Zeinalipour-Yazdi, C. D. & Efstathiou, A. M. Mechanistic aspects of the water-gas shift reaction on alumina-supported noble metal catalysts: In situ DRIFTS and SSITKA-mass spectrometry studies. *Catal. Today* **127,** 304–318 (2007).

20. Kalamaras, C. M., Petallidou, K. C. & Efstathiou, A. M. The effect of La3+-doping of CeO2 support on the water-gas shift reaction mechanism and kinetics over Pt/Ce1-xLaxO2-delta. *Appl. Catal. B-Environmental* **136-137,** 225–238 (2013).

21. Smith R.J., B., Loganathan, M. & Shekhar Shantha, M. A Review of the Water Gas Shift Reaction Kinetics. *Int. J. Chem. React. Eng.* **8,** 1–32 (2010).

22. Grabow, L. C., Gokhale, A. A., Evans, S. T., Dumesic, J. A. & Mavrikakis, M. Mechanism of the water gas shift reaction on Pt: First principles, experiments, and microkinetic modeling. *J. Phys. Chem. C* **112,** 4608–4617 (2008).

23. Clay, J. P., Greeley, J. P., Ribeiro, F. H., Delgass, W. N. & Schneider, W. F. DFT Comparison of Intrinsic WGS Kinetics over Pd and Pt. *J. Catal.* **320,** 106–117 (2014).

24. Phatak, A. A., Delgass, W. N., Ribeiro, F. H. & Schneider, W. F. Density Functional Theory Comparison of Water Dissociation Steps on Cu, Au, Ni, Pd, and Pt. *J. Phys. Chem. C* **113,** 7269–7276 (2009).

25. Madon, R. J. *et al.* Microkinetic analysis and mechanism of the water gas shift reaction over copper catalysts. *J. Catal.* **281,** 1–

11 (2011).

26. Huang, S.-C., Lin, C.-H. & Wang, J.-H. Trends of Water Gas Shift Reaction on Close-Packed Transition Metal Surfaces. *J. Phys. Chem. C* **114,** 9826–9834 (2010).

27. Gokhale, A. A., Dumesic, J. A. & Mavrikakis, M. On the Mechanism of Low-Temperature Water Gas Shift Reaction on Copper. *J. Am. Chem. Soc.* **130,** 1402–1414 (2008).

28. Zhao, Z.-J. *et al.* Importance of metal-oxide interfaces in heterogeneous catalysis: A combined DFT, microkinetic, and experimental study of water-gas shift on Au/MgO. *J. Catal.* **345,** 157–169 (2017).

29. Tonkovich, A. L. Y., Zilka, J. L., LaMont, M. J., Wang, Y. & Wegeng, R. S. Microchannel reactors for fuel processing applications. I. Water gas shift reactor. *Chem. Eng. Sci.* **54,** 2947–2951 (1999).

30. González-Castaño, M. *et al.* O2-assisted Water Gas Shift reaction over structured Au and Pt catalysts. *Appl. Catal. B Environ.* **185,** 337–343 (2016).

31. Milt, V. G. *et al.* Au/TiO2 supported on ferritic stainless steel monoliths as CO oxidation catalysts. *Appl. Surf. Sci.* **270,** 169–177 (2013).

32. Govender, S. & Friedrich, H. B. Monoliths: A Review of the Basics, Preparation Methods and Their Relevance to Oxidation. *Catalysts* **7,** 1–29 (2017).

33. Gonzalez Castaño, M., Reina, T. R., Ivanova, S., Centeno, M. A. & Odriozola, J. A. Pt vs. Au in water-gas shift reaction. *J. Catal.* **314,** 1–9 (2014).

34. Dupont, N. *et al.* Specificities of micro-structured reactors for hydrogen production and purification. *Int. J. Hydrogen Energy* **32,** 1443–1449 (2007).

35. Odriozola, J. A. *et al.* Spanish Patent ES 2 595 937 A1 'Complejo catalítico conformado por la mezcla de catalizador y conductor iónico'. 1–17 (2017).

36. Frías, D. M. *et al.* Nucleation and growth of manganese oxides on metallic surfaces as a tool to prepare metallic monoliths. *Appl. Catal. A Gen.* **325,** 205–212 (2007).

37. Domínguez, M. I., Pérez, A., Centeno, M. A. & Odriozola, J. A. Metallic structured catalysts: Influence of the substrate on the catalytic activity. *Appl. Catal. A Gen.* **478,** 45–57 (2014).

38. Martínez T., L. M. *et al.* Preparation of Au-CeO2 and Au-Al2O3/AISI 304 austenitic stainless steel monoliths and their performance in the catalytic oxidation of CO. *Chem. Eng. J.* **136,** 390–397 (2008).

39. Martínez T., L. M., Sanz, O., Domínguez, M. I., Centeno, M. A. & Odriozola, J. A. AISI 304 Austenitic stainless steels monoliths for catalytic applications. *Chem. Eng. J.* **148,** 191–200 (2009).

40. Martínez T., L. M., Sanz, O., Centeno, M. A. & Odriozola, J. A. AISI 304 austenitic stainless steel monoliths: Modification of the oxidation layer and catalytic coatings after deposition and its catalytic implications. *Chem. Eng. J.* **162,** 1082–1090 (2010).

41. Sanz, O., Echave, F. J., Romero-Sarria, F., Odriozola, J. A. & Montes, M. in *Renewable Hydrogen Technologies: Production, Purification, Storage, Applications and Safety* 201–224 (Elsevier B.V., 2013). doi:10.1016/B978-0-444-56352-1.00001-5

42. Almeida, L. C. *et al. Washcoating of metallic monoliths and microchannel reactors*. *Studies in Surface Science and Catalysis* **175,** (Elsevier B.V., 2010).

43. Laguna, O. H., González Castaño, M., Centeno, M. A. & Odriozola, J. A. Microreactors technology for hydrogen purification: Effect of the catalytic layer thickness on CuOx/CeO2-coated microchannel reactors for the PROX reaction. *Chem. Eng. J.* **275,** 45–52 (2015).

44. Potemkin, D. I., Snytnikov, P. V., Belyaev, V. D. & Sobyanin, V. A. Preferential CO oxidation over Cu/CeO2-x catalyst: Internal mass transport limitation. *Chem. Eng. J.* **176-177,**

165–171 (2011).

45. Yasaki, S., Yoshino, Y., Ihara, K. & Ohkubo, K. US Patent 5,208,206 Method of manufacturing an exhaust gas purifying catalyst. 1–10 (1993).

46. Adams, S. CDW Superstructures in Hydrogen Molybdenum Bronzes HxMoO3. *J. Solid State Chem.* **149,** 75–87 (2000).

47. Schöllhorn, R., Kuhlmann, R. & Besenhard, J. O. Topotactic redox reactions and ion exchange of layered MoO3 bronzes. *Mater. Res. Bull.* **11,** 83–90 (1976).

48. Schöllhorn, R., Schulte-Nölle, T. & Steinhoff, G. Layered intercalation complexes of the hydrogen bronze H0.5MoO3 with organic lewis bases. *J. Less-Common Met.* **71,** 71–78 (1980).

49. Krebs, B. The crystal structure of MoO3,2H2O: a metal aquoxide with both co-ordinated and hydrate water. *J. Chem. Soc. D Chem. Commun.* **0,** 50–51 (1970).

50. Ressler, T., Wienold, J. & Jentoft, R. E. Formation of Bronzes during Temperature-programmed Reduction of MoO3 with Hydrogen - An In situ XRD and XAFS Study. *Solid State Ionics* **141-142,** 243–252 (2001).

51. Wang, X., Gorte, R. J. & Wagner, J. P. Deactivation Mechanisms for Pd/Ceria during the Water–Gas-Shift Reaction. *J. Catal.* **212,** 225–230 (2002).

52. Ruettinger, W., Liu, X. & Farrauto, R. J. Mechanism of aging for a Pt/CeO2-ZrO2 water gas shift catalyst. *Appl. Catal. B Environ.* **65,** 135–141 (2006).

53. Hilaire, S., Wang, X., Luo, T., Gorte, R. J. & Wagner, J. A comparative study of water-gas-shift reaction over ceria-supported metallic catalysts. *Appl. Catal. A Gen.* **215,** 271–278 (2001).

54. Liu, X., Ruettinger, W., Xu, X. & Farrauto, R. Deactivation of Pt/CeO2 water-gas shift catalysts due to shutdown/startup modes for fuel cell applications. *Appl. Catal. B Environ.* **56,**

69–75 (2005).

55. Trueba, M. & Trasatti, S. P. γ-alumina as a support for catalysts: a review of fundamental aspects. *Eur. J. Inorg. Chem.* 3393–3403 (2005). doi:10.1002/ejic.200500348

56. Zhang, F. X., Tracy, C. L., Lang, M. & Ewing, R. C. Stability of fluorite-type La2Ce2O7 under extreme conditions. *J. Alloys Compd.* **674,** 168–173 (2016).

57. Lv, J., Wang, L., Lei, D., Guo, H. & Kumar, R. V. Sintering, chemical stability and electrical conductivity of the perovskite proton conductors BaCe0.45Zr0.45M0.1O3-delta (M = In, Y, Gd, Sm). *J. Alloys Compd.* **467,** 376–382 (2009).

58. Phair, J. W. & Badwal, S. P. S. Review of proton conductors for hydrogen separation. *Ionics (Kiel).* **12,** 103–115 (2006).

59. Joulia, A., Vardelle, M. & Rossignol, S. Synthesis and thermal stability of Re2Zr2O7, (Re=La, Gd) and La2(Zr1-xCex)2O7-δ compounds under reducing and oxidant atmospheres for thermal barrier coatings. *J. Eur. Ceram. Soc.* **33,** 2633–2644 (2013).

CHAPTER 6.

KINETICS AND *OPERANDO* STUDIES OF THE WGS REACTION

Abstract

The kinetics of the WGS reaction on powdered and micromonolithic catalysts have been studied. An associative Langmuir – Hinshelwood (L-H) mechanism is proposed and the data have been fitted to a hyperbolic kinetic equation. Mass diffusional problems are rejected since the estimated Thiele modulus is below 1 for powdered sample. In the same context, mass or thermal diffusional problems are also not considered in structured catalyst since the layer thickness is *ca.* 3 μm and the measured temperature profile along the monolith results in an isothermal behaviour during all tested conditions.

The obtained order of the water is meanly low in good agreement with the proposed promoter effect of the proton conductor on the rate-limiting step. The H_2 adsorption seems to be an important negative effect, which is besides modified by Mo reduction from 300 ºC.

The *operando* DRIFTS experiments support the coexistence of dissociated and physisorbed water for the Grotthuss' mechanism provided by the ZrEuMo_5 proton conductor, even for temperatures above 300 ºC.

6.1. INTRODUCTION

As it has been mentioned before, the WGS reaction mechanism as well as the role of the possible formed intermediates are still under discussion. In this regard, two general mechanisms are proposed depending on the catalysts and the reaction conditions. Accordingly, in the *redox* mechanism the adsorbed CO is oxidized to CO_2 by dissociated water or, in a bifunctional supported catalyst, by a labile oxygen from the support creating an oxygen vacancy. The support is then reoxidized by water leading to hydrogen formation.[1–4] On the contrary, the *associative* mechanism proceeds via carbonates, carboxylates or formates as intermediate species.[5–8] The adsorbed H_2O is dissociated and the terminal –OH interacts with adsorbed CO forming the different intermediates. The subsequent decomposition of this species leads to CO_2 and H_2 formation.

Not only the operating mechanism is under discussion. The role of the intermediates, this is, which one is a spectator or acts as an active specie, is also controversial. For instance, carboxyl species seem to be the most probable active intermediates since the energy barrier for its formation and further decomposition is lower than that for formates according to DFT (Density Functional Theory) analysis reported in the literature.[9–11] However, formates formation is normally observed during the WGS reaction in agreement with different FTIR, SSITKA or DRIFTS analysis.[3,12–14] Several authors proposed these species as simple spectators.[3,11,12] Others stand out the inactive role of the formates but ascribe them a deactivation function by blocking the active sites, mainly the water activation sites on the support.[3,11,12,15–17]

On the contrary, some authors defend an active role of the formates as intermediates[18,19] and some cases a secondary role having a small contribution have been reported, depending on the reaction conditions ~10 % of CO_2 may be produced through the formate pathway.[20,21]

In addition to this, the coexistence of the redox and associative mechanisms is also accepted by some authors.[9,13,22] Depending on the temperature and the composition of the feed one prevails over the other.[22–25] In the same context, the proposed rate-determining step is also uncertain and again varies with the experimental conditions. In any case, it is accepted that water dissociation requires to surpass high energy barriers whatever the mechanism is,[10,22,26,27] meaning a slow pathway. Moreover, the diffusion of the dissociated water and the availability of OH species to interact with adsorbed CO have been pointed out as a rate-limiting step.[3,28–30] Accordingly, partially reducible oxide as support and the creation of oxygen vacancies have been reported to enhance the water dissociation and the amount of available OH species providing higher WGS reaction rates and better catalyst' performances, not only to improve the water activation step, but also to favour the decomposition of the intermediate species to produce H_2 and CO_2.[8,11,31–35]

In relation to this, many kinetic studies and different rate expressions have been developed. Specifically for Pt-based catalysts, a zero order is adopted for CO since its concentration appears with no influence in the rate and a high surface CO coverage is obtained. Moreover, CO_2 order usually present negative almost zero order with a fast desorption.[8,10,11,25,36,37] Contrary, water and hydrogen

concentration present high influence in the reaction rate and they are normally involved in the rate-determining steps. Thus, the rate is increased by higher amount of water, but hydrogen presents meaningful negative order indicating unfavourable effect on the WGS reaction rate.[3,8,11,36–40]

Since the influence of proton conductor has been demonstrated for PtCeAl catalyst, kinetic analysis and operando DRIFTS have been carried out in order to delve into the water-enhancer effect. Therefore, the kinetics of the WGS reaction on PtCeAl + ZrEuMo_5 sample mixed in a mass ratio of 1:5 has been studied. Both powdered and structured systems have been tested. In addition, operando DRIFTS of powdered PtCeAl and ZrEuMo_5 samples were investigated in WGS reaction conditions in order to study the CO and water adsorptions as well as the possible formed intermediates.

6.2. KINETICS ON POWDERED CATALYST

The kinetic analysis was constantly performed at atmospheric pressure and at 80000 $mL \cdot h^{-1} \cdot g_{cat}^{-1}$ space velocity according to the previous catalytic tests. Moreover, the amount of PtCeAl catalyst was also maintained in 0.1 g as well as the mass ratio Cat/IC of 1:5. The particle sizes were selected slightly higher, between 800 and 1000 µm, as consequence of instrumental conditions.

Experiments were carried out in a fixed bed reactor from 175 to 400 ºC, as it is explained in Chapter 2. For the kinetic analysis a feed composition of 1.3 % CO and 2.8 % H_2O balanced with N_2 was used as a *reference* test. Then, the composition of the feed was varied in

the ranges of 1.2 – 4.2 vol.% for CO, 2.7 – 5.1 vol.% of H_2O and 0 – 21 vol.% of H_2, balanced with N_2, thereby keeping constant the total flow rate and the space velocity during the whole study. The first experiment was carried out with the selected feeding conditions as *reference* test described above. This reference test was then sometimes repeated and at the end of the kinetic analysis in order to observe the decrease of the activity. In the next table are summarized the performed experiments indicating the feed composition:

Table 6.1 Summary of feed composition (%) of the experiments for the kinetic study.

Test	CO	H_2O	CO_2	H_2	N_2
Reference A	**1.28**	**2.87**	**0**	**0**	**95.85**
Reference B	**1.30**	**2.82**	**0**	**0**	**95.88**
CO_1	1.65	2.81	0	0	95.54
CO_2	2.19	2.80	0	0	95.01
CO_3	4.20	2.83	0	0	92.97
Reference C	**1.30**	**2.76**	**0**	**0**	**95.94**
H_2_1	1.28	3.03	0	1.93	93.76
H_2_2	1.28	2.80	0	5.30	90.62
H_2_3	1.26	2.87	0	10.69	85.18
H_2_4	1.25	2.87	0	21.29	74.59
Reference D	**1.29**	**2.87**	**0**	**0**	**95.84**
H_2O_1	1.31	3.58	0	0	95.11
H_2O_2	1.40	5.1	0	0	93.50
Reference E	**1.27**	**2.78**	**0**	**0**	**95.95**

A preliminary analysis by a differential reactor approach was considered for a first estimation of the kinetic orders using experiments where CO conversions were below 20 %.[41,42]. In these conditions, the reaction rate was calculated as follows:

$$-r_{CO} = \frac{\xi_{CO} \cdot F_{CO}^{In}}{W} \quad [6.1]$$

where the rate is expressed in $mol \cdot s^{-1} \cdot g_{cat}^{-1}$, ξ_{CO} is the CO conversion, F_{CO} is the inlet molar flow rate of CO ($mol \cdot s^{-1}$) and W is the catalyst weight (g).

The reaction rate can be generally expressed by

$$-r = k(T) \prod_i^N P_i^{\alpha_i} \quad [6.2]$$

known as "power law",[43] where *k* is the apparent kinetic constant as function of the temperature as defined by the Arrhenius equation and being the rate proportional to the partial pressures of each component (*i*):

$$k = k_0 \exp[\frac{-E_a}{RT}] \quad [6.3]$$

Therefore, varying the inlet concentration of each component one by one and keeping the rest constant in isothermal conditions, the relative reaction orders (α_i) can be estimated in this low conversion condition as

$$\ln(-r) = \ln(k) + \sum \alpha_i \cdot \ln(P_i) \quad [6.4]$$

and whose representation provides the estimated reaction order as slope of the straight line.

Figure 6.1 presents the rates calculated by equation 6.1 on varying the partial pressures of every component according to equation 6.4 at different temperatures in the 175-240ºC range, which are selected for presenting CO conversions below 20 %. Not surprisingly, the reaction order for CO is around zero (except at 175 ºC, where the conversion is too low and the experimental error too high) in agreement with extensively reported data. Therefore, the CO concentration exhibits no meaningful influence in the reaction rate. On the other side, the higher reaction order for H_2O and the negative one for H_2 are also expected for WGS reaction rates on Pt-based catalysts.[3,4,8,11,37] At this point, it is important to declare that the carbon and the hydrogen mass balances have been controlled during all the tests and kept at 1 ± 0.1 and 1 ± 0.2, respectively. Only for temperatures ≤ 200 ºC the error is higher, since the conversion is too low.

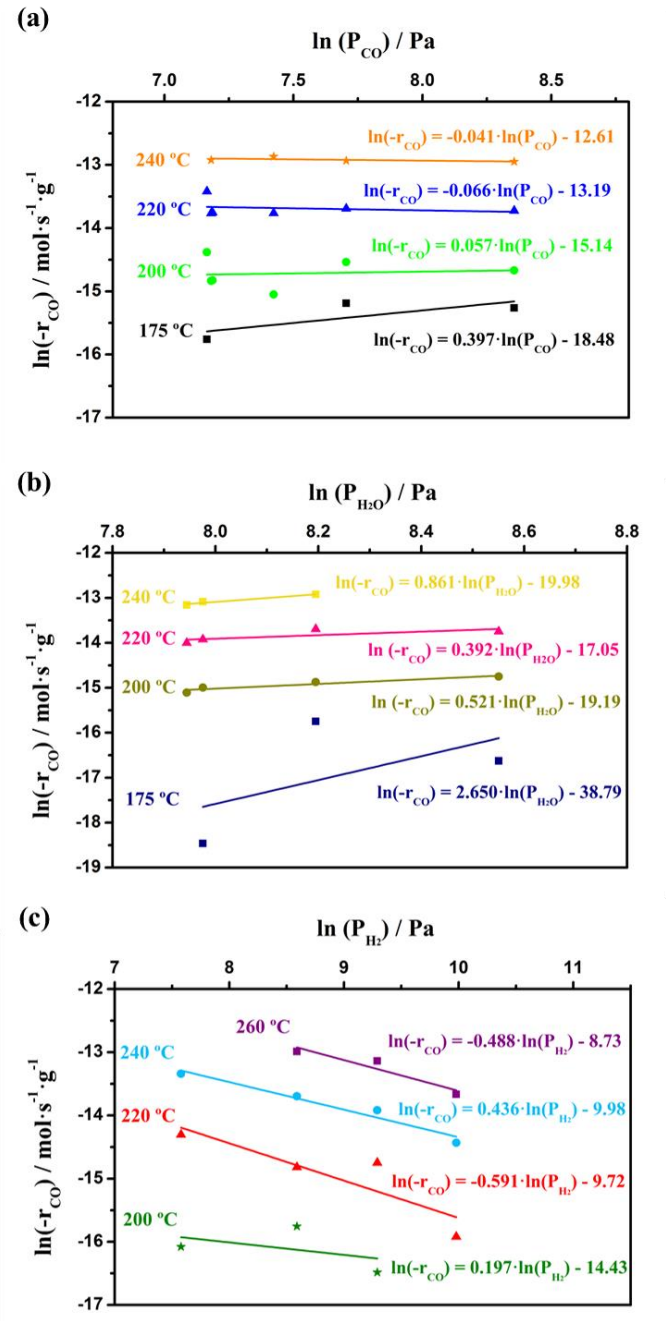

Figure 6.1 Variation of WGS reaction rates on PtCeAl+ZrEuMo_5 (1:5) for CO conversions below 20 % with the different tested partial pressures.

Afterwards, the complete reactions for all tested temperatures, including high conversions, were evaluated by an isotherm integral reactor approach in a PFR type. Then, in a differential volume is assumed a perfect distribution of the concentrations in the transversal section and the differential equation to solve is:

$$\frac{-r_{CO}}{F^{In}} = \frac{d\chi_{CO}}{dW} \qquad [6.5]$$

Where F^{In} is the total inlet molar flow ($mol \cdot s^{-1}$), χ_{CO} is the CO molar fraction, $-r_{CO}$ is the reaction rate ($mol \cdot s^{-1} \cdot g_{cat}^{-1}$) and W is the catalyst weight (g). Therefore, at initial conditions, dW = 0 and the $d\chi_{CO} = \chi_{CO}^{0}$ (inlet CO concentration). For differential volumes, the variation can be approximated to increments, so:

$$\chi_{CO}^{i+1} = \chi_{CO}^{i} - \frac{\Delta W}{F^{In}}(-r_{CO}) \qquad [6.6]$$

Then, the parameters of the proposed rate expression will be estimated by minimization of the sum of the square difference between the χ_{CO} from the experimental data and the calculated ones by equation 6.6 with a proposed rate expression ($-r_{CO}$) at every temperature in each tested condition (Eq. 6.7) using the GRG (Generalized Reduced Gradient) nonlinear solving method:

$$\sum\left(\chi_{CO}^{Exp.\ Data} - \chi_{CO}^{Eq.\ 6.6}\right)^2 \qquad [6.7]$$

The reaction rate expression was generated from the general definitions described by Hougen and co-workers[44,45] as a combination of kinetic terms, potential terms and adsorption terms:

$$r = \frac{(kinetic\ terms)(potential\ terms)}{(adsorption\ terms)^n} \qquad [6.8]$$

According to the first approximation for the reaction orders using a differential reactor approach, which is also in agreement with that reported in the literature for Pt-based catalysts, the rate expression was simplified as previously reported in the literature.[45–49] Moreover, contrary to H_2 and H_2O species behaviour, the analysis of the data when CO partial pressures are varied shows again the independency of the catalytic activity on changing the CO amount in the kinetic control range (Figure 6.2).

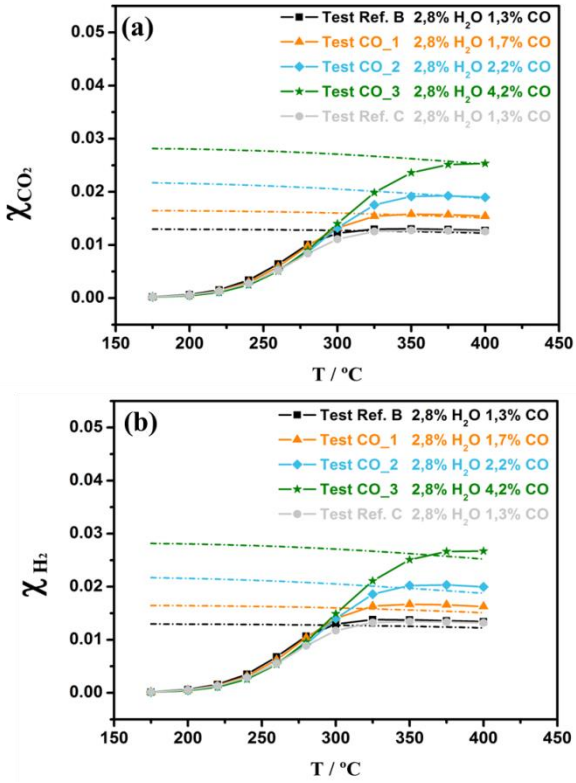

Figure 6.2 Molar fraction of (a) CO_2 and (b) H_2 produced by WGS reaction on powdered PtCeAl+ZrEuMo_5 sample with different CO partial pressure (see Table 6.1). Equilibrium composition is shown as dotted line.

Thus, a Langmuir-Hinshelwood mechanism was proposed[50,51], the contribution of CO partial pressure was neglected and the strong influence of H_2 adsorption has been considered. Therefore, the proposed simplified rate expression was:

$$-r_{CO} = \frac{kP_{H_2O}^{\beta}(1-\eta)}{1+AP_{H_2}^{\alpha}} \quad [6.9]$$

where pressures are in Pa and the rate in $mol \cdot s^{-1} \cdot g_{cat}^{-1}$. The reaction orders are α and β for H_2 and H_2O, respectively. The H_2 adsorption constant (A) has been considered invariable in the temperature range studied to simplify calculations and the kinetic constant (k) has been evaluated with respect to a reference temperature (T_0) to reduce the correlation between the preexponential factor (k_0) and the activation energy (E_a) from equation 6.3:[41]

$$k = k_0 \exp\left[\frac{-E_a}{R}\left(\frac{1}{T}-\frac{1}{T_0}\right)\right] \quad [6.10]$$

The η factor, also known as reversibility factor,[8] is calculated as the ratio between the pressure constant and the thermodynamic constant (Eq. 6.11). Therefore, its value oscillates between 0 and 1, where the latter (η = 1) means that the thermodynamic equilibrium conversion has been achieved:

$$\eta = \frac{P_{CO_2}P_{H_2}}{P_{H_2O}P_{CO}K_{eq}} \quad [6.11]$$

The equilibrium constant (K_{eq}) has been estimated by the generally used good correlation proposed by Moe[52] for WGS reaction studies:

$$K_{eq} = exp\left(\frac{4577.8}{T} - 4.33\right) \quad [6.12]$$

Moreover, a parameter (D) related to the deactivation was included in the rate expression, since the deactivation process is quite significant as it was shown previously, thereby changing the kinetic constant value. Then, for the *reference* tests, a preliminary determination of the E_a, A, α and β values were estimated and fixed, evaluating thereby the value of the k_0 parameter, which decreases as is shown in Figure 6.3. The behaviour followed by k_0 parameter is in good agreement with the deactivation profile observed in the previous deactivation study (see Figure 5.10) probably caused by the deactivation of the ceria support. Consequently, the factor "D" was introduced in the rate equation and was defined as:

$$D_i = \frac{k_0^{Ref.\ i}}{k_0^{Ref.\ A}} \quad [6.13]$$

where $k_0^{Ref.\ i}$ is the preexponential factor (k_0) of a reference test and $k_0^{Ref.\ A}$ is the preexponential factor of the first test (Reference A). Thus, the D_i factor is different and smaller on increasing time; this is, for consecutive experiments.

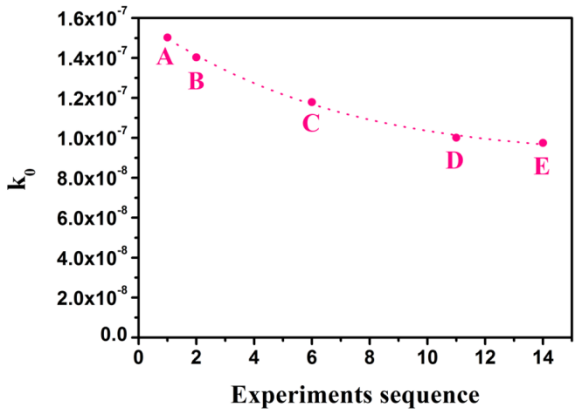

Figure 6.3 Decrease of the estimated preexponential factor of the reference tests.

Finally, a mathematical factor ($\sigma_{CO} \cong 1$) to avoid some problems with the solving method was added:

$$\sigma_{CO} = \frac{\chi_{CO}}{10^{-4}+\chi_{CO}} \qquad [6.14]$$

Therefore, by adding equations 6.10, 6.11, 6.12, 6.13 and 6.14 to equation 6.9 the final reaction rate expression is defined as:

$$-r_{CO} = \frac{kP_{H_2O}^{\beta}(1-\eta)}{1+AP_{H_2}^{\alpha}} \cdot D_i \cdot \sigma_{CO} \qquad [6.15]$$

This expression is then used in equation 6.6 to calculate the kinetic parameters by minimization of equation 6.7. The values in Table 6.2 are obtained considering a reference temperature (T_0) of 473.15 K and data satisfying $\eta \leq 0.1$, this is, data belonging to the kinetic control range that are far from the equilibrium conditions. To estimate equation 6.6 temperatures are expressed in K, partial pressures in Pa and the rate in $mol \cdot s^{-1} \cdot g_{cat}^{-1}$.

Table 6.2 Calculated kinetic parameters for the proposed reaction rate expression (Eq. 6.15) for WGS reaction on powdered PtCeAl+ZrEuMo_5 sample (1:5).

k_0	$5.35 \cdot 10^{-8}$
A	0.052
E_a (kJ/mol)	80.62
β (H_2O)	0.359
T_0 (K)	473.15
R ($kJ \cdot mol^{-1} \cdot K^{-1}$)	$8.31 \cdot 10^{-3}$
α (H_2)	0.428

These kinetic values are in good agreement with those found for similar Pt-based catalysts. For instance, the activation energy as well as the reaction orders are comparable to those reported by Phatak *et al.*,[4] where the activation energies vary between 68 and 84 kJ/mol and the reaction orders are close to zero for CO and CO_2, from -0.38 to -0.49 for H_2, and high values, between 0.77 and 1.1 are reported for H_2O. Only when the Pt is supported on CeO_2 a reaction order for H_2O as low as 0.44 is reported. This is probably due to the promoter effect of ceria on water activation, which is also in concordance with the idea proposed in this work. Similar results for E_a (~70 kJ/mol) and reaction orders (-0.36 and 0.63 for H_2 and H_2O, respectively) are obtained by Grabow *et al.*[11] using both theoretical DFT analysis and experimental data for a Pt/Al_2O_3 catalyst. Furthermore, Germani *et al.* determined the kinetic parameters using both *power law* based and LH based reaction rate expressions for the WGS reaction on microstructured $Pt/CeO_2/Al_2O_3$ catalysts.[8,53] These authors fit their

data considering reaction orders equal to 0.49 and -0.45 for H_2O and H_2, respectively, and activation energies of 86 kJ/mol and 76.8 kJ/mol for the Pt-based catalysts depending on the catalyst preparation method. On considering the LH-based rate law expression, an activation energy of 78.2 kJ/mol is calculated. Moreover, the highest adsorption constant is obtained for H_2 that they assume, as in this work, independent of temperature. Therefore, the kinetic model proposed in equation 6.15 and the resulting parameters are in good agreement with the previously reported analysis.

It is worth mentioning the low value obtained for the reaction order of water (0.36) in relation to those found in the literature. This indicates an improvement in the water activation step that must be associated to the presence of the ionic conductor, which would provide a higher amount of the available dissociated water. Consequently, the concentration of reactive OH species next to adsorbed CO is likely higher, decreasing the limitation of this step. Then, this fact turns into a decrease of the necessary water partial pressure (lower reaction order). This behaviour is also in good agreement with that observed when ceria support was used instead of alumina support as described above, but more intense by the addition of the ionic conductor.

The calculated CO conversion using the proposed model (eq. 6.15 and table 6.2) is plotted against the experimental CO conversion in Figure 6.4. In this figure, the CO conversions observed in all tests at every temperature are plotted. The good correspondence between the model and the data is noticeable; this supports again the good

estimate of the kinetic parameters. However, in the 300 - 350 ºC temperature range, the model slightly over-estimates CO conversions by less than 20 %. The competitive methanation reaction may be a possible explanation. However, methane formation was only detected at temperatures above ~350 ºC and the small amount detected allows neglecting it in the model. Then, the presence of Mo oxide appears as the most probably reason for this model deviation. As previously analysed Mo oxide is reducible in the 300-350ºC temperature range and therefore H_2 consumption in this process results in over-estimating the CO conversion rate. A further analysis of the interaction between Mo and H_2 becomes mandatory to assess the kinetic rate law. In addition to this, more kinetic studies should be carried out to propose an improved rate equation that considers this reduction phenomenon. Moreover, a more exact determination of the H_2 adsorption constant as well as the introduction of the Mo oxide reduction kinetics in the rate expression would also improve the CO conversion estimate.

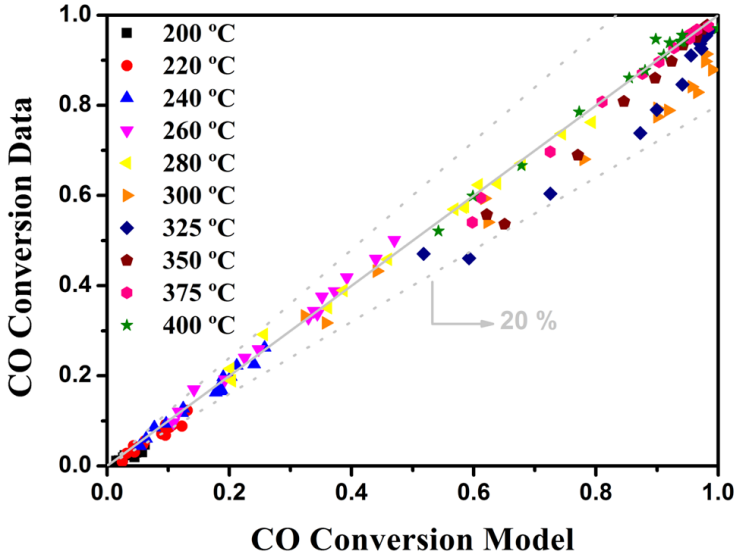

Figure 6.4 Plot of the calculated* vs. *the observed CO conversion using the proposed kinetic model for the WGS reaction, equation 6.15, on powdered PtCeAl+ZrEuMo_5 (1:5) catalyst.

The CO conversion vs Temperature plots have also been plotted in Figure 6.5. The conversion over-estimate in the 300-350 ºC temperature range discussed above is again observed in all tests. Moreover, paying attention to the reference test plots (Figure 6.5a), the deactivation effect is evident on experimental progression. These reference tests present, besides the same kinetic parameters, the same partial pressures and conditions. The only difference is the previously defined D_i factor. Then, this graph allows to validate the adopted D_i value in each case since the model also exhibit the same deactivation behaviour in good concordance with the experimental data. Moreover, from test D the deactivation is unappreciable, indicating that the stabilization was accomplished. This behaviour is again

consistent with that previously observed (see Chapter 3), where a lower stable activity is finally achieved.

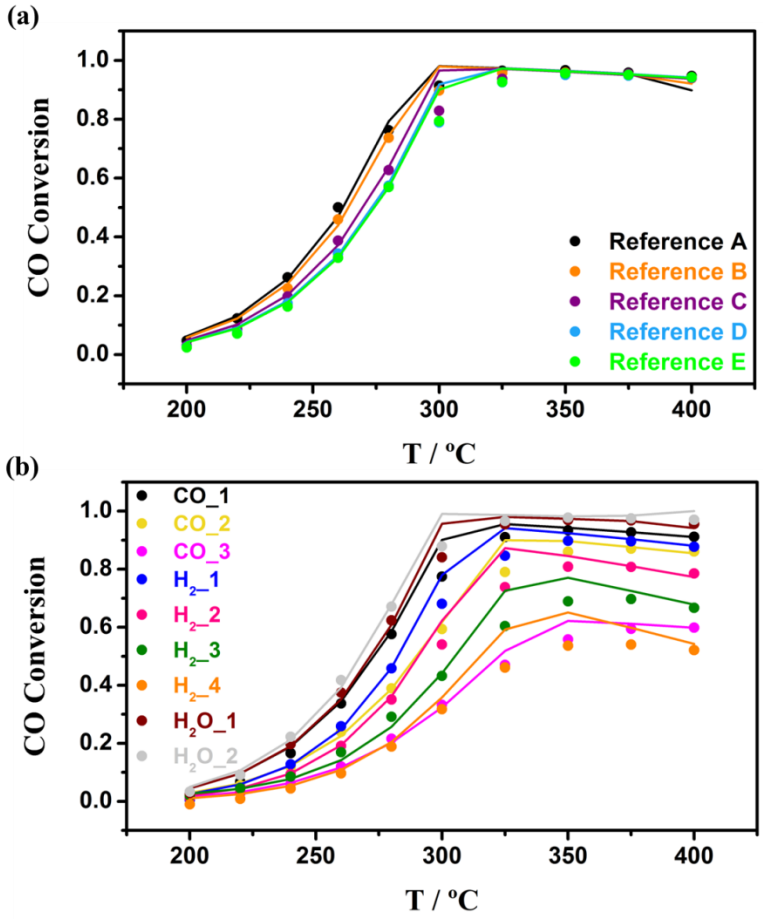

Figure 6.5 CO Conversion vs Temperature plots: (a) reference tests and (b) tests of partial pressures variation. The experimental data is plotted as dots. Model data is plotted as solid lines.

In addition to the kinetic analysis, the reference test was also carried out without the ionic conductor and using quartz as diluent with the same particle size and conditions (Figure 6.6). There is, an analogous comparison to that carried out in Chapter 5 (in Sevilla's laboratory). The objective was, not only to see the promoter effect of

the ionic conductor in different setups and conditions, but to also determine if internal diffusion problems exist.

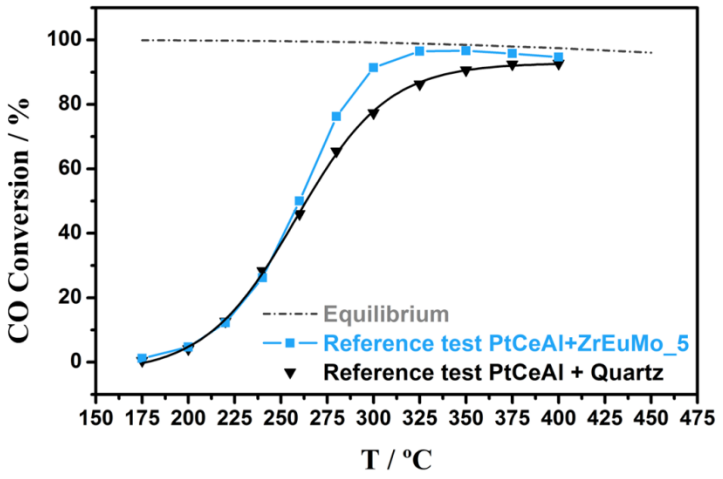

Figure 6.6 CO conversion plots. Comparison between PtCeAl+ZrEuMo_5 (1:5) sample and the bare PtCeAl catalyst. Experiments in reference conditions for calculation of Thiele Modulus.

Since the PtCeAl particles are diluted by the ZrEuMo_5 ionic conductor, the promoter effect observed could be attributed to an improvement of the internal diffusion. Thus, the use of quartz as diluent allows compare PtCeAl and PtCeAl+ZrEuMo_5 samples according to the space velocity, external diffusion and also thermal diffusion in the catalytic bed. However, internal diffusion is different between particles formed only by PtCeAl and particles formed by the catalyst-ionic conductor physical mixture. Therefore, to discard the internal diffusion problems and also support the water conductivity promoter effect, the Thiele modulus in both cases was estimated, according to expression 6.16:

$$\phi^2 = \frac{Surface\ reaction\ rate}{Diffusion\ rate} \qquad [6.16]$$

that for a general reaction order (n) can be described as:[42,43,54]

$$\phi^2 = \frac{R^2 k C_{A_S}^{n-1}}{D_{eff}} \qquad [6.17]$$

where R is the volume of the particles (V_p) divided by their surface (S_p), k is the kinetic constant, C_{As} is the concentration of the specie A on the catalytic surface and D_{eff} is the effective diffusivity.

In this case, C_{COs} is considered the same as C^0_{CO}, this is the inlet concentration with no external diffusion problems. The D_{eff} parameter is usually approximated to 0.1 $cm^2 \cdot s^{-1}$ in these conditions. Moreover, spherical particles are assumed, then the R factor can be re-defined by the particle diameter, d_p:

$$R = \frac{V_p}{S_p} = \frac{{}^4/_3 \pi r^3}{4\pi r^2} = \frac{d_p}{6} \qquad [6.18]$$

The Thiele modulus is then estimated as:

$$\phi = \frac{d_p}{6} \sqrt{\frac{(-r_{CO})}{D_{eff} C_{Co}}} \qquad [6.19]$$

The estimated Thiele moduli for the reference test conditions are reported in Table 6.3. To estimate these values the previously calculated $-r_{CO}$ are expressed in $mol \cdot s^{-1} \cdot m^{-3}$ considering the density of the porous catalyst and an average particle size of $925 \cdot 10^{-6}$ m (particles sieved between 850 and 1000 μm).

Table 6.3 Estimated Thiele Modulus for reference test conditions.

T (ºC)	Φ_{PtCeAl}	$\Phi_{PtCeAl + ZrEuMo\_5}$
175	0.0460	0.0256
200	0.0837	0.0467
220	0.1290	0.0722
240	0.1940	0.1080
260	0.2810	0.1570
280	0.3940	0.2180
300	0.5330	0.2740
325	0.7220	0.1890
350	0.8800*	0*
375	0.9370*	0*
400	0.8670*	0*

** reaction rates are close to zero since the thermodynamic equilibrium has been achieved at high temperatures.*

As the estimated Thiele modulus values are all below 1 internal diffusion problems can be discarded. The diffusion rate is higher than reaction rate for both samples. Therefore, kinetics is controlled by the superficial reaction rate during the complete tested temperature range. Consequently, the higher activity must be only related to the water-enhancement effect caused by the proton conductor, supporting thereby the conclusions previously discussed from the catalytic tests in Chapter 5.

6.3. KINETICS ON STRUCTURED CATALYST

Experiments were carried out in a plug-flow reactor at temperatures ranging from 200 to 400 ºC and at atmospheric pressure. Previous to the measurements, the isothermal zone of the reactor was found to position the micromonolith (see Scheme 2.2, Chapter 2). The

temperature of the reactor was controlled by a thermocouple in the internal wall of the tubular furnace. Moreover, a mobile thermocouple located in the central channel of the micromonolith allows measure the temperature along the micromonolith during the reaction. Thus, regarding the micromonolith, this system provided longitudinal internal temperature profile and a fixed external temperature during the whole reaction. The collected data indicate a maximal deviation of ± 2 ºC at the micromonolith endings at the highest tested temperatures. Therefore, isothermal conditions were considered and thermal diffusion problems were neglected.

Analogously to the kinetic study on the powdered sample, the used space velocity was always 80000 $mL \cdot h^{-1} \cdot g_{cat}^{-1}$ respect to the 0.1 g of PtCeAl catalyst mixed with ZrEuMo_5 in a mass ratio of 1:5. Also, *reference* tests were used to estimate the catalyst deactivation included in the kinetic equation. However, this set up allows higher water concentrations as well as the introduction of CO_2 in the inlet stream. Therefore, the feed compositions tested in this kinetic study were:

Table 6.4 Summary of feed composition (%) of the experiments for the kinetic study.

Test	CO	H_2O	CO_2	H_2	N_2
Reference A	**4.39**	**20.35**	**7.11**	**19.82**	**48.33**
CO_1	11.12	20.96	7.13	20.13	40.66
CO_2_1	4.32	20.36	12.26	19.34	43.72
H_2_1	4.67	20.14	7.28	40.76	27.15
Reference B	**4.39**	**20.32**	**7.15**	**19.97**	**48.17**
CO_2	16.72	20.75	7.13	20.24	35.16
CO_2_2	4.38	20.16	0.00	20.26	55.20
H_2_2	4.12	19.75	6.98	0.00	69.15
Reference C	**4.41**	**20.60**	**7.17**	**20.03**	**47.79**
H_2O_1	4.33	8.63	6.97	19.33	60.74
H_2O_2	4.62	31.23	7.50	21.20	35.45
Reference D	**4.51**	**20.48**	**7.24**	**20.29**	**47.48**
H_2O_3	4.25	14.81	6.89	19.22	54.83
Reference E	**4.49**	**20.26**	**7.22**	**20.24**	**47.79**

Following the same procedure as before for the powdered sample, a preliminary differential reactor approach was considered for conversions below 20 %. In a similar way to that discussed above for the powdered samples, the estimated reaction orders (Figure 6.7) are strongly negative for H_2 and around 0.45 for H_2O. However, the analysis shows an uncertain value for CO, apparently different to zero, but also sometimes reported for Pt-based catalysts.[3,11,53] In the case of the reaction rate of CO_2, there are not reliable points enough in this conversion range, but it seems to tend to a strong negative value.

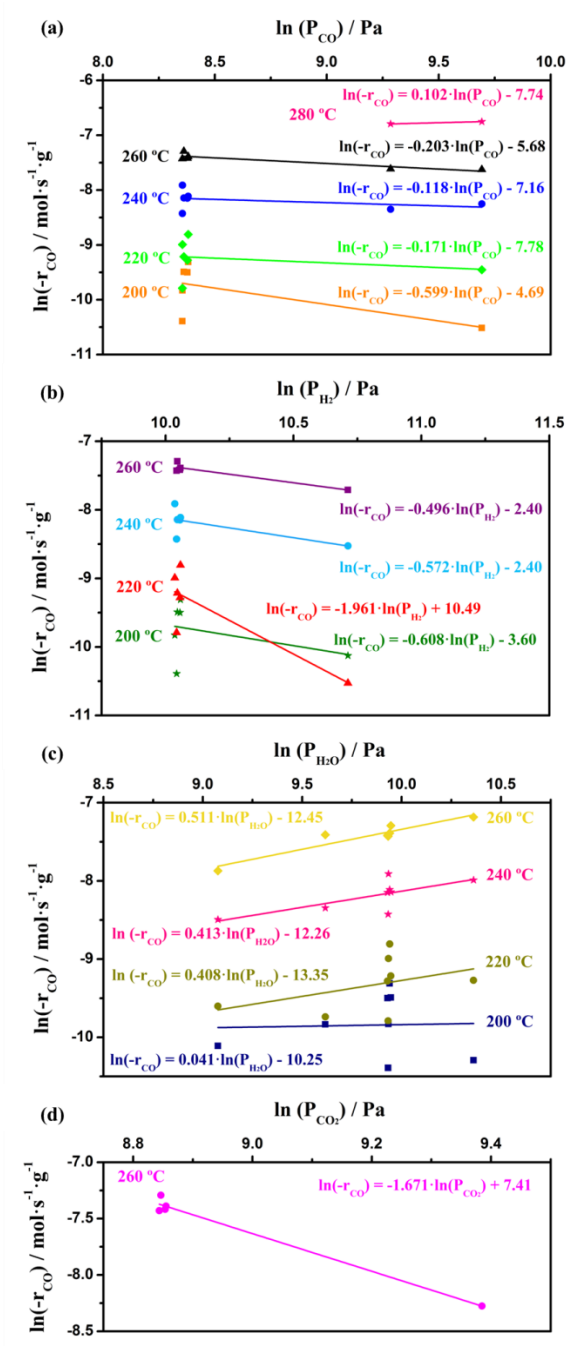

Figure 6.7 Variation of WGS reaction rates on structured PtCeAl+ZrEuMo_5 (1:5) for CO conversions below 20 % with the different tested partial pressures.

Then, the analysis for an integral reactor was carried out exactly as was described above for the powdered sample. The deactivation factor (D_i) was also calculated respect to the behaviour of the preexponential factor (k_0). As it is shown in Figure 6.8, the decrease of the k_0 value are in good agreement with that exhibited by the powdered sample and again in concordance with the studied deactivation behaviour of this sample (see Chapter 5, Figure 5.10).

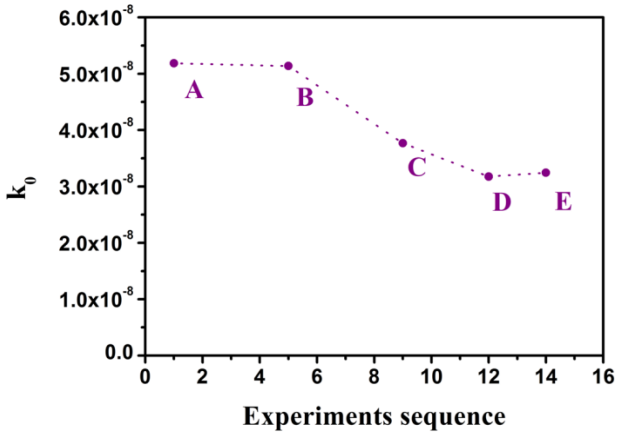

Figure 6.8 Decrease of the estimated preexponential factor of the reference tests of the structured sample.

For comparison, the same rate expression as in the powdered sample (Equation 6.15) was proven by the fitting method. However, an acceptable solution was unsuccessful. Consequently, and regarding the estimated reaction orders from the differential reactor approach, where the CO presents a reaction order of *c.a.* -0.2, the CO adsorption was considered:

$$-r_{CO} = \frac{kP_{H_2O}^{\beta}P_{CO}^{\delta}(1-\eta)}{\left(1+AP_{H_2}^{\alpha}+BP_{CO}^{\delta}\right)^2}\cdot D_i \qquad [6.20]$$

Although with this expression the obtained kinetic parameters (Table 6.5) are similar to the ones of the powdered sample, the fitting does not result in a good description of the observed CO conversions as shown in Figure 6.9. Moreover, the kinetic parameters related to CO (B and δ) tend to zero. Actually, different values of these parameters lead a worse fit.

Table 6.5 Calculated kinetic parameters for the proposed reaction rate expression (Eq. 6.20) for WGS reaction on structured PtCeAl+ZrEuMo_5 sample (1:5).

k_0	$5.01 \cdot 10^{-8}$
A	$4.00 \cdot 10^{-4}$
B	0
E_a (kJ/mol)	80.02
β (H_2O)	0.30
T_0 (K)	473.15
R ($kJ \cdot mol^{-1} \cdot K^{-1}$)	$8.31 \cdot 10^{-3}$
α (H_2)	0.50
δ (CO)	0

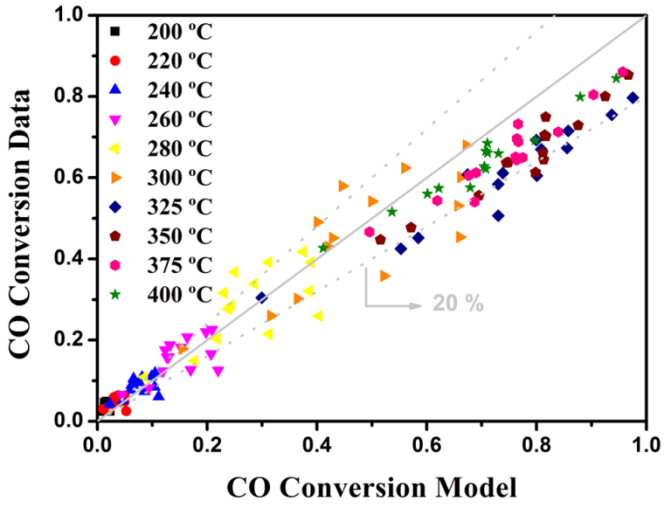

Figure 6.9 Comparison of CO conversion between the experimental data and the calculated by the proposed kinetic model (Eq. 6.20) for the WGS reaction on structured PtCeAl+ZrEuMo_5 (1:5) sample.

Hence, another reaction rate was proposed considering the CO_2 adsorption, since the unreliable value of the reaction order (~ -1) could indicate an important influence of the CO_2 adsorption/desorption step. Thus, the proposed reaction rate expression is described as follows:

$$-r_{CO} = \frac{kP_{H_2O}^{\beta}(1-\eta)}{\left(1+AP_{H_2}^{\alpha}+BP_{CO_2}^{\delta}\right)^2} \cdot D_i \qquad [6.21]$$

Fitting of the experimental data with this expression is acceptable (Figures 6.10 and 6.11). However, this fit allows two interesting conclusions that could lead to a better kinetic rate law. First, for temperatures above 300 ºC, the model strongly over-estimates the experimental data as observed for the powdered sample although the

effect is more pronounced. A second consideration is the unexpected extremely high value of the α parameter for H_2 (Table 6.6).

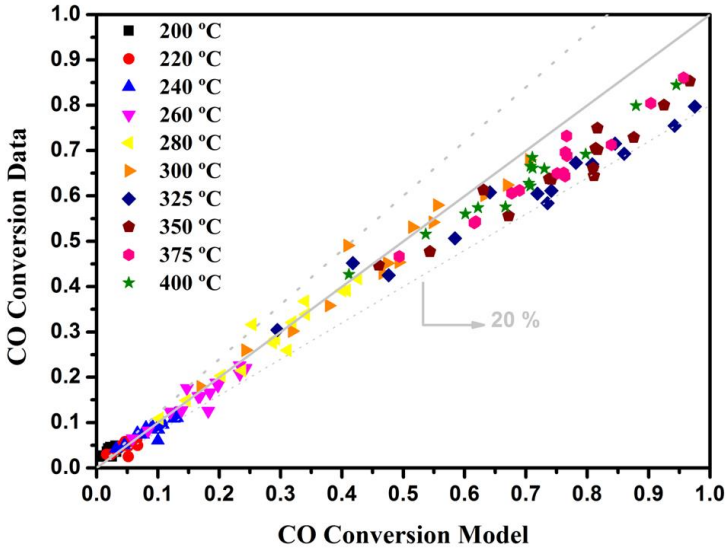

Figure 6.10 Comparison of CO conversion between the experimental data and the calculated by the proposed kinetic model (Eq. 6.21) for the WGS reaction on structured PtCeAl+ZrEuMo_5 (1:5) sample.

Table 6.6 Calculated kinetic parameters for the proposed reaction rate expression (Eq. 6.21) for WGS reaction on structured PtCeAl+ZrEuMo_5 sample (1:5).

k_0	$3.90 \cdot 10^{-9}$
A	$5.07 \cdot 10^{-10}$
B	$2.88 \cdot 10^{-6}$
E_a (kJ/mol)	71.28
β (H_2O)	0.60
T_0 (K)	473.15
R ($kJ \cdot mol^{-1} \cdot K^{-1}$)	$8.31 \cdot 10^{-3}$
α (H_2)	1.79
δ (CO_2)	1.10

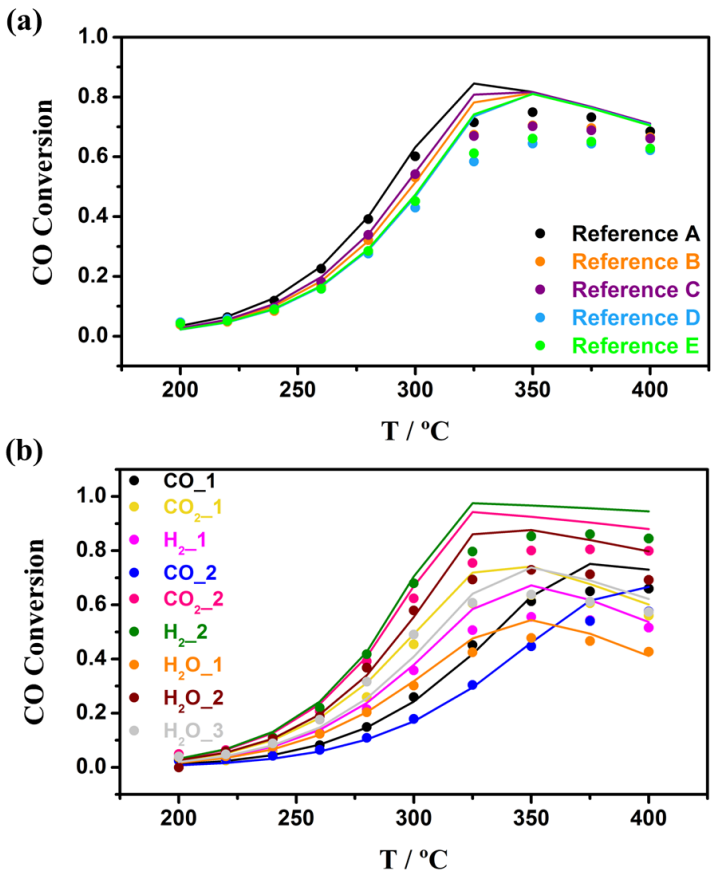

Figure 6.11 CO Conversion vs Temperature plots: (a) reference tests and (b) tests of partial pressures variation. The experimental data is plotted as dots. Model data is plotted as solid lines.

Therefore, as it was proposed above, the significant deviation of the model for temperatures above 300 ºC could be related to the reduction of Mo oxide by H_2 according to the TPR analysis. Moreover, the high value of α also indicates more influence of the H_2 adsorption term. Hence, perhaps the mechanism is modified from this temperature and a new rate expression should be defined. In addition, the necessity of adding the CO_2 adsorption term for the fit, also with

an extremely high δ value compared to the literature, means that a new addend in the denominator of the rate expression was mandatory. Consequently, the CO_2 adsorption term may be substituted by a Mo oxide reduction kinetic term. Furthermore, this addend should be defined as $P_{H_2}^{\gamma}$ multiplied by a reduction kinetic constant for Mo oxide according to Arrhenius equation which depends on the temperature and should be relevant from 300 ºC.

Therefore, it would be interesting to evaluate the kinetics of the Mo oxide reduction by TPR analysis and formulate a new rate expression that includes this step as part of the mechanism to improve the fit and explain the previous observations.

6.4. *OPERANDO* STUDY BY DRIFTS ON POWDERED SAMPLES

In order to elucidate the possible intermediates formed during the WGS reaction and to obtain some clues on the occurred mechanism that explains the observations from the kinetic analysis, *operando* DRIFTS with PtCeAl catalyst in WGS reaction conditions has been performed. Analogously, the same experiments were also executed on ZrEuMo_5 sample to analyse the role of the proton conductor in the reaction mechanism, getting some information about water and hydrogen adsorption phenomena.

Since instrumental requirements, *Model* and *Industrial* feeding conditions analogous to those previously used in the catalytic tests (Chapter 5) were used but slightly modified. A total flow rate of 50 $ml \cdot min^{-1}$ with Ar as balance, 4 % of CO and 10 % H_2O were used as *Model* conditions, whereas 4% CO, 5% CO_2, 10% H_2O and 25% H_2

were used as *Industrial* conditions. Prior to measurements in the 180-350 ºC temperature range, as for the catalytic tests, an activation step in 50 ml·min^{-1} of 10% of H_2/Ar at 350 ºC for 30 min was performed. Afterwards, the system was cooled down to 180 ºC to start the reaction that was carried out in Ar flow. Spectra were collected before the activation at RT, after activation in H_2/Ar at 350 ºC, before reaction in Ar at 180 ºC and during the WGS reaction on increasing the temperature.

6.4.1. DRIFTS analysis of PtCeAl in WGS reaction conditions.

For the analysis of the PtCeAl sample, 70 mg of catalyst were necessary. Figure 6.12a plots the initial spectrum at RT as well as the activated spectra at 350 ºC in H_2/Ar and at 180 ºC in Ar before reaction. In addition, in Figure 6.12b, difference spectra taking the initial one at RT as reference are also shown. In this difference spectra positive bands indicate formed species whereas negative ones species that disappear during the activation step. Thus, a reduction of the broad band centered at 3470 cm^{-1} associated to water interacting via hydrogen-bonds is observed during the activation step. More clearly, in the difference spectra the elimination of the molecular water is shown as negative bands at 3470 and 1642 cm^{-1}, whose disappearance leads to the observation of OH groups over the ceria/alumina support (3732 and 3680 cm^{-1}),[55] as is described in Scheme 6.1.

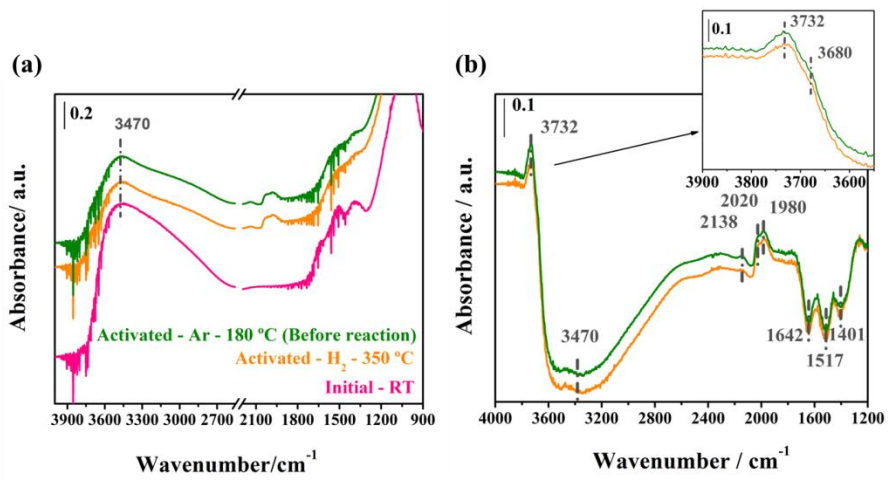

Figure 6.12 (a) DRIFT spectra of PtCeAl sample: initial at RT (pink line), activated after 30 min in H_2 atmosphere (orange line), and after activation at 180 ºC in Ar before reaction conditions (green line); (b) difference spectra of activated sample at 350 ºC in H_2 (orange line) and at 180 ºC in Ar before reaction (green line) respect to the initial spectrum.

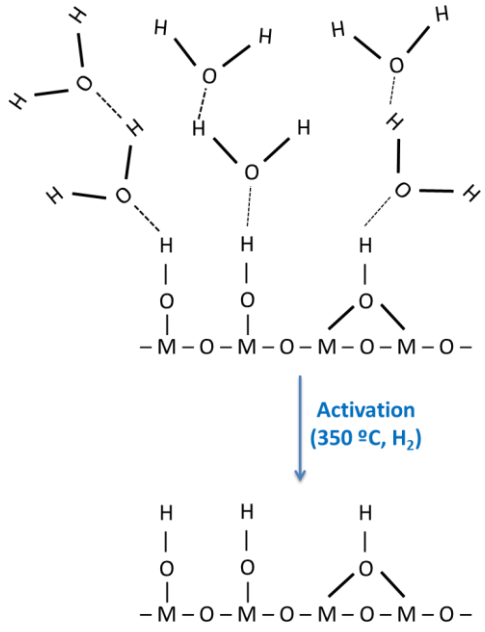

Scheme 6.1 Dehydration process by activation in H_2 at 350 ºC.

On the other side, the bands at 2020 and 1980 cm^{-1} are associated to the creation of Pt – CO bonds, which are formed upon decomposition of carboxylates whose disappearance is assessed by the intensity decrease of the bands at 1517 and 1401 cm^{-1} assigned to υ_{OCO}.[56,57] Not surprisingly, an intensity increase of a band at 2138 cm^{-1} in H_2 atmosphere is also observed. This is attributed to the $^2F_{5/2} \rightarrow {}^2F_{7/2}$ electronic transition of Ce^{3+}.[58]

After the activation step, two different reaction conditions were tested as is describe above:

- ***Model Conditions (CO + H_2O)***

The difference spectra in WGS reaction *Model* conditions from 180 to 350 ºC respect to the activated one at 180 ºC in Ar are discussed.

In the 4000 and 3400 cm^{-1} region (Figure 6.13) bands associated to OH groups are observed. In particular, negative bands are observed at 3759, 3730 and 3682 cm^{-1} corresponding to isolated OH groups bonded to the ceria/alumina support,[55] which means that these species disappear once the reaction starts. At the same time a broad band peaking at *ca.* 3400 cm^{-1} appears. This indicates H-bonded molecular water to the initially isolated OH species. This supports the role of the support hydroxyl groups in the reaction mechanism as previously discussed. On increasing the reaction temperature these negative bands become less intense and the positive broad band almost disappears. This likely means that free OH groups regenerates, which

also indicates that molecular water no longer remains adsorbed on the support surface.

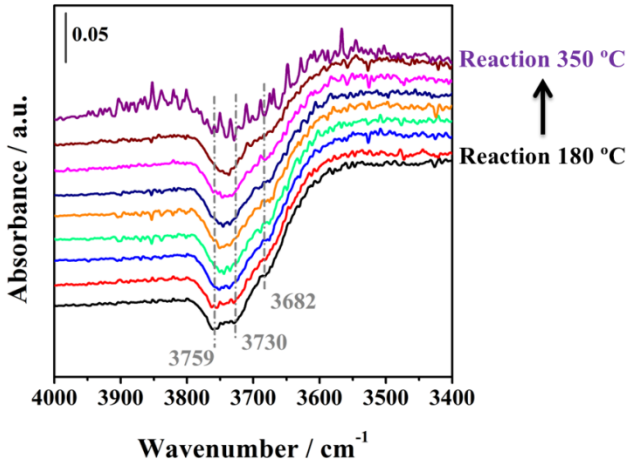

Figure 6.13 Difference spectra during WGS reaction in Model conditions on PtCeAl from 180 to 350 ºC respect to the activated spectrum at 180 ºC in Ar (4000 – 3400 cm^{-1} range).

On the other side, the interaction of CO with Pt during the reaction as well as the formation/elimination of carbonate-carboxylate species are also studied (Figure 6.14). The minimum observed at 2143 cm^{-1} corresponds to molecular CO present in the IR cell volume. In addition, bands at 2073, 2052 and 2020 cm^{-1} are associated to υ_{CO} bonded over Pt. The presence of several bands indicates that CO are adsorbed on Pt with different electron density which also depends on the Pt particle sizes. The chemical bond between CO and Pt involves the 5σ and 2π* orbitals of CO molecule. When the coordination of Pt particles is low, its electron density is high, which increases the 2π* the back-donation phenomenon that consequently debilitates the C-O bond. Hence, the associated υ_{CO} band shifts to lower frequencies.[59]

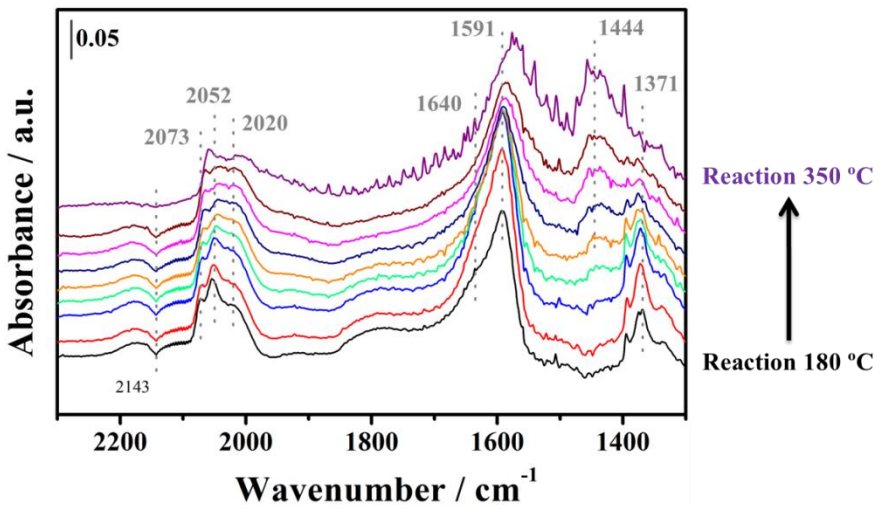

Figure 6.14 Difference spectra during WGS reaction in Model conditions on PtCeAl from 180 to 350 ºC respect to the activated spectrum at 180 ºC in Ar (2300 – 1300 cm^{-1} range).

Accordingly, the observed band at 2073 cm^{-1} corresponds to Pt particles with low electron density, which can be associated to bigger particle sizes or particles with higher coordination. In the same sense, the intense band at 2052 cm^{-1} is assigned to reduced Pt particles (Pt^0) with a small particle size around 1.5 nm or the CO is adsorbed on terrace sites. The band at 2020 cm^{-1} can be related to the linear CO adsorbed on the smallest reduced Pt particles (d_p < 1.5 nm).[57,59] However, this band at 2020 cm^{-1} can also be explained by the adsorption of terminal CO on metallic Pt in contact with the Ce^{3+} in the metal-support interface (Pt-$\square_s$-Ce^{3+}).[23]

Furthermore, it is noticeable band shifts and changes in intensities on increasing the temperature during the WGS reaction. This may indicate a variation of the Pt electron density, a different Pt coordination, a different Pt oxidation state or a variation of Pt particle

size. Actually, at 350 ºC (Fig. 6.14), a new band at 2007 cm^{-1} is observed. This band can be related to a shift from the band at 2020 cm^{-1} by a reduction of Pt particles (d_p < 1.5 nm)[59] or can be attributed to adsorbed CO in presence of superficial carbon on Pt, this latter caused by CO dissociation.[56]

On the other side, in the region of 1700 – 1300 cm^{-1} are shown the symmetric and asymmetric stretching modes characteristic of superficial carbonates, formates or carboxylates. The bands at 1591 and 1371 cm^{-1} has been attributed to monodentate carbonates[60,61] whereas the shoulder at 1640 cm^{-1} is associated to physisorbed water. The intensities of both bands decrease on increasing the temperature during the reaction as is expected. Nevertheless, it is observed the appearance and increase with the temperature of a band at 1444 cm^{-1}, which can be assigned to C-H vibrational mode (υ_{C-H}) and/or C=C bond stretch ($\upsilon_{C=C}$) due to the slightly amorphous adsorbed carbon as cyclic system on Pt from the CO dissociation.[56,62] The increase of this band during the reaction indicates an increment of generated superficial carbon amount. This phenomenon could lead to the deactivation of the catalyst previously observed.

- ***Industrial Conditions ($CO + H_2O + CO_2 + H_2$)***

Analogously to *Model* conditions, the bands associated to OH groups at 3756, 3725 and 3697 cm^{-1} follow the same behaviour discussed above (Figure 6.15a). In the same way, the bands attributed to CO adsorbed on Pt (2071, 2054 and 2022 cm^{-1}) are again formed and their variation on increasing the temperature present similar behaviour (Figure 6.15b). This fact indicates that Pt active sites are

not strongly modified by the different feed. This supports the idea of the high CO coverage for Pt catalyst independently of the feeding conditions, which lead to a neglected influence of the CO concentration for the kinetics wherever the conditions. In this region is also observed bands at 2349 and 2143 cm^{-1} associated to molecular CO_2 and CO, respectively.

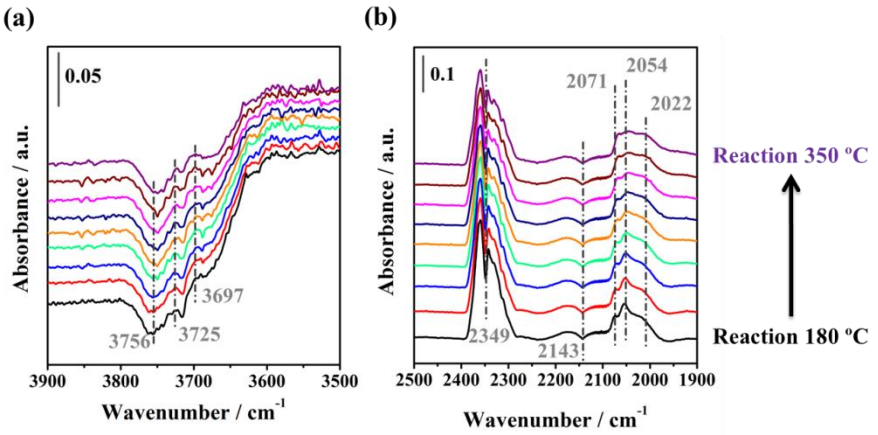

Figure 6.15 Difference spectra during WGS reaction in Industrial conditions on PtCeAl from 180 to 350 ºC respect to the activated spectrum at 180 ºC in Ar (OH and CO bands range).

Finally, the region between 1800 and 1200 cm^{-1} (Figure 6.16b) for the carbonate, carboxylate and formate species show again similar bands than those found in *Model* conditions. However, regarding such amount of H_2 introduced in this experiment, the region between 3100 and 2700 cm^{-1} has been studied (Figure 6.16a). Indeed, bands around 2968 and 2838 cm^{-1} are formed. These new bands can be assigned to υ_{CH} of partially hydrogenated carbon formed by dissociation of CO over Pt discussed above.[56]

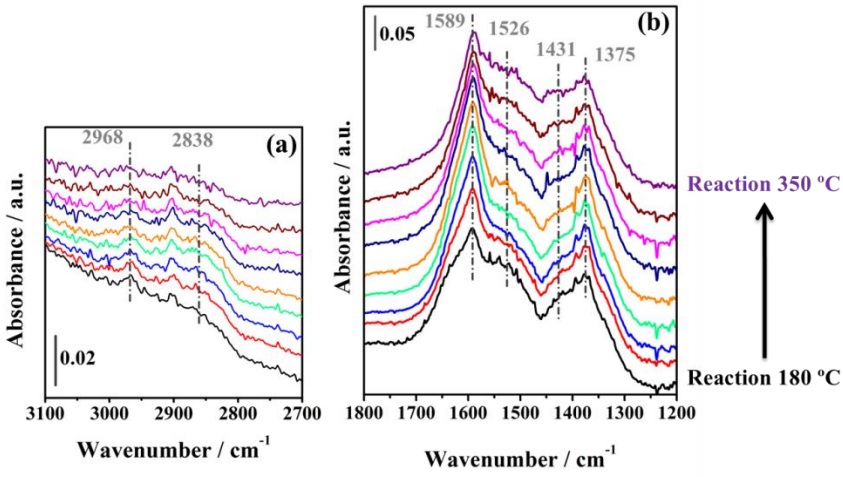

Figure 6.16 Difference spectra during WGS reaction in Industrial conditions on PtCeAl from 180 to 350 ºC respect to the activated spectrum at 180 ºC in Ar.

6.4.2. DRIFTS analysis of ZrEuMo_5 in WGS reaction conditions.

Identical activation conditions and analysis were carried out on the ZrEuMo_5 proton conductor as described before for PtCeAl catalyst.

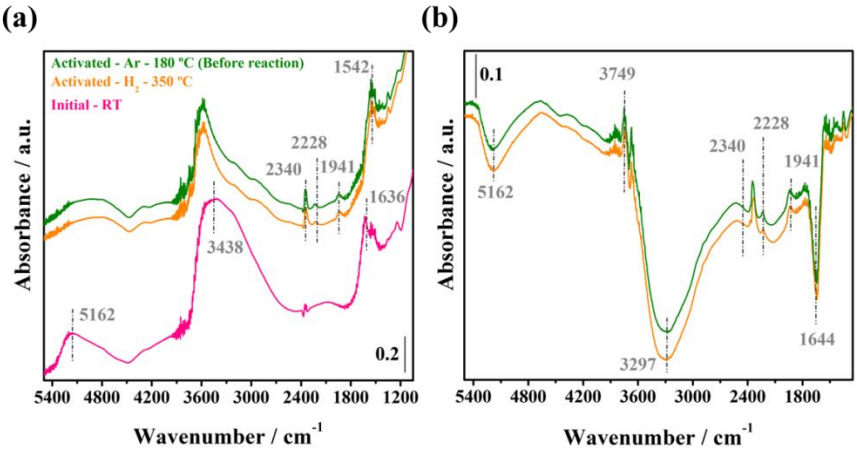

Figure 6.17 (a) Direct spectra of ZrEuMo_5 sample: initial at RT (pink line), activated after 30 min in H_2 atmosphere (orange line), and after

activation at 180 ºC in Ar before reaction conditions (green line); (b) difference spectra of activated sample at 350 ºC in H_2 (orange line) and at 180 ºC in Ar before reaction (green line) respect to the initial spectrum.

Similarly, the spectra before and after the activation process, and the respective difference spectra respect to that at RT before activation step are shown in Figure 6.17. Before the activation step the spectrum is dominated by physisorbed water bands (υ_{OH}) centered at 3438 cm^{-1} caused by the interaction between molecular water and hydroxyl groups via hydrogen-bonds. Besides, the bands at 1636 and 5162 cm^{-1} correspond to the scissoring bend (δ_{HOH}) and combination band ($\upsilon_{OH} + \delta_{HOH}$), respectively (Figure 6.17a). After H_2 treatment, it is noticeable the disappearance of the broad band associated to non-dissociated water and the appearance of a new hydroxyl species (shown in the difference spectra, Figure 6.17b). The interaction via hydrogen-bonds between the water molecules and the hydroxyl species is responsible for the non-appearance of this hydroxyl bands before activation. This new bands (more detailed in Figure 6.18a) at 3749, 3722 and 3671 cm^{-1} are assigned to monodentate (linear, type I) and tricoordinate (tribridge) OH groups over ZrO_2.[63,64] These observations are the same found for ZrEu_5 sample studied in Chapter 4.

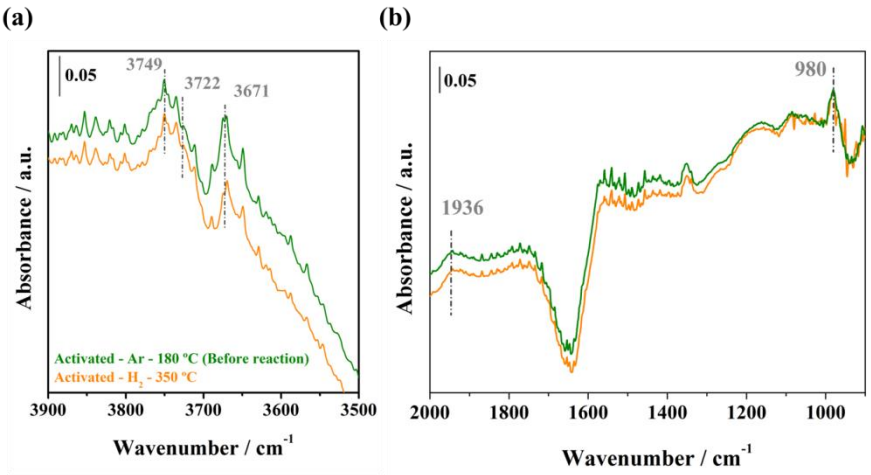

Figure 6.18 Difference spectra of activated ZrEuMo_5 sample at 350 ºC in H_2 (green line) and at 180 ºC in Ar before WGS reaction (orange line) in the OH and hydrated Mo oxide ranges.

To facilitate the analysis, the region from 2000 to 900 cm^{-1} has also been magnified (Figure 6.18b), where besides the negative band at 1636 cm^{-1} due to the elimination of the physisorbed water, other two bands appear. Unlike ZrEu_5 sample, new bands at 980 cm^{-1} and 1936 cm^{-1} appear associated to Mo=O bond stretch and its overtone. The increase of these bands after activation step may be related to the dehydration of superficial Mo oxide of the sample:

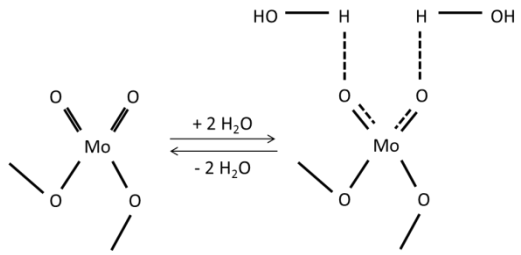

Scheme 6.2 Hydration/Dehydration process by activation in H_2 at 350 ºC.

Moreover, there are some bands between 1600 and 1100 cm^{-1} which can be ascribable to residual carbonates/carboxylates like compounds. The presence of these species are unavoidable due to the atmospheric CO_2 adsorption on Eu-doped zirconia during the calcination process, forming thereby these carbon-species which stay occluded in the pores according to the high porosity of the material and in good agreement with the same analysis on ZrEu_5 sample.[65,66]

Finally, the new bands also formed during the activation in the range of 2400 – 2150 cm^{-1} are more detailed in Figure 6.19. At these frequencies can be observed low energy f-f transitions of Eu^{3+}.[67] In particular, the band at 2236 cm^{-1} is attributed to $^7F_0 \rightarrow {}^7F_J$ transition, which is shifted on reducing temperature to 2236 cm^{-1}, since these transitions are highly sensitive to temperature changes according to the previous study carried out on ZrEu_x and ZrEuMo_x samples (see chapters 3 and 4) and to the literature.

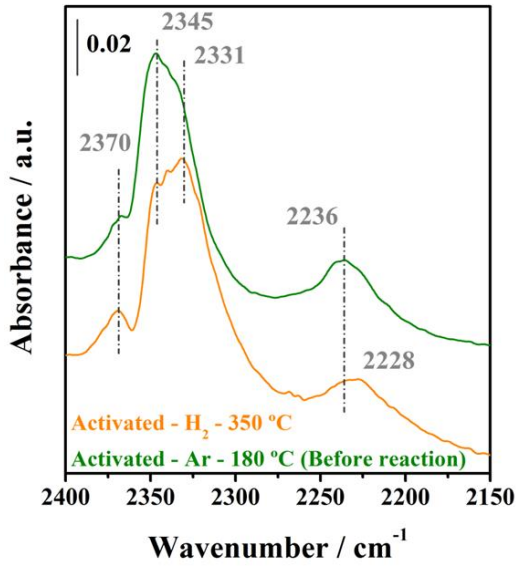

Figure 6.19 Difference spectra of activated ZrEuMo_5 sample at 350 ºC in H_2 (green line) and at 180 ºC in Ar before WGS reaction (orange line).

Moreover, in this region are observed bands (between 2400 - 2300 cm^{-1}) associated to occluded CO_2 in the pores of the sample. Hence, $O{=}C{=}O\cdots M^{n+}$ interactions produce splitting of the bands.[68] In addition, due to the molecular CO_2 presence, the attribution of these bands result complex.

- ***Model Conditions***

Under *Model* conditions the interesting and meaningful variations occur by water adsorption/desorption processes. Thus, the spectra are quite similar to those obtained for ZrEu_5 sample. However, some differences by Mo presence are significant.

The negative band observed at 3760 cm^{-1} (Figure 6.20b) indicates the disappearance of the monodentate OH groups when the reaction starts. However, on increasing the temperature this disappearance

becomes smaller at the same time as the band at 3701 cm^{-1} increases. As it was discussed for ZrEu_5 sample,[63] monodentate hydroxyls (type I) of monoclinic ZrO_2 present higher basicity respect to the multicoordinated hydroxyls. Then, these monodentate OH groups interact weakly with water molecules since they have lower capacity to accept electrons, which provokes a shift to lower wavenumbers. These data permits to attribute the band at 3701 cm^{-1} to type (I) hydroxyls weakly interacting with water molecules. However, the interaction of hydroxyls at 3671 cm^{-1} (tribridged, more acidic ones) with water is stronger and generates a broad band at lower wavenumbers (3350 cm^{-1}) analogous to that observed for ZrEu_5 sample. The new band appearing in presence of water at 3724 cm^{-1} is attributed to dissociated water in the oxygen vacancies created by doping zirconia with Eu^{3+} as it was discussed for ZrEu_5 sample (see chapter 4). In the same way, in Figure 6.20a is shown the band at 5239 cm^{-1} associated to physisorbed water which reappears when the water is feeding but decreases on increasing the temperature. As it was stablished for ZrEu_5, the presence of both dissociated (3724 cm^{-1}) and physisorbed (5239 cm^{-1}) water is mandatory for the proton conductivity. The difference between this sample and the ZrEu_5 is the presence of Mo, which is responsible for the appearance of the band at 3633 cm^{-1}, which can be attributed to hydrated of Mo=O bond under wet atmosphere according to Scheme 6.2.[69] In order to verify this Mo oxide hydration, it has been analysed the band at 1954 cm^{-1} corresponding to the disappearance of the Mo=O overtone by the hydration phenomenon (Figure 6.20c). In addition, the band at 3633 cm^{-1} could be associated to υ_{OH} of hydrogen carbonates instead of

hydrated Mo oxide. However, the absence of the associated band at ~1218 cm^{-1} (assigned to δ_{OH} vibration of hydrogen carbonates) rejects this possibility.[70] Therefore, the band at 3633 cm^{-1} is ascribed to hydrated Mo oxide, which increases with the temperature. This "extra" adsorbed water could provide proton conductivity for temperatures over 300 ºC unlike the ZrEu_5 sample. Moreover, according to characterization data (see Chapter 3), the Mo is located over Eu atoms, around which the oxygen vacancies are created. Consequently, a close contact between dissociated water in the oxygen vacancies and the adsorbed water on Mo oxide is expected to promote the proton conductivity.

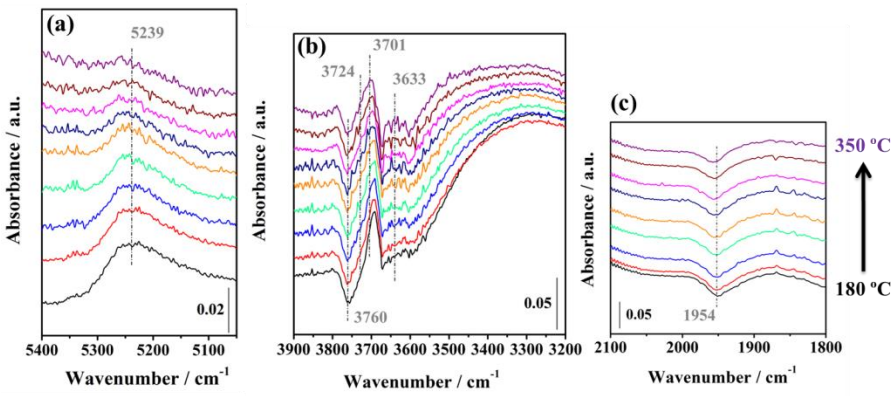

Figure 6.20 Difference spectra during WGS reaction in Model conditions on ZrEuMo_5 from 180 to 350 ºC respect to the activated spectrum at 180 ºC in Ar.

- ***Industrial Conditions***

The spectra observed under *Industrial* conditions are quite similar to those obtained in *Model* conditions. Essentially, it is remarkable the higher intensity of the band ascribed to dissociated water in the oxygen vacancies (3721 cm^{-1}, Figure 6.21a) as well as the band at

1620 cm^{-1} (Figure 6.21b) assigned to physisorbed water (δ_{HOH}). The higher amount of both species could lead to higher proton conductivity even at temperatures above 300 ºC. Moreover, the better capacity of dissociating and adsorbing water may be related to the presence of hydrogen in these conditions, since the interaction between Mo oxide and H_2 creates reduced Mo species and/or bronzes capable of accumulating water and provide ion exchange.[71,72]

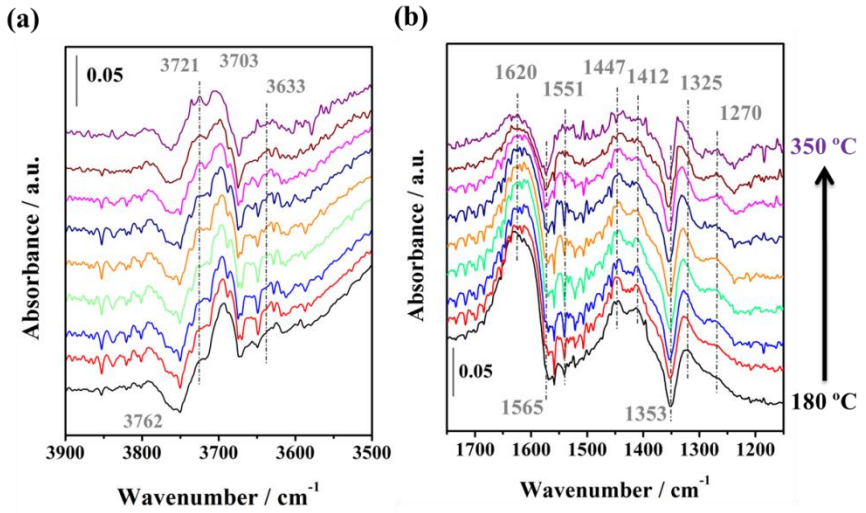

Figure 6.21 Difference spectra during WGS reaction in Industrial conditions on ZrEuMo_5 from 180 to 350 ºC respect to the activated spectrum at 180 ºC in Ar.

The observed bands between 1600 and 1200 cm^{-1} are the same as exhibited in *Model* conditions (data not shown). Different (bi)carbonates are formed on zirconia support during the reaction in good agreement with those reported in the literature.[73] The $\upsilon_{as}(CO_3^{-2})$ of polydentate (~1551 cm^{-1}) and bridged (1353 cm^{-1}) carbonates increases during the reaction on increasing the temperature. Contrary, the bicarbonates seem to be reduced (~1440 - 1450 cm^{-1}) indicating a

loss of H species. The formation of these carbon-species during the reaction is in good agreement with the observed deactivation behaviour previously discussed.

6.5 PARTIAL CONCLUSIONS

The kinetic analysis according to a L-H mechanism of WGS reaction on PtCeAl+ZrEuMo_5 (1:5) sample shows indeed a low value of the reaction order for the water (0.36 and 0.6 for powdered and structured samples, respectively) respect to those reported in the literature. This is in agreement with a reduction of the influence of the limiting water activation step by the addition of the proton conductor which provides labile dissociated water to react with adsorbed CO on Pt. These observations are also supported by *operando* DRIFTS experiments, where has been found bands assigned to OH in the oxygen vacancies by dissociation of the water coexisting with physisorbed water. Moreover, and unlike Mo-undoped sample (ZrEu_5), physisorbed water continue present at temperatures above 300 ºC related to the superficial Mo oxide of the sample.

On the other side, further experiments are mandatory to elucidate the mechanism in these conditions, likewise more TPR analysis (meanly on variation of the heating ramp rate). With these experiments, the Mo oxide reduction kinetics can be defined and then included in the proposed WGS reaction rate expression, since a high influence of this phenomenon is observed above 300 ºC.

However, to undoubtedly investigate reaction mechanism and reaction intermediates would be interesting to include a full

quantitative analysis with *in situ/operando* methods as well as isotopic exchange and steady-state isotopic transient kinetic analysis.

REFERENCES

1. Hilaire, S., Wang, X., Luo, T., Gorte, R. J. & Wagner, J. A comparative study of water-gas-shift reaction over ceria supported metallic catalysts. *Appl. Catal. A Gen.* **215,** 271–278 (2001).

2. Gorte, R. J. & Zhao, S. Studies of the water-gas-shift reaction with ceria-supported precious metals. *Catal. Today* **104,** 18–24 (2005).

3. Kalamaras, C. M., Panagiotopoulou, P., Kondarides, D. I. & Efstathiou, A. M. Kinetic and mechanistic studies of the water-gas shift reaction on Pt/TiO2 catalyst. *J. Catal.* **264,** 117–129 (2009).

4. Phatak, A. A. *et al.* Kinetics of the water-gas shift reaction on Pt catalysts supported on alumina and ceria. *Catal. Today* **123,** 224–234 (2007).

5. Madon, R. J. *et al.* Microkinetic analysis and mechanism of the water gas shift reaction over copper catalysts. *J. Catal.* **281,** 1–11 (2011).

6. Gokhale, A. A., Dumesic, J. A. & Mavrikakis, M. On the Mechanism of Low-Temperature Water Gas Shift Reaction on Copper. *J. Am. Chem. Soc.* **130,** 1402–1414 (2008).

7. Jacobs, G. *et al.* Low-temperature water-gas shift: impact of Pt promoter loading on the partial reduction of ceria and consequences for catalyst design. *J. Catal.* **229,** 499–512 (2005).

8. Germani, G. & Schuurman, Y. Water-Gas Shift Reaction Kinetics Over micro-Structured Pt/CeO2/Al2O3 Catalysts. *Am. Inst. Chem. Eng.* **52,** 1806–1813 (2006).

9. Aranifard, S., Ammal, S. C. & Heyden, A. On the Importance of the Associative Carboxyl Mechanism for the Water-Gas

Shift Reaction at Pt/CeO2 Interface Sites. *J. Phys. Chem. C* **118,** 6314–6323 (2014).

10. Clay, J. P., Greeley, J. P., Ribeiro, F. H., Delgass, W. N. & Schneider, W. F. DFT comparison of intrinsic WGS kinetics over Pd and Pt. *J. Catal.* **320,** 106–117 (2014).

11. Grabow, L. C., Gokhale, A. A., Evans, S. T., Dumesic, J. A. & Mavrikakis, M. Mechanism of the Water Gas Shift Reaction on Pt: First Principles, Experiments, and Microkinetic Modeling. *J. Phys. Chem. C* **112,** 4608–4617 (2008).

12. Cybulskis, V. J., Wang, J., Pazmiño, J. H., Ribeiro, F. H. & Delgass, W. N. Isotopic transient studies of sodium promotion of Pt/Al2O3 for the water-gas shift reaction. *J. Catal.* **339,** 163–172 (2016).

13. Kalamaras, C. M., Americanou, S. & Efstathiou, A. M. 'Redox' vs 'associative formate with -OH group regeneration' WGS reaction mechanism on Pt/CeO2: Effect of platinum particle size. *J. Catal.* **279,** 287–300 (2011).

14. Tibiletti, D. *et al.* An investigation of possible mechanisms for the water-gas shift reaction over a ZrO2-supported Pt catalyst. *J. Catal.* **244,** 183–191 (2006).

15. Liu, X., Ruettinger, W., Xu, X. & Farrauto, R. Deactivation of Pt/CeO2 water-gas shift catalysts due to shutdown/startup modes for fuel cell applications. *Appl. Catal. B Environ.* **56,** 69–75 (2005).

16. Kim, C. H. & Thompson, L. T. Deactivation of Au/CeOx water gas shift catalysts. *J. Catal.* **230,** 66–74 (2005).

17. Li, L. *et al.* Water-gas shift reaction over CuO/CeO2 catalysts: Effect of CeO2 supports previously prepared by precipitation with different precipitants. *Int. J. Hydrogen Energy* **36,** 8839–8849 (2011).

18. Sato, Y., Terada, K., Soma, Y., Miyao, T. & Naito, S. Marked addition effect of Re upon the water gas shift reaction over TiO2 supported Pt, Pd and Ir catalysts. *Catal. Commun.* **7,** 91–95 (2006).

19. Shido, T. & Iwasawa, Y. Reactant-Promoted Reaction Mechanism for Water-Gas Shift Reaction on Rh-Doped CeO2. *Journal of Catalysis* **141,** 71–81 (1993).

20. Burch, R., Goguet, A. & Meunier, F. C. A critical analysis of the experimental evidence for and against a formate mechanism for high activity water-gas shift catalysts. *Appl. Catal. A Gen.* **409-410,** 3–12 (2011).

21. Meunier, F. C., Goguet, A., Hardacre, C., Burch, R. & Thompsett, D. Quantitative DRIFTS investigation of possible reaction mechanisms for the water-gas shift reaction on high-activity Pt- and Au-based catalysts. *J. Catal.* **252,** 18–22 (2007).

22. Huang, S.-C., Lin, C.-H. & Wang, J.-H. Trends of Water Gas Shift Reaction on Close-Packed Transition Metal Surfaces. *J. Phys. Chem. C* **114,** 9826–9834 (2010).

23. Kalamaras, C. M., Dionysiou, D. D. & Efstathiou, A. M. Mechanistic Studies of the Water–Gas Shift Reaction over Pt/CexZr1–xO2 Catalysts: The Effect of Pt Particle Size and Zr Dopant. *ACS Catal.* **2,** 2729–2742 (2012).

24. Meunier, F. C. *et al.* On the complexity of the water-gas shift reaction mechanism over a Pt/CeO2 catalyst: Effect of the temperature on the reactivity of formate surface species studied by operando DRIFT during isotopic transient at chemical steady-state. *Catal. Today* **126,** 143–147 (2007).

25. Ratnasamy, C. & Wagner, J. P. Water Gas Shift Catalysis. *Catal. Rev. Sci. Eng.* **51,** 325–440 (2009).

26. Liu, P. & Rodriguez, J. A. Water-gas-shift reaction on metal nanoparticles and surfaces. *J. Chem. Phys.* **126,** 164705–1 – 164705–8 (2007).

27. Phatak, A. A., Delgass, W. N., Ribeiro, F. H. & Schneider, W. F. Density Functional Theory Comparison of Water Dissociation Steps on Cu, Au, Ni, Pd, and Pt. *J. Phys. Chem. C* **113,** 7269–7276 (2009).

28. González-Castaño, M. *et al.* Structuring Pt/CeO2/Al2O3 WGS

catalyst: Introduction of buffer layer. *Appl. Catal. B Environ.* **200,** 420–427 (2017).

29. González-Castaño, M., Ivanova, S., Ioannides, T., Centeno, M. A. & Odriozola, J. A. Deep insight into Zr/Fe combination for successful Pt/CeO2/Al2O3 WGS catalyst doping. *Catal. Sci. Technol.* **7,** 1556–1564 (2017).

30. Olympiou, G. G., Kalamaras, C. M., Zeinalipour-Yazdi, C. D. & Efstathiou, A. M. Mechanistic aspects of the water-gas shift reaction on alumina-supported noble metal catalysts: In situ DRIFTS and SSITKA-mass spectrometry studies. *Catal. Today* **127,** 304–318 (2007).

31. Kalamaras, C. M., Petallidou, K. C. & Efstathiou, A. M. The effect of La3+-doping of CeO2 support on the water-gas shift reaction mechanism and kinetics over Pt/Ce1-xLaxO2-delta. *Appl. Catal. B Environ.* **136-137,** 225–238 (2013).

32. Panagiotopoulou, P. & Kondarides, D. I. Effect of the nature of the support on the catalytic performance of noble metal catalysts for the water-gas shift reaction. *Catal. Today* **112,** 49–52 (2006).

33. Panagiotopoulou, P., Papavasiliou, J., Avgouropoulos, G., Ioannides, T. & Kondarides, D. I. Water-gas shift activity of doped Pt/CeO2 catalysts. *Chem. Eng. J.* **134,** 16–22 (2007).

34. Rodriguez, J. A., Liu, P., Hrbek, J., Evans, J. & Pérez, M. Water Gas Shift Reaction on Cu and Au Nanoparticles Supported on CeO2(111) and ZnO(0001): Intrinsic Activity and Importance of Support Interactions. *Angew. Chemie - Int. Ed.* **46,** 1329–1332 (2007).

35. Thinon, O., Diehl, F., Avenier, P. & Schuurman, Y. Screening of bifunctional water-gas shift catalysts. *Catal. Today* **137,** 29–35 (2008).

36. Grenoble, D. C., Estadt, M. M. & Ollis, D. F. The Chemistry and Catalysis of the Water Gas Shift Reaction. *J. Catal.* **67,** 90–102 (1981).

37. Thinon, O., Rachedi, K., Diehl, F., Avenier, P. & Schuurman,

Y. Kinetics and Mechanism of the Water-Gas Shift Reaction Over Platinum Supported Catalysts. *Top. Catal.* **52,** 1940–1945 (2009).

38. Aranifard, S., Ammal, S. C. & Heyden, A. Nature of Ptn/CeO2 (111) Surface under Water-Gas Shift Reaction Conditions: A Constrained ab Initio Thermodynamics Study. *J. Phys. Chem. C* **116,** 9029–9042 (2012).

39. Gong, X.-Q., Hu, P. & Raval, R. The catalytic role of water in CO oxidation. *J. Chem. Phys.* **119,** 6324–6334 (2003).

40. Koryabkina, N. A., Phatak, A. A., Ruettinger, W. F., Farrauto, R. J. & Ribeiro, F. H. Determination of kinetic parameters for the water-gas shift reaction on copper catalysts under realistic conditions for fuel cell applications. *J. Catal.* **217,** 233–239 (2003).

41. Ayastuy, J. L., Gutiérrez-Ortiz, M. A., González-Marcos, J. A., Aranzabal, A. & González-Velasco, J. R. Kinetics of the Low-Temperature WGS Reaction over a CuO/ZnO/Al2O3 catalyst. *Ind. Eng. Chem. Res.* **44,** 41–50 (2005).

42. Levenspiel, O. *Chemical Reaction Engineering*. (John Wiley & Sons, Inc., 1998).

43. Vannice, M. A. *Kinetics of Catalytic Reactions*. (Springer, 2005). doi:10.1007/b136380

44. Hougen, O. A. & Watson, K. M. Solid catalysts and reaction rates. General Principles. *Ind. Eng. Chem.* **35,** 529–541 (1943).

45. Yang, K. H. & Hougen, O. A. Determination of mechanism of catalyzed gaseous reactions. *Chem. Eng. Prog.* **46,** 146–157 (1950).

46. Sun, J., DesJardins, J., Buglass, J. & Liu, K. Noble metal water gas shift catalysis: Kinetics study and reactor design. *Int. J. Hydrogen Energy* **30,** 1259–1264 (2005).

47. Smith R.J., B., Loganathan, M. & Shekhar Shantha, M. A Review of the Water Gas Shift Reaction Kinetics. *Int. J. Chem. React. Eng.* **8,** 1–32 (2010).

48. Maestri, M., Livio, D., Beretta, A. & Groppi, G. Hierarchical Refinement of Microkinetic Models: Assessment of the Role of the WGS and r-WGS Pathways in CH4 Partial Oxidation on Rh. *Ind. Eng. Chem. Res.* **53,** 10914–10928 (2014).

49. Maestri, M., Vlachos, D. G., Beretta, A., Groppi, G. & Tronconi, E. Steam and dry reforming of methane on Rh: Microkinetic analysis and hierarchy of kinetic models. *J. Catal.* **259,** 211–222 (2008).

50. Kumar, K. V., Porkodi, K. & Rocha, F. Langmuir-Hinshelwood kinetics - A theoretical study. *Catal. Commun.* **9,** 82–84 (2008).

51. Vannice, M. A., Hyun, S. H., Kalpakci, B. & Liauh, W. C. Entropies of Adsorption in Heterogeneous Catalytic Reactions. *J. Catal.* **56,** 358–362 (1979).

52. Moe, J. M. Design of water-gas shift reactors. *Chem. Eng. Prog.* **58,** 33–36 (1962).

53. Germani, G., Alphonse, P., Courty, M., Schuurman, Y. & Mirodatos, C. Platinum/ceria/alumina catalysts on microstructures for carbon monoxide conversion. *Catal. Today* **110,** 114–120 (2005).

54. Fogler, H. S. *Elements of Chemical Reaction Engineering*. (Prentice Hall PTR, 2006).

55. Vuurman, M. A., Stufkens, D. J., Oskam, A., Deo, G. & Wachs, I. E. Combined Raman and IR study of MOx-V2O5/Al2O3(MOx = MoO3, WO3, NiO, CoO) catalysts under dehydrated conditions. *J. Chem. Soc. Faraday Trans.* **92,** 3259–3265 (1996).

56. Romero-Sarria, F. *et al.* The role of carbon overlayers on Pt-based catalysts for H2-cleanup by CO-PROX. *Surf. Sci.* **648,** 84–91 (2016).

57. Kalamaras, C. M., Gonzalez, I. D., Navarro, R. M., Fierro, J. L. G. & Efstathiou, A. M. Effects of Reaction Temperature and Support Composition on the Mechanism of Water - Gas Shift Reaction over Supported-Pt Catalysts. *J. Phys. Chem. C* **115,**

11595–11610 (2011).

58. Tabakova, T., Boccuzzi, F., Manzoli, M. & Andreeva, D. FTIR study of low-temperature water-gas shift reaction on gold/ceria catalyst. *Appl. Catal. A Gen.* **252,** 385–397 (2003).

59. Bazin, P., Saur, O., Lavalley, J. C., Daturi, M. & Blanchard, G. FT-IR study of CO adsorption on Pt/CeO2: characterisation and structural rearrangement of small Pt particles. *Phys. Chem. Chem. Phys.* **7,** 187–194 (2005).

60. Li, C. *et al.* Carbon Monoxide and Carbon Dioxide Adsorption on Cerium Oxide studied by Fourier- transform Infrared Spectroscopy. *J. Chem. Soc. Faraday Trans.* **85,** 929–943 (1989).

61. Goguet, A., Meunier, F. C., Tibiletti, D., Breen, J. P. & Burch, R. Spectrokinetic investigation of reverse water-gas-shift reaction intermediates over a Pt/CeO2 catalyst. *J. Phys. Chem. B* **108,** 20240–20246 (2004).

62. Jackson, S. D. *et al.* Deactivation and Regeneration of Alkane Dehydrogenation Catalysts. *Catal. Deactiv.* **2,** 167–174 (1997).

63. Cerrato, G., Bordiga, S., Barbera, S. & Morterra, C. Surface characterization of monoclinic ZrO2. I Morphology, FTIR spectral features, and computer modelling. *Appl. Surf. Sci.* **115,** 53–65 (1997).

64. Köck, E.-M., Kogler, M., Klötzer, B., Noisternig, M. F. & Penner, S. Structural and Electrochemical Properties of Physisorbed and Chemisorbed Water Layers on the Ceramic Oxides Y2O3, YSZ, and ZrO2. *ACS Appl. Mater. Interfaces* **8,** 16428–16443 (2016).

65. Merle-Méjean, T., Barberis, P., Othmane, S. Ben, Nardou, F. & Quintard, P. E. Chemical Forms of Hydroxyls on/in Zirconia: An FT-IR Study. *J. Eur. Ceram. Soc.* **18,** 1579–1586 (1998).

66. Daturi, M., Binet, C., Bernal, S., Pérez Omil, J. A. & Lavalley, J. C. FTIR study of defects produced in ZrO2 samples by thermal treatment. Residual species into cavities and surface

defects. *J. Chem. Soc. Faraday Trans.* **94,** 1143–1147 (1998).

67. Binnemans, K. Interpretation of europium(III) spectra. *Coord. Chem. Rev.* **295,** 1–45 (2015).

68. Fitzgerald, S. A. *et al.* Insights into the Anomalous Vibrational Frequency Shifts of CO2 Adsorbed to Metal Sites in Microporous Frameworks. *J. Phys. Chem. C* **119,** 5293–5300 (2015).

69. Du, X., Dong, L., Li, C., Liang, Y. & Chen, Y. Diffuse Reflectance Infrared Fourier Transform and Raman Spectroscopic Studies of MoO Dispersed on CeO Support. *Langmuir* **15,** 1693–1697 (1999).

70. Binet, C., Daturi, M. & Lavalley, J.-C. {IR} study of polycrystalline ceria properties in oxidised and reduced states. *Catal. Today* **50,** 207–225 (1999).

71. Seguin, L., Figlarz, M., Cavagnat, R. & Lassègues, J.-C. Infrared and Raman spectra of MOO3 molybdenum trioxides and MoO3·xH2O molybdenum trioxide hydrates. *Spectrochim. Acta Part A* **51,** 1323–1344 (1995).

72. Adams, S. CDW Superstructures in Hydrogen Molybdenum Bronzes HxMoO3. *J. Solid State Chem.* **149,** 75–87 (2000).

73. Köck, E.-M., Kogler, M., Bielz, T., Klötzer, B. & Penner, S. In Situ FT-IR Spectroscopic Study of CO2 and CO Adsorption on Y2O3 , ZrO2 , and Yttria-Stabilized ZrO2. *J. Phys. Chem. C* **117,** 17666–17673 (2013).

General Conclusions

The preparation of mixed oxides as proton conductors has been successful.

The synthesized samples (ZrEu_x, x=2, 5, 7, 9, 10, 12 and 15 mol.% of Eu_2O_3) exhibited the formation of solid solution with cubic fluorite-type structure up to 9 mol.% of Eu oxide dopant, from which a segregated cubic Eu oxide phase appears. The elemental characterization has shown a mesoporous homogeneous Zr-Eu mixed oxides, where homogeneous oxygen vacancies distribution is also expected.

The addition of Mo to ZrEu_5 sample (ZrEuMo_x samples, with x = 5, 7 and 10 mol.% of MoO_3) has not modified the Zr-Eu solid solution structure since the Mo oxide has been situated on the surface, preferentially on Eu atoms. The specific structure of Mo oxide is complex, but molybdates and polymolybdates have been formed in the surface, where the sample with the highest Mo loading is close to create a MoO_3 monolayer. The Mo-doped samples show bronzes formation (H_xMoO_3) over ~200 ºC and partial reduction to MoO_2 phase over 380 ºC under H_2 atmosphere.

The prepared mixed oxides exhibit ionic conductivity typical of a p-type semiconductor created by the presence of oxygen vacancies. They show activation energies around 1 eV according to a pure ionic conductor material. Moreover, the maximal conductivity is found for ZrEu_5 sample, indicating an optimal amount of dopant (5 mol.% of Eu_2O_3).

It has been demonstrated additional proton conductivity by Grotthuss' mechanism under wet conditions for low temperatures, where superficial water is still present. It is required dissociated water in the oxygen vacancies and superficial water to generate the proton conductivity. Thus, only for temperatures below ~300 ºC both conditions exist and an increment of the total conductivity is observed as is schematized in the figure:

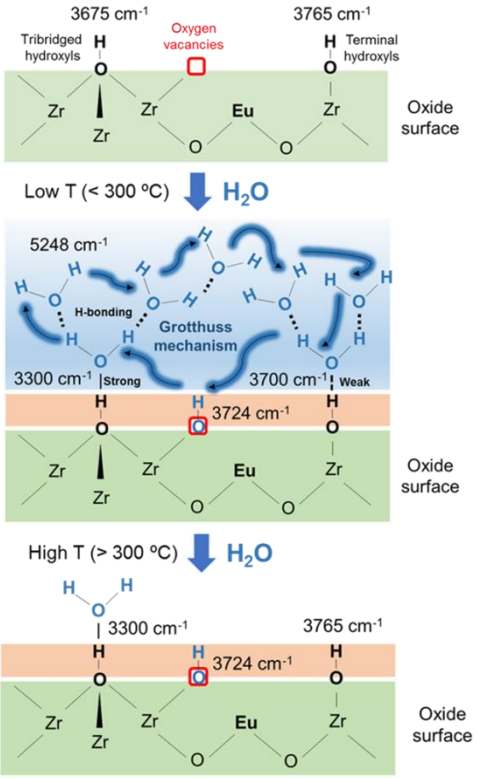

The catalytic experiments in WGS reaction at 80000 $ml \cdot h^{-1} \cdot g_{cat}^{-1}$ with physical mixture of PtCeAl catalyst and different proton conductors (ZrEu_x and ZrEuMo_x samples) in a mass ratio of 1:5 show that the presence of ionic conductor always increases the

activity of the reference PtCeAl catalyst in terms of CO conversion, being the benefit in good agreement with sample' proton conductivity observed by IS. Thus, the higher the conductivity, the higher the observed CO conversion. Moreover, the beneficial effect only appears when the catalyst starts to work, thereby acting as a promoter of the catalyst' proper mechanism in the WGS reaction. The role of proton conductors is then the promotion of the water activation step.

The change of the catalyst / ionic conductor ratio show that the activity promotion could occur at lower proton conductor charge. On the other side, the variation of the space velocity reveals different behaviours for Mo-doped and undoped materials in *Model* and *Industrial* conditions, due to the important interaction between the H_2 and the Mo oxide.

The structuration of the catalysts has been successful and thermal or internal diffusion problems can be neglected, supporting again that the observed promoter effect for the mixed sample is due to the improvement of the water activation step by the proton conductor.

The analysis of the catalyst' deactivation indicates a fast loss of activity probably due to the carbonate species formation on the support, which inhibits the water activation site. Indeed, the formation of these species is later observed by *operando* DRIFTS analysis on PtCeAl and ZrEuMo_5 samples in WGS reaction operation conditions.

The kinetic analysis according to a L-H mechanism of WGS reaction on PtCeAl+ZrEuMo_5 (1:5) sample shows indeed a low

value of the reaction order for the water (0.36 and 0.6 for powdered and structured samples, respectively) respect to those reported in the literature. This is in agreement with a reduction of the influence of the limiting water activation step by the addition of the proton conductor which provides labile dissociated water to react with adsorbed CO on Pt. These observations are also supported by *operando* DRIFTS experiments, where has been found bands assigned to OH in the oxygen vacancies by dissociation of the water coexisting with physisorbed water. Moreover, and unlike Mo-undoped sample (ZrEu_5), physisorbed water continue present at temperatures above 300 ºC related to the hydrated Mo oxide of the sample.

On the other side, high influence of H_2 – MoO_x interaction is observed above 300 ºC, which deflects the fit to an over-estimation of the CO conversion data. Therefore, further experiments are mandatory to elucidate the mechanism in these conditions, likewise more TPR analysis (meanly on variation of the heating ramp rate), which allow determine the Mo oxide reduction kinetics and can be then included in the proposed WGS reaction rate expression.

RESUMEN

La reacción de desplazamiento del gas de agua o Water Gas Shift (WGS) fue descubierta en 1780 por el físico italiano Felice Fontana.[1] Poco después, en 1783, Lavoisier la formuló:[2]

$$CO + H_2O \leftrightarrows CO_2 + H_2 \qquad [1]$$

Las primeras investigaciones de la reacción de WGS datan de 1888 y no fue hasta el s. XX cuando experimentó un gran desarrollo gracias al proceso de síntesis del amoniaco de la mano de Fritz Haber y la empresa BASF.[3,4] Durante todo este siglo, la producción de H_2 y su aplicación como vector energético fue en aumento, implicando así un amplio estudio de la reacción de WGS muy útil en todos estos procesos, ya que, además de aumentar la producción a H_2, disminuye a su vez la de CO, siempre presente y muy contaminante para los dispositivos que usan hidrógeno como combustible, como es el caso de las celdas de combustible.

En este contexto, el requerimiento de un mayor rendimiento de la reacción de WGS promovió el estudio y desarrollo de catalizadores que, teniendo en cuenta la exotermicidad de la reacción (-41 kJ/mol), era necesario un compromiso entre la termodinámica y la cinética. Desde la segunda mitad del s. XX y hasta la actualidad, la reacción de WGS se desarrolla industrialmente en dos reactores adiabáticos en serie. El primero, denominado reactor de alta temperatura (HT-WGS), opera entre 310 – 450 ºC sobre un catalizador de óxidos de Fe-Cr. En esta primera etapa se reduce el contenido de CO proveniente de los gases de reformado hasta una concentración *c.a.* 1-3 %. El segundo reactor, de baja temperatura (LT-WGS), opera entre 150 – 250 ºC sobre un catalizador de Cu reduciendo la concentración

de CO hasta niveles del 0.1 %.[4] Estos dos reactores, ampliamente establecidos a nivel industrial, requieren volúmenes muy elevados ya que la reacción de WGS se desarrolla a velocidades de ~3000 – 4000 h^{-1} en el reactor de alta temperatura y a ~1000 – 2000 h^{-1} en el de baja temperatura, requiriendo tamaños que los hacen inadecuados para una posible aplicación móvil.

Ante esta problemática y debido a la necesidad de generar combustibles y energía alternativos a los procedentes de los residuos fósiles, durante el s. XXI la producción de hidrógeno ha sufrido un gran desarrollo y, consecuentemente, una amplia investigación sobre catalizadores de WGS más eficientes. Además, el empleo de H_2 como combustible alternativo ha llevado a la búsqueda de catalizadores que permitieran velocidades espaciales de 40000 h^{-1} para su aplicabilidad en dispositivos móviles y, que además, evitaran desventajas como la piroforicidad del Cu o la toxicidad del Cr.[5,6] Tal es el caso de los catalizadores basados en metales preciosos (Pt, Au, Pd, Rh…) que, generalmente soportados sobre óxidos parcialmente reducibles, han proporcionado resultados muy prometedores a temperaturas intermedias y bajas. Sin embargo, estas formulaciones resultan aún ineficientes para su aplicabilidad móvil o a pequeña escala.[5,7]

De acuerdo con la multitud de estudios sobre el mecanismo de la reacción sobre los distintos catalizadores propuestos, se establecen dos mecanismos generales: el mecanismo redox y el mecanismo asociativo. El mecanismo desarrollado, o cuál prevalece más, depende de las condiciones de reacción y de la naturaleza del catalizador. Sin embargo, cualquiera que sea el mecanismo que se

desarrolle, ha quedado reflejado la importancia de la etapa de activación del agua, esto es, de la adsorción y disociación del agua, así como de su disponibilidad para reaccionar con el CO adsorbido. Así, se han encontrado importantes mejoras en el rendimiento de un catalizador cuando éste es soportado sobre óxidos capaces de adsorber y disociar agua.[5,8,9] También, diversos autores han realizado estudios cinéticos y mecanísticos, así como cálculos energéticos, donde la disociación de agua se presenta como etapa lenta y de alto requerimiento energético en la reacción de WGS, cualquiera que sea el mecanismo propuesto.[10–12] Además, diversas formulaciones catalíticas patentadas reflejan la presencia de óxidos mixtos que mejoran la capacidad de disociación y disponibilidad del agua para reaccionar con el CO.[13–15]

Consecuentemente, parece que la adición de óxidos mixtos y, más específicamente, aquellos que contienen tierras raras, son beneficiosos para el rendimiento de los catalizadores de WGS. Éstos parecen ser conductores protónicos, ya que dichos materiales, a través de sus vacantes de oxígeno (O_v) son capaces de disociar y difundir especies iónicas a través de su red,[16,17] facilitando, en este caso, la disociación del agua y su movilidad para reaccionar más fácilmente.

Así surge la idea y el objetivo de la presente tesis: el estudio de la influencia de óxidos mixtos como conductores protónicos añadidos físicamente a un catalizador tipo de WGS. Concretamente, un catalizador de Pt soportado sobre una CeO_2/Al_2O_3 comercial (Puralox, 20:80 ceria-alúmina), nombrado PtCeAl, y conductores

protónicos basados en zirconias cúbicas dopadas, ya que presentan conductividad protónica y alta estabilidad.[16,18,19]

Tanto el catalizador, PtCeAl, como los diversos conductores protónicos han sido sintetizados y ampliamente caracterizados (capítulo 3) mediante varias técnicas (detalladas en el capítulo 2). Concretamente, el catalizador ha sido sintetizado mediante impregnación húmeda del Pt sobre el soporte comercial. Las técnicas de caracterización realizadas han determinado la síntesis de un material mesoporoso de 110 m^2/g de superficie específica con un ~2 %pp. de Pt, tal y como se esperaba. Por su parte, el tamaño de partícula de Pt no ha podido ser determinado mediante DRX o TEM. Sin embargo, experimentos de adsorción de CO analizados *in situ* mediante espectroscopía FTIR han permitido estimar una alta dispersión de Pt (79 %) con un tamaño de partícula comprendido entre 1.5 – 2 nm, lo que explicaría que fueran difíciles de detectar mediante DRX o TEM. Esta alta dispersión queda también respaldada por el análisis EXAFS del material, donde el estudio de la perturbación tras excitar al cerio (Ce L_3-edge) no ha causado contribución correspondiente a la dispersión causada por los átomos de Pt superficiales.

Mediante el análisis XANES-EXAFS, se ha determinado la estructura del catalizador sintetizado, donde la γ-Al_2O_3 expone la cara (111), sobre la que casi una monocapa (~89 % de la monocapa) de ceria cúbica $Fm\bar{3}m$ es formada en estado oxidado Ce^{4+}.

Finalmente, el estudio de TPR en H_2 del catalizador determina que hay un exceso de consumo de hidrógeno debido, además de la

reducción del Pt (~220 ºC), a la reducción de posibles impurezas de especies carbonáceas así como de la ceria del soporte. Por lo tanto, se ha determinado el proceso de activación del catalizador en un 10 % de H_2 a 350 ºC durante 30 min., para asegurar así la completa reducción del Pt sin sobrepasar la temperatura de calcinación.

Por otro lado, conductores iónicos han sido preparados mediante co-precipitación. Óxidos mixtos de ZrO_2 y Eu_2O_3 (ZrEu_x) con distinto contenido molar del óxido de europio (x = 2, 5, 7, 9, 10, 12 y 15 % molar de Eu_2O_3) y óxidos mixtos de ZrO_2, Eu_2O_3 y MoO_3 (ZrEuMo_x) con ZrO_2-Eu_2O_3 en proporción molar fija de 95-5 y distinto contenido molar del óxido de molibdeno (x = 5, 7 y 10 % molar de MoO_3) han sido sintetizados.

Los materiales ZrEu_x han formado solución sólida con estructura cúbica tipo fluorita ($Fm\bar{3}m$) hasta un contenido máximo de 9 % molar de Eu_2O_3, a partir del cual fase segregada de óxido de europio es identificable. La formación de estas soluciones sólidas y similares han sido ampliamente estudiadas.[20,21] La adición de Mo, sin embargo, no ha supuesto ninguna alteración en la estructura de la solución sólida formada por el Zr y el Eu, con lo que la introducción del Mo en la estructura puede ser, en principio, descartada. Esta estimación queda respaldada cuando los análisis por FRX y XPS determinan que las composiciones de todos los óxidos mixtos están en concordancia con los valores deseados en la síntesis, sin embargo, los de XPS muestran una clara concentración de Mo en la superficie. Además, el estudio de estos materiales mediante espectroscopías UV, RAMAN y XPS han permitido concluir que el óxido de Mo no sólo se coloca en

la superficie, sino que lo hace de manera preferencial sobre los átomos de europio, influyendo en el entorno y simetría de éste afectando a su luminiscencia y a su energía de absorción. Además, de acuerdo con los datos recogidos de la literatura y con los experimentos mediante espectroscopía RAMAN con láser rojo, se ha podido determinar que el óxido de molibdeno superficial está formando molibdatos y polimolibdatos octaédricos sin llegar a formar una monocapa de MoO_3 completa. Estas estructuras superficiales también quedan justificadas mediante los análisis de reducción con H_2 (TPR) ya que muestran un desplazamiento a más bajas temperaturas con respecto a una muestra MoO_3 no soportada.[22] Además, los perfiles de reducción muestran muy probablemente la formación de estructuras *bronzes* (H_xMoO_3) en torno a los 200 ºC previas a la reducción hacia la fase MoO_2 (T > 380 ºC).[23]

Todos estos materiales muestran una mesoporosidad en torno a 2 - 3 nm y cuya superficie específica es mayor para los sólidos que contienen Mo (~80 m^2/g). Además, la creación homogénea de vacantes de oxígeno es esperada ya que las soluciones sólidas ZrEu_x muestran homogeneidad en composición interior y superficial, cuya formulación en notación de Kröger-Vink queda:

$$x\,Eu_2O_3\,(ZrO_2) \rightarrow 2x\,Eu'_{Zr} + 3x\,O_O^x + x\,V_O^{2\bullet} \qquad [2]$$

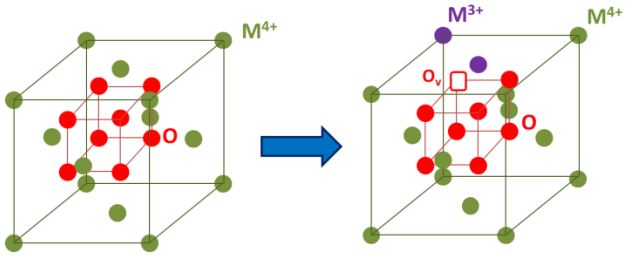

Esquema 1. Formación de V_O en la estructura de ZrO_2 (M^{4+}) dopada con europio (M^{3+}).

Estos defectos (V_O) son los que permiten la conductividad iónica y la cual ha sido medida mediante espectroscopía de impedancia (IS) en distintas atmósferas desde temperatura ambiente hasta 700 ºC (capítulo 4).

Cabe destacar que la máxima conductividad la presenta la muestra ZrEu_5 (Figura 1) en todas las atmósferas en el rango de temperatura investigado. Esto indica un contenido óptimo de dopante (5 % molar de Eu_2O_3) de acuerdo con este tipo de conductores iónicos.[16] Los materiales preparados en este trabajo son semiconductores tipo p, cuya conductividad se debe a la movilidad de las vacantes formadas. El aumento de dopante implica una mayor formación de vacantes de oxígeno, las cuales, a partir de un cierto valor, se asocian con los iones dopantes (Eu en este caso) disminuyendo su movilidad, aumentando la energía de activación requerida y, consecuentemente, reduciendo su conductividad.

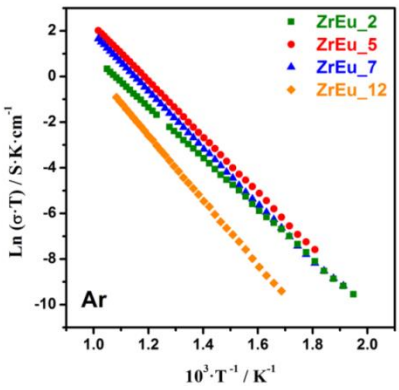

Figura 1. Conductividad total en atmósfera inerte (Ar) de las muestras preparadas en el rango de temperatura investigado.

Además, las medidas de impedancia en atmósfera húmeda así como el análisis de adsorción de agua mediante *in situ* DRIFTS, han permitido determinar la aparición de conductividad protónica a bajas temperaturas (< 300 ºC) cuya contribución supone el aumento de conductividad total de la muestra en este rango de operación (Figura 2a). Esta conductividad protónica sigue el mecanismo de Grotthuss, el cual requiere de agua disociada en las vacantes de oxígeno y de agua superficial fisisorbida, cuyo modelo se representa en la Figura 2b.

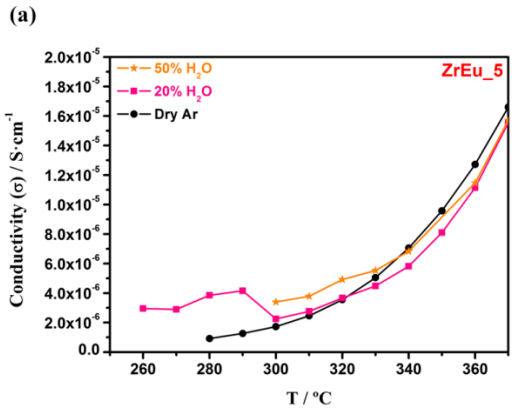

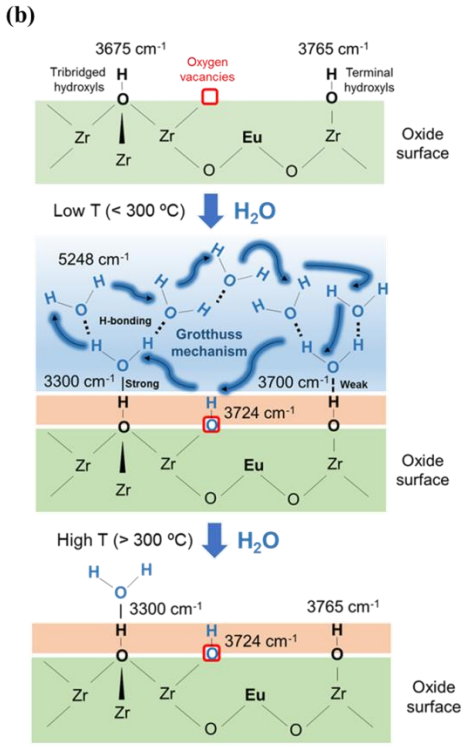

Figura 2. (a) Conductividad de la muestra ZrEu_5 en atmósfera inerte (seca) y húmeda frente al aumento de la temperatura. (b) Modelo de la conductividad protónica y sus condiciones sobre los materiales sintetizados (ZrO_2 dopado con Eu).

Posteriormente, en el capítulo 5, se ha investigado la actividad catalítica del catalizador de PtCeAl combinado físicamente con los diversos conductores iónicos sintetizados (ZrEu_x y ZrEuMo_x) en la reacción de WGS. Manteniendo siempre las mismas condiciones de operación (tamaño de partícula, volumen de lecho de reacción, velocidad espacial de 80000 $ml \cdot h^{-1} \cdot g_{cat}^{-1}$) y cantidad de catalizador (0.1g de PtCeAl), se han ensayado dos composiciones de alimentación, denominadas *Model* (4.5 % CO y 30 % H_2O diluidos en N_2) e *Industrial* (9 % CO, 30 % H_2O, 11 % CO_2 y 50 % H_2). La

velocidad espacial empleada es muy elevada con respecto a las usadas comercialmente y en los estudios recogidos en la literatura[24,25] con el objetivo de dificultar el alcance de conversión de equilibrio termodinámico, para así ampliar el rango de temperaturas de control cinético y poder observar el efecto del conductor iónico. Además, atendiendo a una futura aplicación móvil, es de especial interés que el efecto promotor del conductor protónico sea aplicable a altas velocidades espaciales.

Todas los catalizadores conformados por la mezcla física (en relación másica 1:5 de catalizador:conductor iónico) proporcionan en todos los casos ensayados un mayor rendimiento catalítico, en términos de conversión de CO, con respecto al catalizador PtCeAl (Figura 3). Además, la comprobada inactividad de los conductores protónicos por sí solos (datos no mostrados), junto con las curvas obtenidas en la Figura 3, donde el efector promotor aparece a partir de los 270 – 290 ºC cuando el propio catalizador PtCeAl ya muestra actividad por sí mismo, indica que los óxidos mixtos no proporcionan actividad catalítica extra, sino que actúan como meros ayudantes del catalizador en la activación del agua en el propio mecanismo desarrollado por el catalizador PtCeAl. Estos conductores protónicos aumentan la cantidad de agua disociada y disponible para reaccionar con el CO adsorbido en el Pt, mejorando así esta etapa limitante y quedando reflejado en un mayor rendimiento del catalizador. Además, esta observación queda también secundada por la diferencia de actividad entre los distintos sistemas catalíticos mezcla. Como puede observarse en la Figura 3, la actividad catalítica presentada por el sistema PtCeAl + ZrEu_12 es claramente menor que los demás

sistemas mezcla (con ZrEu_2, ZrEu_5 y ZrEu_7), lo cual está en perfecta congruencia con la tendencia en conductividades iónicas obtenidas para cada material (ver Figura 1).

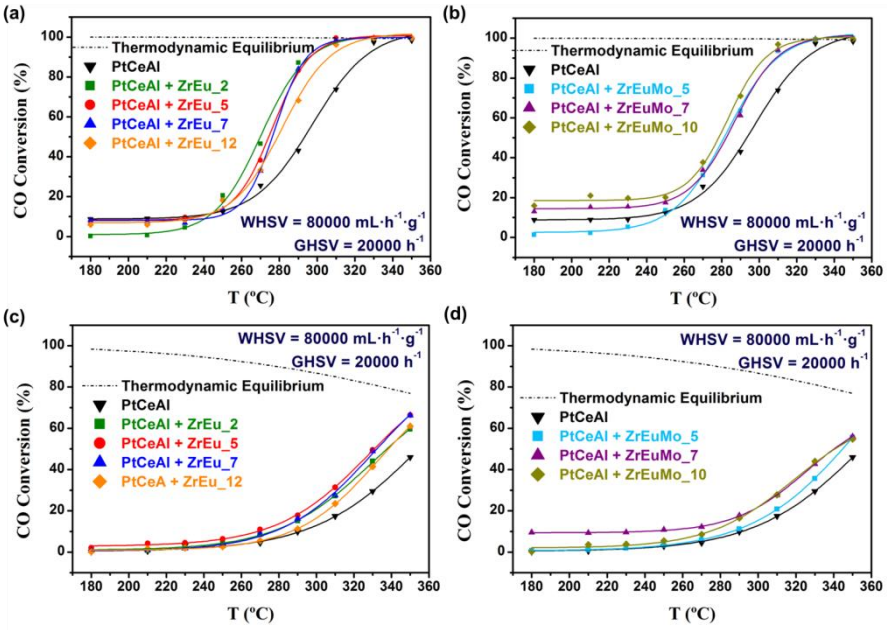

Figura 3. Actividad catalítica de los sistemas conformados por la mezcla física (1:5) de PtCeAl y los distintos conductors protónicos, comparados con el catalizador PtCeAl. (a) y (b) en condiciones Model. (c) y (d) en condiciones Industrial. GHSV = 20000 h^{-1}. WHSV = 80000 $mL \cdot h^{-1} \cdot g_{cat}^{-1}$.

Además, se han llevado a cabo ensayos variando el ratio catalizador – conductor iónico y variando la velocidad espacial. En ellos se ha comprobado que el conductor iónico está en exceso, pudiendo reducirse su cantidad y, así, aún más el volumen de lecho, llevando a una mayor velocidad espacial, especialmente interesante para aplicaciones móviles. Por su parte, el estudio de la velocidad espacial ha indicado distintos comportamientos según la composición del flujo de alimentación (*Model* o *Industrial*) y distinta tendencia

cuando el Mo está presente, tal que en condiciones *Model* la disminución de actividad con el aumento de velocidad espacial es menor para el catalizador con Mo. Probablemente, la mayor capacidad de adsorción de agua aportada por el material con Mo conlleve a un mayor efecto promotor con respecto a los materiales sin Mo, aguantando así mejor el aumento de velocidad espacial. Sin embargo, en las condiciones *Industrial*, los materiales con Mo muestran una menor conversión a altas velocidades espaciales, probablemente debido a la alta concentración de H_2 presente en el medio que, como se ha discutido anteriormente, interacciona con el óxido de Mo de la muestra formando bronzes y reduciéndolo.

Durante el capítulo 5 también se estudia la estructuración del catalizador PtCeAl y del sistema catalítico PtCeAl+ZrEuMo_5 (1:5) sobre micromonolitos metálicos, para descartar así que la favorable influencia del óxido mixto se pudiera deber a efectos térmicos en vez de a un efecto promotor del conductor protónico. La caracterización elemental llevada a cabo demuestra la conservación de las propiedades físico-químicas de los materiales tras su estructuración. Además, se han obtenido espesores de capa ~ 1 µm y ~ 3 µm para los catalizadores estructurados de PtCeAl y PtCeAl+ZrEuMo_5 respectivamente, pudiendo también descartar así posibles problemas de difusión interna[26,27] y, consecuentemente, que la mejora observada anteriormente se debiera a un efecto de dilución y mejora de difusión (térmica o másica).

De acuerdo con todo lo anterior, los ensayos catalíticos de los catalizadores estructurados (en las mismas condiciones de operación

que las muestras en polvo) en la reacción de WGS muestran también una clara mejora de actividad para el sistema conformado por la mezcla de catalizador y conductor iónico:

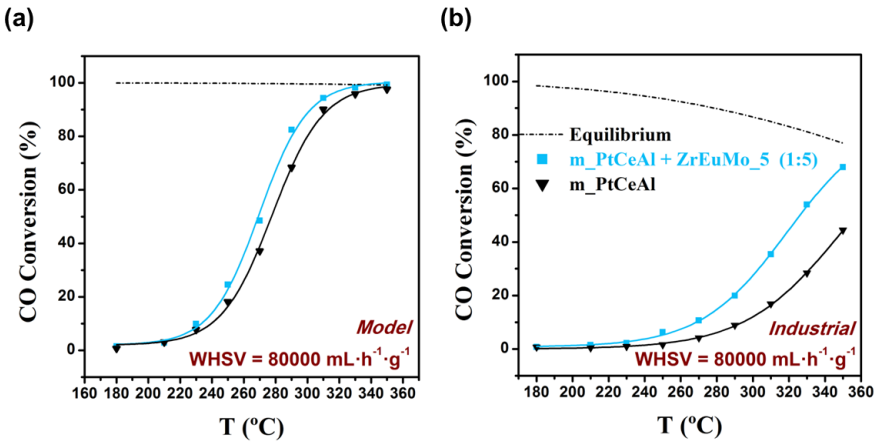

Figura 4. Actividad catalítica de los sistemas estructurados en condiciones Model (a) y en condiciones Industrial (b). WHSV = 80000 mL·h^{-1}·g$_{cat}^{-1}$.

Por último, el estudio de estabilidad del catalizador también se realiza en este capítulo poniendo de manifiesto una gran desventaja de los catalizadores basados en metales preciosos: su rápida desactivación. Se observa una rápida pérdida de actividad (~ 50 % en unas 40 h) antes de su estabilización y que, por tanto, deberá ser tenida en cuenta en el estudio cinético. La comparación entre la desactivación del catalizador mezcla y del PtCeAl solo, además de una estudio de los datos recogidos en la literatura, parece indicar que la desactivación es principalmente debida a la deposición de especies carbonáceas generadas durante la reacción (carbonatos, formiatos…) sobre los sitios activos, especialmente sobre los sitios de activación del agua en el soporte.

Finalmente, en el último capítulo 6, el estudio cinético de los catalizadores PtCeAl+ZrEuMo_5 (1:5) en polvo y estructurado a la misma velocidad espacial (80000 $ml \cdot h^{-1} \cdot g_{cat}^{-1}$) es analizado. Cabe mencionar que dichos experimentos se llevaron a cabo en colaboración con el Prof. Gianpiero Groppi y la Prof. Alessandra Beretta una estancia de 3 meses en el grupo de *Catalisi e Processi Catalitici* (Laboratory of Catalysis and Catalytic Processes – LCCP) de la *Politecnico di Milano* (Milán, Italia).

De dichos experimentos, mediante un análisis de aproximación a un reactor integral, se han podido extraer expresiones de la ecuación de velocidad para la reacción de WGS que, de acuerdo con la literatura, la velocidad de reacción apenas está influenciada por la concentración de CO, pero es altamente modificada positivamente por la concentración de agua y negativamente por la concentración de H_2. Con respecto a la muestra en polvo, se determina la ausencia de problemas de difusión interna mediante el cálculo del módulo de Thiele (< 1). Para la ecuación cinética propuesta (Ecuación 3, ver Chapter 6, Eq.6.15), se obtiene un buen ajuste de los datos experimentales (Figura 5), con una energía de activación, E_a, de 80.62 kJ/mol (Tabla 1) comparable a las encontradas para muestras similares en la literatura.[28,29] Sin embargo, cabe destacar un significante menor valor del orden de reacción de agua ($\beta = 0.36$), el cual contribuye una vez más a la idea del efecto promotor del óxido mixto como conductor protónico, que aumenta y favorece la concentración de agua disponible para la reacción, haciendo que la velocidad de reacción esté menos limitada por este factor.

$$-r_{CO} = \frac{kP_{H_2O}^{\beta}(1-\eta)}{1+AP_{H_2}^{\alpha}} \cdot D_i \cdot \sigma_{CO} \qquad [3]$$

Tabla 1. Parámetros cinéticos calculados mediante el ajuste de la Ecuación 3 a los datos experimentales para la reacción de WGS sobre el catalizador PtCeAl+ZrEuMo_5 (1:5) en polvo.

k_0	$5.35 \cdot 10^{-8}$
A	0.052
E_a (kJ/mol)	80.62
β (H_2O)	0.359
T_0 (K)	473.15
R ($kJ \cdot mol^{-1} \cdot K^{-1}$)	$8.31 \cdot 10^{-3}$
α (H_2)	0.428

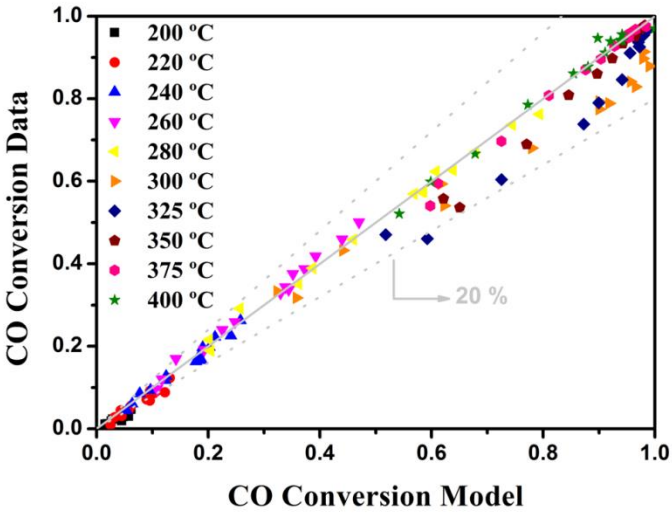

Figura 5. Representación de la conversión de CO calculada mediante el ajuste de la Ec. 3 con los datos recogidos en la Tabla 1 vs. la conversión de CO observada (experimental) para la reacción de WGS sobre el catalizador en polvo PtCeAl+ZrEuMo_5 (1:5).

Se puede observar también una ligera sobre-estimación de los datos calculados en el rango de temperaturas de 300 – 350 ºC. Este hecho podría deberse a la aparición de la reacción de metanación. Sin embargo, la cantidad de metano apreciada es despreciable y, además, se da por encima de los 350 ºC. Por otro lado, es más probable que este efecto se deba a la interacción que tiene lugar entre el H_2 de la mezcla y el óxido de Mo del catalizador que, como se ha discutido previamente, a los ~300 º C se pueden estar formando bronzes y una reducción parcial del Mo. Este hecho se observa más intensamente en el análisis cinético de la muestra estructurada (Figura 6), cuya expresión cinética ha tenido que ser modificada con respecto a la anterior de la muestra en polvo (Ecuación 4).

$$-r_{CO} = \frac{kP_{H_2O}^{\beta}(1-\eta)}{\left(1+AP_{H_2}^{\alpha}+BP_{CO_2}^{\delta}\right)^2} \cdot D_i \qquad [4]$$

Tabla 2. Parámetros cinéticos calculados mediante el ajuste de la Ecuación 4 a los datos experimentales para la reacción de WGS sobre el catalizador estructurado PtCeAl+ZrEuMo_5 (1:5).

k_0	$3.90 \cdot 10^{-9}$
A	$5.07 \cdot 10^{-10}$
B	$2.88 \cdot 10^{-6}$
E_a (kJ/mol)	71.28
β (H_2O)	0.60
T_0 (K)	473.15
R ($kJ \cdot mol^{-1} \cdot K^{-1}$)	$8.31 \cdot 10^{-3}$
α (H_2)	1.79
δ (CO_2)	1.10

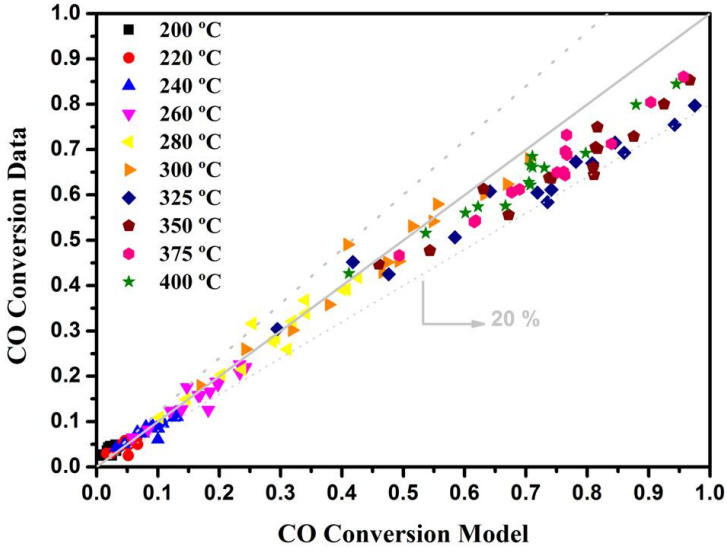

Figura 6. Representación de la conversión de CO calculada mediante el ajuste de la Ec. 4 con los datos recogidos en la Tabla 2 vs. la conversión de CO observada (experimental) para la reacción de WGS sobre el catalizador estructurado PtCeAl+ZrEuMo_5 (1:5).

En este caso y, de acuerdo con la discusión anterior, la destacada sobre-estimación a alta temperatura y la modificación de la ecuación que ha llevado a tener que incluir otro término de adsorción (CO_2) cuyo ajuste proporciona, además, un valor inusualmente alto para el orden de reacción del H_2 (α = 1.79), indican que el término de adsorción de H_2 considerado puede ser inadecuado. Cabría la posibilidad de considerar que los procesos de formación de bronze y reducción parcial del óxido de Mo a dichas temperaturas analizados previamente por TPR fueran tenidos en cuenta en la ecuación de velocidad, como otro término de adsorción cuya constante se definiera mediante la ecuación de Arrhenius, mostrando así su efecto a las temperaturas adecuadas. Para ello sería interesante previamente

realizar estudios de la cinética de los procesos estudiados mediante TPR y, así, incluirlo posteriormente en la ecuación 3.

El último análisis desarrollado durante esta tesis doctoral (estudios en operando de la reacción de WGS mediante DRIFTS en condiciones Model e Industrial) ha llevado a la confirmación de la presencia de bandas asociadas a especies OH generadas en las vacantes de oxígeno (~3724 cm^{-1}) así como la presencia de agua superficial (~5239 cm^{-1}) que llevan a la aparición de conductividad protónica. Además del agua superficial observada en los materiales ZrEu_x (capítulo 4), cuando el Mo está presente hay mayor cantidad de agua molecular en la superficie, observándose bandas asociadas a óxido de Mo hidratado (~3633 cm^{-1}).

Finalmente, dichos experimentos en condiciones de operación de la reacción de WGS ha puesto de manifiesto la formación de especies carbonáceas (carbonatos, carboxilatos, formiatos) sobre el soporte ceria/alúmina así como sobre la zirconia. Estas observaciones están en concordancia con la desactivación del catalizador previamente observada y discutida.

REFERENCIAS

1. Burns, D. T., Piccardi, G. & Sabbatini, L. Some people and places important in the history of analytical chemistry in Italy. *Microchim. Acta* **160,** 57–87 (2008).

2. Lavoisier, A. L. *Oeuvres de Lavoisier, Vol. II*. (Imprimerie Impériale, 1862).

3. Pattabathula, V. & Richardson, J. Introduction to Ammonia Production. *Chem. Eng. Prog.* **112,** (2016).

4. Rhodes, C., Hutchings, G. J. & Ward, A. M. Water-gas shift reaction: finding the mechanistic boundary. *Catal. Today* **23,** 43–58 (1995).

5. Ratnasamy, C. & Wagner, J. P. Water Gas Shift Catalysis. *Catal. Rev. Sci. Eng.* **51,** 325–440 (2009).

6. Kam, R., Scott, J., Amal, R. & Selomulya, C. Pyrophoricity and stability of copper and platinum based water-gas shift catalysts during oxidative shut-down/start-up operation. *Chem. Eng. Sci.* **65,** 6461–6470 (2010).

7. Farrauto, R. J. *et al.* Precious Metal Catalysts Supported on Ceramic and Metal Monolithic Structures for the Hydrogen Economy. *Catal. Rev. Sci. Eng.* **49,** 141–196 (2007).

8. Panagiotopoulou, P., Papavasiliou, J., Avgouropoulos, G., Ioannides, T. & Kondarides, D. I. Water-gas shift activity of doped Pt/CeO2 catalysts. *Chem. Eng. J.* **134,** 16–22 (2007).

9. González-Castaño, M., Ivanova, S., Ioannides, T., Centeno, M. A. & Odriozola, J. A. Deep insight into Zr/Fe combination for successful Pt/CeO2/Al2O3 WGS catalyst doping. *Catal. Sci. Technol.* (2017). doi:10.1039/C6CY02551J

10. Grabow, L. C., Gokhale, A. A., Evans, S. T., Dumesic, J. A. & Mavrikakis, M. Mechanism of the water gas shift reaction on Pt: First principles, experiments, and microkinetic modeling. *J. Phys. Chem. C* **112,** 4608–4617 (2008).

11. Germani, G. & Schuurman, Y. Water-Gas Shift Reaction Kinetics Over ?-Structured Pt/CeO2/Al2O3 Catalysts. *Am. Inst. Chem. Eng.* **52,** 1806–1813 (2006).

12. Clay, J. P., Greeley, J. P., Ribeiro, F. H., Delgass, W. N. & Schneider, W. F. DFT Comparison of Intrinsic WGS Kinetics over Pd and Pt. *J. Catal.* **320,** 106–117 (2014).

13. Daza Bertrand, L., Benito González, M. J., Isabel Gómez, R. & Padilla Palma, R. Catalizadores para conversión de monóxido de carbono en hidrógeno y su uso en el proceso catalítico de enriquecimiento en hidrógeno de una corriente de gas que puede alimentar una pila de combustible. 11 (2008).

14. Ilinich, O. M., Farrauto, R. J., Reuttinger, W. F. & Yang, X. Precious metal water-gas shift catalyst with oxide support modified with rare earth elements. 6 (2010).

15. Wachsman, E. D., Yoon, H. S., Oh, T. & Li, J. Proton conducting membranes for hydrogen production and separation. 25 (2015).

16. Malavasi, L., Fisher, C. A. J. & Islam, M. S. Oxide-ion and proton conducting electrolyte materials for clean energy applications: structural and mechanistic features. *Chem. Soc. Rev.* **39,** 4370–4387 (2010).

17. Kreuer, K. Proton Conductivity : Materials and Applications. *Chem. Mater.* **8,** 610–641 (1996).

18. Kreuer, K. D. Aspects of the formation and mobility of protonic charge carriers and the stability of perovskite-type oxides. *Solid State Ionics* **125,** 285–302 (1999).

19. Xia, X.-L., Liu, Z.-G., Ouyang, J.-H. & Zheng, Y. Preparation, Structural Characterization, and Enhanced Electrical Conductivity of Pyrochlore-type (Sm1-xEux)2Zr2O7 Ceramics. *Fuel Cells* **12,** 624–632 (2012).

20. Fabrichnaya, O. *et al.* Heat capacity for the Eu2Zr2O7 and phase relations in the ZrO2-Eu2O3 system: Experimental studies and calculations. *Thermochim. Acta* **558,** 74–82 (2013).

21. Maram, P. S., Ushakov, S. V., Weber, R. J. K., Benmore, C. J. & Navrotsky, A. In situ Diffraction from Levitated Solids Under Extreme Conditions-Structure and Thermal Expansion in the Eu2O3-ZrO2 System. *J. Am. Ceram. Soc.* **98,** 1292–1299 (2015).

22. Chary, K. V. R., Reddy, K. R., Kishan, G., Niemantsverdriet, J. W. & Mestl, G. Structure and catalytic properties of molybdenum oxide catalysts supported on zirconia. *J. Catal.* **226,** 283–291 (2004).

23. Ressler, T., Wienold, J. & Jentoft, R. E. Formation of Bronzes during Temperature-programmed Reduction of MoO3 with Hydrogen - An In situ XRD and XAFS Study. *Solid State*

Ionics **141-142,** 243–252 (2001).

24. Dupont, N. *et al.* Specificities of micro-structured reactors for hydrogen production and purification. *Int. J. Hydrogen Energy* **32,** 1443–1449 (2007).

25. Gonzalez Castaño, M., Reina, T. R., Ivanova, S., Centeno, M. A. & Odriozola, J. A. Pt vs. Au in water-gas shift reaction. *J. Catal.* **314,** 1–9 (2014).

26. Laguna, O. H., González Castaño, M., Centeno, M. A. & Odriozola, J. A. Microreactors technology for hydrogen purification: Effect of the catalytic layer thickness on CuOx/CeO2-coated microchannel reactors for the PROX reaction. *Chem. Eng. J.* **275,** 45–52 (2015).

27. Potemkin, D. I., Snytnikov, P. V., Belyaev, V. D. & Sobyanin, V. A. Preferential CO oxidation over Cu/CeO2-x catalyst: Internal mass transport limitation. *Chem. Eng. J.* **176-177,** 165–171 (2011).

28. Phatak, A. A. *et al.* Kinetics of the water-gas shift reaction on Pt catalysts supported on alumina and ceria. *Catal. Today* **123,** 224–234 (2007).

29. Grabow, L. C., Gokhale, A. A., Evans, S. T., Dumesic, J. A. & Mavrikakis, M. Mechanism of the Water Gas Shift Reaction on Pt: First Principles, Experiments, and Microkinetic Modeling. *J. Phys. Chem. C* **112,** 4608–4617 (2008).

ANNEXES

(19) OFICINA ESPAÑOLA DE PATENTES Y MARCAS

ESPAÑA

(11) Número de publicación: **2 595 937**

(21) Número de solicitud: 201500441

(51) Int. CI.:

B01J 23/63 (2006.01)
B01J 23/38 (2006.01)
B01J 23/72 (2006.01)

(12) SOLICITUD DE PATENTE A1

(22) Fecha de presentación:
02.06.2015

(43) Fecha de publicación de la solicitud:
03.01.2017

(56) Se remite a la solicitud internacional:
PCT/ES2016/070412

(71) Solicitantes:
UNIVERSIDAD DE SEVILLA (83.0%)
Po. de las Delicias s/n - Pabellón de Brasil
41013 Sevilla ES y
CONSEJO SUPERIOR INVESTIGACIONES CIENTIFICAS (17.0%)

(72) Inventor/es:
ODRIOZOLA GORDON, Jose Antonio;
LYUBOMIROVA IVANOVA, Svetlana;
ROMERO SARRIA , Francisca ;
GARCÍA MONCADA , Nuria ;
GONZÁLEZ CASTAÑO , Miriam y
CENTENO GALLEGO, Miguel Ángel

(54) Título: **Complejo catalítico conformado por la mezcla de catalizador y conductor iónico**

(57) Resumen:
Complejo catalítico conformado por la mezcla de catalizador y conductor iónico.
La invención describe un complejo catalítico formado por la mezcla física de un catalizador y un conductor iónico, y su uso en la conversión de monóxido de carbono en hidrógeno, a través de la reacción de desplazamiento del gas de agua. El objeto de la presente invención es el desarrollo de sistemas más eficientes tanto en actividad como en estabilidad para la conversión de monóxido de carbono en hidrógeno a través de la reacción de desplazamiento del gas de agua o "water gas shift" mediante la generación de un sistema compuesto por un catalizador en íntimo contacto físico con un conductor iónico.

ES 2 595 937 A1

Edited by Pascal Granger, Vasile I. Parvulescu,
Serge Kaliaguine, and Wilfrid Prellier

Perovskites and Related Mixed Oxides

Concepts and Applications

Volume 2

WILEY-VCH
Verlag GmbH & Co. KGaA

32
Development of Robust Mixed-Conducting Membranes with High Permeability and Stability

Tomás Ramírez-Reina, José Luis Santos, Nuria García-Moncada, Svetlana Ivanova, and José Antonio Odriozola

32.1
Overview

Literally almost 90% of the periodic table can form perovskite compounds with an ideal compositional formula of $A^{2+}B^{4+}O_3$, the compositions $A^{+}B^{5+}O_3$ and $A^{3+}B^{3+}O_3$ also being possible if the total charge of the A and B cations equals that of oxygen [1,2]. The A-site cation can be a rare earth, alkali, or alkaline earth ion, such as La, Na, Ca, Sr, or Ba, while the B-site cation is a transition metal, such as Ti, Zr, Fe, Co, Ni, or Cu [3,4].

The perovskite cubic structure allows partial substitution of A and B cations by other cations with different ionic radius and valence [4]. This substitution, however, could result in the formation of other structures, such as orthorhombic or rhombohedral. Another effect of the substitution is the perovskite nonstoichiometry, resulting from the deficiency or excess of A, B, or O sites. The A and O sites could be partially empty still preserving the perovskite structure, in contrast to the smaller energetically unfavorable B sites. Thus, compounds of interest are principally of $ABO_{3-\delta}$ type, where the δ parameter is envisaged as the number of vacancies or defects and it is directly associated with the oxygen permeation capacity of the perovskite [5]. Adequate metal substitutions at the A and B sites could carefully tailor the conduction properties. Substitutions at the A sites are related to the concentration of oxygen vacancies, while substitutions at the B sites are responsible for the electron conductivity. In these mixed conductors, the ionic conductivity takes place by the so-called hopping mechanism in which oxide ions move from one oxygen vacancy to another; in addition, electronic conduction occurs through B^{n+}–O–$B^{(n+1)+}$ pairs formed to ensure the overall electroneutrality of the material. Therefore, materials of $A_xA'_{1-x}B_yB'_{1-y}O_{3-\delta}$ composition result in mixed conductors whose conductivity depends on the nature of the doping cations [1,2]. The defect chemistry of perovskites decides their application. The ability to retain the structure, although slightly deformed to accommodate different charges, allows continuous adjustment of the properties, for example, high degree of oxygen nonstoichiometry and high ionic, electronic,

Perovskites and Related Mixed Oxides: Concepts and Applications, First Edition.
Edited by Pascal Granger, Vasile I. Parvulescu, Serge Kaliaguine, and Wilfrid Prellier.